Titre: Title:	Réinventer les systèmes RF pour l'ère post-5G : vers une convergence harmonique entre communication, détection et transfert de puissance
Auteur: Author:	Thomas Micallef
Date:	2025
Type:	Mémoire ou thèse / Dissertation or Thesis
Référence: Citation:	Micallef, T. (2025). Réinventer les systèmes RF pour l'ère post-5G : vers une convergence harmonique entre communication, détection et transfert de puissance [Thèse de doctorat, Polytechnique Montréal]. PolyPublie. https://publications.polymtl.ca/69317/

URL de PolyPublie: PolyPublie URL:	https://publications.polymtl.ca/69317/
Directeurs de recherche: Advisors:	Ke Wu
Programme: Program:	Génie électrique

POLYTECHNIQUE MONTRÉAL
affiliée à l'Université de Montréal

Réinventer les systèmes RF pour l'ère post-5G : vers une convergence harmonique entre communication, détection et transfert de puissance

THOMAS MICALLEF
Département de génie électrique

Thèse présentée en vue de l'obtention du diplôme de *Philosophiæ Doctor*
Génie électrique

Octobre 2025

POLYTECHNIQUE MONTRÉAL
affiliée à l'Université de Montréal

Cette thèse intitulée :

Réinventer les systèmes RF pour l'ère post-5G : vers une convergence harmonique entre communication, détection et transfert de puissance

présentée par **Thomas MICALLEF**
en vue de l'obtention du diplôme de *Philosophiæ Doctor*
a été dûment acceptée par le jury d'examen constitué de :

Chahé NERGUIZIAN, président
Ke WU, membre et directeur de recherche
Elham BALADI, membre
Tayeb DENIDNI, membre externe

DÉDICACE

Ad Majorem Dei Gloriam

REMERCIEMENTS

Je tiens tout d'abord à exprimer ma plus profonde gratitude à mon directeur de recherche, le professeur Ke Wu, pour m'avoir offert l'opportunité d'effectuer cette thèse au sein du centre de recherche Poly-Grames. Sa rigueur scientifique, son inégalable vision des systèmes de demain, et sa confiance constante ont été des piliers tout au long de ce parcours. C'est un privilège d'avoir pu bénéficier de ses conseils et de son encadrement à la fois éminemment exigeant et particulièrement bienveillant.

Je souhaite également remercier tout particulièrement le professeur Xiaoqiang Gu, ami précieux et superviseur officieux, dont la disponibilité, la patience et la maîtrise technique ont profondément nourri mes réflexions. Nos échanges, souvent informels mais toujours stimulants, ont été essentiels dans l'élaboration de plusieurs parties de cette thèse. Son soutien quasi-quotidien, à la fois scientifique et humain, a été pour moi un moteur.

Je tiens aussi à souligner le rôle fondamental de l'équipe du centre Poly-Grames, particulièrement Dr. Pascal Burasa, M. Traian Antonescu et M. Steve Dubé, dont l'expertise, le professionnalisme et la réactivité ont rendu possible la réalisation concrète de nombreux prototypes et bancs d'essais. Leur accompagnement dans les phases expérimentales a largement contribué à la solidité et à la crédibilité des solutions présentées.

À tous ceux – collègues, collaborateurs, amis, membres de la communauté Polytechnique, et membres de la section IEEE de Montréal – qui, de près ou de loin, ont enrichi ce travail et cette aventure humaine : je vous remercie.

Enfin, je tiens à exprimer ma profonde gratitude à ma famille la plus proche. À ma compagne, Francesca, pour son amour, sa patience et sa présence indéfectible, ainsi qu'à ses parents, pour leur bienveillance. À ma mère, Patricia, à mon père, Emmanuel, à ma belle-mère, Nathalie, à mes frères, Jean et Pierre, et à mes grands-parents, pour leur soutien et leur confiance tout au long de ces années. Leur appui discret mais fondamental m'a donné la force de persévérer dans les étapes les plus exigeantes de ce parcours. Ce travail leur revient en grande partie.

RÉSUMÉ

À l'ère post-5G, les systèmes sans fil sont appelés à dépasser leur fonction classique de transmission de données pour intégrer simultanément des capacités de détection, de communication et de transfert d'énergie. Cette convergence fonctionnelle représente une rupture de paradigme dans la conception des architectures radiofréquences, historiquement pensées comme des blocs dédiés, indépendants et spécialisés. L'objet de cette thèse est de démontrer qu'il est possible de concevoir des transcepteurs radiofréquences multifonctionnels, à la fois compacts, efficaces et capables de supporter plusieurs fonctions simultanément sur des ressources partagées, notamment harmoniques.

Pour répondre à cet objectif, la thèse s'appuie sur trois ensembles de contributions majeures. Premièrement, elle exploite les propriétés non-linéaires de diodes pour générer des harmoniques larges bandes, permettant la création de canaux fréquentiels multiples à partir d'un seul signal fondamental. Deuxièmement, elle introduit une méthode de fusion de sous-bandes non contiguës, qui améliore significativement la résolution radar tout en s'adaptant à la fragmentation du spectre. Troisièmement, elle propose l'architecture d'un récepteur interférométrique multi-bande capable de démoduler des signaux de communication et de détecter simultanément des signaux radar sur plusieurs bandes harmoniques, jusqu'à la septième dans ce travail.

L'ensemble de ces contributions sont validées par des démonstrations théoriques et expérimentales, incluant des prototypes de radars non-linéaires multifréquentiels, ainsi qu'un système de surveillance biomédicale en temps réel combinant détection des signes vitaux et communication bidirectionnelle, entre autres.

L'enjeu principal de cette démonstration est de proposer une voie crédible vers l'unification fonctionnelle des systèmes radiofréquences de demain, adaptée aux contraintes de miniaturisation, de sobriété énergétique et de congestion spectrale. Ces résultats prometteurs ouvrent la voie à de nouvelles générations de dispositifs sans fil intelligents pour les villes connectées, la santé numérique, les systèmes embarqués et les applications spatiales.

ABSTRACT

In the post-5G era, wireless systems are evolving beyond mere data transmission to incorporate simultaneous sensing, communication, and energy transfer capabilities. This functional convergence marks a paradigm shift in radiofrequency system design, traditionally centered on dedicated, isolated subsystems. This thesis aims to demonstrate that it is possible to design compact, efficient, and truly multifunctional radiofrequency transceivers capable of operating several functions simultaneously over shared hardware resources and spectrum, in particular the harmonics.

The research is structured around three core parts of contributions. First, it leverages the nonlinear properties of diodes to generate wideband harmonics, enabling the synthesis of multiple frequency bands from a single input chirp. Second, it introduces a non-contiguous sub-band fusion technique, which enhances radar resolution while efficiently adapting to fragmented spectrum conditions. Third, the work presents a multiband interferometric receiver architecture that can concurrently demodulate communication signals and perform radar sensing using up to the seventh harmonic band in this work.

All of these contributions are validated through analytical modeling, simulation, and experimental prototyping—including a nonlinear radar sensing setup and a real-time biomedical monitoring system that combines vital sign detection with bidirectional wireless communication, among others.

The overarching challenge addressed by this work is the unification of radiofrequency functions into a single, intelligent, and spectrally efficient platform, aligned with the demands of future wireless systems in terms of integration, power efficiency, and performance. The proposed approaches pave the way for next-generation multifunctional wireless devices tailored for smart cities, digital health, embedded applications and spatial systems.

TABLE DES MATIÈRES

LISTE DES TABLEAUX

LISTE DES FIGURES

LISTE DES SIGLES ET ABRÉVIATIONS

ADAS	Advanced Driver Assistance Systems.
ADC	Analog-to-Digital Converter.
ADS	Advanced Design System.
AI	Artificial Intelligence.
AM	Amplitude Modulation.
AOA	Angle of Arrival.
AWG	Arbitrary Waveform Generator.
BPSK	Binary Phase Shift Keying.
CDM	Code Domain Multiplexing.
CL	Conversion Loss.
CMOS	Complementary Metal-Oxide-Semiconductor.
CW	Continuous Wave.
DC	Direct Current.
DDS	Direct Digital Synthesis.
DFRC	Dual-Functional Radar-Communication.
DSP	Digital Signal Processor.
EV	Electric Vehicle.
EVM	Error Vector Magnitude.
FDD	Frequency Domain Diplexing.
FDM	Frequency Domain Multiplexing.
FFT	Fast Fourier Transform.
FM	Frequency Modulation.
FMCW	Frequency Modulated Continuous Wave.
FoM	Figure of Merit.
FPGA	Field-Programmable Gate Array.

FSK	Frequency Shift Keying.
I/Q	In-phase/Quadrature.
IBFD	In-band Full-Duplex.
ID	Identification.
IF	Intermediate Frequency.
IoT	Internet of Things.
ISAC	Integrated Sensing and Communication.
ISI	Intersymbol Interference.
ISM	Industrial, Scientific, and Medical.
JCAS	Joint Communication and Sensing.
JRC	Joint Radar and Communication.
LHCP	Left-Handed Circularly Polarized.
LNA	Low Noise Amplifier.
LO	Local Oscillator.
MIMO	Multiple Input Multiple Output.
NF	Noise Figure.
Op-Amp	Operational Amplifier.
PA	Power Amplifier.
PC	Power Combiner.
PCB	Printed Circuit Board.
PD	Power Divider.
PRF	Pulse Repetition Frequency.
QAM	Quadrature Amplitude Modulation.
RadCom	Radar-Communication.

RCS	Radar Cross Section.
RF	Radio Frequency.
RFID	Radio Frequency Identification Devices.
RHCP	Right-Handed Circularly Polarized.
Rx	Receiver.
SDR	Software-Defined Radio.
SIMO	Single Input Multiple Output.
SISO	Single Input Single Output.
SNR	Signal-to-Noise Ratio.
SPICE	Simulation Program with Integrated Circuit Emphasis.
SRD	Strep Recovery Diode.
SSPW	Single Sinusoid Pulsed Waveform.
SWIPT	Simultaneous Wireless Information and Power Transfer.
TDM	Time Domain Multiplexing.
TFMCW	Trapezoidal Frequency Modulated Continuous Wave.
TS	Time Slot.
Tx	Transmitter.
UWB	Ultra-Wideband.
VRM	Virtual Receiver Matrix.
WPD	Wilkinson Power Divider.
WPT	Wireless Power Transfer.
WRN	Wireless Radar Network.
WSN	Wireless Sensing Network.

LISTE DES ANNEXES

CHAPITRE 1 INTRODUCTION

1.1 Motivations et objectifs

Les systèmes sans fil de l'ère post-5G, 6G et au-delà, ne se limiteront plus à la seule transmission d'information : ils tendront vers une convergence fonctionnelle entre communication, détection, localisation, transfert de puissance, récupération d'énergie et intelligence artificielle. Cette évolution est portée par les besoins croissants en terme de connectivité intelligente dans des environnements de plus en plus complexes tels que les villes intelligentes, les systèmes de santé, les véhicules autonomes et les prochains systèmes satellitaires, entre autres. Dans ce contexte, le développement de plateformes multifonctionnelles représente un tournant stratégique dans l'architecture des systèmes radiofréquences et constitue un nouveau paradigme.

L'objet de cette thèse est de démontrer qu'il est possible de concevoir des architectures radiofréquences capables de combiner simultanément la communication de données, la détection radar et, dans certains cas, le transfert de puissance, au sein d'un système unifié, sans compromis majeur sur les performances. Cette démonstration repose sur l'exploitation novatrice de techniques telles que la génération harmonique large bande, la fusion de sous-bandes non contiguës, et la détection non linéaire par composants passifs.

L'enjeu de cette démonstration est double. Il s'agit, d'une part, de répondre à la contrainte physique et spectrale qui pèse sur les systèmes radiofréquences actuels, en permettant une cohabitation systémique de plusieurs fonctions sur des ressources partagées, d'autre part, cette approche vise à accroître l'efficacité énergétique, la compacité et l'intelligence des futurs dispositifs sans fil, dans une logique de durabilité et de déploiement massif. Cette multifonctionnalité ouvre la voie à des usages jusqu'alors incompatibles, comme la détection passive par rétrodiffusion dans des dispositifs à très faible consommation, ou la surveillance biomédicale sans contact.

Le problème qui se pose est celui de l'intégration cohérente de fonctions fondamentalement hétérogènes — aux exigences souvent conflictuelles — dans une architecture commune. Par exemple, la communication impose une stabilité spectrale, tandis que la détection radar requiert des signaux à large bande et à haute linéarité temporelle. Le transfert d'énergie, quant à lui, induit des contraintes de couplage et d'efficacité de conversion. À cela s'ajoute la contrainte croissante de congestion spectrale, qui limite l'attribution de bandes de fréquence dédiées à chaque fonction.

Face à ces défis, cette thèse de doctorat explore un ensemble de solutions qui répondent aux objectifs suivants :

- **Objectif 1 :** la compréhension de l'état de l'art des systèmes radiofréquences multifonctions afin de mieux situer les solutions techniques proposées ;
- **Objectif 2 :** l'utilisation de composants passifs non-linéaires pour la génération de signaux harmoniques à faible coût et faible consommation ;
- **Objectif 3 :** la réutilisation intelligente des ressources spectrales via la fusion de sous-bandes dans les systèmes radars multi-bandes, afin de créer une bande de fréquence synthétique ;
- **Objectif 4 :** le développement d'une plateforme de radar multi-bandes multi-harmoniques utilisant la fusion des sous-bandes ;
- **Objectif 5 :** l'analyse des signaux vitaux dans le domaine de la santé en utilisant plusieurs bandes de fréquences simultanément, tout en permettant la communication de données ;
- **Objectif 6 :** la conception de récepteurs interférométriques multi-bandes multi-harmoniques capables de traiter plusieurs fonctions en parallèle.

Les travaux présentés dans cette thèse s'inscrivent dans une perspective à la fois théorique, expérimentale et applicative, et visent à démontrer la faisabilité, la robustesse et la pertinence de ces nouvelles approches pour les systèmes sans fil intégrés de demain.

1.2 Plan de la thèse et contributions

Les travaux présentés dans cette thèse ont donné lieu à une production scientifique significative, incluant sept articles de journaux évalués par des pairs, six articles présentés lors de conférences internationales, un article dans une conférence nationale, une présentation par affiche, ainsi qu'un brevet actuellement en cours de validation.

Cette thèse adopte un format par articles, réunissant six publications scientifiques évaluées par les pairs. Chaque chapitre est rédigé dans la langue originale de rédaction et de parution des articles.

Chapitre 1 : Introduction

Ce chapitre introductif détaille les motivations originelles de ce travail de thèse et présente le plan de la thèse ainsi que les contributions de chaque chapitre.

Chapitre 2 : Article 1 : Multifunction Transceiver for Data Communication, Radar Sensing and Power Transfer.

Ce chapitre de revue présente un état de l'art sur les architectures émergentes capables d'intégrer plusieurs fonctions sans fil — notamment la communication, la détection radar, et le transfert de puissance — dans une même plateforme. Il souligne que cette intégration soulève des défis majeurs en raison des exigences souvent conflictuelles en termes de spécification d'architecture de transcepteur et de traitement du signal.

Ainsi, trois couples d'intégration sont examinés. Le premier est le couple radar et communication en considérant les cas coopératifs et non coopératifs, ainsi que les architectures conventionnelles et interférométriques. Le deuxième est le couple communication et récupération d'énergie en s'appuyant sur la récupération d'énergie radiofréquence et le recyclage interne. Le troisième est le couple radar et transfert d'énergie via des approches innovantes telles que la rétrodiffusion harmonique et les radars auto-alimentés.

Ce chapitre propose finalement une feuille de route vers des systèmes véritablement multifonctionnels en analysant les scénarios de multiplexage et les différentes configurations possibles.

Chapitre 3 : Article 2 : Diode-Based Wideband Harmonic Generation for Future Nonlinear Sensing Applications.

Ce chapitre étudie la génération d'harmoniques à haute fréquence (GHz), essentielle pour les technologies de détection non linéaire de nouvelle génération.

Une analyse théorique et expérimentale est menée sur les générateurs harmoniques à base de diodes, en particulier les diodes Schottky, varactor et à récupération par étapes. Des équations en domaine temporel sont développées pour estimer les amplitudes harmoniques en fonction des tensions d'entrée et des conditions de polarisation, en prenant en compte les non-linéarités résistives et capacitives spécifiques à chaque type de diode. Des prototypes sont fabriqués et mesurés, alimentés par un signal à 1 GHz et une bande de fréquence totale de sortie de 600 MHz. Les résultats montrent une variation moyenne de la puissance de sortie de ±3,4 dBm pour la SMS7630 et ±5,2 dBm pour la SMV1213.

Les résultats confirment que ces dispositifs sont adaptés aux applications à faible puissance et sans batterie, tout en apportant un sous-bassement théorique robuste pour la conception de systèmes radiofréquences avancés.

Chapitre 4 : Article 3 : Enhancing Radar System Performances via the Fusion of Scattered Non-Contiguous Frequency Sub-Bands.

Cet article présente une technique originale de « superfusion » permettant de combiner plusieurs sous-bandes de fréquences non contiguës (et de largeurs différentes) afin d'améliorer les performances clefs des radars, notamment la résolution en distance et en vitesse.

La méthode consiste à partitionner la bande requise d'un radar à modulation de fréquence en plusieurs sous-bandes plus étroites et dispersées dans le spectre, facilitant ainsi une utilisation plus efficace des ressources spectrales tout en évitant les interférences dues à la congestion du spectre. Un cadre théorique complet est établi pour modéliser ce processus de fusion et anticiper les performances. L'expérimentation repose sur trois sous-bandes centrées à 1, 2 et 3 GHz avec des largeurs respectives de 100, 200 et 300 MHz. La fusion aboutit à une bande effective de 600 MHz, permettant une résolution de 37,6 cm, et permet de distinguer des cibles espacées de 40 cm — performance impossible à atteindre en utilisant uniquement une des sous-bandes.

La méthode proposée est une solution facilement applicable pour les systèmes radars opérant dans des environnements congestionnés. En outre, la méthode se distingue par une complexité de traitement particulièrement réduite pour la phase de fusion.

Chapitre 5 : Article 4 : Improving Radar System Resolution through Nonlinear Sensing.

Ce chapitre développe une méthode de détection non linéaire visant à améliorer la résolution des radars à modulation de fréquence au travers de la génération harmonique par diode et de la fusion de la première, de la deuxième et de la troisième bande harmonique, concepts détaillés aux chapitre 3 et 4, respectivement.

Un balayage fréquentiel unique de 100 MHz est utilisé pour alimenter une diode SMS7630, générant, de fait, trois bandes de fréquence indépendantes. Ces bandes sont ensuite fusionnées pour produire une bande synthétique équivalente de 600 MHz. La résolution obtenue est de 42 cm, ce qui représente une amélioration d'un facteur 4,4 par rapport à l'utilisation seule de la bande fondamentale de 100 MHz. Le comportement fréquentiel et thermique du dispositif est également étudié : les résultats montrent une variation de puissance de ±3,4 dBm sur la bande utile, et une stabilité remarquable avec ±1 dBm de fluctuation moyenne malgré des variations de température de 120°C.

Ce système de radar démontre le potentiel considérable de la détection non linéaire pour repousser les limites actuelles des radars, tout en utilisant une seule source d'alimentation et des composants passifs.

Chapitre 6 : Article 5 : Multi-Mode Multi-Band ISAC Technique for Real-Time Healthcare Monitoring.

Ce chapitre introduit un système intégré de communication et de détection multi-mode et multi-bande spécifiquement conçu pour la surveillance médicale en temps réel, en particulier dans des environnements intérieurs avec la surveillance de personnes âgées.

Le système allie communication bidirectionnelle et détection radar à double mode, avec un traitement localisé des signaux pour améliorer la réactivité. Deux bandes de fréquence sont simultanément utilisées (100 MHz et 200 MHz), permettant à la fois : un suivi de position avec une précision de 68,7 cm, une mesure de la fréquence respiratoire avec une résolution de ±15,50 mHz (via radar à déphasage). Le système fonctionne en continu, assurant la transmission de données même pendant les cycles radar.

Cette approche démontre que les systèmes intégrés de communication et de détection multi-bandes peuvent jouer un rôle clef dans le déploiement de réseaux de santé intelligents.

Chapitre 7 : Article 6 : Harmonic Interferometric Receiver for Multifunction Wireless Systems.

Ce chapitre présente un récepteur interférométrique linéaire multifonction à quatre ports, capable d'exploiter la diversité harmonique afin d'intégrer simultanément les fonctions de communication et de détection.

L'architecture utilise un schéma de multiplexage hybride s'appuyant sur les harmoniques impaires jusqu'au 7e ordre de la fréquence de conception. Un prototype est conçu pour valider ce concept et montre la capacité du système à démoduler efficacement des signaux modulés en amplitude (QAM 4, 32, 64 et 128) tout en détectant des chirps radars sur quatre bandes : 2.75, 8.25, 13.75 et 19.25 GHz. Il s'agit du premier récepteur interférométrique multibande exploitant jusqu'à la septième harmonique pour assurer des fonctions radiofréquences multiples en parallèle.

Ce travail constitue une avancée significative dans la conception de récepteurs radiofréquences multifonctionnels pour les systèmes sans fil complexes de demain.

Chapitre 8 : Conclusion.

Ce dernier chapitre conclut la thèse en soulignant les principaux apports scientifiques et en ouvrant la voie à de potentielles extensions des travaux présentés.

CHAPITRE 2 ARTICLE 1 : MULTIFUNCTION TRANSCEIVER FOR DATA COMMUNICATION, RADAR SENSING AND POWER TRANSFER

Thomas Micallef, Intikhab Hussain et Ke Wu

Publié dans : *Electromagnetic Science*
Date de parution : 24 Février 2025

2.1 Abstract

The future of wireless systems is anticipated to revolutionize human connectivity through a diverse range of applications. The integration of multiple wireless functionalities into a unified system presents a critical challenge due to conflicting requirements in transceiver architecture and signal processing. Recent investigations are directing attention towards the development of systems that serve dual functions, like simultaneous wireless information and power transfer and radar-communication, aimed at boosting operational efficiency and ensuring seamless communication among different wireless capabilities. This review paper aims to discuss architectural aspects of the integration of radar sensing, data communication and power transfer. Firstly, the integration of radar sensing and data communication is studied for both cooperating and non-cooperating radar systems with conventional and interferometric architectures. Secondly, the power harvesting approach and internal energy recycling are discussed for the fusion of data communication and energy harvesting. Thirdly, radar sensing and power transfer integration is considered with special focus on harmonic backscattering and self-powered radars. Lastly, a roadmap for next-generation multifunction systems is outlined by considering several scenarios of multiplexing and architectures.

2.2 Introduction

The future of wireless systems, fundamentally propelled by continuous innovations in Radio Frequency (RF) and microwave technology, promises a vast and dynamic array of applications. The full extent of their potential is hard to foresee due to their increasing complexity and expansive reach. As electromagnetic waves span the globe at every frequency, wireless technologies are set to drive the advancement of human knowledge and exploration into both well-known and unexplored realms. These systems have already transformed the way we connect with the world [1, 2], necessitating the development of adaptive, scalable, and reconfigurable RF/microwave transceivers. Key wireless applications, such as data communication, radar sensing, and power transfer [3], as shown in Figure 2.1, are foundational to wireless technology and critical to its future evolution.

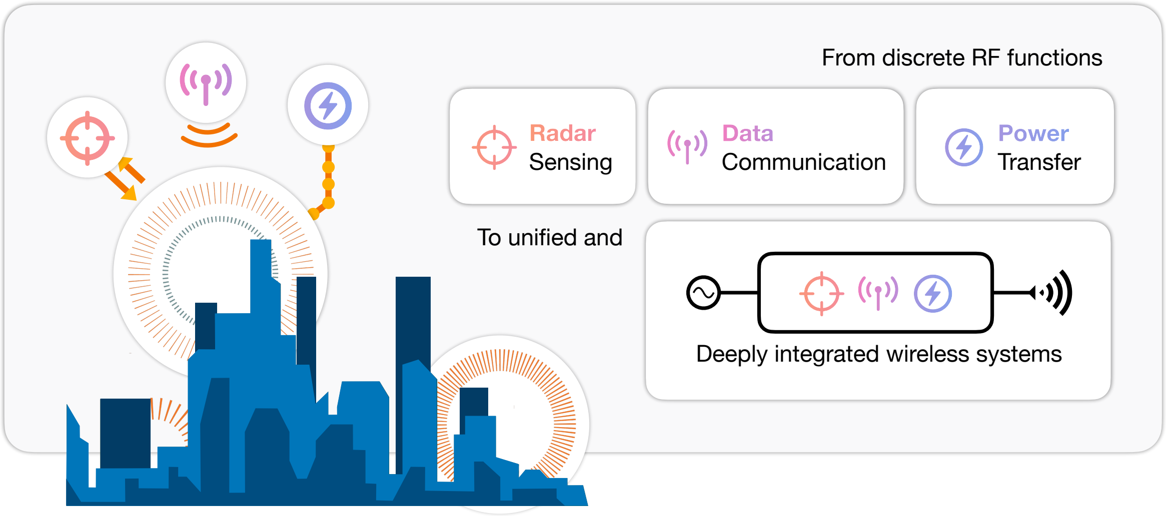

FIGURE 2.1 The three core functionalities of wireless technology—radar sensing, data communication, and power transfer—can be seamlessly integrated and unified within a single architecture [3].

The integration of multiple wireless functionalities into a unified system has gained prominence due to its advantages in achieving a smaller form factor, reduced costs, enhanced spectral efficiency, smarter functional interplay, and lower power consumption [4–6]. However, the fundamental challenge arises from the distinct operating principles of these functions, each imposing stringent and often conflicting requirements on transceiver architecture, waveform design, and signal processing. These complexities underscore the multifaceted obstacles in developing a truly unified multifunctional wireless system.

Conventional and past multifunction wireless systems have typically been implemented by placing multiple independent transceiver architectures side by side, each handling a distinct function on a shared hardware platform [7, 8]. While functional, this approach falls short of creating an intelligent, fully integrated wireless platform where diverse functions seamlessly interact to maximize the benefits of joint operations. Recent research efforts have focused on unifying multiple functions within a single system, such as Simultaneous Wireless Information and Power Transfer (SWIPT) [9–16], wirelessly powered backscatter communication [17–20], Radar-Communication (RadCom). RadCom systems—also known as Dual-Functional Radar-

Communication (DFRC), Joint Communication and Sensing (JCAS), or recently popularized Integrated Sensing and Communication (ISAC)—have been particularly well explored in terms of signal waveforms and RF transceiver architectures [21–24]. Interest in these dual-function systems is rapidly increasing, as evidenced by the growing number of publications over time, as shown in Figure 2.2.

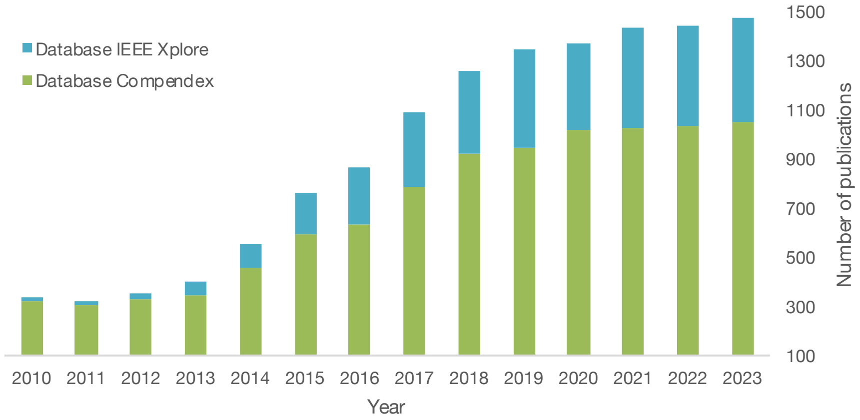

FIGURE 2.2 The number of publications on dual-function systems in the Compendex and IEEE Xplore databases has steadily increased over the past decade, with an average annual growth rate of 13%.

Emerging sustainable intelligent wireless technologies are paving the way for the integration of at least two key functions within a single system [25]. This functional fusion and convergence promise to create smart, energy-efficient wireless platforms by incorporating energy recycling [26, 27] and power harvesting techniques [28–32] in a RadCom system, thereby uniting all three fundamental functionalities : data communication, radar sensing, and power transfer. In this article, we revisit dual-function systems from an RF front-end perspective, examining their advantages and limitations. We also review recent advancements in combining or integrating two distinct operations, such as radar sensing with data communication, data communication with energy harvesting, and radar sensing with energy harvesting. Finally, we outline a roadmap for next-generation multifunctional systems that seamlessly integrate data communication, radar sensing, and power transfer.

2.3 Radar Sensing and Data Communication

Joint Radar and Communication (JRC) or ISAC systems have emerged as fundamental components of novel and advanced architectures, sparking ongoing debates within the field

[33–39]. The simultaneous utilization of radar sensing and data communication has never been more crucial due to several compelling reasons [40]. Firstly, it enhances safety across various domains, such as automotive and aerospace applications. For example, JRC enables moving vehicles to detect and communicate with one another, reducing the risk of collisions and improving overall road safety [41]. This capability supports Advanced Driver Assistance Systems (ADAS), which are essential for advancing autonomous driving and mobility [42]. The same scenarios can be envisaged for the safety of drones in flight where JRC would play a critical role.

Additionally, the integration of radar and data communication improves flexibility and reliability. In logistics and warehouse management, JRC facilitates real-time tracking of parcels and materials, enhancing efficiency and strengthening supply chain reliability [43]. Furthermore, JRC is anticipated to be a defining feature of next-generation wireless networks (6G and beyond) [44], expected to reach maturity around 2030. These networks will demand diverse functionalities, from ultra-high-speed data transfer to low-latency parametric sensing, making JRC crucial for meeting these requirements.

A significant advantage of JRC is its potential to address spectral congestion by combining communication signals with radar pulses or utilizing the same frequency band sequentially [45, 46]. By sharing the same frequency band for both radar sensing and data communication, the required bandwidth can be reduced [47]. To implement these functionalities, three primary multiplexing techniques can be used within the same architecture : Time Domain Multiplexing (TDM), Frequency Domain Multiplexing (FDM), and Code Domain Multiplexing (CDM) [22, 23]. These methods involve operating at the same frequency band at different times, using non-overlapping frequency bands simultaneously, or encoding signals differently, as illustrated in Figure 2.3. The choice of multiplexing technique is determined by design considerations and waveform engineering, rather than the specific architecture or type of radar (cooperative or non-cooperative).

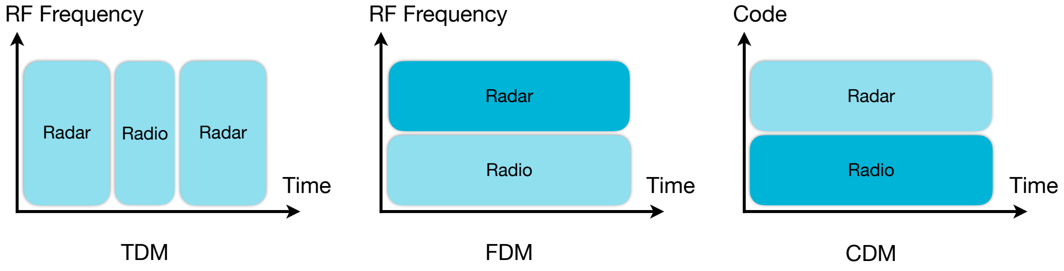

FIGURE 2.3 A simple description of TDM, FDM and CDM techniques applied to the fusion of radar sensing and data communication.

By allocating resources by dividing signals into time slots TDM, frequency bands FDM, or unique codes CDM, multiplexing methods such as TDM, FDM, and CDM allow several users or functions to effectively use a single communication channel. The FDM architecture offers several advantages over TDM. Notably, FDM enables simultaneous radar sensing and data communication within the same time slot, making it suitable for real-time applications. Additionally, FDM can avoid potential issues associated with TDM, such as echo signal interference from radar operations that could affect subsequent timeslots [48]. However, TDM has its own advantages. One significant benefit is that it helps mitigate spectral congestion by allowing both functions to share the same frequency band, thus optimizing bandwidth usage for multifunctional purposes. In contrast, FDM requires distinct carrier frequencies for radar and communication, which increases circuit complexity and necessitates more advanced antenna designs. TDM, on the other hand, can utilize a common antenna, simplifying the overall system. CDM is another approach that allows multiple signals to be transmitted simultaneously at the same carrier frequency by employing unique codes [49]. While CDM can provide more secure data transmission [50], it does increase the required bandwidth of the transmitted signal. However, to separate and decode signals, CDM systems architecturally need correlation-based signal processing, which increases computing complexity but resists interference through efficient code separation [51]. Main recent trends in CDM-based RadCom systems leverage the spectrum-spreading phase-coding technique [52, 53].

From a RF front-end architecture perspective, several approaches exist for realizing multi-functional systems and circuits. Most current systems rely on super-heterodyne or double-heterodyne transceivers, where incoming RF signals are down-converted using multiplicative mixers [54]. However, an alternative architecture, the multiport interferometric receiver, first introduced around 1993-1994 as a novel solution to heterodyne techniques [55], presents an evolution in multifunctional system design, as illustrated in Figure 2.4.

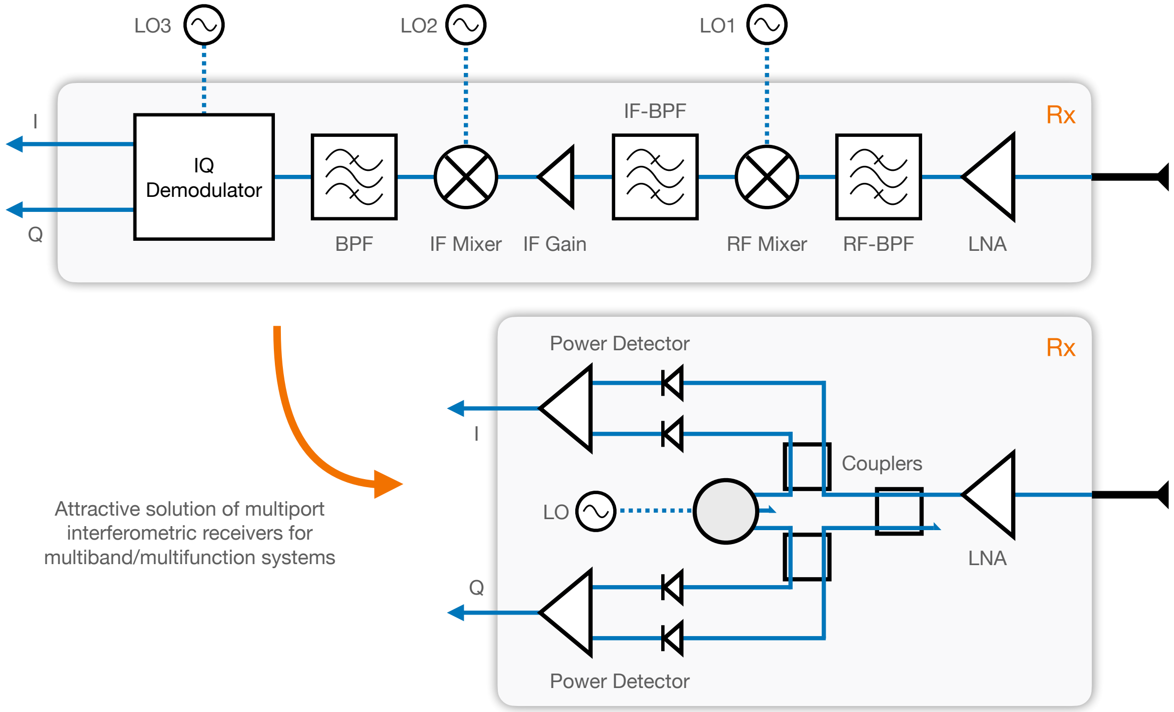

FIGURE 2.4 Conceptual evolution of receiver architectures from a standard double superheterodyne receiver to a multiport interferometric-based receiver.

Compared to traditional heterodyne architectures, the multiport interferometric receiver offers a cost-effective option for multifunctional applications, owing to its linear interferometric mechanism, which supports wide bandwidth operation and low power consumption [56]. This technique uses additive mixing to down-convert the RF signal, significantly reducing the filtering requirements typically needed in conventional architectures.

For applications like Software-Defined Radio (SDR) or Ultra-Wideband (UWB) systems, which demand wideband or multiband flexibility, the multiport interferometric approach provides distinct advantages over heterodyne and homodyne schemes [57]. To guarantee accurate target identification and range resolution for radar applications, the suggested architecture places a high priority on output power, low noise figure, and high instantaneous bandwidth [58]. Long- and short-range detection are among the operating circumstances where features like adaptive gain control and frequency tuning further maximize performance [59].

To facilitate data transfer and compliance with communication standards, interferometric-based communication systems are designed with an emphasis on linearity and modulation fidelity, among other specificities [60] The architecture makes use of reconfigurable RF front-end components, such as variable gain amplifiers and tunable filters, to enable effective mode switching and dynamic resource allocation to meet the varying requirements of radar and communication systems [61]. In addition, Complementary Metal-Oxide-Semiconductor (CMOS) single-chip integration of such interferometric architecture was presented by [62] while enabling low-cost, low-complexity, low Direct Current (DC) power and broad bandwidth at 60 GHz in 0.13um technology. More recently, a 300-GHz-CMOS-based communication interferometric receiver was presented in a 65-nm process [63]. Both designs feature small-scale footprints of 2.5 mm2 and 1.5 mm2, respectively. Over the past decade, interest in RF/microwave front-end architectures has increasingly turned toward interferometric solutions, positioning interferometric receivers as a competitive alternative poised to challenge existing technologies.

The following section explores and describes advanced RF/microwave front-end architectures that integrate both radar sensing and data communication functionalities. It provides a detailed discussion of both conventional and interferometric transceiver designs, covering their applications in both cooperative and non-cooperative radar systems.

2.3.1 Non-Cooperating Radar and Data Communication

Non-cooperative radars, also referred to as primary radars, operate based on the principle of echolocation and do not require prior acquiescence or active response from the monitored target. The subsequent sub-section details dual-functional front-end architectures, including both conventional and interferometric transceivers, designed for such radar systems.

Using Conventional Transceivers

In [47], a cutting-edge dual-function architecture based on TDM is built upon a heterodyne transceiver design, utilizing a Single Input Multiple Output (SIMO) antenna configuration, as illustrated in Figure 2.5. This system features a Direct Digital Synthesis (DDS) controlled by a Field-Programmable Gate Array (FPGA), which transmits both radar information (Frequency Modulated Continuous Wave (FMCW) signal) and communication data at a frequency of 5.8 GHz.

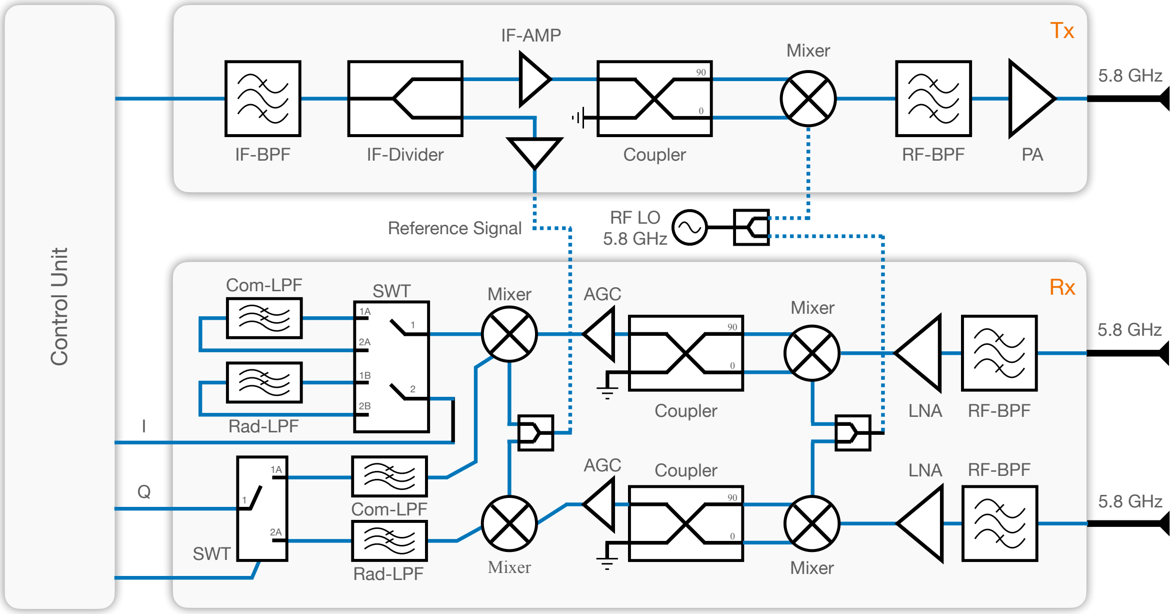

Figure 2.5 The block diagram of a heterodyne-based transceiver architecture employing TDM for non-cooperative radar and radio communication within the 5.8 GHz frequency band. The system enables AOA detection through a dual-antenna setup. The control unit manages the sequential transmission of radar signals and communication data, ensuring their time-sharing operation [47].

By integrating both the transmitter and receiver on a single board, the architecture benefits from shared reference and Local Oscillator (LO) signals. The Intermediate Frequency (IF) signal is upconverted to RF and then amplified through a Power Amplifier (PA). The receiver front-end employs two separate antennas for Angle of Arrival (AOA) detection. The incoming RF signals are amplified by Low Noise Amplifiers (LNAs), downconverted by a first mixer, and then demodulated by a second mixer for signal analysis. With a bandwidth of 150 MHz, this system supports AOA detection, as well as ranging and velocity estimation, and achieves a communication data rate of 25 Mb/s.

A notable feature of this architecture is its reconfigurability : the system can switch between radar and communication modes on command and can operate either jointly or in a single mode. This software-defined design feature represents a significant advancement in integrating radar sensing and data communication functionalities.

An alternative method for achieving simultaneous dual functions is through FDM. As described in [64], this approach in this example allocates separate frequency bands for radar and data communication : radar operates at 750 MHz, while data communication utilizes a 1.5 GHz carrier frequency. The architecture in question is based on a traditional heterodyne design, as depicted in Figure 2.6.

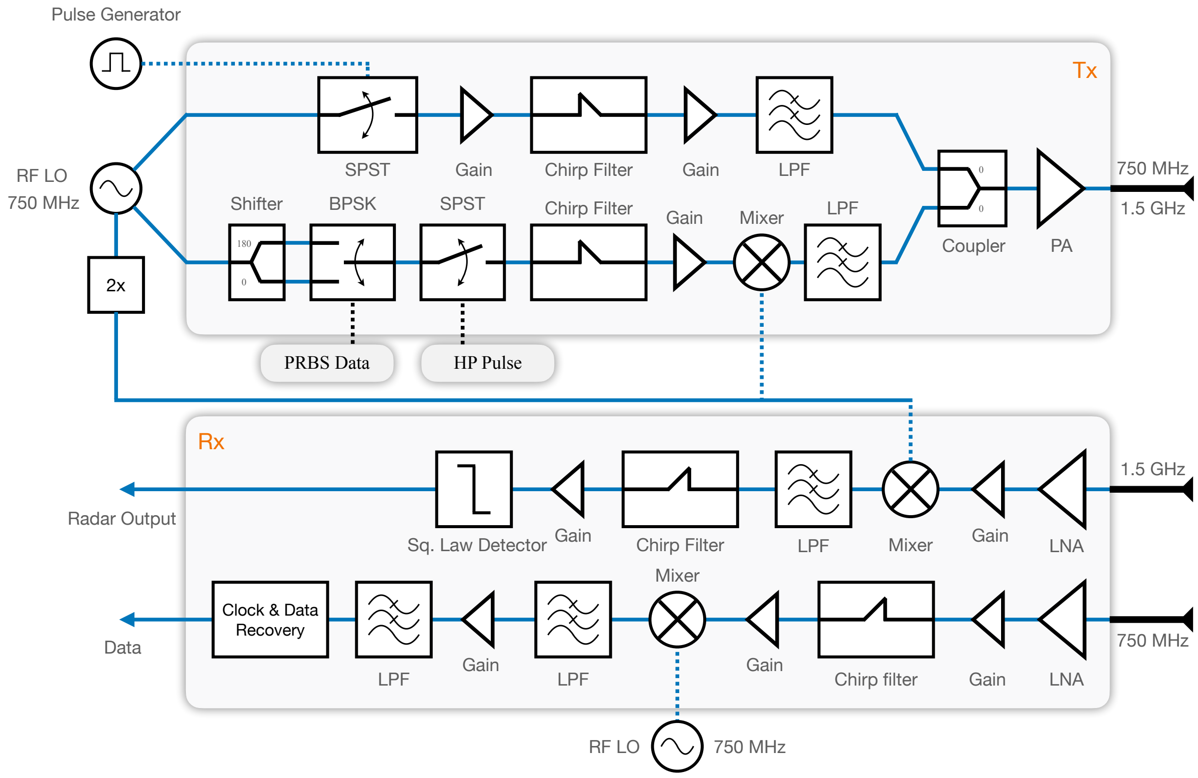

FIGURE 2.6 The block diagram of a heterodyne-based transceiver architecture utilizing FDM for non-cooperative radar and radio communication. In this setup, radar operates with an SSPW at 750 MHz, while data communication employs BPSK at 1.5 GHz. Both functions are facilitated through a dual-polarization antenna configuration [64].

In this configuration, the antenna setup is Single Input Single Output (SISO) with a dual-polarization helical antenna that supports Right-Handed Circularly Polarized (RHCP) and Left-Handed Circularly Polarized (LHCP) modes. This setup effectively emulates a Multiple Input Multiple Output (MIMO) system, where RHCP is designated for data communication and LHCP for radar. For the radio front-end, Binary Phase Shift Keying (BPSK) modulation at 1 Mb/s is applied, filtered using a chirp filter, and then upconverted to 1.5 GHz. The radar function employs a 750 MHz Single Sinusoid Pulsed Waveform (SSPW) with a pulse duration of 1.5 ns and a Pulse Repetition Frequency (PRF) of 150 kHz. Both signals are combined using a power coupler, amplified by a PA, and transmitted through the helical antenna.

The receiver front-end is designed to handle the two distinct frequency bands, distinguishing it from the TDM system described in [47]. The received signals are downconverted at their respective frequencies : radar signals are processed by square law detectors, while data communication signals are managed by a clock/data recovery system.

Using Interferometric Transceivers

Recent advancements in linearly operating interferometric transceivers with low power consumption have led to the development of dual-function wireless systems. In [65], an innovative design of an interferometric receiver is showcased, as illustrated in Figure 2.7. This design enables simultaneous retrieval of modulated Quadrature Amplitude Modulation (QAM) signals, AOA, and polarization information of the incoming signal.

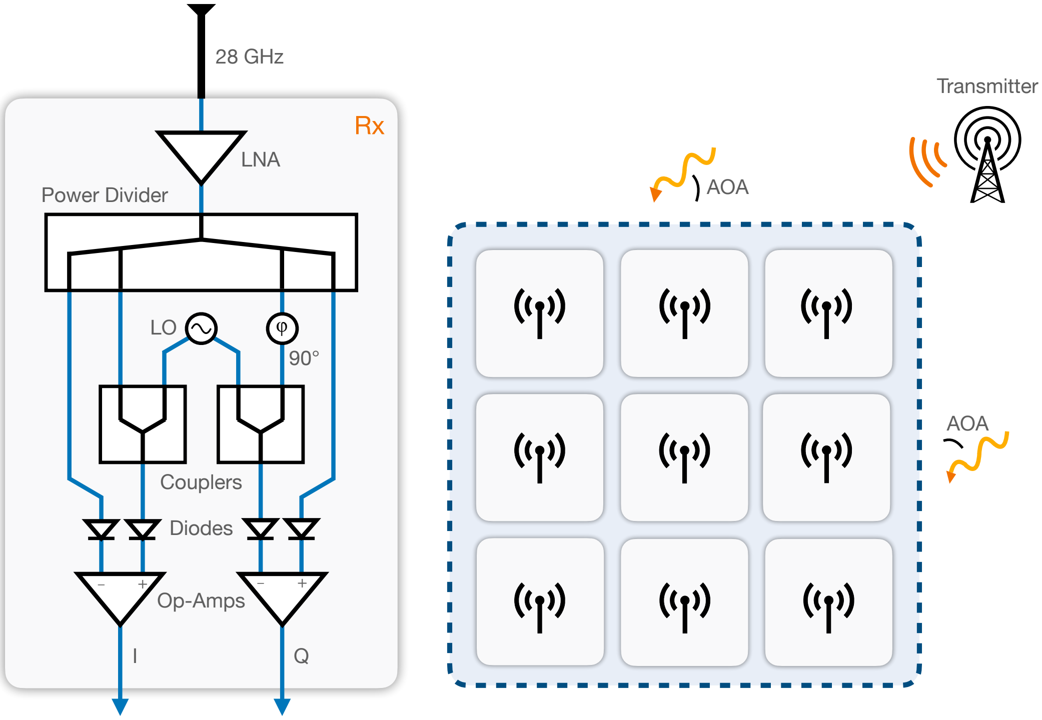

FIGURE 2.7 The block diagram of interferometric-based receiver at 28 GHz for simultaneously retrieving QAM signal, AOA of the incoming signal, and the polarization of the incoming signal. The structure demodulates the incoming signal through a 1-to-4 PD and PCs. I and Q signals are recovered using diode based power detectors and Op-Amps 2D receiver array [65].

Initially, the received RF signal is amplified by an LNA. The amplified signal is then split and distributed using a 1-to-4 Power Divider (PD) to multiple components. One branch of the signal is combined with a LO signal via a Power Combiner (PC) and fed into the positive input of an Operational Amplifier (Op-Amp), while the remaining signal is routed to the negative input of the Op-Amp, generating an in-phase signal. Similarly, a quadrature-phase signal is obtained using a 90° phase shifter before being combined with the LO signal. The study detailed in [65] employs multiple receivers, as depicted in Figure 2.7, to construct a 2D array of receivers for 2D AOA detection. This setup compares the phase of the incoming signal at each receiver with that of adjacent receivers to accurately estimate the AOA.

To support both non-cooperative radar and data communication with a linear interferometric front-end, [66] presents a straightforward six-port architecture that utilizes TDM, as depicted in Figure 2.8.

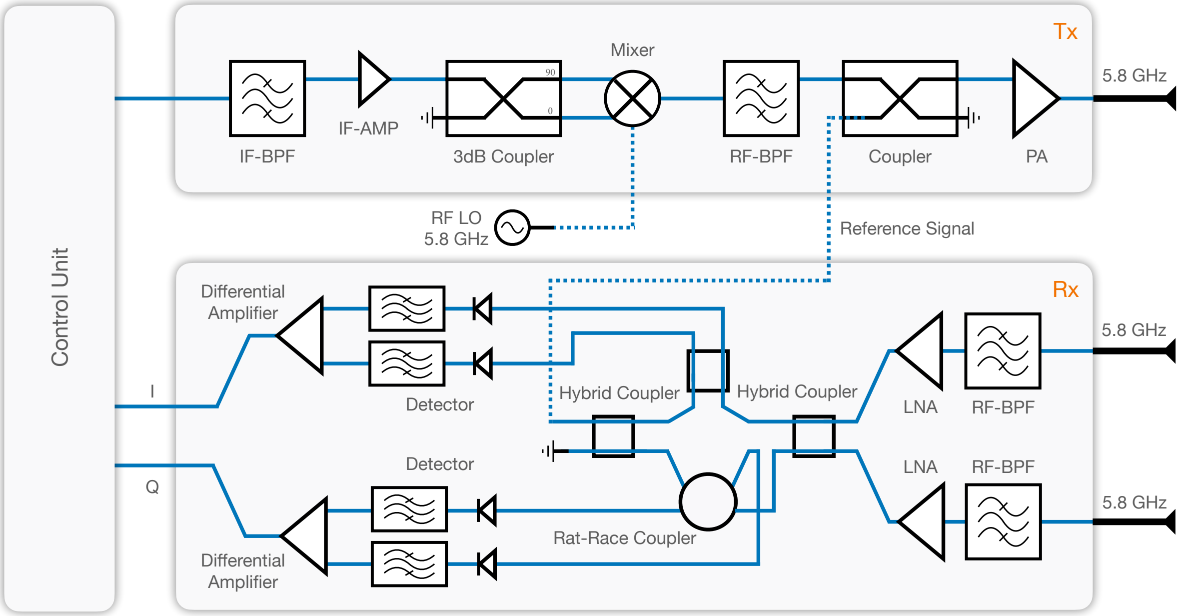

FIGURE 2.8 The block diagram of an interferometric-based transceiver architecture using TDM technique at 5.8 GHz for non-cooperative radar and radio communication. Radar signal is a TFMCW along with BPSK modulation for data communication. SIMO antenna configuration allows AOA detection [67].

This design transmits data by modulating the BPSK over a Trapezoidal Frequency Modulated Continuous Wave (TFMCW) radar signal with a 50 MHz bandwidth. The receiver uses this specific frequency for demodulation. In this setup, the control unit drives the Transmitter (Tx) front-end, which upconverts the signal to the desired RF carrier frequency of 5.8 GHz. The Receiver (Rx) front-end features a two-antenna configuration, creating a SIMO setup for AOA detection. Received signals are amplified by LNAs and processed through the six-port interferometric circuit, which also receives the reference LO signal. Four diodes at each end perform power detection, allowing extraction of the desired signal components for further analysis by the control unit.

Like the system shown in Figure 2.5, this architecture enables sequenced functionality (radar or radio), accommodating any modulation scheme and maximizing reconfigurability and multifunctionality. This design achieves a robust integration and joint operation of radar sensing and data communication through a unified RF front end.

2.3.2 Cooperating Radar and Data Communication

Cooperative radars operate on the principle of collaboration between the radar system and the detected object or objects. Unlike non-cooperative radars, where the monitored object does not need to actively respond, cooperative radars require the object to actively transmit signals back to the radar system to facilitate accurate information retrieval. This interaction necessitates at least two units for effective cooperation. For instance, in automotive applications, as illustrated in Figure 2.9, two vehicles equipped with cooperative radar systems can measure both relative speed and distance between them. Each vehicle's radar system can interact with the other, enabling precise measurements and enhancing overall situational awareness.

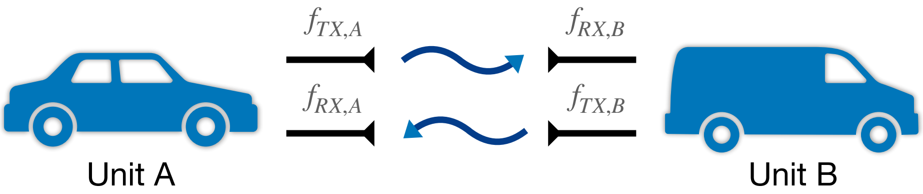

Figure 2.9 Example case of units A and B performing a fully cooperative radar measurement. Both units can transmit and receive signals from the other.

The time synchronization in cooperative radar systems is challenging and critical for effective operation, as highlighted in [68]. This study introduces a method for synchronizing radar nodes within a network using a 2.4 GHz co-emitter based on IEEE 802.15.4 standards and a 24 GHz FMCW technique. The 2.4 GHz data exchanges facilitate a self-synchronizing network, enabling nodes to join or leave the network dynamically. The FMCW chirp emission is precisely controlled by these data exchanges, achieving synchronization accuracy with an error margin of less than 125 ns, thanks to the IEEE protocol's suitability. Additionally, [69] explores a synchronization principle that adjusts time and frequency offsets using beat frequencies from upchirp and downchirp FMCW signals. This method achieves exceptional precision, with time synchronization accuracy of less than 100 ps and frequency accuracy of 10 Hz.

Using Conventional Transceivers

[70] described a precise distance measurement using cooperative but unsynchronized FMCW radars, with capabilities for both distance measurement and data communication (see Figure 2.10).

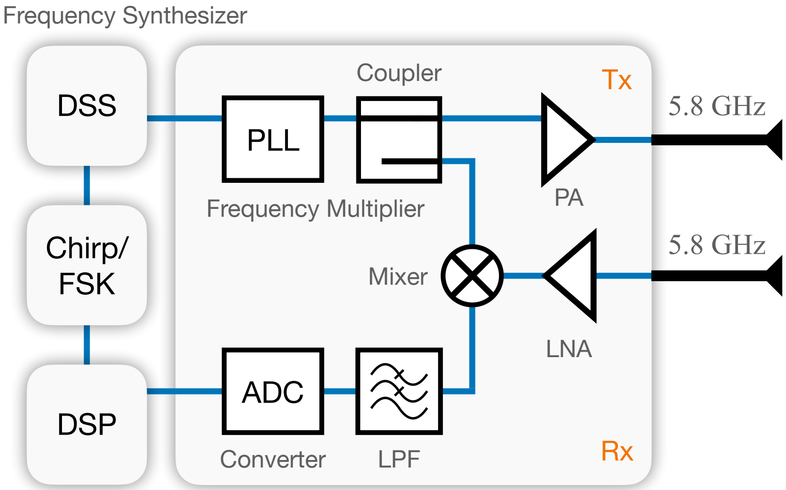

Figure 2.10 The block diagram of a homodyne-based transceiver architecture of units A and B. This uses TDM technique at 5.8 GHz with dual antenna setup for data communication and cooperative radar sensing. Unit A sends an unsynchronized signal, and unit B responds to it [70].

In this configuration, Unit A serves as the master and Unit B as the slave. The slave unit remains inactive until a measurement cycle is initiated by the master, which requires an external trigger to begin operation. For data communication, the slave unit awaits a command from the master to transmit data using Frequency Shift Keying (FSK) modulation.

The architecture integrates both Tx and Rx front ends on a single board, with Units A and B being nearly identical. The frequency synthesizer and frequency multiplier generate radar and communication signals, respectively. These signals are amplified by a PA and transmitted via the antenna. The reference signal is routed to the Rx front-end. Upon signal return, it is amplified by a LNA, mixed with the reference signal, filtered, and analyzed using a Digital Signal Processor (DSP).

References [24, 71] explore a similar approach where FSK is superimposed onto the ramp chirps of cooperative FMCW radar nodes. This method embeds data directly into the transmitted radar signal through multiplicative mixing, with a demonstrated data rate of 256 kbit/s at a 77 GHz radar station. At the receiver, the ramp chirp signal is decoded, enabling the extraction of the embedded data from the radar signal.

Using Interferometric Transceivers

Due to the limited dynamic range of interferometric-based front-ends, which is constrained by the linear region of power detectors, [72] investigates a cooperative approach to unify radio communication with QAM and radar sensing. This approach effectively reduces path loss dependence to $1/R^2$ for individual functions, where R represents the operational range of the wireless system. The proposed system utilizes multiple units operating in different time slots to achieve multifunctionality. The transceiver front-end is illustrated in Figure 2.11, and its operational waveform is depicted in Figure 2.12.

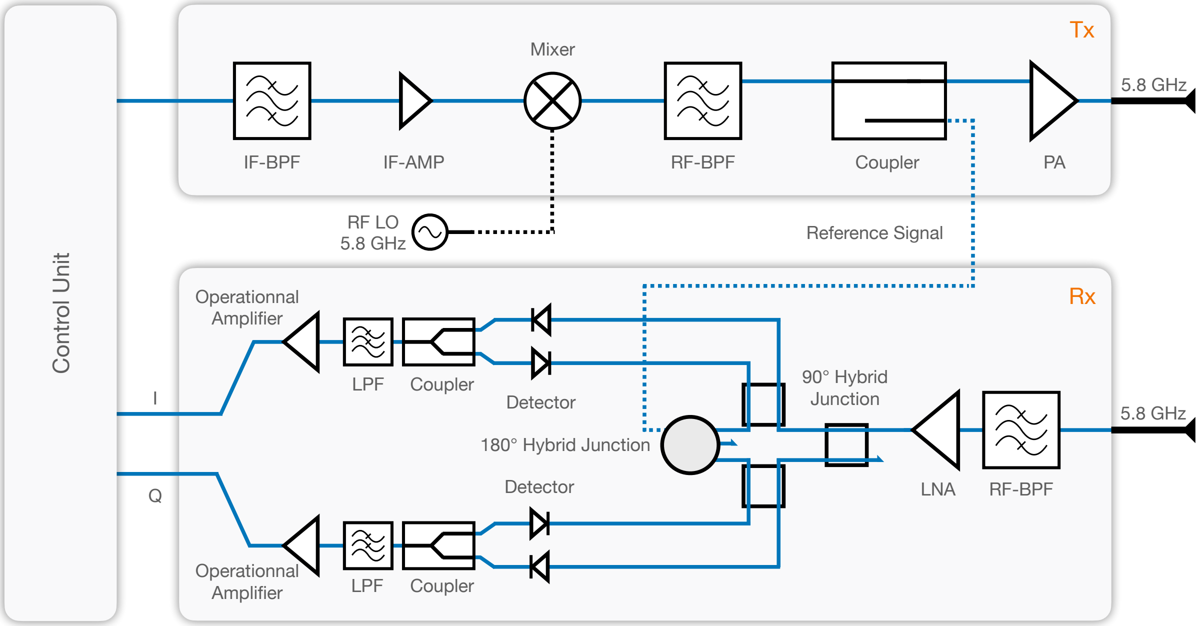

FIGURE 2.11 The block diagram of a cooperative interferometric front-end with time-agile radar sensing and radio communication capability. FMCW radar scheme is used along with QAM scheme for data communication [72].

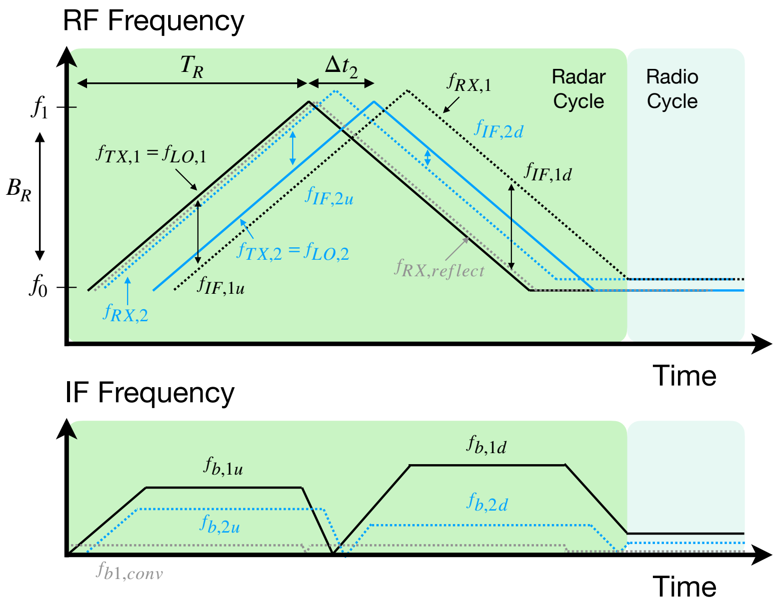

FIGURE 2.12 A description of operation waveform engineering scheme in which $f_{b,1u},\ldots,f_{b,2d}$ represents the desired beat signals from the cooperative radar responses and $f_{b1,conv}$ represents the conventional radar response [72].

In the radar cycle, each unit generates a triangular FMCW signal for transmission, along with a reference signal that includes an arbitrary time delay Δ_{tn}. This separation of signals allows for the differentiation of cooperative radar responses from radar echoes and enables the extension of the system to multiple units. This setup facilitates accurate distance and velocity measurements without encountering issues such as ghost targets. The IF frequency is adjusted based on the distance r and the relative velocity v between units. During the radio cycle, the frequency observations gathered during the radar cycle are used to extract target distance and relative velocity. The following relationships can be employed to perform these calculations :

$$f_{b,1u} + f_{b,2u} = 2f_0 v_{velocity} + 2k_r r_{range} \tag{2.1}$$

$$f_{b,1d} + f_{b,2d} = 2f_1 v_{velocity} - 2k_r r_{range} \tag{2.2}$$

where f_0 and f_1 are the sweep start frequencies for upchirp and downchirp, respectively. k_r is the chirp slope defined by the sweep bandwidth B_r and the sweep time $k_r = B_r/T_r$. The proposed interferometric receiver front-end incorporates a balanced detection scheme, which effectively suppresses mixing components between cooperative radar responses and radar echoes. This design significantly reduces unwanted interference and mitigates the risk of false target classifications. Additionally, the balanced detection scheme enhances the receiver's performance by doubling the amplitude of the desired detected signal, resulting in a 6 dB improvement in conversion performance compared to conventional interferometric receiver architectures that use a single-ended detection scheme. Table 2.1 provides a summary of the key benefits and challenges associated with conventional and interferometric receivers in the context of JRC.

Tableau 2.1 Key benefits and challenges of both conventional and interferometric architectures for JRC with cooperative and non-cooperative radar types

Type of Radar	**Receiver Architecture**	**References**	**Benefits**	**Challenges**
Non-cooperative	Conventional	[47,64]	— Well documented — Wide dynamic range	— Complex transceiver circuitry — Limited multi-standard capability
	Interferometric	[66,67]	— Low LO power level — Broadband capability — Passive additive downconversion — AOA detection	— Large footprint — Short operational range — Calibration technique
Cooperative	Conventional	[24,70,71]	— Wide dynamic range — Narrow-band high selectivity and sensitivity — Allows both single and dual antenna configurations	— Relatively high-power consumption — One downconversion path for one frequency — DC offset due to LO leakage with homodyne
	Interferometric	[72]	— Strong against power-level variations — Cost-effective topology — LO frequency can be changed for dual band — Reduces path loss to $1/R^2$ — 6 dB improvement in conversion performance with the balanced detection	— Dynamic range reduced by the square law region of power detectors (global drawback) — Synchronization

2.4 Data Communication and Energy Harvesting

SWIPT [10], which combines data communication with energy harvesting or transfer, is gaining significant interest within the community [73–75]. While energy harvesting alone is crucial for renewable energy applications, integrating it with data communication enhances multifunctionality in microwave and wireless technologies [9, 15, 76–80]. This fusion offers a range of practical applications as follows. (1) Wireless Sensing Networks (WSNs) : Distributed devices in WSNs use ambient energy sources, such as solar, wind, or RF energy, to charge batteries or capacitors, enabling off-grid operation and data transmission [31]. This capability supports environmental monitoring, including air and water quality, noise levels, and biodiversity [81–83]. (2) Biomedicine : Intelligent clothing equipped with embedded sensors can monitor physiological metrics like heart rate, physical activity, and body temperature [29,84]. In these applications, energy is harvested from body movements using piezoelectric generators or bend sensors [85]. Similarly, watchmaking has demonstrated how wrist movement can power a watch without a battery, illustrating practical applications of energy harvesting [28].

This section will delve into architectures that integrate data communication with RF energy harvesting. Note that RF ambient energy, ranging from 3 kHz to 300 GHz, is highly effective for harvesting and has diverse applications, including Amplitude Modulation (AM)/Frequency Modulation (FM) radio, television, mobile services, and satellite communication bands [18]. The following architectures focus on receivers that utilize data transmitted from conventional transmitters. This section also explores two power harvesting techniques : external and internal energy sources.

2.4.1 Power Harvesting Approach

Receivers with Power Harvesting Capabilities

Multiple antennas technique The first type of receiver architecture for power harvesting and data communication employs a multi-antenna design [10,12,14], where dedicated antennas are allocated for either information reception or energy harvesting, as depicted in Figure 2.13a. This approach offers a significant advantage in terms of performance efficiency, as each antenna can be purposefully designed and optimized for its specific function [86]. Additionally, the use of separate antennas enables operation across non-contiguous frequency bands. For instance, data communication can be carried out on the 1.8 GHz mobile communication band, while the 2.4 GHz band is utilized for energy harvesting [87].

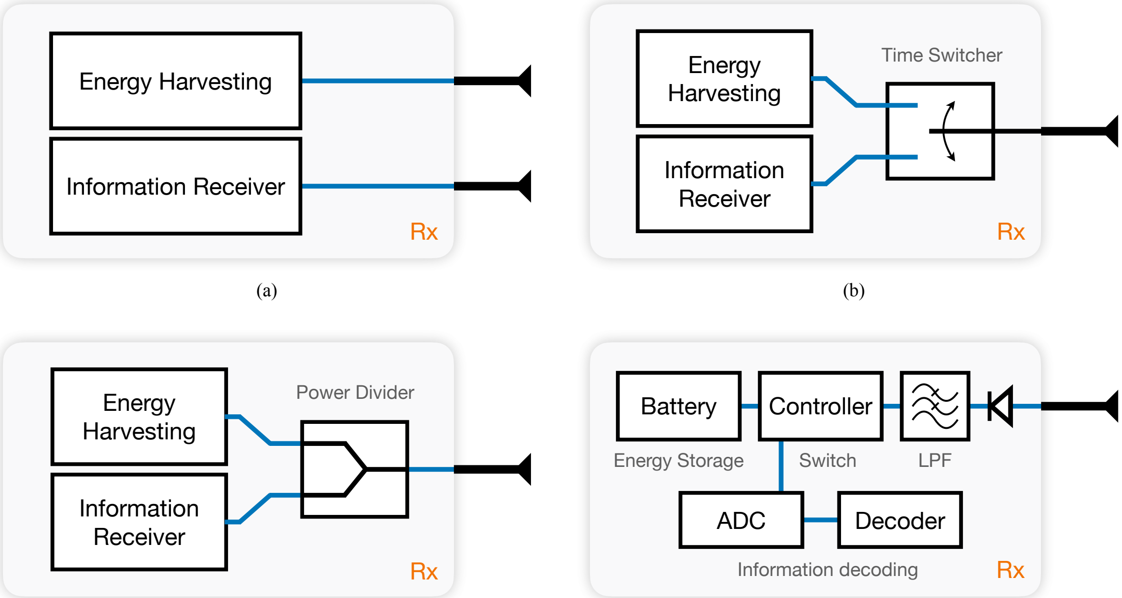

(a) (b) (c) (d)

Figure 2.13 The block diagram of (a) a typical multiple antenna's architecture for SWIPT (b) a typical time switching architecture for SWIPT (c) a typical power splitting architecture for SWIPT and (d) an integrated rectifier receiver architecture for SWIPT.

The inherent drawbacks of this separate antenna architecture include the added complexity of multiple antennas, which becomes particularly problematic at lower frequencies. This design poses challenges to miniaturization due to the increased surface area required, thereby limiting its practicality for applications such as WSNs.

Time switching technique The second receiver architecture, depicted in Figure 2.13b, utilizes a single antenna design with a time-switching mechanism to direct the RF signal to either the information receiver or the energy harvester, as explored in [88–92]. This approach leverages a TDM scheme, where time slot durations can be adjusted to suit the system's requirements. If data communication is the primary focus, the energy harvesting phase can be minimized, allowing for longer data transmission periods. However, since the harvested energy is typically modest, longer accumulation periods are often required [93]. For instance, in environmental monitoring, data might need to be transmitted only once per hour or less, depending on the scenario [94]. In such cases, the energy harvesting time slot would be significantly longer than the data transmission slot. This design requires only one antenna, which reduces both the system's overall footprint and cost.

Additionally, during the switching process, synchronization issues may cause packets to be only partially received. To mitigate this, multiple redundant packets of the same information can be transmitted, helping to reduce the likelihood of missing or corrupted data [95]. However, implementing RF switches can be challenging and may introduce parasitic power consumption, which reduces overall system efficiency. This can be a significant concern, particularly for ultra-low-power nodes like those used in WSNs [96].

Power splitting technique The third receiver architecture is based on a power-splitting technique using a single antenna (or antenna array) that supports simultaneous data transmission and energy harvesting, as illustrated in Figure 2.13c. This design employs a PD to enable both functions to occur concurrently on the same frequency, a concept explored in [13, 97–100]. This approach expands the potential for real-time applications. Additionally, the design complexity is significantly reduced, as a PD is simple to implement [101]. Like the previous architecture, the single-antenna configuration is space-efficient, lowering both fabrication costs and overall footprint.

However, splitting the received RF signal into two weaker signals can degrade transmission quality by negatively affecting the Signal-to-Noise Ratio (SNR) [80]. Additionally, when using a dynamic PD that adjusts the power ratio between outputs, even a small amount of DC power consumption may impact the system's overall energy efficiency [16].

Integrated rectifier receiver The fourth technique, illustrated in Figure 2.13d, features a single-antenna configuration where the fusion of data communication and energy harvesting occurs within the energy harvester using a specific modulation scheme [102–104]. Information decoding through downconversion is integrated into the energy harvester, along with the rectifier, utilizing a predefined modulation technique [103]. This approach can incorporate either a time-switching or power-splitting method, with all necessary hardware fully integrated. The key advancement over previous architectures lies in its integrated design [104], which results in a more compact system, minimizing the physical footprint—a significant advantage for miniaturization. Additionally, this architecture improves power efficiency by reducing parasitic losses [80]. The diode and low-pass filter in Figure 2.13d, connected to the antenna, rectify the signal, which is then routed via the controller.

Despite its numerous advantages, this architecture may be prone to distortions caused by self-mixing, which can restrict the use of certain digital modulation schemes that have strict performance requirements [105]. If the input power falls outside the expected range, the non-linear components can introduce harmonic distortions, leading to a reduction in the SNR. Table 2.2 summarizes the key advantages and disadvantages of multi-antenna, time-switching, power-splitting, and integrated rectifier receiver architectures for SWIPT, along with recommended use cases based on their strengths.

Tableau 2.2 Key characteristics and suggested use cases of the presented approaches for SWIPT

Approach	**References**	**Advantages**	**Drawbacks**	**Use Cases**
Multiple Antennas	[10, 12, 14, 87]	— In-band and out-of-band capabilities — Independence of functions	— Large antenna footprint	To be used when wide frequency band gap is necessary
Time Switching	[88–92]	— Programmable time slot duration — Same RF channels — Small form factor	— Subject to synchronization issues — Parasite power consumption of the switch	To be used when high-speed time synchronization is possible
Power Splitting	[13, 97–100]	— Simultaneous operation — Easy implementation — Same RF channels — Small form factor	— Less power for both functions — DC power consumption for dynamic power splitters	To be used when a high SNR is available
Integrated Rectifier Receivers	[102–104]	— Harvester circuit for downconversion — Same RF channels	— No well-established modulation schemes — Self-mixing prone to different distortions	To be used when the received modulation scheme is suited

Receiver based on Six-port Architecture for SWIPT

To address the limitations of existing receiver architectures with energy harvesting capabilities, a novel six-port receiver architecture has been proposed based on the principle of separating received frequencies [106]. In this SWIPT scenario, maintaining radio sensitivity and employing appropriate digital modulation techniques are crucial. Diplexers are utilized to capture out-of-band interferers and recycle harmonics generated by the multiport system, as illustrated in Figure 2.14. In this architecture, sensitivity and dynamic range are primarily governed by the LNA and power detectors. By separating incoming signals for information decoding, the system supports the use of digital modulation techniques essential for Internet of Things (IoT) applications.

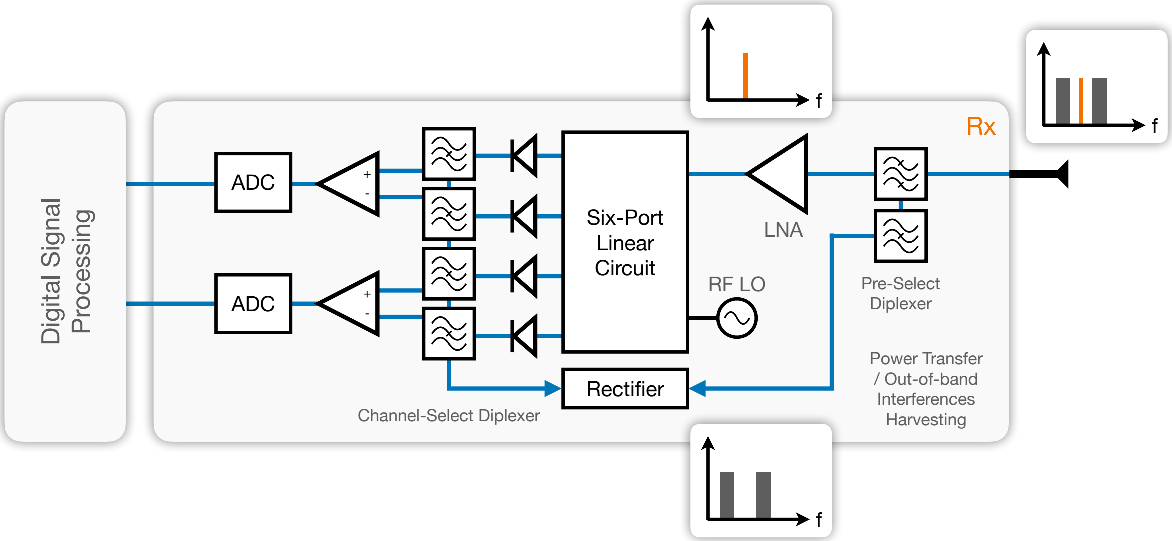

FIGURE 2.14 The block diagram of the six-port receiver architecture for SWIPT with out-of-band energy harvesting capability. The first diplexer allows for out-of-band energy harvesting while the second permits energy recycling of the multiport generated-harmonics [106].

2.4.2 Internal Energy Recycling

Energy recycling is also an important aspect of energy harvesting, focusing on capturing lost energy within the system itself rather than relying on external power sources. Unlike the external power harvesting methods discussed previously, energy recycling aims to utilize the energy lost in various internal processes. For example, during the demodulation procedure, losses can occur after downconversion, leaving several frequencies in the spectrum, including

f_{RF}, f_{LO}, DC and associated frequency shifts $f_{RF} - f_{LO}$ and $f_{RF} + f_{LO}$. A study referenced in [26] introduced an innovative energy recycling approach that capitalizes on the mixing process. It was demonstrated that after downconversion, the DC power exhibits relatively higher signal strength compared to other frequencies, underscoring the potential for harnessing this characteristic, as illustrated in the frequency spectrum shown in Figure 2.15.

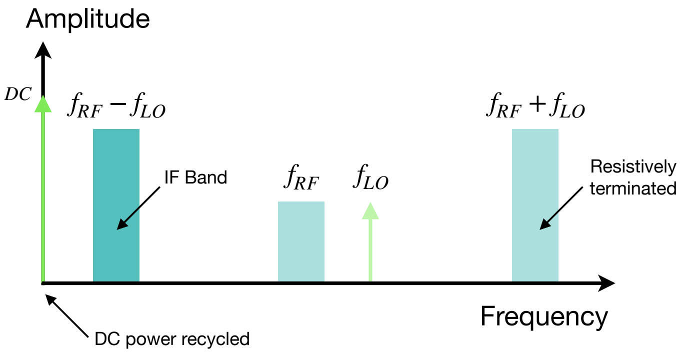

FIGURE 2.15 Frequency spectrum of the technique used for internal energy recycling in a diplexer bank, where $f_{RF} + f_{LO}$ is resistively terminated. $f_{RF} - f_{LO}$ and DC signals are preserved for further operations [26].

In this approach, the sum frequency $f_{RF} + f_{LO}$ was resistively terminated to achieve a wider instantaneous bandwidth, while the IF band $f_{RF} - f_{LO}$ was preserved for demodulation. Figure 2.16 presents a single-ended power-recycling mixer topology, which can be adapted for other mixer circuit designs.

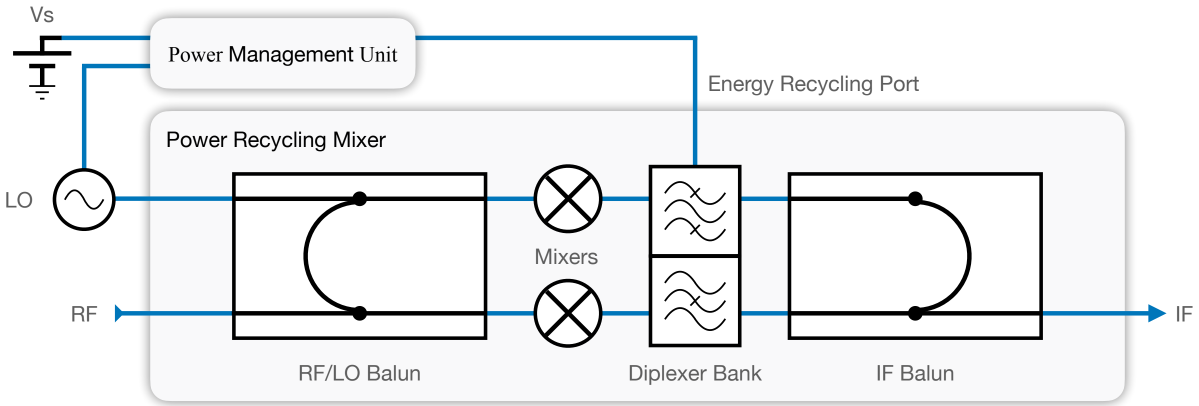

FIGURE 2.16 The block diagram of an energy recycling receiver architecture. $f_{RF} - f_{LO}$ (IF) is recovered at the output of the IF balun while the DC signal is extracted due to the diplexer and connected to a power management unit [26].

The RF and LO signals are connected to the RF/LO balun to drive the mixing elements, while the diplexer bank extracts the DC signal from the output. This research demonstrates that with a single balanced diode-switching mixer integrated with a diplexer bank, approximately 30% of the driving signal power can be found in the DC signal under optimal conversion efficiency conditions.

2.5 Radar Sensing and Power Transfer

The integration of radar systems with power transfer has been extensively explored in the literature, focusing on various aspects such as self-powered radar development [107], harmonic backscattering [17–20], and specialized antenna designs [108, 109]. This integration aims to improve the power efficiency of wireless systems, thereby reducing dependence on external power sources. The use of energy harvesters is expected to enhance off-grid solutions for radars operating in remote or inaccessible areas, enabling these systems to function autonomously without human intervention.

Recent studies reveal that there are currently about twice as many connected IoT devices as there are people on Earth, with this number expected to grow exponentially in the future [110]. This underscores the urgent need for self-powered and self-sustaining systems. In this context, we will review typical radar systems and harmonic radars. Harmonic radars, which involve harmonic backscattering, utilize an RF transmitter operating at a carrier frequency f_0 to track a transponder or tag [111] that returns a signal at frequency $2f_0$ due to a non-linear element, as illustrated in Figure 2.17.

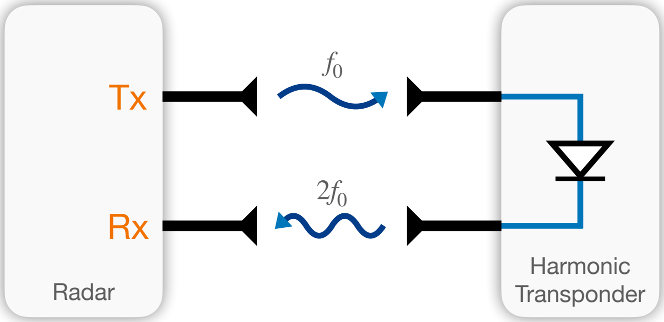

FIGURE 2.17 The block diagram of a typical harmonic backscattering system featuring a non-linear element for frequency multiplication or conversion, from f_0 to $2f_0$.

This allows for the detection of the target's presence and location, as well as information extraction from sensors [19]. By employing multiple receiving antennas, AOA detection systems can be implemented on the radar receiver side [112]. Since the tag transmits a signal using the incoming power, this can be considered a form of energy recycling or harvesting. Harmonic radars are particularly suited for applications requiring compact designs, such as Radio Frequency Identification Devices (RFID) [113] and insect tracking [114–116].

The following section presents state-of-the-art architectures that integrate radar sensing with energy harvesting. It focuses on harmonic transponders, exploring both traditional and contemporary configurations, as well as a solar-powered primary radar system.

2.5.1 Harmonic Backscattering Techniques

Traditional dual-antenna architecture

The first topology for harmonic backscattering utilizes a dual-antenna architecture to receive frequencies f_0 and backscatter frequency $2f_0$, as explored in [116–121]. This configuration is commonly used due to the simplicity of tuning each antenna to a specific frequency, as illustrated in Figure 2.18.

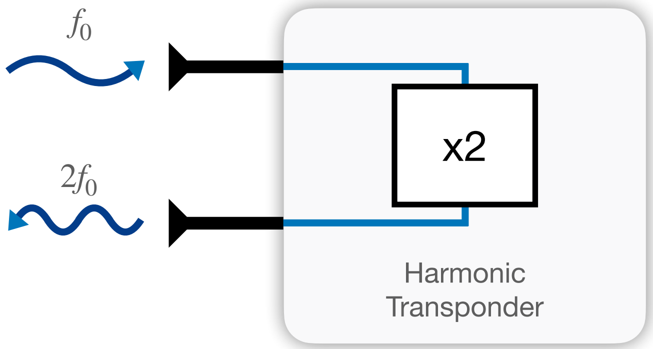

Figure 2.18 A simplified block diagram of dual-antenna harmonic transponder architecture in which the first antenna receives a signal at f_0 and the second sends back a modulated (backscattered) signal at $2f_0$.

However, despite its popularity, this design has several drawbacks, including a relatively large footprint required for the dual antennas and the need for strong isolation between the

Tx and Rx antennas, particularly in long-range applications [122]. Some designs have been specifically engineered for flexibility [123], allowing them to be easily mounted on non-planar surfaces.

In certain scenarios, the frequency of the backscattered signal can be adjusted based on sensor readings and modulated by the tag Identification (ID) in WSN applications [117]. The backscattered frequency can thus be represented as :

$$f_{backscattered} = 2f_0 \pm \Delta f \tag{2.3}$$

where the frequency shift Δf depends on the sensor value (i.e. data to be embedded).

Single antenna architecture

The second topology for harmonic backscattering integrates two antennas into a single dual-band antenna capable of handling both f_0 and $2f_0$ frequencies, as demonstrated in [20, 124–128]. Notably, [124] has proposed a 5G-compatible, diplexer-based harmonic transponder for applications below 6 GHz. A simplified version of this topology is illustrated in Figure 2.19.

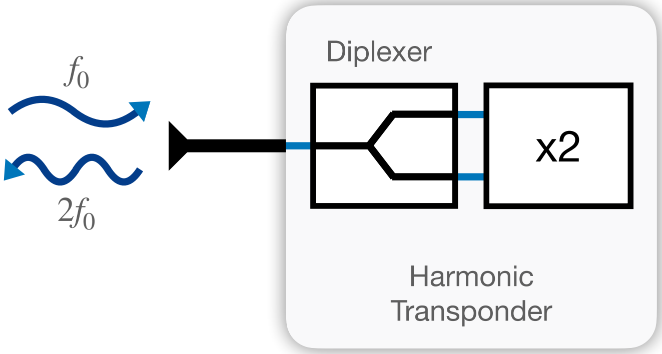

FIGURE 2.19 A simplified block diagram of diplexer-based single antenna harmonic transponder architecture where the diplexer connects the two ends of a non-linear element to the single dual-band antenna [124].

The dual-band antenna addresses several issues associated with the use of separate antennas. By utilizing a single antenna, the tag's footprint is significantly reduced (e.g., 35x35 mm^2 at 3.5/7 GHz [124] and 95x40 mm^2 at 869/1734 MHz [128]). Additionally, a well-designed diplexer improves isolation between the Tx and Rx components of the tag, leading to enhanced overall performance. However, when diodes are employed as the non-linear elements, [129] demonstrates that temperature can significantly affect the associated Conversion Losss (CLs) :

$$CL(dB) = P_{f_0(dBm)} - P_{2f_0(dBm)} \tag{2.4}$$

where P_{f_0} is the received power and P_{2f_0} is the backscattered power. In [129], the maximum read-out distance was increased by 10% at -40°C, compared to the results at +40°C, due to a reduction in CL.

2.5.2 Self-powered Six-port Based Radar

In contrast to other RF harvesting techniques discussed in this study, [107] introduces an innovative architecture that enables simultaneous radar sensing and solar energy harvesting, as illustrated in Figure 2.20.

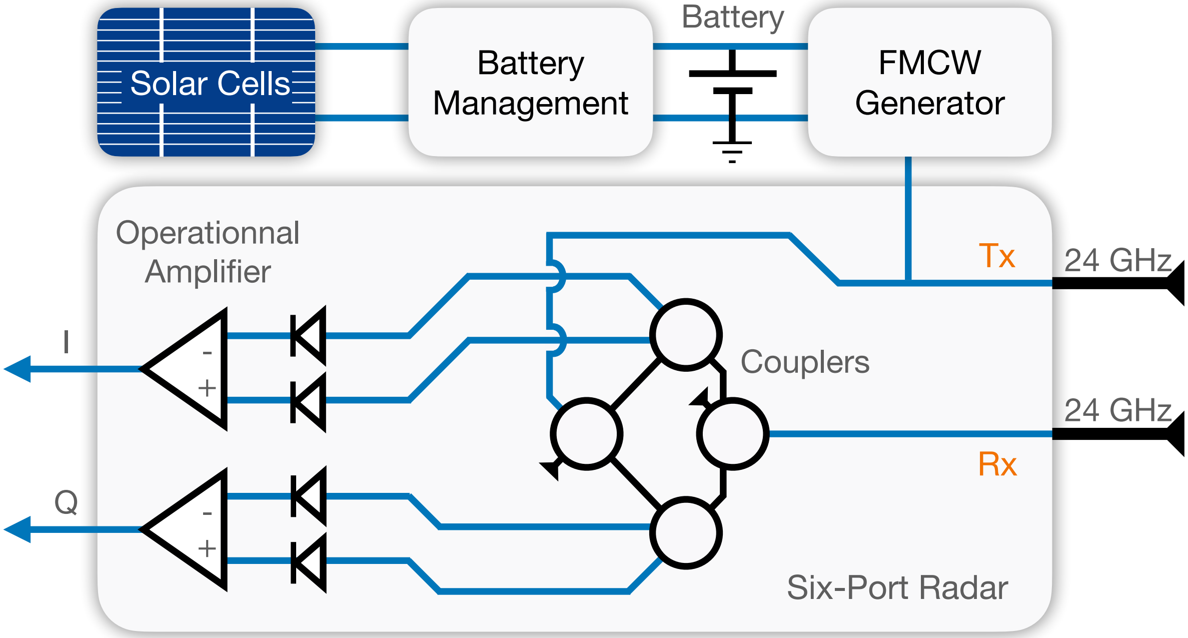

FIGURE 2.20 A simplified block diagram of solar-powered 24 GHz six-port non-cooperative Doppler radar architecture. Solar cells are set to harvest light-based ambient energy and to power the FMCW generator [107].

The solar cells are capable of sustaining the 50-mW power consumption of the 24-GHz Doppler radar of interest. While RF energy harvesting methods are suitable for certain scenarios, solar-based harvesters offer a more potent energy source, particularly for systems with higher power demands. In some cases, solar energy harvesters can even provide a continuous power supply for WSNs [130]. This design integrates photovoltaic cells with a battery management system and a boost charger controller, which are set together to power the FMCW generator. To further reduce power consumption, an RF sleep control unit puts the radar system into sleep mode 10 times per second. The radar system employs a SISO antenna configuration, and the In-phase/Quadrature (I/Q) signals are processed using a six-port topology.

2.6 Combining Radar Sensing, Data Communication and Power Transfer in the Same Architecture

Multiple examples of dual-function systems have been reviewed, including combinations of radar sensing with data communication, data communication with energy harvesting, and radar sensing with energy harvesting. The future of multifunction systems is expected to involve the integration of all the three fundamental wireless functions into a single architecture [131,132]. Previous studies have highlighted the benefits of multifunction RF/microwave systems, noting their superior versatility and adaptability [133, 134]. Next-generation wireless multifunctional systems must seamlessly integrate into diverse scenarios, such as smart cities and WSNs. From a hardware perspective, multifunction systems not only tackle the miniaturization challenge—a major concern for RF/microwave systems—but also enable the integration of multiple functions on a single Printed Circuit Board (PCB)/chip, optimizing power efficiency to unprecedented levels [135, 136].

Wireless Radar Networks (WRNs) [137] are gaining attention for their potential to make radar systems more intelligent and networked, although they currently lack energy harvesting capabilities [138–141]. To date, no state-of-the-art architecture fully achieves a comprehensive wireless multifunction experience. The following section will address the considerations for integrating multiple functions across various frequency bands, explore the implementation of TDM as a potential solution, and examine the hardware challenges associated with designing antennas for multifunction systems.

2.6.1 Multiplexing Considerations

Frequency domain multiplexing for unification

Utilizing multi-band systems is an effective solution for performing multiple tasks simultaneously. In this approach, each function is allocated a specific frequency band : the first band B_1 for power transfer, the second band B_2 for data communication, and the third band B_3 for radar sensing. It is important to note that those bands do not need to be equally wide ; each band should be tailored to meet the specific requirements of the system. For example, the energy harvesting band B_1 can be narrower if a particular frequency band is designated as the power source. Conversely, the radar band B_3 should be the widest to improve the range resolution d_{res} of the radar :

$$d_{res} = \frac{speed\,of\,light}{2B_3} \tag{2.5}$$

Figure 2.21 illustrates a multi-band configuration that facilitates the simultaneous operation of three functions across the bandwidth $B_1 + B_2 + B_3$.

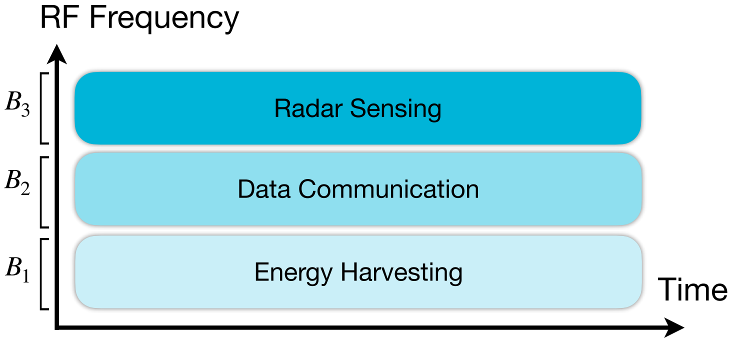

Figure 2.21 Frequency domain multiplexing for simultaneous operation of functions.

This FDM approach offers several advantages and disadvantages, which can be summarized as follows :

Advantages - (1) Optimal Function Allocation : Assigning specific frequency bands to distinct functions ensures that each function operates within its optimal frequency range. For instance, the energy harvesting band can be tailored to match the ambient RF sources, enhancing self-sufficiency. (2) Simultaneous Operation : Multi-band systems enable all functions to operate concurrently, a crucial feature for real-time applications. As depicted in Figure 2.23, this allows for simultaneous radar sensing and data communication within the same time slot, facilitating multitasking.

Disadvantages - (1) Reduced Spectral Efficiency : The allocation of multiple frequency bands can decrease overall spectral efficiency, as it occupies more space in the RF spectrum. This issue is exacerbated by global spectral congestion, particularly in urban environments [142]. (2) Increased Antenna Requirements : Implementing multiple frequency bands typically necessitates the use of several antennas or multi-band/wideband antennas. This requirement can complicate miniaturization and increase the overall antenna count, which is a significant drawback for compact designs.

Time domain multiplexing of functions

Another solution for achieving multi-functionality in RF systems is TDM [6,67,72,143]. This approach allows all functions to operate within the same frequency band but sequentially, based on predefined time slots (TS_i). The system performs each function in turn : TS_1 for energy harvesting, TS_2 for radar sensing, and TS_3 for data communication. Each time slot can have different durations tailored to the specific needs of the system. For example, in WSNs, the time slot for energy harvesting (TS_1) may be significantly longer than those for radar sensing (TS_2) or data communication (TS_3) due to the extended duration required for effective energy collection, as discussed earlier.

Figure 2.22 illustrates a simple TDM scenario where functions are performed sequentially.

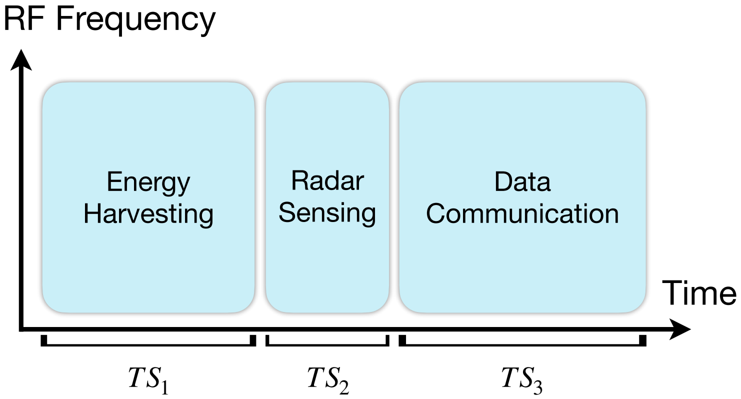

FIGURE 2.22 Time domain multiplexing with determined TS for sequential operating of functions.

This approach addresses some issues present in previous methods but introduces new challenges. One key advantage is improved spectrum efficiency, as multiple functions share the same frequency band, reducing the overall bandwidth required and thus minimizing the system's footprint on the RF spectrum. Additionally, the sequential operation allows for real-time adjustment of Time Slot (TS) durations. For instance, if the energy harvester needs to charge a capacitor to power other functions, the time required for this can vary based on conditions, allowing for flexible TS durations and enhanced adaptability—a significant advancement for future intelligent wireless systems.

However, using a single frequency band means the system must find a compromise in selecting the optimal band for all functions. The ideal frequency for energy harvesting or data communication might not align with the optimal band for Doppler radar. Moreover, the length of the time slot for energy harvesting (TS_1) can impact the overall cycle period, potentially limiting applications requiring low latency if TS_1 is prolonged. Additionally, managing synchronization across varying time slots can introduce further complexity.

Hybrid multiplexing of Functions

Another intriguing multiplexing approach is the hybrid scheme, as shown in Figure 2.23. This hybrid method combines aspects of both FDM and TDM, allowing for simultaneous energy harvesting at any time ($TS_1 + TS_2$) while performing radar sensing and data communication sequentially.

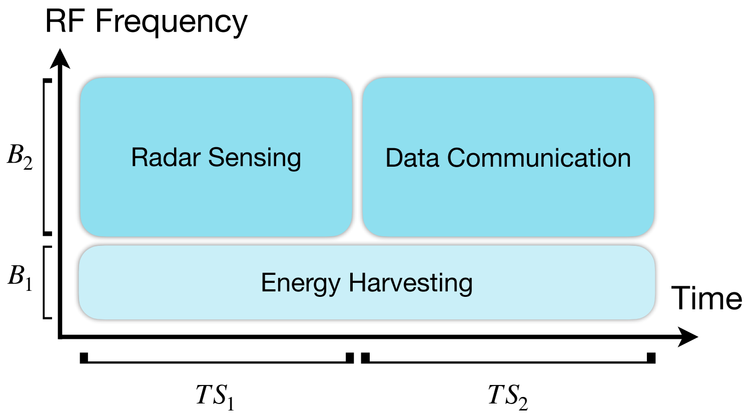

FIGURE 2.23 Hybrid multiplexing with multiband time-agile capabilities for the synergy of functions.

By integrating features from both schemes, the hybrid approach overcomes the limitations of a pure TDM by providing a greater flexibility in frequency band selection. Energy harvesting can be optimized to target the frequency with the highest power density in the environment (B_1), while radar sensing can operate on a different frequency band (B_2), either further away or slightly off from the primary harvesting frequency.

One significant advantage of this hybrid approach is its ability to address the bandwidth constraints of FDM. By using TDM within a narrower frequency band (B_2), it reduces the overall bandwidth requirement compared to the broader combined band ($B_1 + B_2$) needed for pure FDM. This makes the hybrid scheme more efficient in terms of spectrum usage while still leveraging the benefits of both FDM and TDM.

Table 2.3 provides a summary of the key benefits and challenges associated with FDM, TDM, and hybrid multiplexing approaches for achieving a truly multifunctional RF architecture, based on the previous analysis.

TABLEAU 2.3 Key characteristics of FDM, TDM and Hybrid multiplexing solutions for truly multifunction RF systems

Multiplexing	**Benefits**	**Challenges**
FDM	— Simultaneous operating — Non-contiguous bands possibility — Optimal frequency bands — Different modulation possibility	— Complex architecture — Multi-carrier — Large bandwidth — Multiple antennas
TDM	— Adaptive time slots — Single antenna — Small bandwidth required — Possibility of reconfiguration	— Non-real-time applications — Compromise over the frequency selection — Synchronization at the receiver
Hybrid	— Optimal frequency bands — Permanent energy harvesting — Relatively small bandwidth required	— Multiple antennas — Synchronization at the receiver — Multi-carrier

2.6.2 Discussion on Architectures

Virtual Receiver Matrix

A truly multifunction system requires a specially designed antenna-circuit system, particularly at the receiver end. The concept of the Virtual Receiver Matrix (VRM), as introduced in [144], addresses this need by leveraging combinatory analog operations with receiving antenna-circuit elements in the matrix. This innovative approach supports multiple functions such as data communication, radar, AOA detection, imaging, and energy harvesting among many others. It is worth noting that the VRM concept can be easily extended to include transmitting functions, thereby creating a comprehensive virtual Tx/Rx matrix.

The primary advantage of the VRM architecture is its reconfigurability, a key feature for intelligent systems. Illustrated in Figure 2.24, the VRM matrix interacts with RF waves of varying polarizations, AOAs, and frequencies.

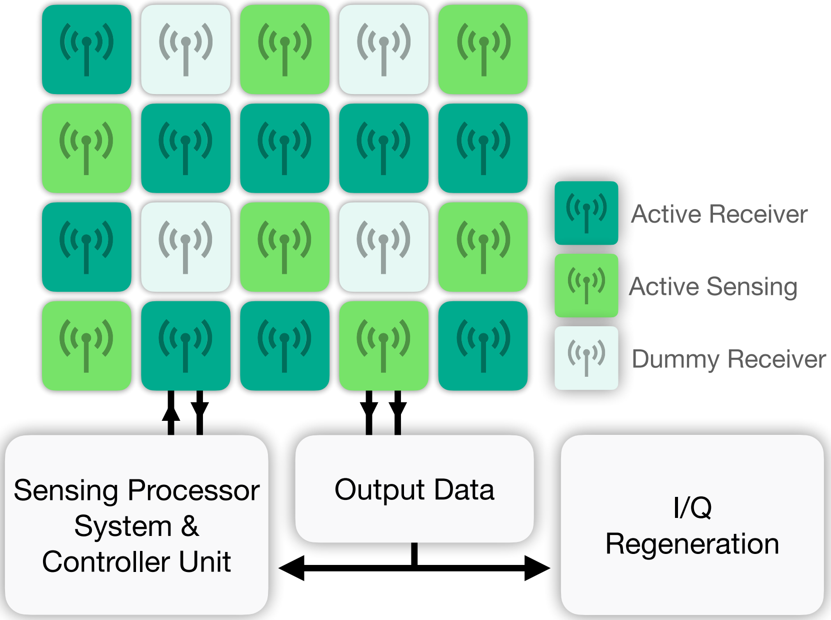

FIGURE 2.24 The block diagram of a VRM architecture for multifunctional RF systems where any channel is virtually synthesized through a combination of multiple receiving cells. Each receiving cell is dynamically controlled by the processing unit to perform different scenarios [144].

Each cell in the matrix can be set to one of several states : active receiver, active sensor, or inactive. The control unit dynamically adjusts the state of each cell based on the received

RF signals, creating a highly adaptable and intelligent antenna-circuit configuration. Demodulation is achieved through a virtual channel synthesis using an interferometric technique similar to that shown in Figure 2.7, where each VRM cell processes either the I/Q signal contents.

In-band full-duplex (IBFD) architectures

One intriguing wireless front-end architecture is full-duplex technology, which has the potential to significantly enhance data throughput and reduce transmission latency by enabling simultaneous in-band transmission and reception of signals [145]. Ongoing research is focused on addressing the well-known challenge of isolation between transmitting and receiving channels that share the same frequency band [146]. In-band Full-Duplex (IBFD) systems naturally support all multifunctional applications, such as simultaneous radar sensing and communication, by utilizing the same frequency channel and reference signals. This makes IBFD an inherently versatile architecture for applications requiring concurrent radar and communication functions, as illustrated in Figure 2.25.

Antenna design perspectives

The design of antennas for multifunctional RF systems introduces several complexities. While some challenges are related to general antenna design principles, others arise specifically from the multifunctional nature of these systems [109]. One major challenge in FDM is ensuring that an antenna or array performs effectively across all frequency bands when different functions operate in distinct frequency ranges. This challenge is closely related to the domain of wideband or ultra-wideband antennas, which must address issues such as large bandwidth, consistent gain, radiation efficiency, and structure size [147]. Additionally, operating multiple functions simultaneously with antennas placed in close proximity can lead to interference and crosstalk [148].

For multifunctional RF systems to integrate seamlessly into IoT ecosystems, the antennas must have relatively small footprints. Large, cumbersome antennas would be counterproductive, negating the benefits of having advanced, compact systems for everyday use. Another critical aspect of multifunctional systems is the control of the radiation pattern or beamforming design [149]. Unlike data communication and energy harvesting, radar typically requires a narrower beam. Thus, MIMO antenna configurations and beamforming techniques become

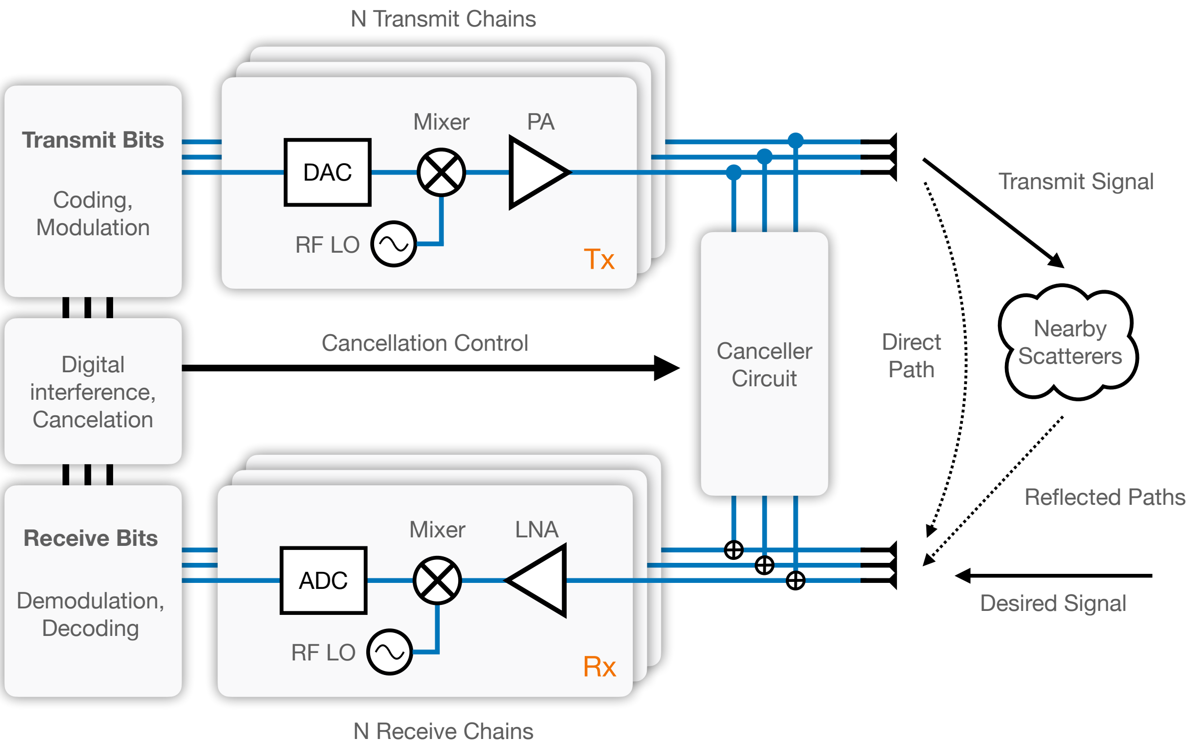

FIGURE 2.25 The block diagram of a typical simplified separated-antenna In-Band Full-Duplex transceiver architecture [146].

essential [150]. Finally, the environmental conditions in which these systems operate—such as temperature fluctuations, humidity, and physical stress—pose significant concerns. Ensuring long-term durability and consistent performance, particularly in off-grid scenarios, is crucial [151, 152].

Figure 2.26 illustrates a truly multifunctional antenna array, where all functionalities interact seamlessly, enabling connectivity between battery-free nodes within the network and the central system.

2.6.3 Practical Implementation Scenarios

Future tri-function systems that integrate radar, communication, and power transmission are being shaped by numerous developments. These developments provide improved capabilities that open new applications and boost efficiency in several industries such as the followings. First, Artificial Intelligence (AI) is being used to optimize resource management in smart city infrastructure. Indeed, 5G networks in smart cities balance power distribution for Elec-

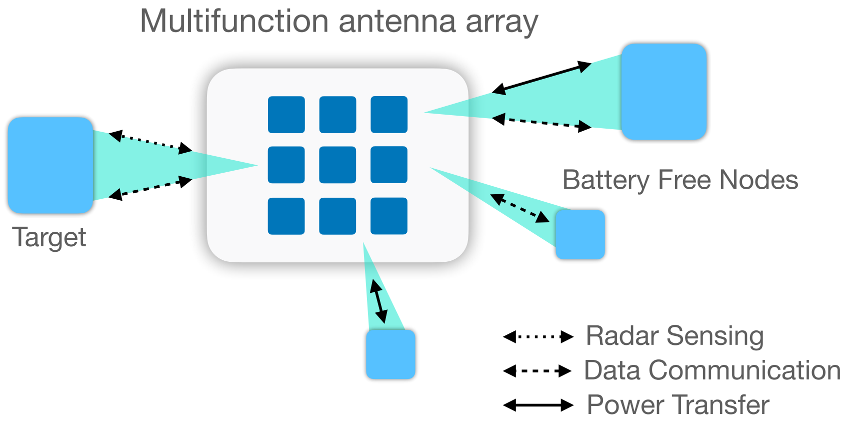

FIGURE 2.26 The block diagram of multifunction antenna array perspectives for realizing joint operations of radar sensing, data communication, and power transfer.

tric Vehicle (EV) charging, communication for data transmission, and radar-based traffic monitoring by using AI-driven algorithms to dynamically regulate spectrum allotment. This is demonstrated by initiatives such as Smart City Dubai, which employ AI to improve the performance of multifunctional systems in real-time for energy efficiency, traffic control, and communication in urban environments [153, 154]. Second, for non-invasive diagnostics, the medical imaging industry is investigating THz radar systems. For telemedicine applications, THz waves provide for quick data transmission and high-resolution imaging. As demonstrated by Verizon's 5G experiments and the UK's 5G Smart City Project, which integrates radar, communication, and electricity in urban deployments, next-generation 5G networks are combining THz communication with radar sensing to provide high-speed communication and precise radar capabilities [155, 156]. Third, smart factories and self-governing drones are two examples of applications that employ Wireless Power Transfer (WPT). For instance, WiTricity's resonant inductive coupling is used for WPT in production settings, enabling sensors and robots to function without requiring human recharging [157]. To reduce the need for battery changes, IoT devices are also incorporating RF energy harvesting technologies, like Powercast, to catch ambient radio waves and power sensors [158].

2.7 Conclusion

The evolution of wireless transceiver architectures towards a truly multifunctionality has emerged has a highly debated topic in our community and is expected to have a deep impact on the way we will design such wireless systems in the next decades. This review paper explored the architectural challenges in the fusion of radar sensing, data communication and power transfer. We demonstrated the potential of interferometric solutions in the pursue of truly integrated multifunction wireless systems. In addition, the importance of sustainable energy solutions was underlined for either data communication or radar sensing and the impact on the architectures was studied. The importance of self-powered systems was also reviewed, and the key features of such architectures were discussed. Ultimately, we believe that the proposed roadmap will guide researchers and future engineers in overcoming present challenges and give a sense of the promising benefits of a truly integrated multifunction system.

CHAPITRE 3 ARTICLE 2 : DIODE-BASED WIDEBAND HARMONIC GENERATION FOR FUTURE NONLINEAR SENSING APPLICATIONS

Thomas Micallef, Xiaoqiang Gu et Ke Wu

Publié dans : *IEEE Transactions on Microwave Theory and Techniques*
Date de publication : 17 Avril 2025

3.1 Abstract

An essential element in advancing next-generation RF systems and sensing applications through nonlinear sensing technology is the efficient production of harmonics at GHz frequencies. This research offers a comprehensive theoretical and practical analysis of diode-based harmonic generators, specifically focusing on Schottky, varactor, and step recovery diodes. The study proposes time-domain current equations to predict harmonic amplitudes under various input voltages and biasing conditions, considering the distinctive resistive and capacitive nonlinearities of the diodes. The theoretical models are validated using fabricated prototypes, which demonstrate wideband harmonic production for a 1 GHz input signal with a frequency-modulated sweep spanning 600 MHz in total bandwidth. The measured average output power variation is ± 3.4 dBm for the SMS7630 and ± 5.2 dBm for the SMV1213. Beyond offering insights into impedance matching and design optimization, the results underscore the diodes' suitability for low-power and batteryless applications. By providing a robust physical foundation for enhancing harmonic generation efficiency, this work aspires to drive the development of state-of-the-art RF systems and components.

3.2 Introduction

The ability to efficiently generate harmonics in the GHz frequency range, such as for nonlinear sensing, has always been crucial for enhancing the capabilities of various RF systems [159]. Generating harmonics, which are integer multiples of the fundamental input frequency, plays a pivotal role in expanding the functionalities of RF systems, including frequency synthesizers, signal modulation, spectrum analysis, and sensing applications, among others [160,161]. The process of producing harmonics relies on the nonlinearity of specific semiconductor components [162]. In a linear resistivity scenario, doubling the input voltage results in a doubled output current, maintaining the same output frequency. In contrast, nonlinear resistivity can distort the signal and subsequently induce higher-order harmonics.

Two primary methods for producing harmonics appear in the literature, namely, transistor-based and diode-based generators [163]. Transistor-based methods leverage the nonlinearity of a transfer characteristic in a nonlinear region, whereas the linear region is typically used for amplification [164]. This approach can drive larger signals but results in increased power consumption due to a high-current biasing required, which disqualifies it from many low-power application solutions that are in high demand today [165]. In contrast, diode-based methods benefit from a very low power consumption of the devices, making them suitable for numerous batteryless applications, such as harmonic transponders [166]. Diode-based generator designs are generally less complex than their transistor counterparts. Given the advantages and drawbacks of both methods, this work focuses on diode-based harmonic generators.

So far, numerous publications have considered several types of diodes, including Schottky diodes [167–170], varactor diodes [171–176], step recovery diodes [177–183], and more rarely, tunnel diodes [184]. Schottky, varactor, and step recovery diodes may behave similarly in the forward bias region, but under particular DC operating points and RF driving settings that maximize harmonic production, their nonlinear characteristics diverge dramatically. Their charge storage effects and junction properties, which affect their effectiveness in nonlinear applications, are the cause of these variations. Resistive and capacitive nonlinearities are the two main types of nonlinearity commonly utilized. Capacitive nonlinearity can be seen from the device's capacitance (C) - voltage (V) characteristic. In contrast, diode's current (I) – voltage (V) relationship clearly illustrates its resistive nonlinearity. The increasing number of publications over the past decades highlights the growing interest in diode-based harmonic generation within the research community. TABLE 3.1 provides a comparative analysis of previous harmonic generator designs and the contributions of this work regarding technology, diode type, input frequency bandwidth and harmonic power distribution.

Tableau 3.1 Comparison with State-of-the-Art Harmonic Generators

Reference	**Diode**	**Technology**	**Input Bandwidth**	**Output Harmonic Power Ratio**		
				1^{st}	2^{nd}	3^{rd}
[167]	24×Schottky	PCB	4.5-5.05 GHz	n/a	8%	1.1%
[170]	58×Schottky	MMIC	4 GHz*	31.6%	3.2%	0.8%
[171]	4×Varactor	MMIC	1.05-1.7 GHz	n/a	0.8%	0.08%
[177]	1×SRD	PCB	300 MHz*	11.8%	3.5%	2.35%
[183]	1×SRD	PCB	500 MHz*	4%	0.4%	0.1%
[This work]	1×Schottky	PCB	0.95-1.05 GHz	7.7%	1.6%	0.04%
	1×Varactor	PCB	0.95-1.05 GHz	3.4%	0.1%	0.01%

* Single-tone input

Although several studies have explored the use of Schottky diodes, varactor diodes, and step recovery diodes as harmonic generators, there is a lack of analytical models examining the influence of input voltage amplitude and biasing voltage on the amplitude of high-order harmonics generated. These self-explanatory models are essential for a deep understanding of the ideal conditions for efficient and optimal utilization of diode nonlinearities.

In pursuit of this goal, this work provides a comprehensive theoretical analysis of the nonlinearities in Schottky diodes, varactor diodes, and step recovery diodes, enabling precise predictions of harmonic amplitudes under varying input and biasing conditions. The core contribution of this work is the development of detailed time-domain equations that accurately describe the current behavior of each type of diode, capturing their distinct resistive and capacitive nonlinearities. By formulating these equations, we establish a unified framework that not only enhances the understanding of diode-based harmonic generation but also aids in optimizing their performance for RF and future sensing applications.

Fabricated prototypes are presented to validate the theoretical analysis. Our focus is on generating and maximizing the first three harmonics of a 1 GHz input sinusoidal wave, specifically the fundamental frequency f_0, the second harmonic $2f_0$, and the third harmonic $3f_0$. A frequency-modulated continuous wave (FMCW) input signal sweeping from f_{min} to f_{max} is employed, resulting in an output frequency spectrum that spans f_{min} to f_{max}, $2f_{min}$ to $2f_{max}$, and $3f_{min}$ to $3f_{max}$. For the specific targeted application of FMCW radar chirps duplication, the limitation in input bandwidth arises primarily from the subsequent harmonic overlapping when the input fundamental bandwidth becomes too wide. Therefore, the maximum harmonic order must be chosen such that the lowest frequency of the next harmonic is at least equal to the highest frequency of the current harmonic. For RF input with a center frequency of 1 GHz, the maximum input bandwidth for preventing overlapping, with a proper safety margin, is around 300 MHz. In this work, to further improve the overall output amplitude consistency, the input frequency sweep will cover 100 MHz around f_0 (1 GHz), resulting in a total output bandwidth of 600 MHz, which is considered wideband harmonic generation. This is supported by the fact that the overall output bandwidth is 60 % of the input center frequency, covering a wide frequency range across several harmonics and representing a six-fold expansion of the input bandwidth. The input and output frequency spectra are depicted in Fig. 3.1.

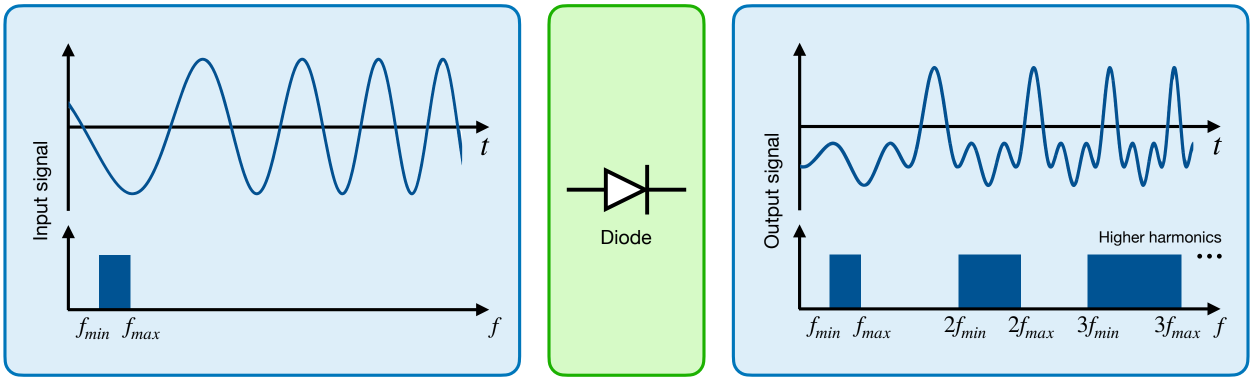

FIGURE 3.1 Input and output frequency spectrum of the proposed diode-based harmonic generator where the input signal is sweeping from 0.95 to 1.05 GHz while the output covers 0.95 to 1.05 GHz, 1.90 to 2.10 GHz, 2.85 to 3.15 GHz and higher.

The presented work begins with a study of nonlinearity sources and proposes time-domain current equations for the Schottky diode, varactor diode, and step recovery diode in Section II. This leads to a semiconductor analysis of the relevant parameters of the diodes, along with potential topologies for harmonic generation and a comparison of the theoretical current equations with numerical tools in Section III. Section IV describes the process of wideband impedance matching for the diodes. Following this, diode-based harmonic generator prototypes are presented, and an overall comparison is provided in Section V. The conclusions are drawn in Section VI.

3.3 Nonlinearity Sources and Harmonic Estimation

This section aims to illustrate the direct impact of biasing voltage and diode input voltage on the amplitudes of the generated harmonics by analyzing the primary sources of nonlinearity. Schottky, varactor, and step recovery diodes—all of which have unique nonlinear properties—were chosen in this work. Skyworks' SMS7630-079LF and SMS3924-079LF are silicon-based Schottky diodes that are appropriate for low-power harmonic generation due to their quick switching and low turn-on voltages. The silicon varactor diodes SMV1213-079LF and SMV1801-079LF, both manufactured by Skyworks, have high capacitance tuning ratios and are perfect for wideband conversion and frequency multiplication. Macom's silicon-based step recovery diode, the MMD830-E28, is designed for precise charge storage and release, allowing for effective harmonic generation.

3.3.1 Diode Modeling

Schottky diode model

The high nonlinearity of the Schottky diodes predominantly arises from the exponential shape of its $I_D(V)$ curve, resulting from the thermionic emission theory [185]. Fig. 3.2 shows the circuit diagram and the related voltages with the internal series resistance of the diode.

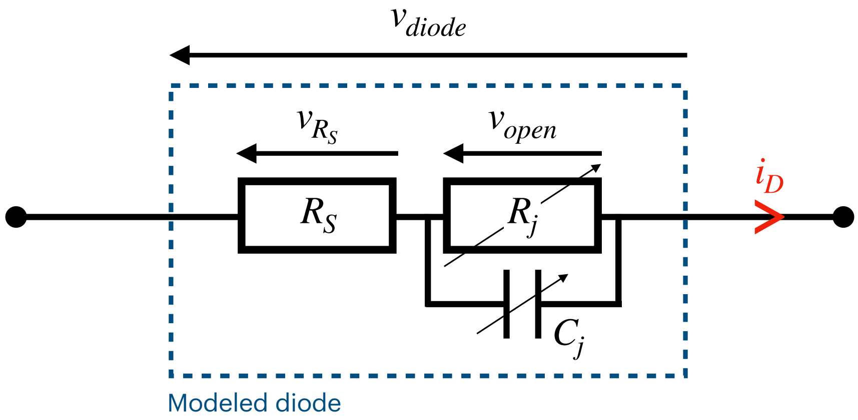

FIGURE 3.2 Model of the diode circuit and corresponding voltages and current. R_S is the series resistor, R_j and C_j are the junction resistor and capacitor, respectively.

Fig. 3.3 presents the typical $I_D(V)$ curve of a Schottky diode, and the extrapolated time-domain output signal.

In the forward-bias region $v_{open}(t) \geq 0$, the current flowing through the Schottky diode over time can be expressed as follows [185] :

$$i_{D,Sch}(t) = I_S \left(e^{\frac{v_{open}(t)}{nV_T}} - 1 \right) \tag{3.1}$$

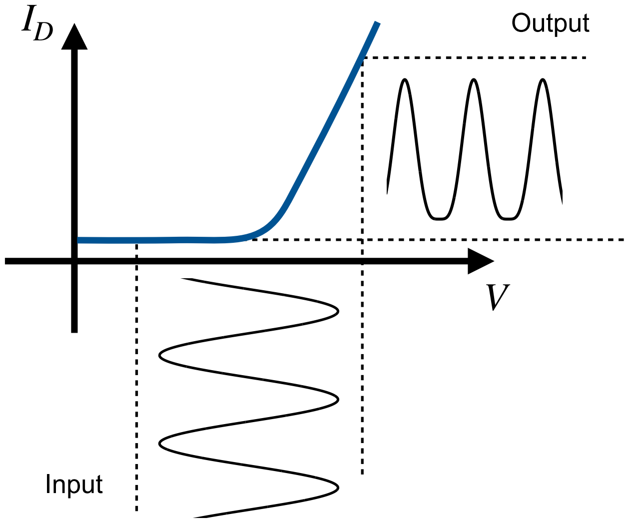

FIGURE 3.3 Typical $I_D(V)$ curve of Schottky diode.

where I_S is the saturation current of the diode, $v_{open}(t)$ is the open voltage across the diode over time, n is the ideality factor and V_T is the thermal voltage, such as $V_T = k_B T q^{-1}$ ($V_T \approx 25$ mV at room temperature). Additionally, to consider the breakdown effects in the reverse-bias region $v_{open}(t) < 0$, a voltage-dependent multiplicative coefficient $M(v_{open}(t))$ of the saturation I_S can be employed as described in [186] :

$$M(v_{open}(t)) = -e^{\frac{|v_{open}(t)|}{V_0}} \tag{3.2}$$

where V_0 is the knee voltage that needs to be extracted from the $I_D(V)$ curve for a given Schottky diode. For a sinusoidal biased mono-frequency excitation of the diode, and considering a series resistor R_S, the open voltage becomes :

$$\begin{aligned} v_{open}(t) &= v_{diode}(t) - v_{R_S} \\ &= V_{bias} + V_m \cos(\omega t) - R_S i_{D,Sch}(t) \end{aligned} \tag{3.3}$$

where V_{bias} is the biasing voltage of the diode, V_m is the amplitude of the sinusoidal wave. Hence, combining (3.1), (3.2) and (3.3), one can determine the analytical equation that represents the current of the diode $i_{D,Sch}(t)$:

$$i_{D,Sch}(t) = \begin{cases} I_S\left(e^{\frac{v_{open}(t)}{nV_T}} - 1\right) & \text{if } v_{open} \geq 0 \\ -I_S e^{\frac{|v_{open}(t)|}{v_0}} & \text{if } v_{open} < 0 \end{cases} \tag{3.4}$$

Using the definition of $v_{open}(t)$, and observing $V_m \in \mathbb{R}_+^*$, the boundaries of the forward-bias and the reverse-bias regions can be approximated by :

$$\begin{aligned} v_{open} \geq 0 &\iff \cos(\omega t) \geq -\frac{V_{bias}}{V_m} \\ v_{open} < 0 &\iff \cos(\omega t) < -\frac{V_{bias}}{V_m} \end{aligned} \tag{3.5}$$

Additionally, the analytical formulation of the current can be obtained by solving (3.4) with the help of W_0, the 0-th branch of the Lambert-W function [187] :

$$i_{D,Sch}(t) = \begin{cases} \frac{nV_T}{R_S} W_0\left(\frac{I_S R_S}{nV_T}\exp\left(\frac{v_{diode}(t)}{nV_T}\right) - 1\right) & \text{if } v_{open} \geq 0 \\ \\ -\frac{V_0}{R_S} W_0\left(-\frac{I_S R_S}{V_0}\exp\left(\frac{|v_{diode}(t)|}{V_0}\right)\right) & \text{if } v_{open} < 0 \end{cases} \tag{3.6}$$

This formulation of $i_{D,Sch}(t)$ highlights the exponential behavior of the Schottky diode. In the forward-bias region, the current rapidly increases when the input open-voltage reaches nV_T, which is the positive knee voltage. Similarly, in the reverse-bias region around V_0, the current negatively and significatively drops because of the breakdown effects. This presupposes that the biasing points with the highest nonlinearities are close to nV_T and V_0. To retrieve the harmonic components of the diode current waveform, one can expand (3.6) as a Fourier series [188] :

$$i_{D,Sch}(t) = \frac{A_0}{2} + \sum_{n=1}^{\infty}(A_n\cos(n\omega t) + B_n\sin(n\omega t)) \tag{3.7}$$

where :

$$
\begin{aligned}
A_{0,Sch} &= \frac{\omega}{\pi}\int_0^{\frac{2\pi}{\omega}} i_{D,Sch}(t)\,dt \\
A_{n,Sch} &= \frac{\omega}{\pi}\int_0^{\frac{2\pi}{\omega}} i_{D,Sch}(t)\cos(n\omega t)\,dt \\
B_{n,Sch} &= \frac{\omega}{\pi}\int_0^{\frac{2\pi}{\omega}} i_{D,Sch}(t)\sin(n\omega t)\,dt
\end{aligned}
\tag{3.8}
$$

The n-th harmonic amplitude C_n is given by :

$$
C_n = \sqrt{A_n^2 + B_n^2} \tag{3.9}
$$

The fundamental output frequency, the second and third harmonics, f_0, $2f_0$, and $3f_0$ respectively, as well as DC output can then be written as :

$$
\begin{aligned}
A_{0,Sch(DC)} &= A_{0,Sch} \\
C_{1,Sch(f_0)} &= \sqrt{A_{1,Sch}^2 + B_{1,Sch}^2} \\
C_{2,Sch(2f_0)} &= \sqrt{A_{2,Sch}^2 + B_{2,Sch}^2} \\
C_{3,Sch(3f_0)} &= \sqrt{A_{3,Sch}^2 + B_{3,Sch}^2}
\end{aligned}
\tag{3.10}
$$

Note that this Fourier series expansion is performed under the assumption that $i_{D,Sch}(t)$ is periodic and does not present severe sharp transitions in the time domain—which is the case in this work's frame—that may lead to an accuracy limitation of the harmonics' amplitude estimation.

Varactor diode model

The nonlinearity of the varactor diode is mainly a consequence of the voltage dependency of its junction capacitance, thus affecting the quantity of charge stored over different voltages. Fig. 3.4 presents the $Q_D(V)$ curve of a typical varactor diode, and the extrapolated time-domain output signal.

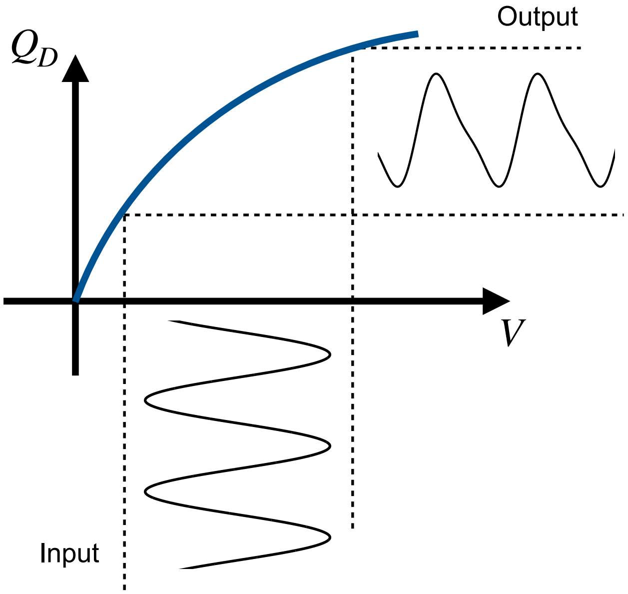

FIGURE 3.4 Typical $Q_D(V)$ curve of varactor diode.

Under the reverse-bias conditions, the nonlinear junction capacitance C of the varactor diode can be expressed as a function of the input open-diode-voltage v_{open} [189]. Under the forward-bias conditions, the capacitance tends to stabilize around a very small value compared to the zero-bias capacitance C_0. Therefore, as a first approximation, the forward-bias capacitance can be considered equal to zero $C_{Forward\,bias} \approx 0$ F [190] :

$$C(v_{open}) = \begin{cases} 0 & \text{if } v_{open} \geq 0 \\ \frac{C_0}{\left(1+\frac{|v_{open}|}{V_j}\right)^{\gamma}} & \text{if } v_{open} < 0 \end{cases} \tag{3.11}$$

where V_j is the junction potential and γ is the doping profile coefficient of the diode. The main types of junctions doping profiles are linear junctions ($\gamma \approx 0.3$), abrupt junctions ($\gamma \approx 0.5$), and hyperabrupt junctions ($\gamma > 1$) [175]. Also, under the reverse-bias, and as a first approximation, the open voltage across the diode can be expressed as $v_{open}(t) = V_{bias} + V_m cos(\omega t)$. For a varactor diode, the quantity of charge Q is known to be $Q = CV$. Then, (3.11) can be rewritten as :

$$Q(v_{open}) = \begin{cases} 0 & \text{if } v_{open} \geq 0 \\ \frac{C_0 v_{diode}(t)}{\left(1+\frac{|v_{diode}(t)|}{V_j}\right)^{\gamma}} & \text{if } v_{open} < 0 \end{cases} \tag{3.12}$$

The current $i_{D,Var}(t)$ is obtainable through [15] :

$$i_{D,Var}(t) = \frac{\partial Q(v_{open})}{\partial t} \tag{3.13}$$

In the forward-bias region, the capacitance of the varactor diode has a negligible effect on its nonlinearity. As a result, the nonlinearity in this region has a similar feature as Schottky diodes, $i_{D,Var}(t)$ is then ruled by the thermionic emission theory with a series resistor R_S (3.1). After some treatments and combining (3.12) with (3.13), the current $i_{D,Var}(t)$ becomes :

$$i_{D,Var}(t) = \begin{cases} \frac{nV_T}{R_S} W_0\left(\frac{I_S R_S}{nV_T}\left(e^{\frac{v_{diode}(t)}{nV_T}} - 1\right)\right) & \text{if } v_{open} \geq 0 \\ -\frac{\omega V_m C_0 \sin(\omega t)(v_{diode}(t)(\gamma-1)-V_j)}{V_j\left(1+\frac{|v_{diode}(t)|}{V_j}\right)^{\gamma+1}} & \text{if } v_{open} < 0 \end{cases} \tag{3.14}$$

From this formulation, one can deduce that the exponential shape of the current in the forward-bias region may conduct to a relative minimization of the amplitude of the harmonics induced by the voltage-dependent junction capacitance of the varactor diode. As a result, the reverse-bias region appears to be more interesting to generate a relatively flat output spectrum among the desired harmonic. A Fourier analysis can also be performed on (3.14) to retrieve the harmonic components. By replacing (3.6) by (3.14) in (3.8) the DC, the fundamental frequency, second and third harmonic amplitudes become :

$$\begin{aligned} A_{0,Var(DC)} &= A_{0,Var} \\ C_{1,Var(f_0)} &= \sqrt{A_{1,Var}^2 + B_{1,Var}^2} \\ C_{2,Var(2f_0)} &= \sqrt{A_{2,Var}^2 + B_{2,Var}^2} \\ C_{3,Var(3f_0)} &= \sqrt{A_{3,Var}^2 + B_{3,Var}^2} \end{aligned} \tag{3.15}$$

Step recovery diode model

The nonlinearity of the step recovery diode is due to the abrupt change of its junction capacitance during reverse recovery, and to the stepped behavior of the recovery part [191]. Fig. 3.5 presents the $Q_D(V)$ curve of a typical varactor diode, and the extrapolated time-domain output signal.

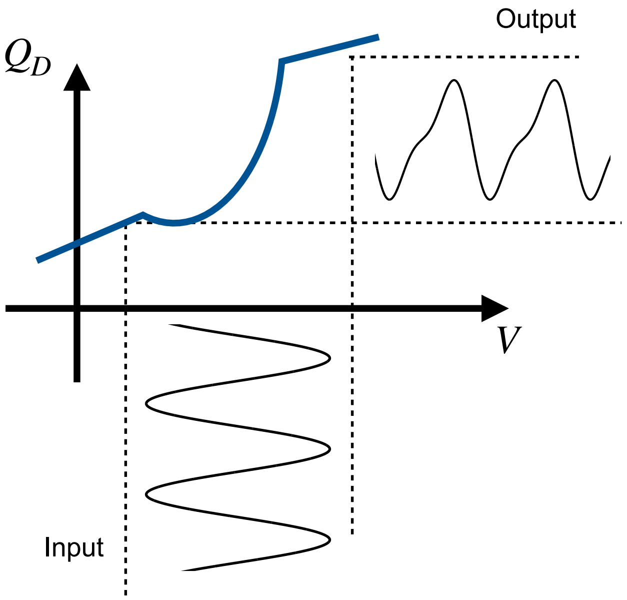

FIGURE 3.5 Typical $Q_D(V)$ curve of a step recovery diode.

The charge Q stored in the step recovery diode, over time, can be modeled as a piecewise-defined function [192, 193] resulting from the voltage-dependency of the inherent junction capacitance :

$$Q(v_{open}) = \begin{cases} C_r v_{open} & \text{if } v_{open} \leq 0 \\ \frac{\Lambda}{V_j}\left(v_{open} + \frac{C_r V_j}{2\Lambda}\right)^2 - \Phi V_j & \text{if } 0 < v_{open} \leq V_j \\ C_f v_{open} - \Lambda V_j & \text{if } v_{open} > V_j \end{cases} \tag{3.16}$$

with :

$$\Lambda = \frac{C_f - C_r}{2} \quad \Phi = \frac{C_r^2}{2(C_f - C_r)} \tag{3.17}$$

where C_r is the reverse bias capacitance of the diode, and C_f is the maximum value of the forward bias capacitance. Then, after some treatments, and applying (3.13), the current flowing through the step recovery diode becomes :

$$i_{D,SRD}(t) = \begin{cases} -C_r \omega V_m \sin(\omega t) & \text{if } v_{open} \leq 0 \\ -\frac{2\omega \Lambda V_m}{V_j} \sin(\omega t) \left(v_{diode}(t) + \frac{C_r V}{2\Lambda} \right) & \text{if } 0 < v_{open} \leq V_J \\ -C_f \omega V_m \sin(\omega t) & \text{if } v_{open} > V_J \end{cases} \tag{3.18}$$

The analytical formulation of the step recovery diode current appears somehow unlike the previously studied diodes. In fact, an in-depth analysis of the parameters will be required to maximize the harmonic generation. This current waveform of $i_{D,SRD}(t)$ yields similar results as those presented in [194]. Additionally, with step recovery diodes, more advanced biasing techniques are enabled [195]. From this analytical formulation of $i_{D,SRD}(t)$, the harmonic components can be found using Fourier's coefficients :

$$\begin{aligned} A_{0,SRD(DC)} &= A_{0,SRD} \\ C_{1,SRD(f_0)} &= \sqrt{A_{1,SRD}^2 + B_{1,SRD}^2} \\ C_{2,SRD(2f_0)} &= \sqrt{A_{2,SRD}^2 + B_{2,SRD}^2} \\ C_{3,SRD(3f_0)} &= \sqrt{A_{3,SRD}^2 + B_{3,SRD}^2} \end{aligned} \tag{3.19}$$

3.3.2 Output Spectrum Analysis

This section provides a visual tool to study the influence of the mentioned parameters (biasing V_{bias} and input voltage amplitude V_m) on generating desired harmonics. Although the harmonic generator produces a DC component, our analysis does not specifically include it because DC does not support the desired functionality. Rather, we concentrate on considering into consideration the power distribution among the harmonics. Fig. 3.6 depicts the power of $C_1(f_0)$, $C_2(2f_0)$ and $C_3(3f_0)$ in dBm for V_m between 0 and 10 dBm and ; V_{bias} from 0 to 1 V for the Schottky diode (SMS7630) ; from -10 to 0V for the varactor diode (SMV1213) ; from 0 to 2 V for the step recovery diode (MMD830). The output powers below -50 dBm are whiten for clearer visualization.

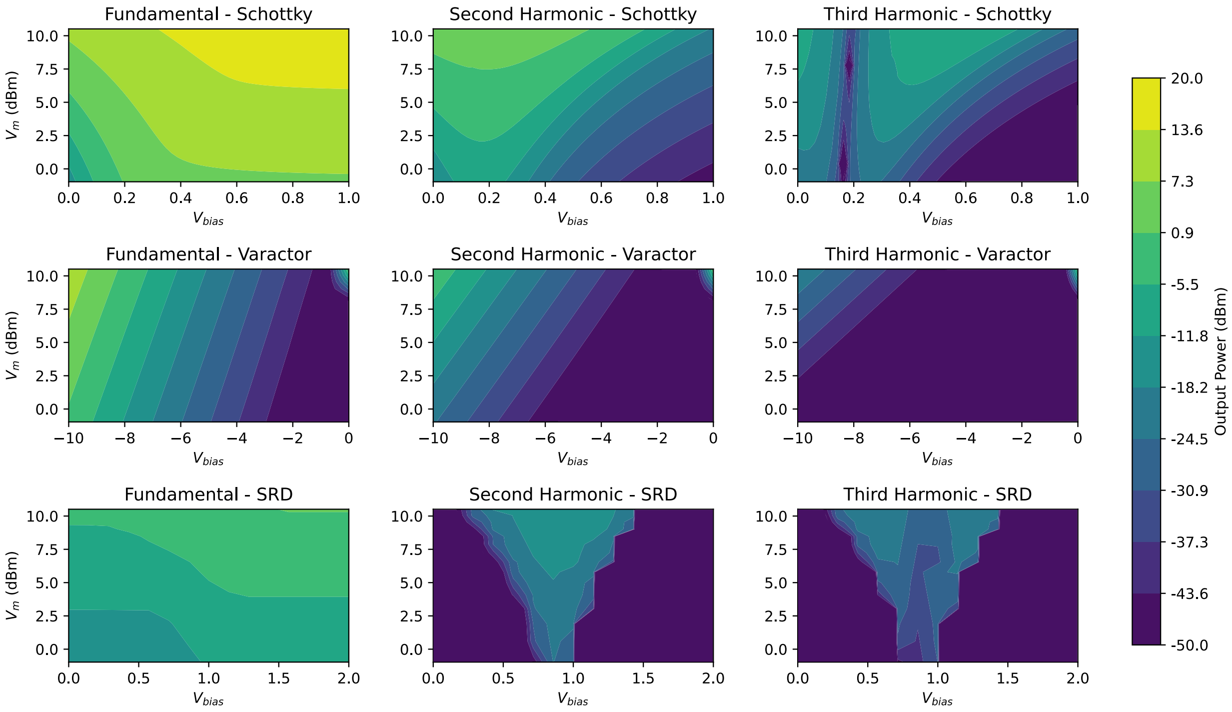

FIGURE 3.6 Fundamental (1 GHz), second (2 GHz) and third harmonic (3 GHz) relative amplitudes of output signals for SMS7630 (Schottky), SMV1213 (varactor) and MMD830 (SRD) with various values of input powers and bias. Only output powers above -50 dBm are shown.

To help identify the optimum set of parameters and further analyze the harmonic generation capabilities of diodes, one can compute the weighted arithmetic mean σ_K of the first K-th normalized harmonic amplitudes (depending on V_m and V_{bias}) by the maximum achievable value of C_n within the range of V_m and V_{bias} and weighted by coefficients β_n :

$$\sigma_K(V_m, V_{bias}) = \frac{\sum_{n=1}^{K} \beta_n \frac{C_n(V_m, V_{bias})}{\max(C_n)}}{\sum_{n=1}^{K} \beta_n} \tag{3.20}$$

Consequently, when each harmonic amplitude is achievable at its maximum for the same parameters, σ_K will be equal to 1. The weighting coefficients β_n allow to give more attention on specific harmonics, hence only maximizing the chosen ones. Fig. 3.7 presents the computed values of σ_3 based on (20).

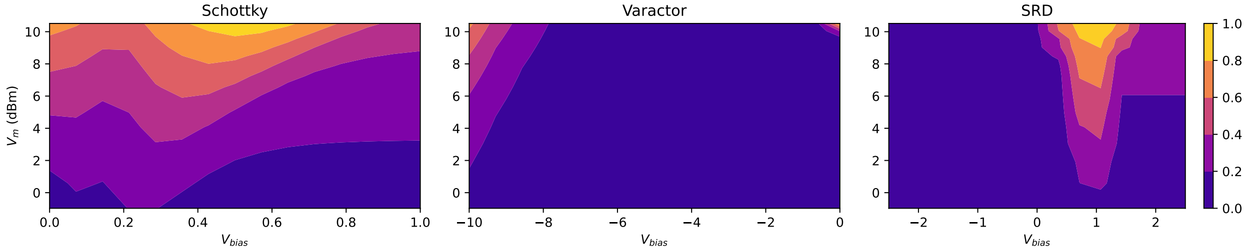

FIGURE 3.7 Computed values of σ_3 for the Schottky, Varactor and SRD diodes across input power and bias.

For the Schottky diode, it is observed that increasing both V_{bias} and V_m have a positive contribution on the fundamental amplitude f_0, which is directly observable in (6) thanks to the exponential term. Interestingly, the second harmonic amplitude $2f_0$ is maximized where the highest nonlinearity is observed, around the knee voltage in the forward-bias ($V_{bias} \approx 0.5$ V). The third harmonic amplitude $3f_0$ presents a symmetrical pattern around $V_{bias} = 0.2$ V and is positively affected by a high input amplitude. The forward-biasing region is then preferred for the application. For the varactor diode, a clear difference is observed, and the reverse-biasing region appears to be the optimum condition for achieving a high nonlinearity. All output components benefit from a relatively high reverse-bias and high input amplitude. For the step recovery diode, it is observed that all components present a common interest point in the generation of harmonics, around $V_{bias} = 0.1$ V. Based on those results, the theoretical optimum biasing V_{bias} and input power V_m, is $V_{bias} = 0.5$ V at 10 dBm input power for the SMS7630, $V_{bias} = -10$ V at 10 dBm input power for the SMV1213 and $V_{bias} =$ 1 V at 10 dBm input power for the MMD830. Indeed, those sets of V_{bias} and V_m minimalize the amplitude gap between the harmonics while maintaining a relatively high fundamental amplitude.

3.4 Diode Profiling and Numerical Models

3.4.1 Diode Characterization

Aiming to verify the nonlinearity source of the studied diodes, one can measure the voltage dependency of the current for Schottky diodes, as well as the voltage dependency of the junction capacitance for both varactor diodes and step recovery diodes. Fig. 3.8 presents the semiconductor measurement results of the SMS7630, SMS3924, SMV1213, SMV1801 and

MMD830 obtained with the Precision LCR Meter E4980A from Keysight as compared to the modeled behavior.

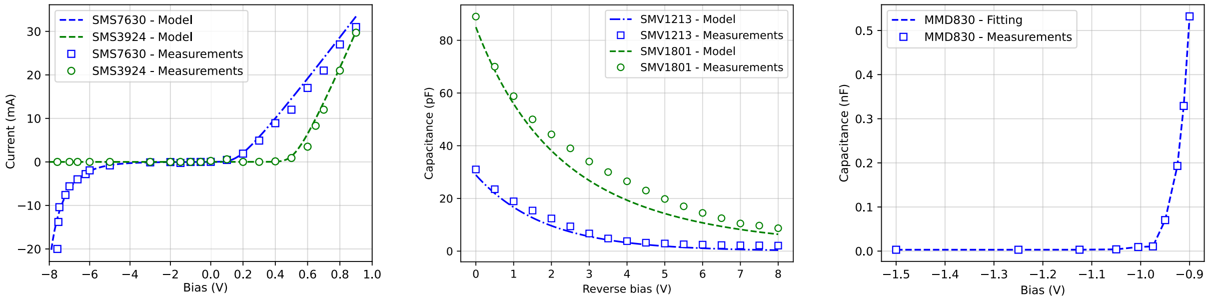

(a) (b) (c)

FIGURE 3.8 Comparison of models and measurements of (a) $I(V)$ curve of SMS7630 and SMS3924, (b) $C(V)$ curve of SMV1213 and SMV1801 and (c) $C(V)$ curve of MMD830.

3.4.2 Diode Configuration

In the realm of a proper control of the generated harmonics, diode configurations play a critical role in the desired outcome. Two primary topologies are discussed with only one diode, namely series and parallel configurations, presented in Fig. 3.9.

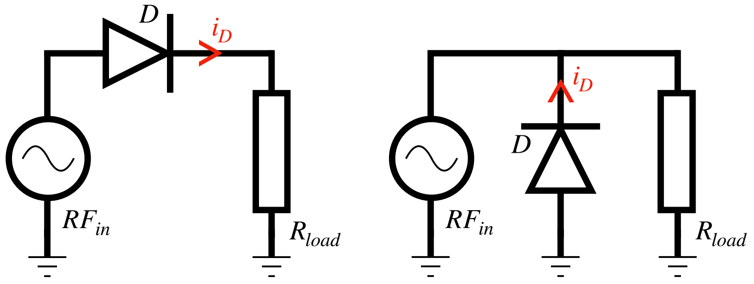

FIGURE 3.9 Series and parallel diode configurations for harmonic generation.

Besides, the diode type may also influence the optimum configuration. The key difference between these configurations lies in the switching states defined by the inherent turn-on voltages V_{ON} of the diodes. For the series diode configuration, when $RF_{in} < V_{ON}$, very little to no current flows into the load ($R_{load} = 50\ \Omega$), and the voltage across the load remains low. When $RF_{in} > V_{ON}$, the diode's voltage drop becomes equal to the input voltage, and the current is driven according to (3.1). In contrast, for the parallel diode configuration, the load voltage remains negligible when $RF_{in} < V_{ON}$, and the load voltage equals the input voltage. However, when $RF_{in} > V_{ON}$, the diode begins to conduct current, effectively short-circuiting the source, which is generally undesirable. To overcome that issue, R_{load} should be high compared to the generator impedance, which is not the case in practice. Hence, a series-diode configuration is employed in this work for the Schottky diode case. The varactor diode has the particularity of being reverse-biased, in that way both topologies are usable. Some previous works using varactor diode for harmonic generation tend to use either series [196] or parallel configurations [197]. Finally, for the step recovery diode, previous examples used a series-diode configuration [182] as well as parallel ones [198].

3.4.3 Harmonic Model Assessment with Numerical Model

As a mean to simulate the diode-based harmonic generators and assess the strengths and limitations of the analytical models, Advanced Design System (ADS) software from Keysight is used for simulation purposes. TABLE 3.2 presents the key SPICE parameters of the SMS7630, SMS3924, SMV1213, SMV1801 and MMD830 used in the ADS simulation, which are provided by the manufacturer.

Tableau 3.2 Key SPICE Parameters of the Selected Diodes

Parameter	**Schottky**		**Varactor**		**SRD**
	SMS7630	SMS3924	SMV1801	SMV1213	MMD830
I_S (A)	5.10^{-6}	2.10^{-11}	1.10^{-14}	1.10^{-14}	1.10^{-12}
R_S (Ω)	20	11	1	1.4	0.13
n	1.05	1.08	1	1	1.3
TT (ps)	10	80	0	0	20.10^{-9}
C_{J0} (pF)	0.14	1.5	85	28.9	1
M	0.4	0.4	4.4	0.5	0.235
B_V (V)	2	100	0	12	25
I_{BV} (A)	1.10^{-4}	1.10^{-5}	1.10^{-13}	1.10^{-5}	1.10^{-5}
V_J (V)	0.34	0.84	0.7	1.1	0.5
L_S (nH)	0.7	0.7	0.7	0.7	0.15
C_P (pF)	-	-	2.6	2.2	-

The chosen Schottky diode mainly differ from their saturation current and breakdown voltages. The two references of varactor diodes have strongly dissimilar capacitance ratios $\beta = C_{0V}/C_{4V}$, i.e. the ration of the series capacitance value at 0 V and 4 V reverse bias ($\beta_{SMV1213} = 8.6$ and $\beta_{SMV1801} = 3.3$). Fig. 3.10 shows the simulated typical packaged diode model, used for each type of diode, that includes the series resistor R_S, the series inductance L_S and the parallel diode C_p. These parameters are meant to enhance the simulated diode and fit as close as possible to the purchased diodes. For the step recovery diode, in addition to the Simulation Program with Integrated Circuit Emphasis (SPICE) parameters, a SDD1P1 ADS block is added to include the variation of the charge depending on the input voltage (3.16).

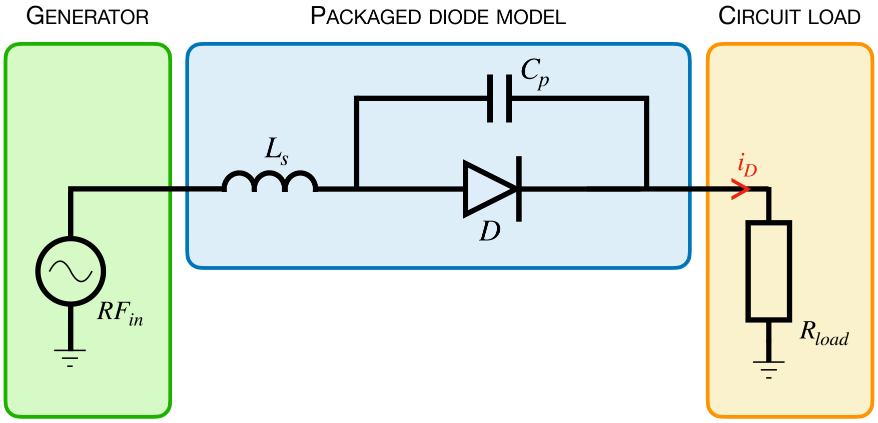

FIGURE 3.10 Schematic of packaged diode using SPICE parameters of TABLE 3.2 for ADS simulation.

To assess the analytical models of Schottky diode (3.6), varactor diode (3.14) and step recovery diode (3.18), a single-period current-waveform comparison with the ADS results is depicted in Fig. 3.11.

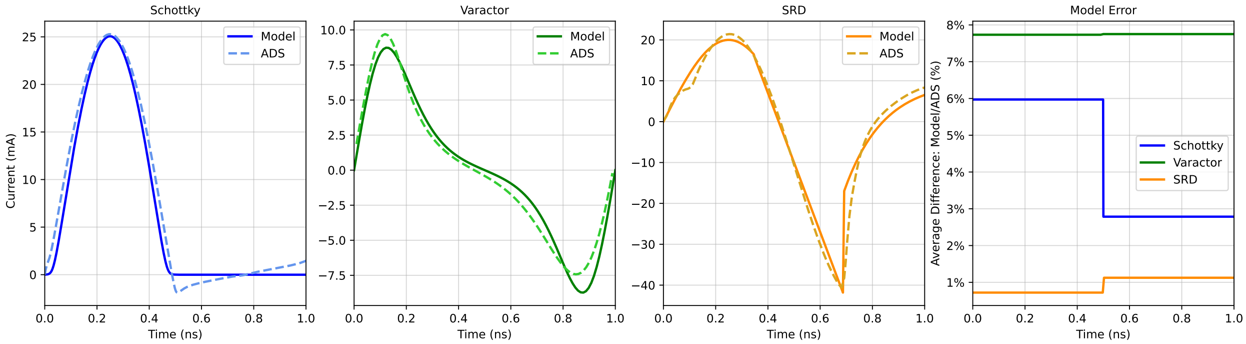

FIGURE 3.11 Comparison of output current waveform simulated in ADS and analytical models for SMS7630 (3.6), SMV1213 (3.14) and MMD830 (3.18). Model error shows the half-period averaged absolute current differences between the analytical models and ADS simulations.

The model error plot yields an average error of 4.5 % between the Schottky diode model and its simulation, 8 % between the varactor diode model and its simulation, and less than 1 % between the step recovery diode model and its simulation. It can then be seen that the previously settled analytical current equations present a satisfactory match with numerical results. It is to be noted that the discrepancy observed in the time-domain current equation of the Schottky diode results from capacitive effects during the recovery stage, which are not included in the theoretical model but are taken into account in the ADS simulation. The proposed method assumes idealized diode behavior, where current is exactly zero in the negative recovery state, whereas ADS takes into consideration parasitic capacitance and reverse leakage, which leads to a small negative currents peak in the negative recovery state. Hence, those models can be used to evaluate the harmonic amplitudes that are contained in each modeled current signals.

3.5 Diode Selection Process

Based on a first set of harmonic estimation using the numerical model of the diodes, the Schottky diodes SMS7630 and SMS3924 both appear to be suitable candidates for harmonic generation. However, it was observed that the harmonic generation capacities of those diodes are much alike while the SMS7630 requires very low to no biasing voltage. For this reason, this is a preferred choice for this work considering that many low-power applications could not afford to provide external DC biasing, making this a crucial stake in futures wireless systems. However, for applications where a DC biasing does not represent a limitation, the

SMS3924 could be relevant.

The cut-off frequency limitation needs to be discussed in the selection process of such non-linear devices, as it must be greater than at least 3.5 GHz. The cut-off frequencies for the SMS7630 and SMS3924, given by the manufacturer, are 24 GHz and 6 GHz, respectively, which do not represent a limitation in our work. Considering the varactor diodes, their cut-off frequency can be expressed as :

$$f_c = \frac{1}{2\pi R_s C_{J0}} \tag{3.21}$$

Using Spice parameters of the SMV1801 and SMV1213, one can compute the specific cut-off frequency of each diode. The SMV1801 presents a cut-off frequency of 1.7 GHz, which does not satisfy the requirements in this work, while the SMV1213 has a cut-off frequency of 3.9 GHz.

Because of their better performance characteristics, the SMS7630 and SMV1213 diodes' prototype fabrication is given priority in this investigation. It is seen from the analysis of Fig. 3.6 that the Strep Recovery Diode (SRD)-based harmonic generator's output power is substantially less than that of the alternatives. Consequently, the SRD design provides fewer encouraging outcomes for the targeted use case. By concentrating on the SMS7630 and SMV1213, resources are allocated to the most effective designs, which is consistent with the study's goals of maximizing the performance of harmonic generation.

3.6 Implementation and Measurements

In the following section, the prototyping stage involves integrating the SMS7630 and SMV1213 diodes into harmonic generation circuits. The objective is to optimize circuit parameters and dimensions to achieve stable harmonic generation across three bands while minimizing circuit losses.

3.6.1 Impedance Matching of the Diodes and Fabricated Circuits

Special concern needs to be addressed when designing the matching networks used for the diode-based harmonic generators. As expected from the $I_D(V)$, the input impedance of the diodes will be likely to vary depending on the operating point [199]. Hence, using the expected optimum values of V_m and V_{bias}, both the input impedance R_{in} and output impedance R_{out}

are simulated and used during the matching procedure. Fig. 3.12 presents the harmonic generator topologies for the SMS7630, and SMV1213.

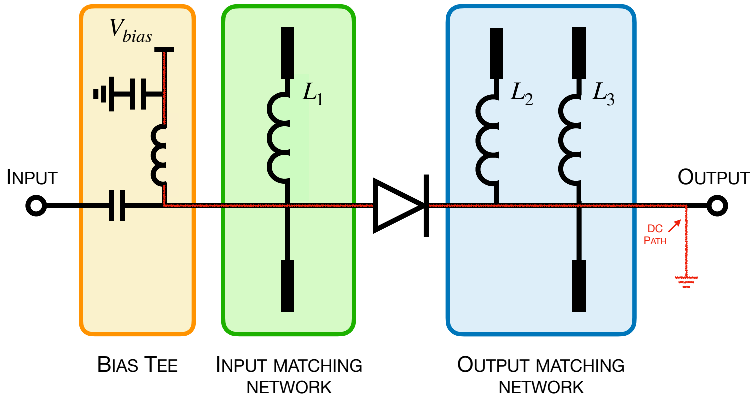

Figure 3.12 Circuit topology for diode-based harmonic generators featuring hybrid structures for input and output matching networks and external biasing. DC grounding is achieved through the external scope.

The input and output matching networks employ hybrid structures : both microstrip technology and discrete components, to satisfy the wideband matching requirements of the system. Indeed, the input signal sweeps from 0.95 GHz to 1.05 GHz, totalizing 100 MHz bandwidth, while the output signal sweeps from 0.95 GHz to 1.05 GHz (fundamental band), 1.90 GHz to 2.10 GHz (second harmonic band) and 2.85 GHz to 3.15 GHz (third harmonic band), hence covering the bands of the first three harmonics.

Eventually, to provide the optional DC biasing to the diode, an external 33150A bias tee from HP is employed. At the same time, the bias tee allows for the diode's ground path. Indeed, the proposed approach completes the DC loop by applying the DC high potential at the bias tee's DC port and establishing the return ground path internally using the scope's common ground.

The fabricated boards, as showed in Fig. 3.13, are manufactured on RT/Duroid 5880 from ROGERS in 31 mil thick substrate.

Fig. 3.14 presents the measured S-parameters values, S11, S22, and S21, based on the fabricated boards. The frequency bands of interest are highlighted in grey.

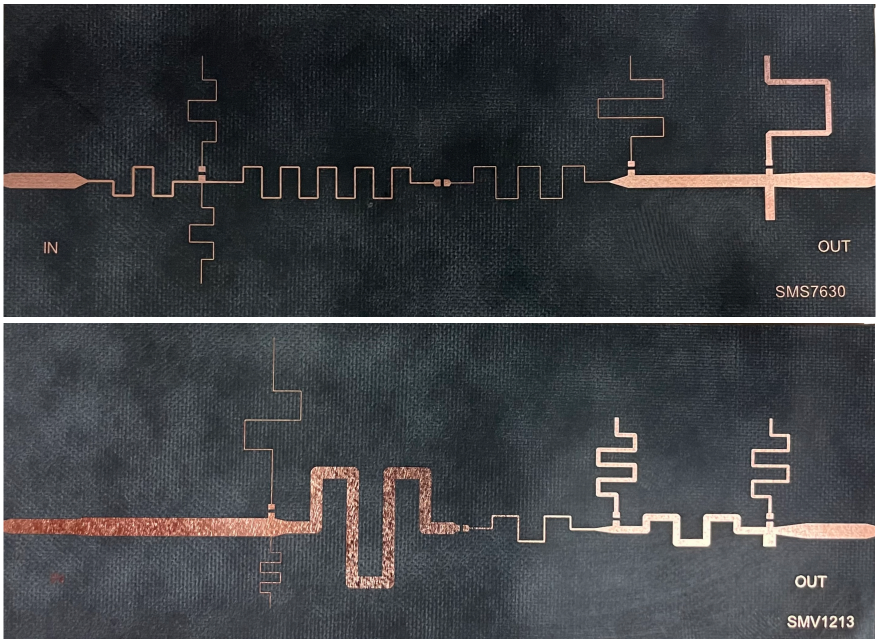

Figure 3.13 Photograph of the fabricated PCBs based on SMS7630 (Top) and SMV1213 (Bottom).

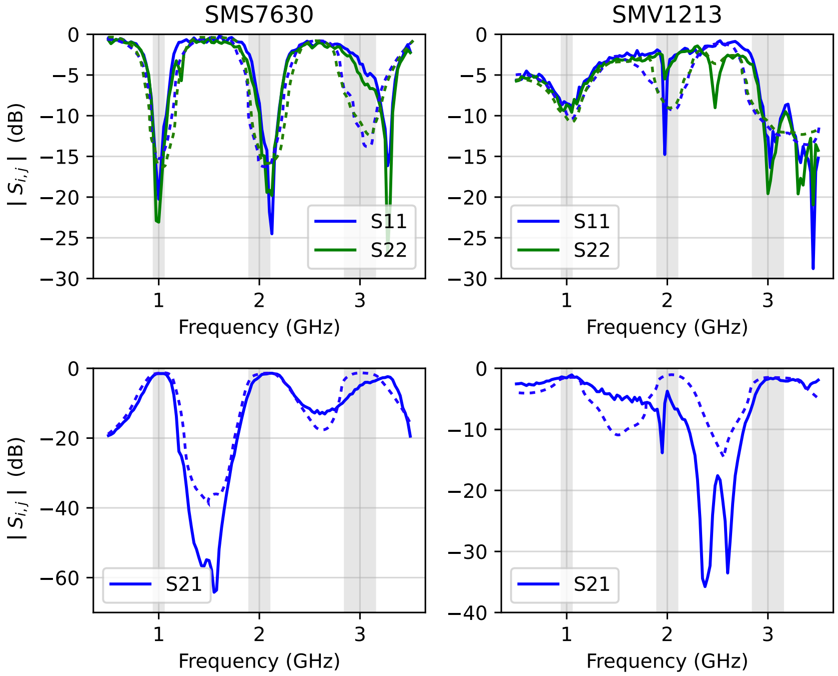

Figure 3.14 Comparison of simulated (dashed lines) and measured (plain lines) S-parameters of the SMS7630 and SMV1213 harmonic generators between 0.5 and 3.5 GHz.

For the SMS7630, the measurements show satisfactory input and output power reflection on all bands of interest. The transmission coefficient is near −3 dB in the fundamental band, in a stable way, whereas it follows a linear variation from −5 dB to −3 dB, and from −10 dB to −5 dB, in the second and third harmonic band, respectively. For the SMV1213, the input and output reflection in the fundamental band is satisfactory, while it is less widely adapted in the second harmonic band. In the third harmonic band, the matching is satisfactory. The transmission coefficient reflects the uneven matching in the third harmonic band but presents a stable −3 dB transmission in the fundamental band. In the second harmonic band, a −5 dB transmission coefficient is observed. The injected power for S-parameter measurements in Fig. 3.14 is kept around 0 dBm, to ensure the diode operates within the specified zone. S-parameter fluctuations with input powers ranging from −10 dBm to 10 dBm are negligible and have no discernible impact on the findings of our analysis.

3.6.2 Output Spectrum Flatness

To validate the wideband capability of the proposed up-to-second-order harmonic generator, assessing the harmonic flatness—the ability of the generator to maintain a stable harmonic amplitude across the entire band—is crucial. The Keysight E8267D single tone generator provides ten input frequencies, equally spaced from 0.95 GHz to 1.05 GHz, at a constant input power of 7 dBm for the SMS7630 and 10 dBm for the SMV1213. The biasing voltages are set to 0.1 V for the SMS7630 and −10 V for the SMV1213, as these settings offer satisfactory compromises between the measured output harmonic levels.

Fig. 3.15 presents the measurement results for the SMS7630 and SMV1213 diodes.

For the SMS7630 : From 0.95 to 1.05 GHz, the fundamental output varies by ± 2 dBm around −4.1 dBm. From 1.90 to 2.10 GHz, the second harmonic output varies by ± 5 dBm around −10.9 dBm. From 2.85 to 3.15 GHz, the third harmonic output varies by ± 4 dBm around −27.3 dBm. For the SMV1213 : From 0.95 to 1.05 GHz, the fundamental output varies by ± 2.5 dBm around −4.6 dBm. From 1.90 to 2.10 GHz, the second harmonic output varies by ± 6 dBm around −20 dBm. From 2.85 to 3.15 GHz, the third harmonic output varies by ± 7 dBm around −31 dBm. From Fig. 3.15, it is evident that a portion of the power is lost during the conversion process. The primary source of these losses is the Joule effect in R_S, which accounts for approximately 8 mW in the Schottky diode and 0.1 mW in the varactor diode. Furthermore, the analysis considers only the first, second, and third harmonics, excluding

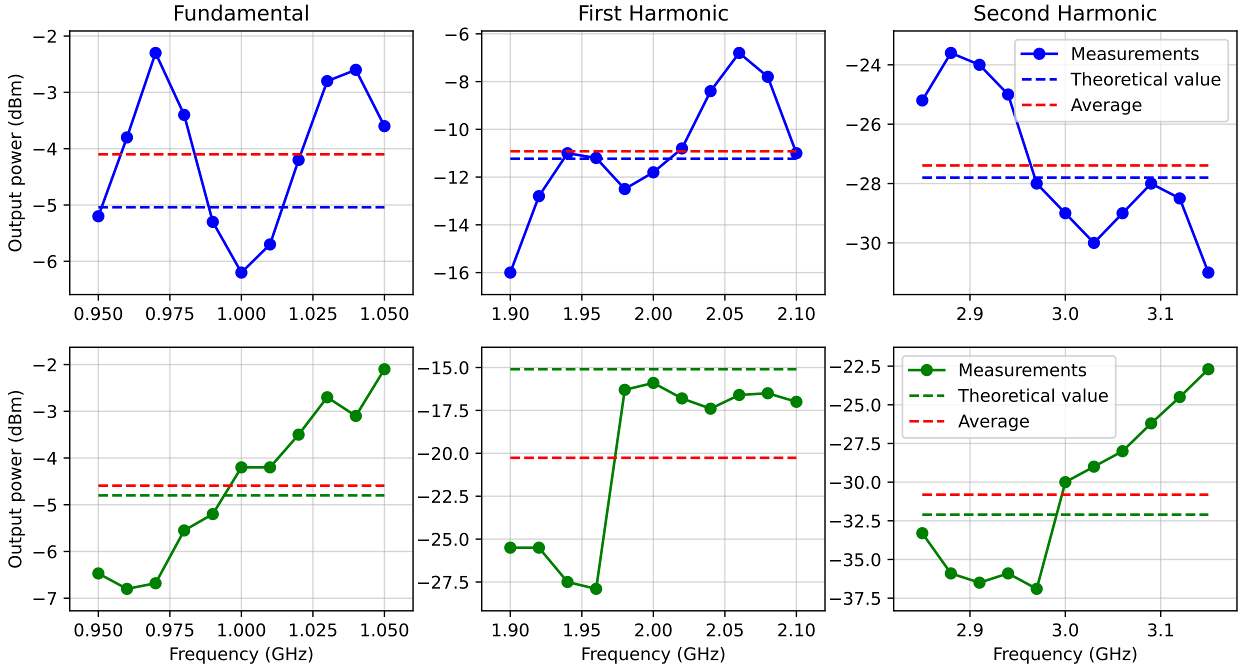

FIGURE 3.15 Measurement results of the output power compared at 7dBm input power for the fundamental, second and third harmonic of the SMS7630 at 0.1 V biasing, and 10 dBm input power for the SMV1213 at -10 V biasing.

both DC power and higher-order harmonics. Additional losses may also arise from return loss and impedance mismatching.

TABLE 3.3 summarizes the measurement results of the manufactured harmonic generators across the fundamental, second and third harmonic.

3.6.3 Losses Consideration

Losses related to the diodes and associated input and output networks were carefully considered when designing the SMS7630 and SMV1213 harmonic generators using ADS software. To effectively predict real-world situations, losses due to parasitic and substrate effects were included in the model. Experimental results for the SMS7630 and SMV1213 diodes' output power and harmonic generation performance closely matched the ADS model's expected values. The agreement between simulated and experimental data confirms that the model's loss assumptions are satisfactory for the proposed application. This consistency assures that the key performance-influencing elements are adequately captured by the ADS model. Consequently, the model can be used as a reliable tool for harmonic generator design and opti-

Tableau 3.3 Measurement Results of Average Output Harmonic Power Ratio and In-Band Variations

Parameter		**Schottky**	**Varactor**
		SMS7630	SMV1213
Fundamental	Power ratio	7.7%*	3.4%**
	Variation	±1.98 dBm	±2.37 dBm
Second harmonic	Power ratio	1.6%*	0.1%**
	Variation	±4.57 dBm	±6.04 dBm
Third harmonic	Power ratio	0.04%*	0.01%**
	Variation	±3.70 dBm	±7.22 dBm

*7 dBm input power, **10 dBm input power

mization, allowing precise system behavior prediction prior to the prototype manufacturing stage.

3.7 Conclusion

Focusing on Schottky, varactor, and step recovery diodes as crucial components of next-generation RF system applications through nonlinear sensing and other emerging technologies, this study provides a comprehensive theoretical and practical analysis of diode-based harmonic generators. The proposed time-domain current equations predict harmonic amplitudes under various input and biasing conditions by thoroughly examining the resistive and capacitive nonlinearities of these diodes. With a 1 GHz input and a frequency-modulated sweep spanning 600 MHz at 7 dBm and 10 dBm, the fabricated prototypes demonstrated robust wideband harmonic production up to the third order. The SMS7630 and SMV1213 diodes achieved average output power fluctuations of ± 3.4 dBm and ± 5.2 dBm, respectively. These results affirm the practical applicability of these diodes, particularly in low-power and batteryless applications, and validate the theoretical models. Moreover, this work establishes a solid foundation for future research and advancements in wideband radio frequency technology by bridging theoretical understanding with experimental validation. Future research could extend the study to millimeter-wave frequencies to optimize diode performance for advanced sensing, 5G, and 6G applications. Additionally, exploring the application of these harmonics generators in small, battery-free wireless systems that integrate energy harvesting, communication, and sensing into multifunctional systems could be highly beneficial.

CHAPITRE 4 ARTICLE 3 : ENHANCING RADAR SYSTEM PERFORMANCES VIA THE FUSION OF SCATTERED NON-CONTIGUOUS FREQUENCY SUB-BANDS

Thomas Micallef, Adrien Murcott, Xiaoqiang Gu and Ke Wu

Soumis à : *IEEE Transactions on Radar Systems*
Date de soumission : 16 Mai 2025

4.1 Abstract

A super-fusion technique is proposed and demonstrated for seamlessly integrating non-equal, non-contiguous frequency sub-bands to enhance key radar system performance metrics such as range and velocity resolution. The method strategically partitions the required bandwidth of an exemplary FMCW radar into multiple narrower and scattered sub-bands, enabling efficient spectrum utilization while mitigating RF congestion challenges. A comprehensive theoretical framework is developed to model the fusion process and predict system resolution. Experimental validation employs three sub-bands centered at 1, 2, and 3 GHz, with respective bandwidths of 100, 200, and 300 MHz. The fusion process achieves an equivalent combined bandwidth of nearly 600 MHz, delivering a resolution of 37.6 cm and confirming the expected linear summation of contributions from individual sub-bands. Notably, the technique distinguishes two closely spaced targets separated by 40 cm—unachievable using any single sub-band alone. This study establishes a scalable and practical approach to multi-band fusion, addressing spectral congestion while enhancing radar performance. The findings underscore the potential of the proposed technique to advance next-generation radar applications in increasingly crowded RF environments.

4.2 Introduction

The growing competing usage for limited RF spectrum resources has led to significant spectral congestion, posing a major challenge to the deployment and performance of radar systems. The L-Band (1–2 GHz) and S-Band (2–4 GHz), two critical frequency ranges for radar applications, are increasingly occupied by 5G, Wi-Fi, and Industrial, Scientific, and Medical (ISM) systems [200]. This congestion adversely affects radar system reliability and performance [201]. Simultaneously, high-resolution radar systems, such as FMCW radars, require progressively wider transmitted bandwidths to achieve their performance objectives. However, expanding bandwidths contiguously has become impractical due to pervasive interference and the lack of available spectrum [202].

In this case, the expansion and performance of radar systems rely on mitigating the challenges posed by contiguous spectrum overcrowding [203, 204]. This can be achieved by partitioning the required bandwidth into narrower sub-bands, which can then be combined to maximize spectrum utilization with minimal interference. The increasing prevalence of weather radar systems, which predominantly operate in the L-Band, S-Band, and C-Band, highlights the critical need for more efficient operational strategies in these heavily congested frequency ranges [205–208].

To enhance radar performance, particularly in range resolution, existing methods have primarily focused on increasing the transmitted radar signal bandwidth contiguously [209–211]. However, this approach faces significant limitations due to spectral congestion and interference in the L-Band and S-Band. A promising technique, multi-band coherent fusion, was first introduced by [212], leveraging beat signal extrapolation between lower and higher transmitted sub-bands. While effective in some scenarios, this method can introduce artifacts in the final beat signal spectrum, leading to potentially undesirable outcomes [213]. To address these limitations, an innovative approach was demonstrated in [214], where three 2-GHz wide photonic-based FMCW radar chirps, transmitted within the 18-to-27 GHz band, were coherently recombined in the time domain. This resulted in an equivalent 8 GHz bandwidth after processing, significantly improving resolution. However, this method was restricted to equal transmitted bandwidths, as non-equal bandwidths generate beat signals with distinct frequencies, complicating the fusion process. A preliminary demonstration of non-equal and non-contiguous sub-band fusion was reported in [161]. While it showcased the feasibility of fusing non-equal sub-bands, the technique lacked comprehensive modeling and a robust phase correction algorithm, leaving room for improvement in its practical implementation.

In contrast, a robust multi-band fusion technique should enable the use of non-equal sub-bands, resulting in distinct beat frequencies. This approach allows for the utilization of all available frequency bands, including narrower ones, without being restricted to only wider bands. The super-fusion technique proposed in this paper addresses these limitations by dividing the required bandwidth into multiple simultaneous sub-bands, which can be equal or unequal, contiguous or non-contiguous, and centered at arbitrary frequencies. This technique not only enhances radar system resolution but also optimally leverages available spectrum resources. In the proposed super-fusion method, the observation durations of beat signals from each sub-band are combined through computational processing of the received multiband FMCW chirp signals. The fusion process demonstrates that increasing the number of sub-bands improves both range and velocity resolution in a linear manner. Specifically, this work focuses on the application of three distinct frequency bands to validate the approach, $B_1 = 3 \pm 0.15$ GHz, $B_2 = 2 \pm 0.10$ GHz and $B_3 = 1 \pm 0.05$ GHz.

First, in Section II, the theory of the sub-band fusion is discussed in addition to the post-processing techniques and multichannel influence. Then, the proposed multi-band architecture together with its experimental implementation is presented in Section III. Following this, in Section IV, a power budget analysis of the experiment, as well as a dynamic range discussion, in preparation of the actual measurements are conducted. Finally, the conclusion is drawn in Section V.

4.3 Combining Dispersed Bands to Synthesize a Large Equivalent Bandwidth

This section presents the multi-band fusion theory, which underpins the combination of scattered frequency bands to synthesize a large equivalent bandwidth. It also provides a detailed analysis of digital post-processing techniques used for fusion, alongside an in-depth discussion of the multichannel effects on the echoed radar chirp.

4.3.1 Multi-Band Fusion Theory

To investigate the multi-band fusion theory and retrieve both the position and speed of the monitored target, this work employs a triangular FMCW chirp. The TFMCW waveform comprises an up-chirp and a down-chirp segment, as illustrated in Fig. 4.1 and the transmitted signals $S_{TX,k}(t)$ may be depicted as follows :

$$S_{TX,k}(t) = \widetilde{S}_{TX,k} \begin{cases} \cos\left[2\pi\left(f_{i,k} + \frac{B_k}{T_C}t\right)t\right] & t < T_C \\ \\ \cos\left[2\pi\left(f_{f,k} - \frac{B_k}{T_C}t\right)t\right] & t \geq T_C \end{cases} \tag{4.1}$$

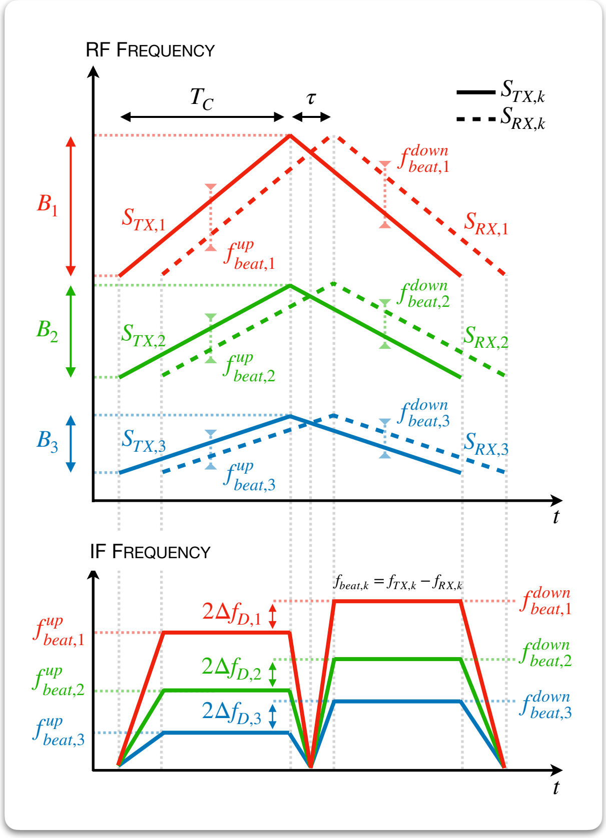

FIGURE 4.1 S_{TX} and S_{RX} signals of FMCW multi-band chirps over B_1, B_2 and B_3 and corresponding up-chirp and down-chirp beat frequencies.

The received signals $S_{RX,k}(t)$, in the assumption that they are shifted by the time delay induced by the range of the target τ, subject to a potential Doppler shift and affected by distinct path losses, can be written as :

$$S_{RX,k}(t) = \widetilde{S}_{RX,k} \begin{cases} \cos\left[2\pi\left(f_{i,k} + \frac{B_k}{T_C}t + \Delta f_D\right)(t-\tau)\right] & t < T_C \\ \cos\left[2\pi\left(f_{f,k} - \frac{B_k}{T_C}t + \Delta f_D\right)(t-\tau)\right] & t \geq T_C \end{cases} \tag{4.2}$$

where $\widetilde{S}_{TX,k}$ is the amplitude of the k^{th} transmitted signal, $\widetilde{S}_{RX,k}$ is the amplitude of the k^{th} received signal (considered constant), $f_{i,k}$ and $f_{f,k}$ are the initial and final frequencies of the k^{th} chirp, respectively. B_k is the bandwidth of the k^{th} chirp, T_C is the chirp sweeping time and Δf_D is the Doppler shift caused by the relative speed of the target.

The amplitude of the received signal depends on the transmitted power and is estimated by the following radar equation :

$$\frac{\widetilde{S}_{RX,k}}{\widetilde{S}_{TX,k}} = \frac{G_{TX} G_{RX} \lambda_k^2 \sigma}{(4\pi)^3 r^4} \tag{4.3}$$

where G_{TX} and G_{RX} are the gain of the transmitting and receiving antennas, respectively, λ_k is the wavelength of the transmitted k^{th} signal, r is the range of the target and σ is the Radar Cross Section (RCS) of the target.

After mixing the transmitted k^{th} chirp with the received k^{th} chirp, a beat frequency, depending on the range r of the target, its relative speed v and the radar parameters (B_k and T_C), can be obtained, for both the up-chirp and the down-chirp :

$$f_{beat,k}^{up} = \frac{B_k}{T_C}\left(\frac{2r}{c_{\epsilon,\mu}}\right) + \frac{2v}{c_{\epsilon,\mu}}\left(\frac{f_{f,k} + f_{i,k}}{2}\right) \tag{4.4}$$

$$f_{beat,k}^{down} = \frac{B_k}{T_C}\left(\frac{2r}{c_{\epsilon,\mu}}\right) - \frac{2v}{c_{\epsilon,\mu}}\left(\frac{f_{f,k} + f_{i,k}}{2}\right) \tag{4.5}$$

where $c_{\epsilon,\mu}$ is the speed of light depending on the permittivity ϵ and the permeability μ of the medium. By performing a Fast Fourier Transform (FFT) on both $f_{beat,k}^{up}$ and $f_{beat,k}^{down}$, one can retrieve the range of the target and its relative speed [215]. Since all bandwidths B_k can be different, with identical T_C (different chirp rates), a unique target causing a time delay $\tau = 2r/c_{\epsilon,\mu}$, results in different beat frequencies (across multiple B_k).

The FMCW radar resolution δr_k is fundamentally dictated by the Fourier transform's capability to resolve two closely spaced frequency components within the analyzed beat signal. This capability is directly influenced by the number of cycles of the sampled beat signal observed over the duration T_C. Consequently, the resolution exhibits an inversely proportional relationship :

$$\delta r_k \propto \frac{1}{N_{P,k}} \tag{4.6}$$

where $N_{P,k}$ is the number of observed periods of the k^{th} beat signal during the chirp time T_C. In other words, expanding the transmitted bandwidth B_k, while maintaining T_C constant, i.e. increasing the chirp rate, results in a thinner resolution of both the position and the speed of the target as more periods of the beat signal will be observed during T_C, such as :

$$\delta r_k = \frac{c_{\varepsilon,\mu}}{2B_k} \tag{4.7}$$

To effectively extend $N_{P,k}$, the present method proposes to combine the observation times $T_{obs,k}$ of each band's beat frequency, which corresponds to an addition of each band's $N_{P,k}$. By establishing a reference beat signal $f_{beat,ref}$, the subsequent bands can contribute to enhancing the resolution of this reference signal. Essentially, the subsequent bands replicate the reference signal's frequency, resulting in a fused IF signal that extends the reference signal in the time domain. Figuratively, the fused beat signal is equivalent to a beat signal of a chirp with an increased chirp rate over the same duration T_C, covering all B_k. The procedure is depicted in Fig. 4.2.

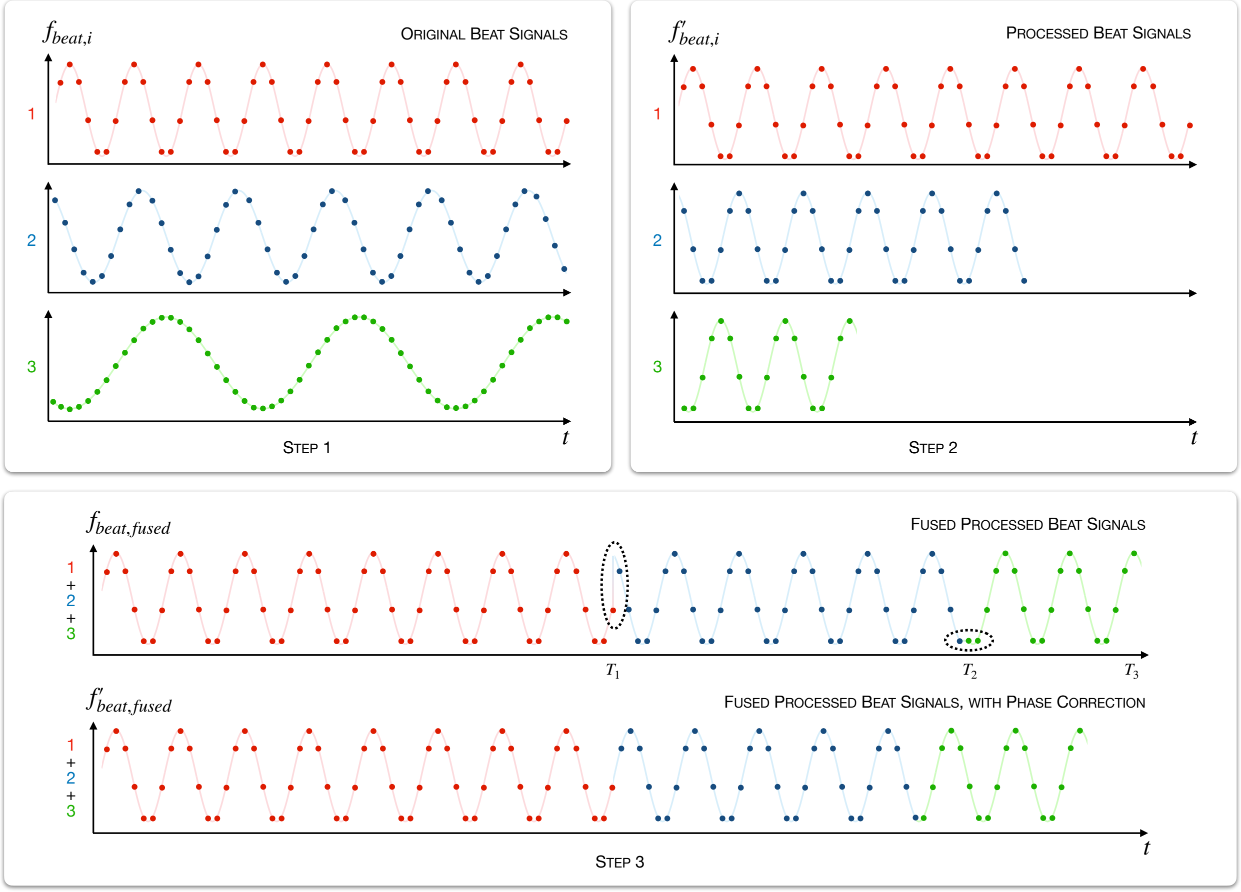

FIGURE 4.2 Super fusion procedure, from original sampled beat signals to processed IF signals to the final fused beat signal over B_1, B_2 and B_3, with and without phase correction. Potential discontinuities in the fused beat signal are circled.

The reference beat frequency and bandwidth are set to the widest bandwidth, B_1 in this work :

$$\begin{cases} f_{beat,ref} = f_{beat,1} \\ B_{ref} = B_1 \end{cases} \tag{4.8}$$

As a result, and keeping other parameters unchanged, each subsequent beat frequency can be expressed as a fraction of the reference beat frequency and bandwidth :

$$f_{beat,k} = f_{beat,ref} \frac{B_k}{B_{ref}} \tag{4.9}$$

It is understood from (4.9) that each bandwidth B_k will affect their corresponding beat frequency $f_{beat,k}$ in a linear manner, which allows the subsequent operation. Following this, by concatenating the beat signals in the time domain, one can extend the overall observation time T_{obs} :

$$T_{obs} = \sum_{k=1}^{N} T_{obs,k} = T_C \sum_{k=1}^{N} \frac{B_k}{B_{ref}} \tag{4.10}$$

Therefore, considering the resolution of the reference band $\delta_{r,ref} = c_{\epsilon,\mu}/2B_{ref}$, and the proportional relation between the resolution and the number of observed periods, the resolution of the fused signal can be rewritten as :

$$\delta r_{fusion} = \delta r_{ref} \times \frac{T_C}{T_{obs}} \tag{4.11}$$

By combining (4.7), (4.10), and (4.11), the resolution of the fused signal becomes :

$$\delta r_{fusion} = \frac{c_{\varepsilon,\mu}}{2B_{ref}} \times \frac{1}{\sum_{k=1}^{N} \frac{B_k}{B_{ref}}} \tag{4.12}$$

which can be simplified by the linear summation of all bands :

$$\delta r_{fusion} = \frac{c_{\varepsilon,\mu}}{2\sum_{k=1}^{N} B_k} \tag{4.13}$$

In the proposed triple-band radar, the resolution yields :

$$\delta r_{fusion} = \frac{c_{\varepsilon,\mu}}{2(B_1 + B_2 + B_3)} \tag{4.14}$$

The proposed method remains effective even when a Doppler shift is introduced to each transmitted chirp. In this case, the received frequencies are shifted by varying amounts, with each band being affected differently. By processing the narrower bands to align with the wider reference band, the method ensures that the actual Doppler shift is accurately captured in the fused beat signal, corresponding to the reference Doppler shift.

Note that repetitively concatenating the beat signal of a single sub-band with itself does not improve δr, as no additional spectral content is introduced. Range resolution is fundamentally limited by the total occupied bandwidth and the effective time-bandwidth product :

$$\sum_{k=1}^{N} T_{obs,k} B_k \tag{4.15}$$

If several B_k describe the same frequency sweep, the sum does not grow in spectral information. Thus, only the fusion of distinct, non-overlapping sub-bands extends the effective spectral support and provides additional information.

Based on the two beat frequencies obtained after the fusion, namely $f^{up}_{beat,fused}$ and $f^{down}_{beat,fused}$, the range r and the speed v of the target can be computed with :

$$r = \frac{c_{\epsilon,\mu} T_C}{4 B_{ref}} \left(f^{up}_{beat,fused} + f^{down}_{beat,fused} \right) \tag{4.16}$$

$$v = \frac{c_{\epsilon,\mu}}{2(f_{f,ref} + f_{i,ref})} \left| f^{up}_{beat,fused} - f^{down}_{beat,fused} \right| \tag{4.17}$$

Also, the limitation of the IF bandwidth ($f_{beat,max}$) restricts the maximum measurable range and velocity :

$$r_{max} = \frac{c_{\epsilon,\mu} T_C f_{beat,max}}{2 B_{ref}} \qquad v_{max} = \frac{c_{\epsilon,\mu} f_{beat,max}}{f_{f,ref} + f_{i,ref}} \tag{4.18}$$

4.3.2 Digital Baseband Procedure

As shown in Fig. 4.2, the received beat signals undergo a digital baseband processing procedure [161]. First, the beat signals are sampled—after initial low-pass filtering— while ensuring they contain an ample number of samples N_S. Specifically, the sampling frequency f_S must exceed twice the ratio of the widest bandwidth (B_1) to the narrowest (B_3), multiplied by the maximum beat frequency, to comply with the Nyquist criterion :

$$f_S \geq 2\frac{B_1}{B_3}f_{beat,max} \tag{4.19}$$

This condition is equivalent to $N_S \geq f_S \times T_C$ and it needs to be satisfied due to the resampling procedure further applied. Second, the widest bandwidth, $B_{ref} = B_1$, is used as the reference, which implies that the objective of the processing is to mimic the frequency $f_{beat,1}$. Then, $(B_2/B_{ref}) \times N_S$ equally spaced samples are removed from $f_{beat,2}$ and $(B_3/B_{ref}) \times N_S$ equally spaced samples are removed from $f_{beat,3}$. Finally, the processed signals $f'_{beat,2}$ and $f'_{beat,3}$ are concatenated with $f_{beat,1}$, and a FFT can be performed on the fused beat signal, over the total time durations T_{obs}. (4.16) and (4.17) can thus be used to retrieve both range and velocity information. The procedure can be summarized as follows :

- Sampling of each beat signal.
- Removing $(B_2/B_{ref}) \times N_S$ samples of $f_{beat,2}$ and $(B_3/B_{ref}) \times N_S$ samples of $f_{beat,3}$.
- Concatenation of original $f_{beat,1}$ with processed $f'_{beat,2}$ and $f'_{beat,3}$.
- Computation of FFT on the fused beat signal.
- Computation of both range and velocity information with (4.16) and (4.17).

This procedure remains perfectly valid when several targets are captured within the measurement time frame. In such a case, multiple frequencies—arising from distinct target ranges—will be scaled up linearly and each frequency will be visible in the final fused beat signal.

Additionally, considering the low number of periods in the processed beat signals, potential phase mismatches and discontinuities between the concatenated beat signals may have a non-negligible outcome in the numerical FFT. Therefore, a proper phase match must be included in the digital baseband analysis.

To ensure that an integer number of samples is removed during the above procedure, N_S should be chosen accordingly. Indeed, in the example of this work, $(B_2/B_{ref}) \times N_S$ and $(B_3/B_{ref}) \times N_S$ should be integers. This implies, with respect to (4.19), $N_S = 60$, 90, 120, etc with $f_{beat,max} = 10$ MHz and $T_C = 1$ us. For computational efficiency, $N_S = 60$ is selected in this work.

The proposed digital baseband procedure relies exclusively on bandwidth considerations for the processing of the beat signals. As a result, Doppler processing is only applicable in specific scenarios where :

$$\frac{B_{ref}}{B_k} = \frac{f_{c,ref}}{f_k} \tag{4.20}$$

where $f_{c,ref}$ and f_k are the center carrier frequencies of the reference and subsequent band, respectively. In this case, as the Doppler effect increases linearly as the carrier frequency increases, after processing, the Doppler shift will be correctly transposed to the fused beat signal. Indeed, it is seen from (4.4) and (4.5) that increasing both the bandwidth and the carrier frequency of the chirp yields a proportional increase on the beat frequency, for either single- or multi-target scenarios. If Doppler measurements are not of interest, then any bandwidth and carrier frequencies may be used—otherwise (4.20) must be respected. Thus in this work, the selected bands are $B_1 = 3 \pm 0.15$ GHz, $B_2 = 2 \pm 0.10$ GHz and $B_3 = 1 \pm 0.05$ GHz.

4.3.3 Phase Matching Procedure

In order to actually perform a proper fusion, a coherent concatenation of the preprocessed beat signals is required. It is important to emphasize that phase matching is unnecessary within the RF front-end (described in Section III). In fact, as shown in the following section, coherent fusion—i.e., phase matching and signal continuity—is only necessary in the digital domain during the beat frequency stitching process.

In the ideal case, the Fourier transform of the fused signal should be identical to the Fourier transform of a wideband signal that extends $B_{wide} = B_1 + B_2 + B_3$.

Single-target scenario

The fused beat signal of Fig. 4.2 is composed of three signals $S_1(t)$, $S_2(t)$ and $S_3(t)$, which differ by their individual amplitudes $\widetilde{S}_{1,2,3}$ and their relative phases $\phi_{1,2,3}$. As a first approximation, the delay caused by the target is considered negligible compared to the overall sweep time T_C. Indeed, for a target located 10 m ahead, the occurred delay is about 60 ns or 6 % of $T_C = 1$ us. Hence, the beat frequency is considered constant during $T_{interval}$. These beat signals are also time-constrained by the rectangle function $\Pi(.)$, such as :

$$S_i(t) = \widetilde{S}_i \cos(2\pi f_a t + \phi_i) \times \Pi\left(\frac{t}{T_{interval,i}}\right) \tag{4.21}$$

where f_a is the beat frequency produced by a single target, which depends on the target's distance (4.4). Note that $T_{interval,1} = T_1$, $T_{interval,2} = T_2 - T_1$ and $T_{interval,3} = T_3 - T_2$ are the concatenated observation times from the initial processing and that $T_{obs} = T_{interval,3} + T_{interval,2} + T_{interval,1} = T_3$. Those time intervals are illustrated in Fig. 4.2. The fused or concatenated signal, S_{fused}, can then be written as a piece-wise function :

$$S_{fused}(t) = \begin{cases} S_1(t) & 0 \leq t \leq T_1 \\ S_2(t) & T_1 < t \leq T_2 \\ S_3(t) & T_2 < t \leq T_3 \end{cases} \tag{4.22}$$

In comparison, the wideband signal $S_{wide}(t)$, lasting from $t = 0$ to $t = T_3$, may be written as :

$$S_{wide}(t) = \widetilde{S}_{wide} \cos(2\pi f_a t + \phi_{wide}) \times \Pi\left(\frac{t}{T_3}\right) \tag{4.23}$$

One can then perform a Fourier transform $\mathcal{F}(.)$ on $S_{fused}(t)$:

$$\mathcal{F}(S_{fused}) = \sum_{i=1}^{3} \int_{T_{i-1}}^{T_i} \widetilde{S}_i \cos(2\pi f_a t + \phi_i) e^{-j2\pi f t} dt \tag{4.24}$$

By applying Euler's relation, (4.24) becomes :

$$\mathcal{F}(S_{fused}) = \sum_{i=1}^{3} \int_{T_{i-1}}^{T_i} \widetilde{S}_i \frac{e^{j(2\pi f_a t + \phi_i)} + e^{-j(2\pi f_a t + \phi_i)}}{2} e^{-j2\pi f t} dt \tag{4.25}$$

After some treatments :

$$\begin{aligned}\mathcal{F}(S_{fused}) = &\underbrace{\sum_{i=1}^{3} \left[\frac{\widetilde{S}_i}{2} e^{j\phi_i} \frac{e^{-j2\pi(f-f_a)T_i} + e^{-j2\pi(f-f_a)T_{i-1}}}{-j2\pi(f-f_a)} \right]}_{\mathcal{F}(S_{fused})^+} \\ &+ \underbrace{\sum_{i=1}^{3} \left[\frac{\widetilde{S}_i}{2} e^{-j\phi_i} \frac{e^{-j2\pi(f+f_a)T_i} + e^{-j2\pi(f+f_a)T_{i-1}}}{j2\pi(f+f_a)} \right]}_{\mathcal{F}(S_{fused})^-}\end{aligned} \tag{4.26}$$

Also, one can compute the Fourier transform of $S_{wide}(t)$:

$$\mathcal{F}(S_{wide}) = \underbrace{\frac{\widetilde{S}_{wide}}{2} e^{j\phi_{wide}} \left[\frac{1 - e^{-j2\pi(f-f_a)T_3}}{-j2\pi(f-f_a)} \right]}_{\mathcal{F}(S_{wide})^+} + \underbrace{\frac{\widetilde{S}_{wide}}{2} e^{-j\phi_{wide}} \left[\frac{1 - e^{-j2\pi(f+f_a)T_3}}{-j2\pi(f+f_a)} \right]}_{\mathcal{F}(S_{wide})^-} \tag{4.27}$$

Therefore, to obtain $\mathcal{F}(S_{fused}) = \mathcal{F}(S_{wide})$, the following conditions must be verified simultaneously :

$$\mathcal{F}(S_{fused})^+ = \mathcal{F}(S_{wide})^+ \tag{4.28}$$

$$\mathcal{F}(S_{fused})^- = \mathcal{F}(S_{wide})^- \tag{4.29}$$

where $\mathcal{F}(S_.)^+$ and $\mathcal{F}(S_.)^-$ are the positive and negative peaks, respectively, in the spectrum. These conditions are verified under the following circumstances :

- Amplitude consistency : $\widetilde{S}_1 + \widetilde{S}_2 + \widetilde{S}_3 = \widetilde{S}_{wide}$.
- Phase continuity : $\phi_1 = \phi_2 = \phi_3 = \phi_{wide}$.
- Signal continuity : $S_1(T_1) = S_2(T_1)$ and $S_2(T_2) = S_3(T_2)$.

Algorithm 1 Signal Stitching with Sample Removal

```
Require: Two signals : $\mathbf{S_1}$ (first signal), $\mathbf{S_2}$ (second signal)
Require: Gap limit value : $G_{limit}$
$N_1 \leftarrow$ length($\mathbf{S_1}$)
$N_2 \leftarrow$ length($\mathbf{S_2}$)
Compute gap : $G = |S_1[N_1] - S_2[1]|$
Compute sign differences :
  $d_1 = \text{sign}(S_1[N_1] - S_1[N_1 - 1])$
  $d_2 = \text{sign}(S_2[2] - S_2[1])$
while $G > G_{limit}$ and $d_1 \neq d_2$ do
    Remove first sample from $\mathbf{S_2}$
    Recompute $G$ and sign differences $d_1, d_2$
end while
Stitch $\mathbf{S_1}$ and remaining $\mathbf{S_2}$
```

Multi-target scenario

When M targets are considered, the individual beat signals will contain several distinct frequencies. Thus, the individual beat signals can be rewritten as :

$$S_i(t) = \left(\sum_{k=1}^{M} \widetilde{S}_{i,k} \cos(2\pi f_{a,k} t + \phi_{i,k}) \right) \times \Pi \left(\frac{t}{T_{interval,i}} \right) \tag{4.30}$$

where $S_{i,k}$, $f_{a,k}$ and $\phi_{i,k}$ are the amplitude, frequency and phase of individual components (targets) contained in each retrieved sub-band, respectively. Also, the wideband signal $S_{wide}(t)$, can be expressed as :

$$S_{wide}(t) = \left(\sum_{k=1}^{M} \widetilde{S}_{wide,k} \cos(2\pi f_{a,k} t + \phi_{wide,k}) \right) \times \Pi \left(\frac{t}{T_3} \right) \tag{4.31}$$

After similar treatments, to effectively obtain the same conclusion as (4.28) and (4.29), the following conditions need to be verified simultaneously for each frequency $f_{a,k}$:

- Amplitude consistency : $\widetilde{S}_{1,k} + \widetilde{S}_{2,k} + \widetilde{S}_{3,k} = \widetilde{S}_{wide,k}$.
- Phase continuity : $\phi_{1,k} = \phi_{2,k} = \phi_{3,k} = \phi_{wide,k}$.
- Signal continuity : $S_1(T_1) = S_2(T_1)$ and $S_2(T_2) = S_3(T_2)$.

Stitching algorithm

While phase continuity and signal continuity are critical, the amplitude consistency condition requires less treatment as even though it will affect the Fourier transform overall spectrum power, it has no influence on the half-power lobe width—hence not affecting the range resolution $\delta_{r,fusion}$.

Discontinuities in the signal, such as those induced by abrupt transitions between concatenated beat signals in the fused signal, can lead to significant spectral artifacts, especially when the number of periods N_P in the signal is low during the measurement time T_C. These discontinuities cause high-frequency components to appear in the Fourier transform, resulting in spectral leakage and a decrease in the range resolution—thus a wider lobe at the expected beat frequency. However, when the number of periods is very large during the measurement time, the impact of these mismatches diminishes because the signal behaves more like a continuous sinusoid, and the energy is distributed more evenly across the frequency spectrum, reducing the effect of the discontinuities in the overall FFT.

To coherently stitch the beat signals, in the digital processing, a loop removing the last sample of the following beat signal to be stitched is conducted while the gap between the last sample of the previous signal and the following sample of the second signal exceeds the gap limit value G_{limit} (signal continuity) and that the sign of the difference between the last two samples of the previous signal and the first two samples of the following signal are unalike (phase continuity). Based on empirical evaluation, the maximum permissible gap limit is approximately 20% to 30% of the signal amplitude ($G_{limit} = 0.05$ V in this work's experimental verification). This matching process is depicted in Algorithm 1.

As a result of the proposed stitching algorithm, while removing samples, the individual phases $\phi_{i,k}$ are not preserved in the fused signal. Thus, if phase information is required, it must be extracted from the original signals prior to the fusion process. Therefore, the proposed method is applicable primarily in scenarios where only the beat frequencies associated with a single target or multiple targets are of interest.

4.3.4 Multichannel Influence

The multiband nature of the proposed radar results in each band being differently influenced by the target's environment [216]. Specific scenarios are favored depending on the operating band : the L band (1–2 GHz) offers long-range capability with minimal weather effects, the S band (2–4 GHz) provides moderate range with moderate weather impact, and the C band (4–8 GHz) is suited for weather observation but experiences increased sensitivity to rain effects, among others. Equation (4.32) estimates the transmission/reception power ratio as a function of the transmitted signal's wavelength, the target's RCS, and its range, and can be expressed as :

$$P_{dBm}^{RX} = P_{dBm}^{TX} + G_{dB}^{TX} + G_{dB}^{RX} + 10\log_{10}\left(\frac{\lambda^2\sigma}{(4\pi)^3 r^4}\right) \tag{4.32}$$

Hence, with P_{dBm}^{TX}= 20 dBm, $G_{dB}^{TX} = G_{dB}^{RX} = 2$ dB, $\sigma = 1$ m^2 and $r = 5$ m, the received power in the 1, 2, and 3-GHz band is -47 dBm, -53 dBm, and -56 dBm, respectively. Fig. 4.3 shows the received power for certain target ranges and frequencies with the previously defined parameters.

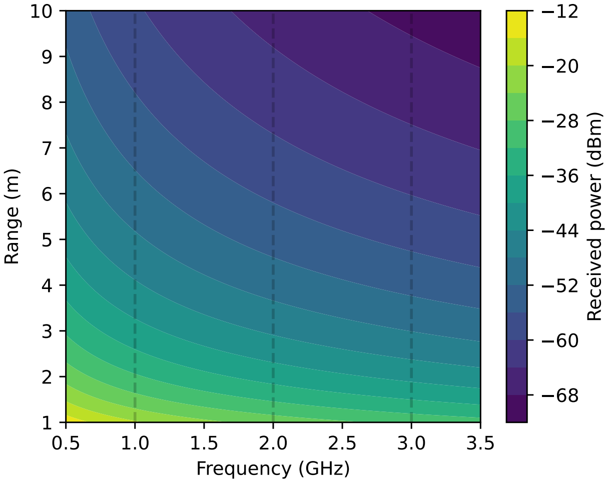

FIGURE 4.3 Received power at RX against variation of frequency and target's range with $P_{dBm}^{TX} = 20$ dBm, $G_{dB}^{TX} = G_{dB}^{RX} = 2$ dB and $\sigma = 1$ m2.

Although a constant-aperture antenna's gain rises with frequency, the received power is not entirely flattened across bands by this effect. A number of variables, such as frequency-dependent antenna efficiency, impedance matching, and propagation losses, affect the demonstrated variation in received power. The wavelength-dependent term in (4.32) may be partially offset by the gain increase, but its effects are not completely eliminated, and there are still noticeable differences in received power across frequency bands.

4.4 Radar Architecture Design

This section presents the proposed multi-band radar architecture to combine the multi-band radar chirp, and it details the practical implementation of every conceived block of the RF front-end. The presented architecture is employed to validate the fusion concept and may differ from the final practical architecture.

4.4.1 Architecture Overview

To verify the proposed multi-band fusion theory, a primary triple-band radar architecture is proposed for demonstration and validation, and its architecture is described in Fig. 4.4.

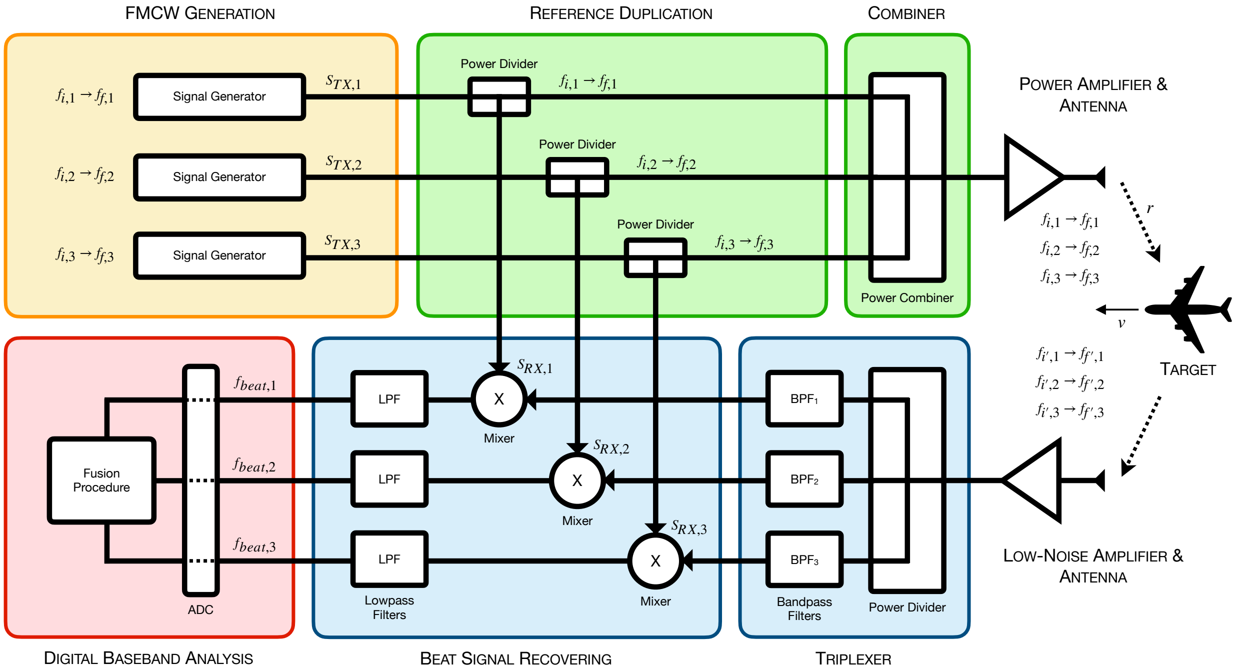

FIGURE 4.4 Block diagram of the triple-band FMCW radar system with three input chirps sweeping from $f_{i,1}$ to $f_{f,1}$, $f_{i,2}$ to $f_{f,2}$ and $f_{i,3}$ to $f_{f,3}$ from a signal generator.

First, to generate the FMCW chirps, three signal generators are set to introduce three signals, $S_{TX,1}$, $S_{TX,2}$ and $S_{TX,3}$, across B_1 from $f_{i,1}$ to $f_{f,1}$, B_2 from $f_{i,2}$ to $f_{f,2}$ and B_3 from $f_{i,3}$ to $f_{f,3}$, respectively. Each of the TX signals are them duplicated as references for the mixing process at the receiving stage, using couplers. Subsequently, the three signals are combined using a three-way combiner and the resulting signal $S_{TX} = S_{TX,1} + S_{TX,2} + S_{TX,3}$ is connected to a wideband power amplifier driving a wideband transmitting antenna. Over the air, S_{TX}

is delayed due to the distance of the target and the velocity of the target induces a Doppler shift. The echo signal is captured by the receiving wideband antenna and amplified with a low-noise wideband amplifier. As a mean to retrieve the individual signals $S_{RX,1}$, $S_{RX,2}$ and $S_{RX,3}$, a triplexer is employed and is composed of a three-way divider and a set of lumped-elements band-pass filters tuned to the corresponding bandwidths of $S_{RX,1}$, $S_{RX,2}$ and $S_{RX,3}$. Those signals are then mixed with the transmitted reference signals $S_{TX,1}$, $S_{TX,2}$ and $S_{TX,3}$ and low-pass filters are used to keep the beat signals containing information about position and velocity. Ultimately, the retrieved beat signals are processed in the digital domain using Python.

4.4.2 Experimental Implementation

The first element of the transmission chain consists of the reference duplication which aims to drive the FMCW signal to the mixer in the receiving part. For that purpose, a basic power divider, illustrated in Fig. 4.5a, is employed.

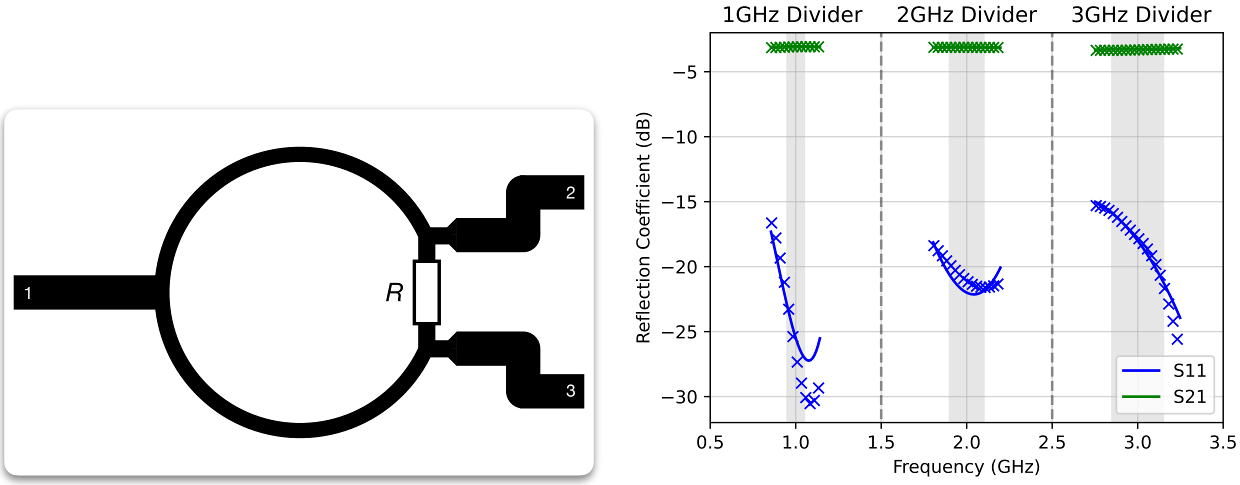

(a) (b)

FIGURE 4.5 (a) Schematic of the quarter-wavelength power dividers and (b) comparison between measurement results and simulations of the S-parameters for the 1-GHz power divider, 2-GHz power divider and 3-GHz power divider (from left to right). Solid lines are simulation and dashed scatters are measurements.

This topology leverages a resistive divider concept with a 100-Ω resistor in between two 50-Ω loads. Also, the lengths of the transmission lines are set to the quarter wavelength of the required center frequency. Three power dividers are then fabricated based on this design, with center frequencies of 1, 2, and 3 GHz. The measurement results ('X' scatters) of the S-parameters, S11 and S21, are presented in Fig. 4.5b, in comparison to the simulation (solid lines). The transmission coefficients S21s are measured to be around −3.1 and −3.3 dB, which are consistent with the theoretical values of -3dB. Note that the reverse transmission coefficients are identical to the transmission ones. Additionally, the measured insertion losses S11s are below 15 dB, assuring a low standing wave ratio.

Then, a three-way Wilkinson PD/PC, originally from [217], is adapted and fabricated to combine the three FMCW signals. This design makes use of three-quarter wavelength transmission lines with a characteristic impedance of 86 Ω, and a resistive power division topology with two 120-Ω resistors. Such design ensures an excellent isolation between the outputs. Fig. 4.6a shows the design of the three-way power divider/combiner and Fig. 4.6b is set to compare the measured S-parameters with the simulated values.

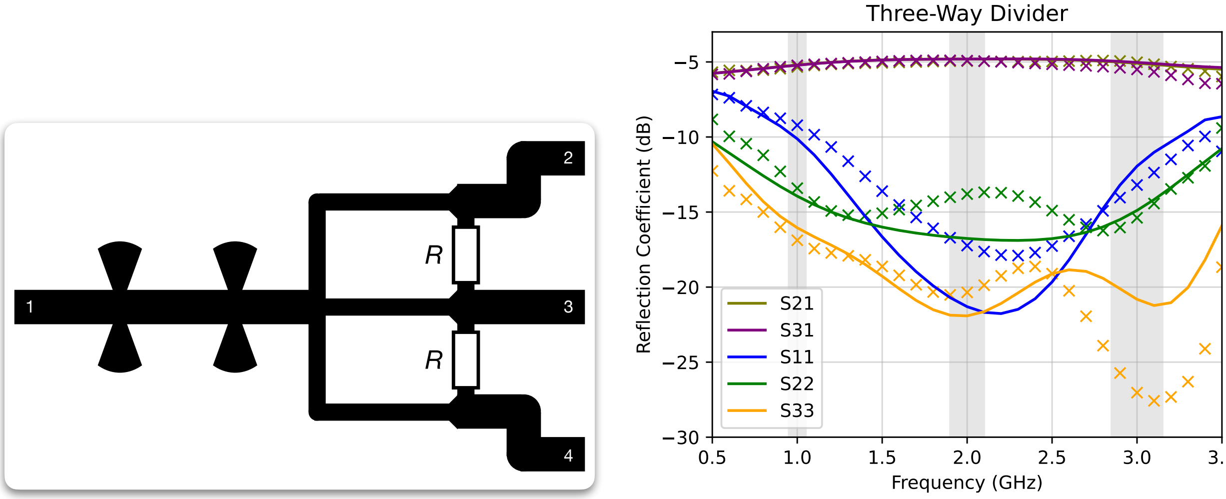

(a) (b)

FIGURE 4.6 (a) Schematic of the quarter-wavelength three-way combiner/divider and (b) comparison between measurement results and simulations of the S-parameters. Solid lines are simulation and dashed scatters are measurements.

Across the 1-, 2-, and 3-GHz bands, the insertion losses of all inputs and outputs (S11, S22, S33, S44) are considered decent. Indeed, they are measured to be between −10 and −20 dB. Notably, all transmission coefficients (S12, S21, S13, S31, S14, S41) are quasi-identical, at around −5 dB. Note that the highest achievable transmission ratio with such topology is −4.7 dB.

After combining the FMCW signals, a wideband ZHL-42 power amplifier with 30 dB gain from Mini-Circuits is used to drive the wideband antenna. To effectively radiate the three-band radar signal, a wideband or multi-band antenna topology is employed. For this purpose, and to achieve both efficiency and cost reduction, a wideband antenna from [218] is selected. This design builds upon a classic monopole/dipole structure, incorporating two asymmetrically stacked radiating elements, as shown in Fig. 4.7a. This configuration enables circularly polarized radiation, which is highly beneficial in radar systems due to its uniform radiation in both the E and H planes. The measured radiation patterns at 1, 2, and 3 GHz are shown in Fig. 4.7b.

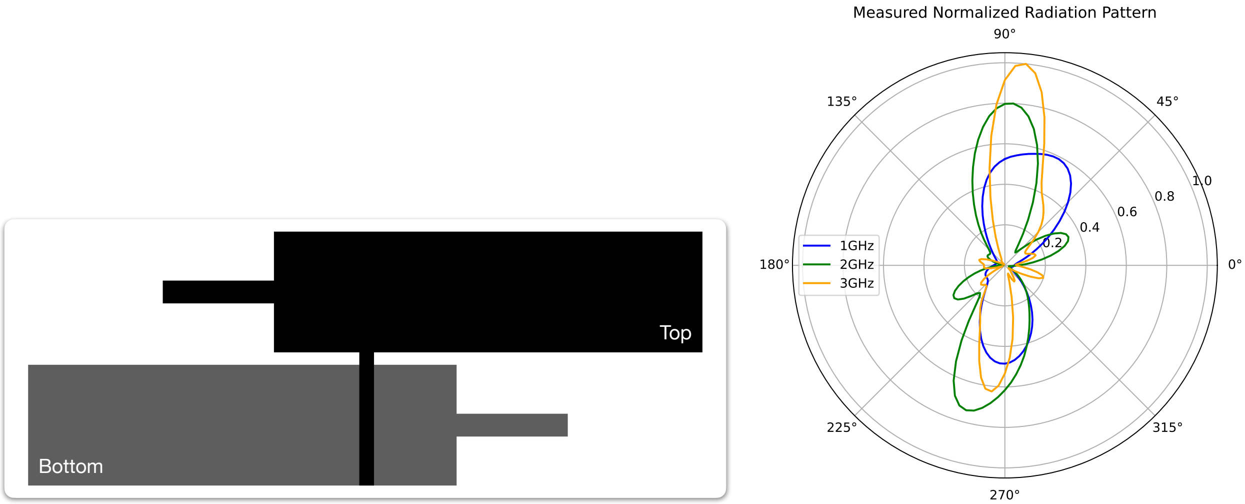

(a) (b)

FIGURE 4.7 (a) Schematic of the double-sided dipole antenna and (b) measured normalized radiation pattern in anechoic chamber.

These patterns are normalized to the maximum gain of 5 dB, measured in the 3-GHz band. The measured gains at the 1, 2, and 3 GHz center frequencies are 2.8 dB, 4.1 dB, and 5 dB, respectively. From the radiation patterns, it is evident that the radiation at 3 GHz is much narrower compared to the other bands, which is a predictable outcome based on this antenna geometry. Additionally, it is noteworthy that this antenna performs well across the operating bands (0.95–1.05 GHz, 1.90–2.10 GHz, 2.85–3.15 GHz), as well as in the intermediate frequencies between these bands. This characteristic must be considered in the receiving chain design.

After traveling back and forth between the radar and the target, the delayed signal is received using the same antenna as in the transmission chain. The low-power echoed signal is initially amplified by an off-the-shelf LNA with 40 dB gain, and is subsequently divided using a three-way Wilkinson PD. To perform the triplexing function—separating the 1-, 2-, and 3-GHz bands—three microstrip bandpass filters are implemented using a coupled-line structure. Each filter is designed to accommodate bandwidths of 100 MHz, 200 MHz, and 300 MHz, centered at 1 GHz, 2 GHz, and 3 GHz, respectively. These filters achieve a rejection of at least 25 dB for the other bands, which is deemed sufficient for this work.

Ultimately, ZX05-C42MH mixers from Mini-Circuits are set to retrieve the beat signals. These mixers were selected due to their high LO-to-RF isolation and double-balanced topology. Three 150-MHz low-pass filters from Mini-Circuits are connected to the output of the mixers to retain the $LO - RF$ subtracted signal and reject the $LO + RF$ summed signal.

4.5 Experimental Verification

This section presents the experimental verification of the proposed radar and discusses the power budget link and dynamic range requirements.

4.5.1 Power Budget Link

To better estimate the power levels involved in the radar's experimental validation, a link budget is outlined in Fig. 4.8, incorporating the average contribution of each component across the 1-, 2-, and 3-GHz bands.

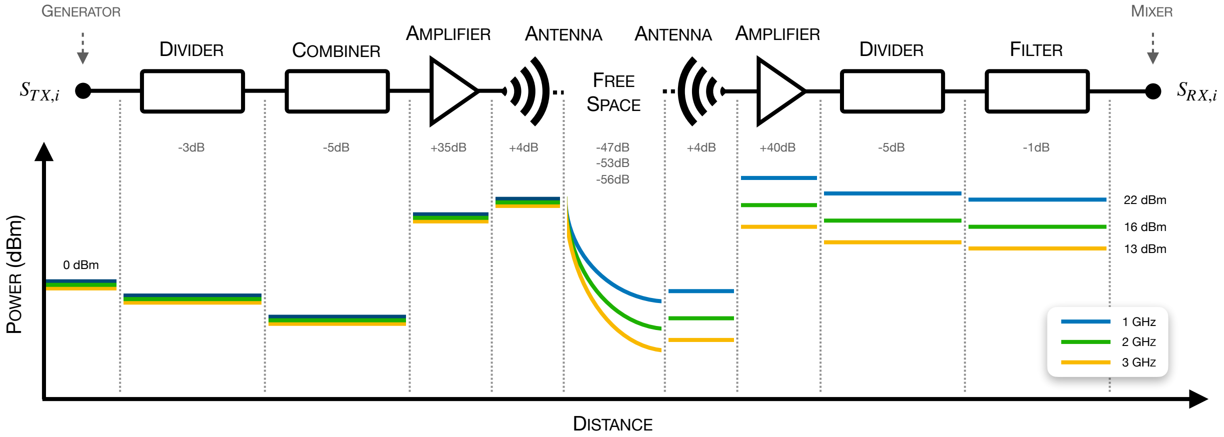

Figure 4.8 Power budget link for one branch of the multi-band architecture, from the generator output to the receiving mixer input.

The power divider and combiner introduce signal losses of 3 dB and 5 dB, respectively. On the other hand, the power amplifier and the transmitting (Tx) antenna positively contribute, adding 39 dB to the signal strength. The free-space path losses are then calculated for each frequency using (4.32), assuming a round-trip distance of 5 meters to the target (with $\sigma = 1$ m^2). On the receiving (Rx) side, the antenna and LNA collectively provide a gain of 44 dB, while the divider and filter contribute to a combined loss of 6 dB.

As a result, a transmitted signal of 0 dBm is expected to yield received signals of approximately 22 dBm, 16 dBm, and 13 dBm for the 1-, 2-, and 3-GHz bands, respectively. It should be noted that these signal levels are averaged and serve as indicative values to provide a general understanding of the power levels across the radar transmission chain.

4.5.2 Dynamic Range Requirements

Using (4.32) and the link budget from Fig. 4.8, the incoming power levels in the Rx chain can be predicted, enabling the determination of the maximum and minimum target ranges. This prediction is based solely on the received power, compared to the thermal noise power, which is expressed as :

$$P_{dBm}^{noise} = 10\log_{10}\left(\frac{k_b B_{total} T}{1 \times 10^{-3}}\right) \tag{4.33}$$

where k_b is the Boltzmann's constant, B_{total} is the total transmitted bandwidth, and T is the temperature during measurements. From −40°C to +40°C, P_{noise} varies from −87 dBm to −85 dBm. The maximum range is then computed as :

$$r_{max} = \left(\frac{\lambda^2 \sigma}{(4\pi)^3 \cdot 10^{\Delta P/10}}\right)^{1/4} \tag{4.34}$$

where $\Delta P = P_{dBm}^{noise} - P_{dBm}^{TX} - G_{dB}^{TX} - G_{dB}^{RX}$. As a result, the multi-band radar system receives a total bandwidth of $B_1 + B_2 + B_3$ at the receiver, resulting in a higher aggregate noise level compared to three independent radar systems, each operating within a single bandwidth B_1, B_2, or B_3. In the present work, the frequency most affected by free space losses is 3 GHz. Hence, with $G_{dB}^{TX} = G_{dB}^{RX} = 5$ dB, $P_{dBm}^{TX} = 31$ dBm, $\sigma = 1$ m2 and bandwidths of B_1, B_2, B_3, $B_1 + B_2 + B_3$, the maximum measurable target distances r_{max} are 86 m, 95 m, 113 m and 72 m, respectively.

In practice, the minimum measurable signal power will be limited by the sensitivity of the receiver, which strongly depends on the noise level of the LNA. Similarly, the minimum measurable target range will be defined by the 1-dB compression point of the LNA.

4.5.3 Measurements Results

The M8196A and M8190A Arbitrary Waveform Generators (AWGs) from Keysight are configured to output three frequency-modulated signals, each at a constant power level of 0 dBm. The parameters of the AWG used in this experiment are summarized in TABLE 4.1.

Tableau 4.1 Parameters of experimental verification.

Parameter		Value
Band 3	Bandwidth	100 MHz : 0.95 → 1.05 GHz
	Resolution	1.5 m (Theoretical)
Band 2	Bandwidth	200 MHz : 1.90 → 2.10 GHz
	Resolution	0.75 m (Theoretical)
Band 1	Bandwidth	300 MHz : 2.85 → 3.15 GHz
	Resolution	0.5 m (Theoretical)
Signal type		Linear ramp
Sweep time T_C		1 us
Signal power at generator		0 dBm

Each AWG output is connected to the reference duplication block in the radar architecture. Subsequently, the Tx and Rx antennas are positioned side by side inside the anechoic chamber. The two targets are statically spaced at range D from the antennas with spacings d, note that $D \gg d$. The three beat signals are then being captured by the DSO81204B Oscilloscope from Agilent at an acquisition rate of 10 M samples per second. The sampled original beat signals are finally transferred into the computer performing the post-processing analysis in Python. Fig. 4.9a and 4.9b present the block diagram of the experimental setup and actual connections of the multi-band radar system in our anechoic chamber at the Poly-Grames Research Center. Fig. 4.10a and 4.10b show the placement of both targets and antennas in the anechoic chamber. The use of large targets in the proof-of-concept setup ensured a strong and reliable return signal, simplifying the validation of the proposed method while minimizing uncertainties related to reflector alignment and radar cross-section variations.

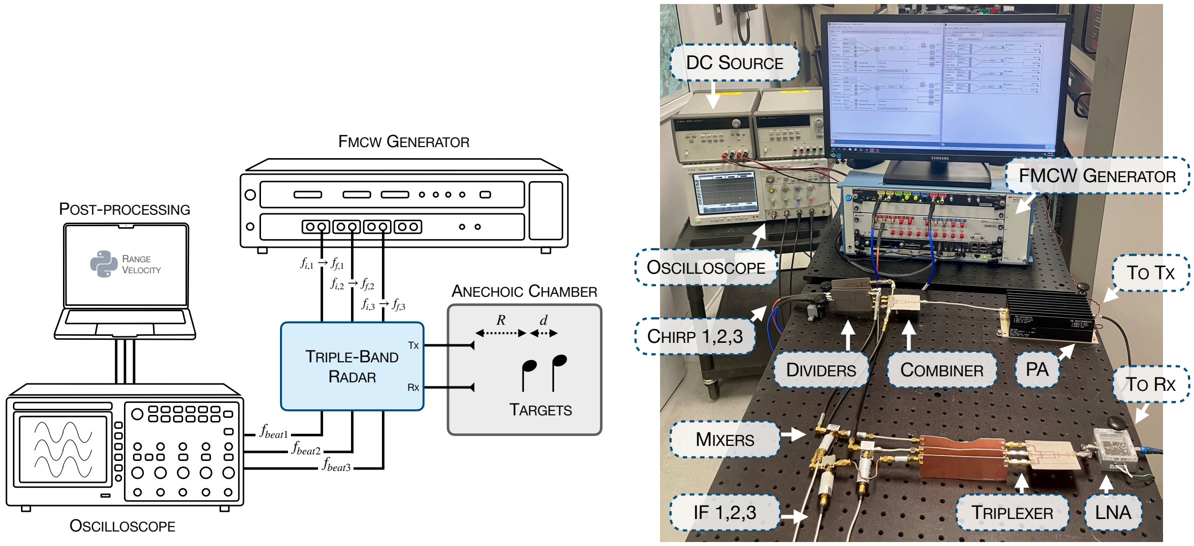

(a) (b)

FIGURE 4.9 (a) Block diagram of the experimental setup and corresponding (b) real connections of the measurement setup. Three bands B_1, B_2 and B_3 are altered by two targets inside the anechoic chamber and their original signals are processed with the altered one before computation with the super fusion procedure.

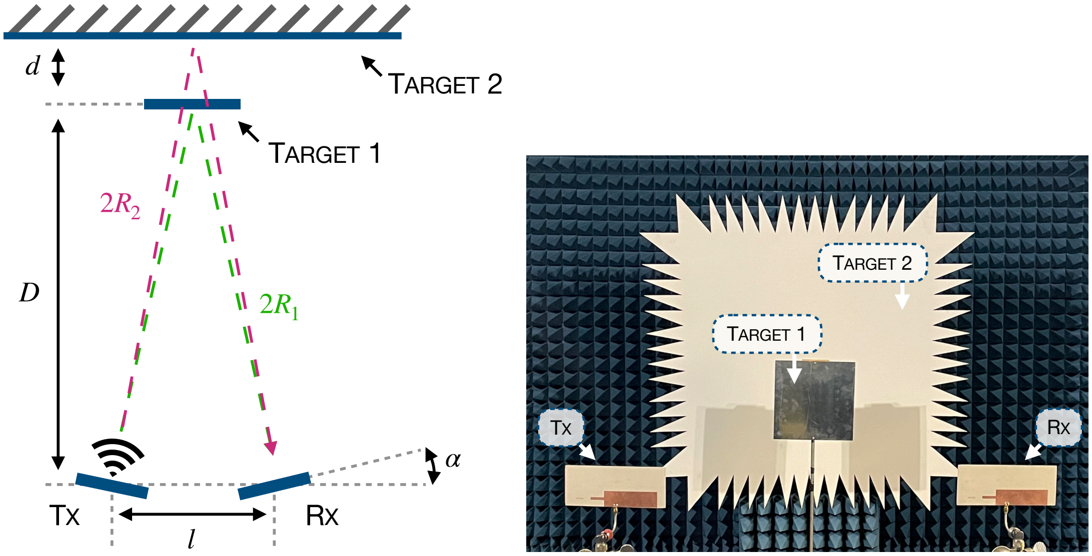

(a) (b)

FIGURE 4.10 (a) Schematic of the targets' placement inside the anechoic chamber and (b) photograph of the targets and TX and RX antennas in-situ.

Fig. 4.11 applies the super fusion procedure, from individual original beat signals to the fusion of their processed counterparts where $f_{beat,1}$ is set as the reference.

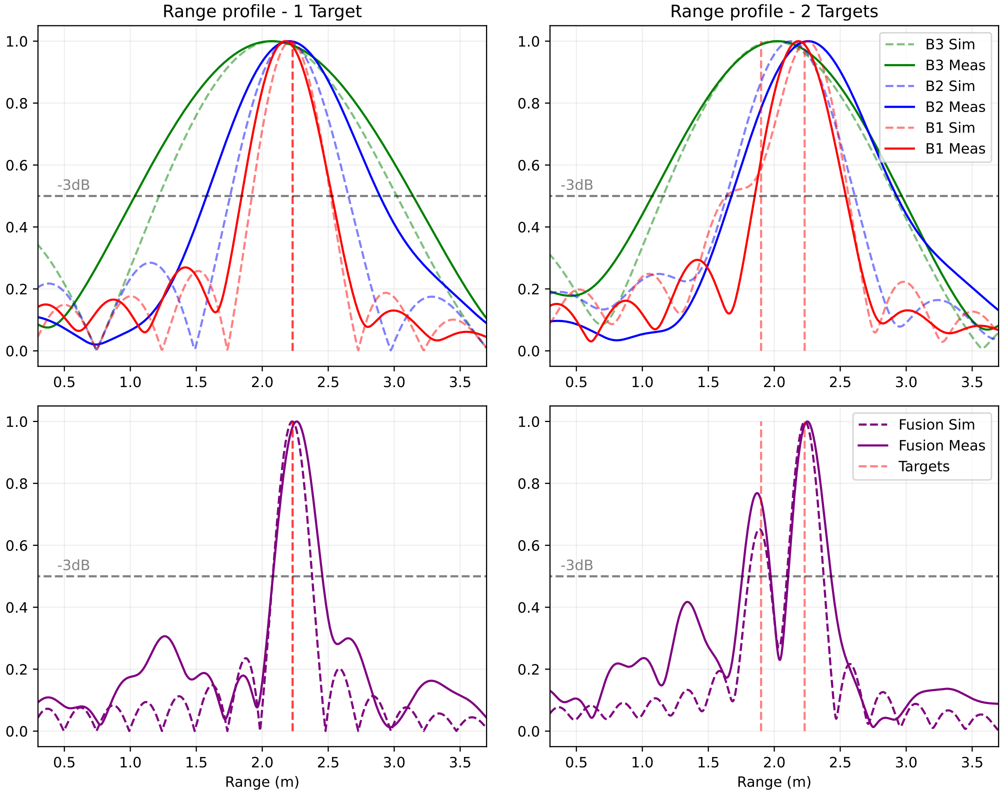

(a) (b)

FIGURE 4.11 Super fusion process applied to measured beat signals from two targets across frequency bands B_1 (red), B_2 (blue), and B_3 (green). The reference beat frequency $f_{beat,1}$ is concatenated with the processed signals $f_{beat,2}$ and $f_{beat,3}$. The Fourier transform results of $f_{beat,1}$ (red), $f_{beat,2}$ (blue) and $f_{beat,3}$ (green), and the fused signal f_{fused}(purple) illustrate target positioning : (a) only target 2 at 2.30 m, and (b) target 1 at 1.90 m alongside target 2 at 2.30 m, compared with theoretical predictions.

As expected, the fused observation time is equal to $2T_C$. Fig. 4.11a and 4.11b present the comparison between the theoretical range profiling measurement with only $B_3 = 100$ MHz, only $B_2 = 200$ MHz, only $B_1 = 300$ MHz, the theoretically synthesized equivalent band $B_{fused,theoretical} = 600$ MHz and actual results for a target distance $D = 1.86$ m and spacing $d = 40$ cm and $\alpha \approx 10°$.

This corresponds to $R_1 = 1.90$ m and $R_2 = 2.30$ m. The measured range resolution is set to the -3 dB width of the main lobe of the FFT and is marked with a dashed line on the figure. Our experiment yields a resolution of 37.6 cm, which represents a 7.7 cm decrease compared to the ideal theoretical 600-MHz bandwidth with a resolution 29.9 cm. Slight discrepancies may be explained by remaining phase inconsistencies in the fused beat signal, but mainly by the applied FFT's windowing which ensures side lobes diminution at the cost of a wider main lobe.

Additionally, the FFT peaks' amplitude in Fig. 4.11b are directly affected by both the targets' range and their RCSs.

Indeed, the relative amplitude of target 1 versus target 2, in dB, can be derived from (4.25) :

$$\Delta_{Target1/Target2} = 10 \log \left[\frac{\sigma_1}{\sigma_2} \left(\frac{R_2}{R_1} \right)^4 \right] \tag{4.35}$$

where σ_1 and σ_2 are the RCSs of targets 1 and 2, respectively and R_1 and R_2 are their corresponding ranges. In our experimental setup, $\sigma_2 \approx 3\sigma_1$ in the line of sight. Thus, $\Delta_{Target1/Target2}$ yields a relative amplitude of -1.45 dB, which means that the peak of target 1 is about 70 % the magnitude of the peak of target 2.

4.6 Conclusion

To address the limitations of next-generation radar systems in crowded radio frequency environments, this research proposes a super fusion method that combines non-equal, non-contiguous, and scattered sub-bands to form a large synthesized equivalent bandwidth in enhancing radar velocity and range resolution. By dividing the required bandwidth into narrower, dispersed sub-bands, this approach mitigates RF spectral congestion while maximizing the use of the available spectrum. A systematic analysis is conducted to predict the resolution achievable with this technique, demonstrating the linear summation of contributions from each sub-band. The theoretical predictions are validated through experimental results, achieving a resolution of 37.6 cm and an equivalent bandwidth of 600 MHz using three sub-bands of 100, 200, and 300 MHz. The proposed method significantly outperforms the resolution of individual sub-bands, successfully distinguishing targets separated by 40 cm.

Looking ahead, incorporating channel diversity introduced by scattered sub-bands into future radar systems employing the super fusion technique could further enhance range resolution while providing additional information about targets, such as their shape and material composition. This method has broad potential for applications, including biomedical radar, synthetic aperture radar, automotive radar, and more.

CHAPITRE 5 ARTICLE 4 : IMPROVING RADAR SYSTEM RESOLUTION THROUGH NONLINEAR SENSING

Thomas Micallef, Xiaoqiang Gu et Ke Wu

Soumis à : *IEEE Transactions on Microwave Theory and Techniques*
Date de soumission : 16 Mai 2025

5.1 Abstract

This work proposes and studies the generation and stitching of the fundamental, second, and third harmonic bands produced by a diode-based harmonic generator, through a nonlinear sensing method, to enhance the range resolution of FMCW radar systems. A preliminary theoretical analysis is conducted to foretell the resolution of such nonlinear sensing with the effective transmission of three simultaneous bandwidths driven by a single fundamental 100-MHz input frequency sweep. The stability of an SMS7630 diode's harmonic output spectrum under the fluctuation of operating temperature and frequency is analytically and experimentally investigated in this work. A complete experimental verification has been conducted to assess the linear equivalent summation of each transmitted sub-band, B_{fund}, B_{2nd} and B_{3rd} to obtain a synthesized 6×100-MHz output bandwidth. Across the 600-MHz output bandwidth, the measured average output power variation was ± 3.4 dBm. Our experiments have successfully shown that the three bands can be fused together to effectively enhance the range resolution by a factor of 4.40 using a single 100-MHz input chirp, reaching 42 cm. Additionally, the findings highlight the diode's reliance on practical use in temperature-variable environments by demonstrating its consistent behavior (± 1 dBm on average) throughout a wide range of operating temperatures. This novel nonlinear sensing method is believed to have great potential in outspreading the current state-of-the-art radar resolution.

5.2 Introduction

The escalatingneed for high-resolution and wideband radar sensing is progressively slowed down by the restricted availability of contiguous spectrum resources. It is challenging to continuously scale radar resolution through conventional approaches due to the bandwidth allocation constraints that arise from congested spectral environments, mainly at lower frequencies [200]. Innovative methods aiming to increase the effective radar bandwidth without using contiguous frequency allocations are therefore highly needed [202, 219, 220]. In order to obtain high-resolution sensing, recent attempts have investigated scattered and multiband techniques, which together exploit non-contiguous spectral components while the majority of conventional solutions to enhance the radar range resolution are focusing on an expansion of the transmitted bandwidth and an increase of the carrier frequency [209, 210].

Meanwhile, generating and transmitting wide bandwidths—even non-contiguously—remains highly challenging. To address such a concern, nonlinear devices may be utilized to produce harmonic bands from a singular narrowband FMCW waveform, facilitating efficient bandwidth extension. Subsequently, these can be coherently combined to surpass spectrum constraints and increase the radar's resolution.

An exploratory study in [161] presented an FMCW-radar fusion technique of non-equal and non-contiguous scattered frequency bands across the S-band and C-band to create an equivalent 600-MHz bandwidth. Although this technique solved some existing limitations, it still requires several frequency sweep generators and potentially complicated multichannel front-end architectures. This represents a significant drawback in minimizing the cost, power consumption, and overall footprint. It is therefore challenging to be implemented in off-grid and batteryless scenarios.

The proposed radar system leverages the nonlinear characteristic of a Schottky diode or possibly any other nonlinear device [159, 221], driven by a single chirp generator, to multiply the input bandwidth around odd and even harmonic frequencies of the input signal. The nonlinear behavior of the proposed third-order harmonic generator results in a fundamental bandwidth around the fundamental input frequency, a doubled additional bandwidth around the second harmonic and a tripled additional bandwidth around the third harmonic. The three received beat signals are then digitally processed to extend the FFT observation time, thus substantially increasing the resolution. The proposed third-order radar prototype aims to enhance range resolution by a factor of six compared to the current state-of-the-art for a fixed FMCW input bandwidth.

In addition, operational conditions like temperature and operation frequency can have a noticeable influence on how these diodes behave [222]. The second objective of this study is to determine how stable the output spectrum of the SMS7630 diode is in different frequency and temperature conditions. It is necessary to measure its resilience and suitability for temperature-critical scenarios.

The proposed technology creates non-contiguous and dispersed frequency sub-bands as a result of the simultaneous generation of the fundamental, second, and third harmonic frequencies. Following this, the fusion process applied to the individual generated beat signals is based upon previous work [161]. Compared to traditional wideband FMCW radar systems, which usually employ a single broad frequency sweep, this method drastically minimizes the contiguous spectrum footprint.

The presented work begins with a comprehensive theoretical formulation of the current equation of a Schottky diode to establish a model for FMCW chirps duplication and discusses the temperature influence on the behavior of the harmonic generator in the first part of Section II. In the second part of Section II, the manufactured harmonic generator prototypes are presented and the theoretical limit of bandwidth expansion is considered. Then, in Section III, the harmonic radar architecture is presented and both the properties of the harmonic generator and the overall radar measurements are analyzed through a laboratory experiment. This aims to validate and verify the accuracy of our theoretical analysis, experiencing the resolution improvement of nonlinear diode-based FMCW radar systems. The conclusions are drawn in Section IV.

5.3 Harmonic Duplication of FMCW Chirps

This section presents the theoretical formulation of the current equation of the Schottky diode and assesses its validity with current-voltage characteristics. It also analytically depicts the thermal effects on the behavior of the diode's current and provides a discussion on the harmonic generator.

5.3.1 Theoretical Formulation

The high nonlinearity of the Schottky diode is the result of the thermionic emission theory that drives the exponential shape of its current (I) and voltage (V) curve. Therefore, a mono-frequency input signal, through the Schottky diode, will result in several subsequent simultaneous higher-order harmonics. Hence, a FMCW input signal sweeping from f_{min} to f_{max} will output sweeps from f_{min} to f_{max}, $2f_{min}$ to $2f_{max}$, $3f_{min}$ to $3f_{max}$, etc. as depicted in Fig. 5.1.

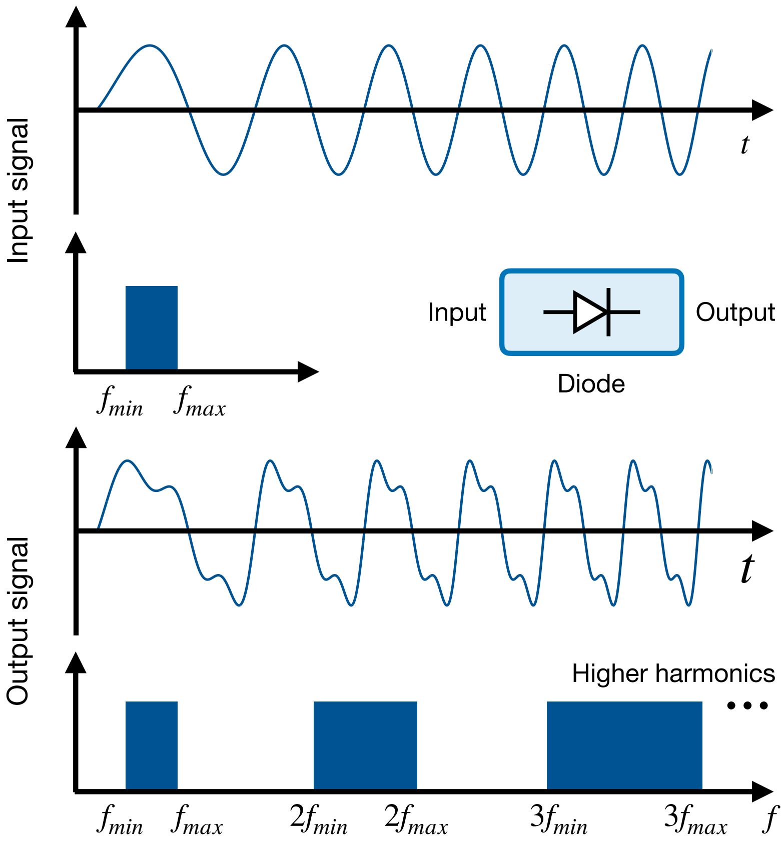

FIGURE 5.1 Input and output frequency spectrums of the proposed diode-based harmonic generator for FMCW radar with frequency sweeping at the input.

For analytical purposes, the diode model used in this study is illustrated in Fig. 5.2.

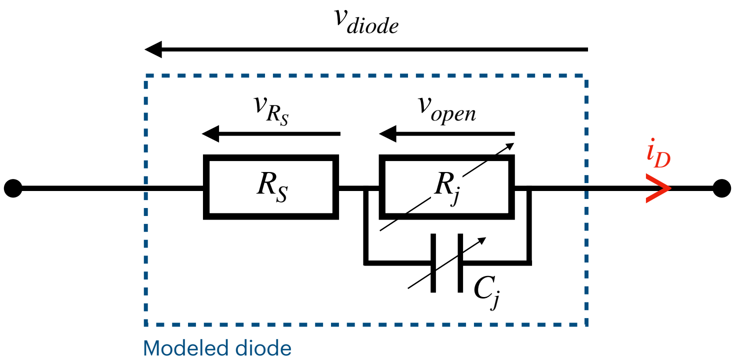

FIGURE 5.2 Model of the diode circuit and corresponding voltages and current. R_S is the series resistor, R_j and C_j are the junction resistor and capacitor, respectively.

According to the datasheet of the SMS7630-079LF, the series resistance R_S is 20 Ω, the junction capacitance C_{j0} is assumed constant at 0.14 pF, and the junction resistance R_{j0} is determined as described in [185]

For a sinusoidal biased mono-frequency excitation V_{bias} of the diode with amplitude V_m, and the consideration of a series resistor R_S, the open voltage can be expressed as :

$$\begin{aligned} v_{open}(t) &= V_{diode}(t) - R_S i_D(t) \\ &= V_{bias} + V_m \cos(\omega t) - R_S i_D(t) \end{aligned} \tag{1}$$

where i_D is the diode current. The current flowing through the Schottky diode over time is expressed as [185] :

$$i_D(t) = I_S \left(e^{\frac{v_{open}(t)}{nV_{T,0}}} - 1 \right) \tag{2}$$

where I_S is the saturation current of the diode at room temperature, n is the ideality factor and $V_{T,0}$ is the thermal voltage at room temperature. Additionally, to consider the breakdown effects in the reverse-bias region, the current may be described as [186] :

$$i_D(t) = -I_S e^{\frac{|v_{open}(t)|}{V_0}} \tag{3}$$

where V_0 is the knee voltage that needs to be extracted from the $I - V$ curve of a given Schottky diode. After some treatments and with the help of W_0, the 0-th branch of the Lambert-W function, the analytical formulation of the diode current can be summarized as :

$$i_D(t) = \begin{cases} \alpha W_0 \left(\frac{I_S}{\alpha} \left(e^{\frac{V_{diode}(t)}{nV_{T,0}}} - 1 \right) \right) & \text{if } v_{open} \geq 0 \\ -\beta W_0 \left(-\frac{I_S}{\beta} e^{\frac{|V_{diode}(t)|}{V_0}} \right) & \text{if } v_{open} < 0 \end{cases} \tag{4}$$

where :

$$\alpha = \frac{nV_T}{R_S} \quad \beta = \frac{V_0}{R_S} \tag{5}$$

Based on this formulation, it is visible that, in the forward-bias region, the current rapidly increases when the input open-voltage reaches nV_T, which is the positive knee voltage. Similarly, in the reverse-bias region around V_0, the current negatively and significantly drops because of the breakdown effects. This indicates that the highest nonlinearities may occur near nV_T.

5.3.2 I-V Curve of Schottky Diodes

To assess the validity of the diode current equation (4), the measured $I-V$ curve of SMS7630 diode is presented in Fig. 5.3 in comparison with the modeled behavior of (4). The measurements are obtained with the Precision LCR Meter E4980A from Keysight. This Schottky diode was selected based on its highly nonlinear characteristics, high availability, and low cost. The observed correlation between the measurements and the model is acceptable, and the current equation can, therefore, be used to predict the amplitude of output harmonics.

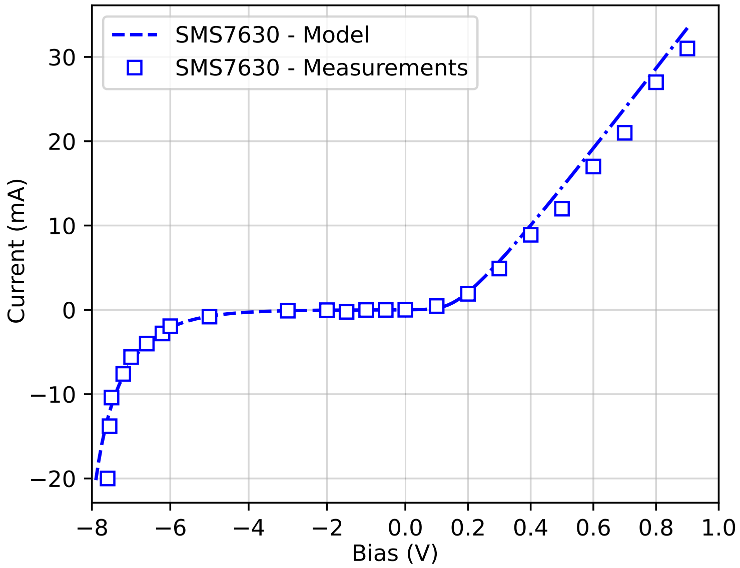

Figure 5.3 Comparison between the measured I-V curves of SMS7630 and the analytical model. Scaling for positive and negative bias voltages are different for easier visibility.

5.3.3 Thermal Effects

The stability of harmonic generation is highly dependent on various environmental conditions, among which temperature variation is one of the most common and essential. To comprehend this specificity, the Schottky diode's $I-V$ relationship shall consider temperature-varying saturation current $I_S(T)$ and thermal voltage $V_T = k_bT/q$, where k_B is the Boltzmann's constant and q is the electrical charge. The voltage-dependent saturation current is expressed by [222] :

$$I_S(T) = I_S \left(\frac{T_0}{T}\right)^{\frac{Xti}{n}} e^{\left(1-\frac{T}{T_0}\right)\frac{E_G q}{nk_B T}} \tag{6}$$

where I_S is the saturation current at room temperature T_0, Xti is the saturation current temperature exponent and E_G is the energy gap. Fig. 5.4 plots the theoretical value of $I_S(T)$ from −40°C to 80°C for the SMS7630 Schottky diode using parameters of its SPICE model.

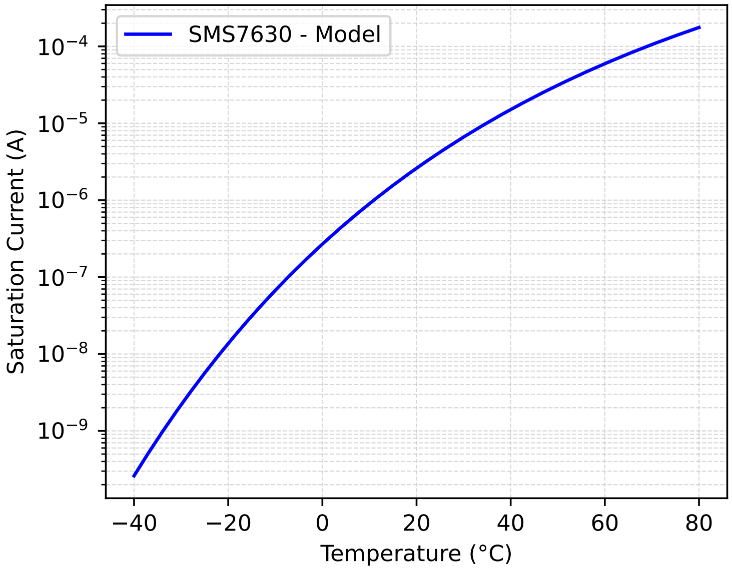

FIGURE 5.4 Theoretical saturation current of SMS7630 Schottky diode from -40°C to +80°C.

After some treatments from (4), the analytical formulation of the temperature-dependent diode's current over time is summarized in (7). The amplitude levels of the fundamental, second and third harmonic can be derived from a Fourier transform on (7) with an input amplitude of 10 dBm and 0 V bias.

$$i_D(t,T) = \begin{cases} \frac{nk_BT}{qR_S} W_0\left(I_S\left(\frac{T_0}{T}\right)^{\frac{Xti}{n}} e^{\left(1-\frac{T}{T_0}\right)\frac{E_G q}{nk_B T}} \frac{qR_S}{nk_BT}\left(e^{\frac{V_{diode}(t)q}{nk_BT}} - 1\right)\right) & \text{if } v_{open} \geq 0 \\ -\frac{V_0}{R_S} W_0\left(-I_S\left(\frac{T_0}{T}\right)^{\frac{Xti}{n}} e^{\left(1-\frac{T}{T_0}\right)\frac{E_G q}{nk_B T}} \frac{R_S}{V_0} e^{\frac{|V_{diode}(t)|}{V_0}}\right) & \text{if } v_{open} < 0 \end{cases} \tag{7}$$

The results are summarized in TABLE 5.1. Theoretically, at high temperatures, the junction resistance of the diode decreases, leading to increased power dissipation as losses, which in turn results in a reduction in the power of the main harmonic components [223].

TABLEAU 5.1 Theoretical Output Harmonic Power

Temperature	**Harmonic Level (dBm)**		
	1 GHz	**2 GHz**	**3 GHz**
−40°C	−3.3	−10.5	−35.2
−20°C	−3.6	−10.6	−33.2
0°C	−3.9	−10.6	−31.6
20°C	−4.1	−10.7	−30.4
40°C	−4.4	−10.9	−29.4
60°C	−4.7	−11.1	−28.5
80°C	−5.0	−11.2	−27.8

5.3.4 Harmonic Generator

The selected frequency bands for this work are 0.95 GHz to 1.05 GHz, 1.9 GHz to 2.1 GHz and 2.85 GHz to 3.15 GHz. Therefore, both the input and output matching networks of the diode must be designed accordingly. Fig. 5.5a and Fig. 5.5b depict the hybrid impedance matching network topologies employed to ensure the proper behavior of the harmonic generator.

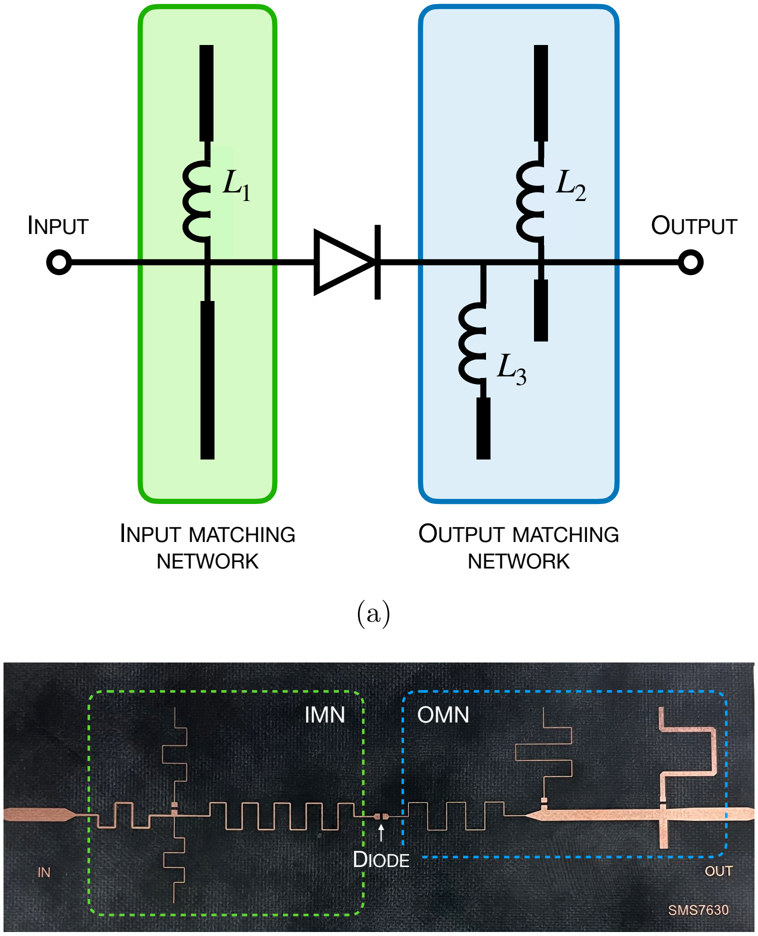

(a)

(b)

FIGURE 5.5 (a) Diode-based harmonic generator architecture with input and output hybrid (inductors and stubs) matching networks and (b) photograph of the fabricated PCBs based on SMS7630 diode. IMN : input matching network, OMN : output matching network.

The manufactured PCB circuit (see Fig. 5.5b) employs a 31-mil thick RT/Duroid 5880 substrate from ROGERS. As anticipated from the $I-V$ curve of the diode, its input and output impedance are likely to vary based on the operating point. Simulation verified that an input power of 7 dBm and a biasing voltage near 0 V delivered an optimal harmonic behavior.

Due to the increase of bandwidth at each subsequent harmonic, the FMCW chirps sub-bands will eventually overlap. Hence, the maximum order expansion is the greater n (harmonic order) that satisfies :

$$(n+1)f_{min} \geq nf_{max} \tag{8}$$

Thus, n_{max} becomes :

$$n_{max} = \lfloor \frac{f_{min}}{f_{max} - f_{min}} \rfloor \tag{9}$$

In the present work, with $f_{min} = 0.95$ GHz and $f_{max} = 1.05$ GHz, $n_{max} = 9$. For practical considerations including the major decrease in harmonic output power as the expansion grows, only the first, second, and third harmonics are considered ($n_{max} = 3$) in this work. TABLE 5.2 presents the theoretical maximum achievable output bandwidth for 0.75, 1 and 1.25 GHz input fundamental center frequencies with input bandwidths ranging from 100 to 500 MHz.

Tableau 5.2 Maximum Achievable Output Bandwidth (MHz) up to Third Harmonic without Overlapping

Input Bandwidth	**Input Center Frequency**		
	0.75 GHz	**1 GHz**	**1.25 GHz**
100 MHz	600	600	600
200 MHz	1200	1200	1200
300 MHz	≬	1800	1800
400 MHz	≬	≬	2400
500 MHz	≬	≬	≬

The overlap indications (≬) refer to the impossibility of generating up to three harmonics without overlapping with lower harmonic sub-bands. It was seen that for the selected 1 GHz input, the maximum input bandwidth is 300 MHz, resulting in a total 1.8 GHz output bandwidth. Although such a harmonic output bandwidth would theoretically be achievable at 1 GHz, to maintain satisfactory output power stability inside the output harmonic bandwidths, the input bandwidth is restricted to 100 MHz in this work, totaling a 600 MHz output bandwidth.

5.4 Experimental Radar Verification

This section presents the harmonic radar architecture and discusses the triple beat signal processing. It also analyzes the output harmonic flatness of the harmonic generator across various frequencies and temperatures, and presents the measurement results of the proposed nonlinear sensing technique. The ultimate practical architecture may be different from the provided architecture, which is primarily used to validate the nonlinear sensing concept.

5.4.1 Harmonic Radar Architecture

Fig. 5.6 shows the proposed architecture for the triple-band nonlinear sensing.

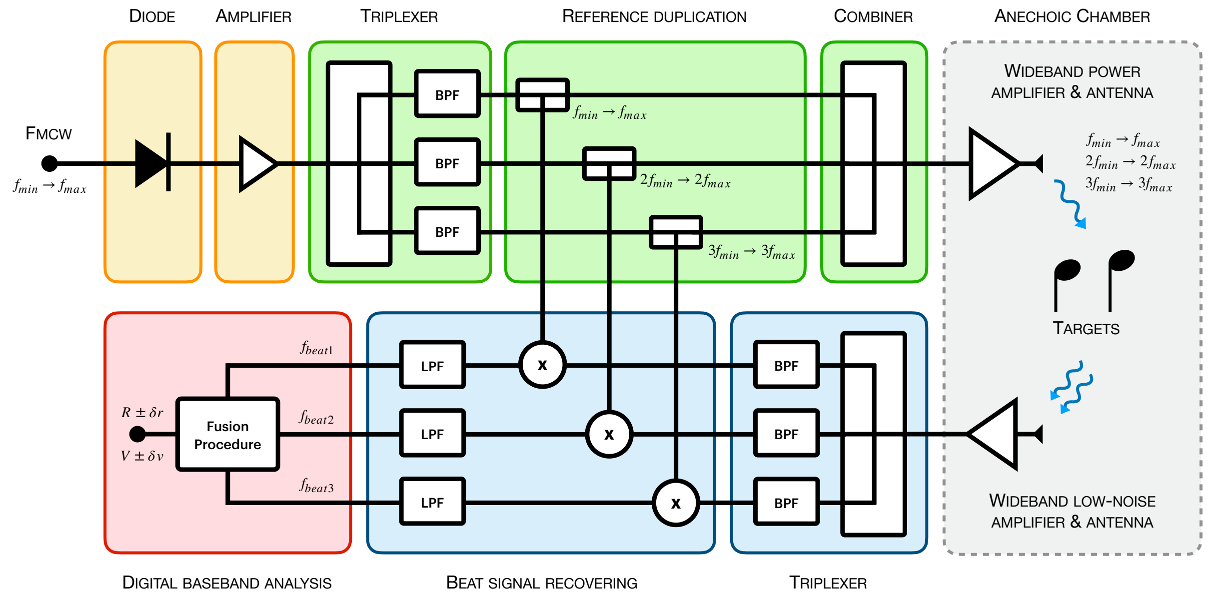

FIGURE 5.6 Block diagram of the architecture of the nonlinear diode-based triple-band FMCW radar system from harmonic duplication of the chirps to the digital baseband analysis and configuration inside the anechoic chamber.

The transmission chain is composed of the following elements. First, the diode-based harmonic generator is connected to the LMT-4035 amplifier from Avantek to counterbalance the low amplitude levels of the harmonics. Because of the amplifier's great linearity at the applied power level, self-harmonic production is considered as insignificant at this stage. Then, the amplifier is connected to a triplexer, which aims to separate the fundamental, the second, and the third harmonic chirps. To facilitate the demonstration of this nonlinear sensing technique, three dividers are designed to duplicate the reference chirps for demodulation. Finally, the original chirps are recombined with a 3-to-1 combiner and amplified with a ZHL-42 30-dB-gain power amplifier from Mini-Circuits. Enhanced iteration of the transceiver architecture may include an equalizer stage to individually set each harmonic amplitude at a specific value. This would allow for a relatively flattened power spectrum across the harmonics.

The reception chain is composed of the following elements. First, an off-the-shelf 40-dB-gain LNA is employed to amplify the received signals. Then, a fabricated triplexer is used to separate the three harmonic frequency bands, which are then mixed with their original chirps to retrieve the beat signals, after low-pass filtering. The signals are finally fused in the digital domain using the fusion procedure. Additionally, a pair of printed-dipole antennas covering 0.7 to 3.3 GHz have been fabricated following the design of [218]. Its fine directivity is well-suited for the purpose of this work's experimental demonstration.

Besides, an end-to-end simulation was performed to confirm the signal chain's integrity during the design procedure. Indeed, guaranteeing that each harmonic component stays contained inside its designated transmit and receive path is key to reduce cross-band interferences. The core parts of the architecture, such as the triplexers, PC/PD and filters were purposely conceived to maintain harmonic isolation and allow, in fine, proper beat signal recovery for subsequent baseband operations.

The consequence of phase and group delay fluctuations across the distinct pathways is reduced by the overall limited transmitted bandwidth ($B_{total} = 600$ MHz) and the minimum propagation lengths (tens of cm). Robust system performances are also guaranteed by the further applied alignment in the baseband operations.

5.4.2 Beat Signal Processing and Fusion

To effectively increase the resolution of the radar, it is required to follow the procedure described in [161]. This fusion procedure leverages a fusion process of the original beat signals obtained from the fundamental, second and third harmonic chirps to increase the observation time. This increase in observation time leads to an increase in the resolution of the FFT, which consequently enhances the range resolution δ_r of the radar. The so-called fused beat signal implies the linear summation of the contribution of each band :

$$\begin{cases} B_{fund} &= f_{max} - f_{min} \\ B_{2nd} &= 2f_{max} - 2f_{min} \\ B_{3rd} &= 3f_{max} - 3f_{min} \end{cases} \tag{10}$$

As a consequence :

$$\delta_{r,fused} = \frac{c}{2(B_{fund} + B_{2nd} + B_{3rd})} \tag{11}$$

The fused resolution $\delta_{r,fused}$ can then be rewritten with (10) as :

$$\begin{aligned} \delta_{r,fused} &= \frac{c}{2(6f_{max} - 6f_{min})} \\ &= \frac{c}{2 \times 6B_{fund}} \end{aligned} \tag{12}$$

Therefore, the fused resolution of the nonlinear triple-band sensing yields a theoretical resolution six times greater than the original sensing method, which only uses the fundamental band B_{fund}.

5.4.3 Output Power Stability of Harmonic Generator

Evaluating the harmonic flatness—the generator's capacity to sustain a constant harmonic amplitude throughout the band—is essential to confirming the wideband capability of the suggested up-to-third-order harmonic generator. Ten input frequencies, evenly spread from 0.95 GHz to 1.05 GHz, are available with the Keysight E8267D single-tone generator at a steady input power of 7 dBm.

Additionally, to assess the temperature dependency of the harmonic generator, measurements were conducted over a regulated temperature range of −40°C to 80°C, at intervals of 20°C. The fundamental frequency and its second and third harmonics, 1 GHz, 2 GHz, and 3 GHz, respectively, were used to examine the output spectrum. The harmonic generator's temperature-dependent output power at these frequencies is shown in Fig. 5.7a for the whole sweeping band (0.95–1.05 GHz, 1.90–2.10 GHz, and 2.85–3.15 GHz).

For an input power of 7 dBm, Fig. 5.7b shows a comparison between the measured findings (solid line) and theoretical predictions (dashed line) at 1 GHz, 2 GHz, and 3 GHz. The measurement setup is shown in Fig. 5.7c, where the frequency generator supplies the sweeping signal, the manufactured harmonic generator is positioned inside a temperature-controlled chamber, and the output is captured using an oscilloscope.

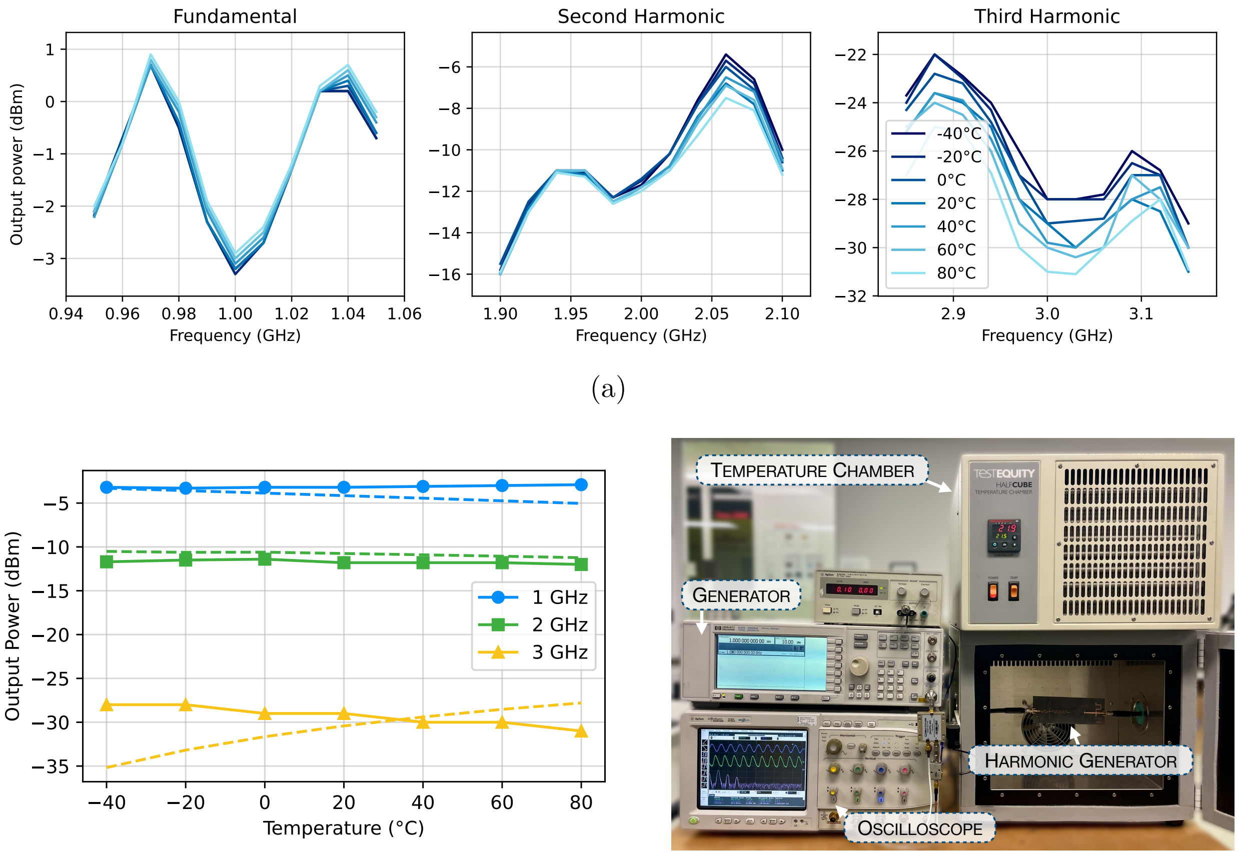

(a)

(b)

(c)

FIGURE 5.7 (a) Measured output power of the fundamental, second, and third harmonics with an input power of 7 dBm from 0.95 to 1.05 GHz. The temperature covers −40°C to 80°C (b) Measured output power at 1, 2 and 3 GHz from −40°C to 80°C with 7-dBm input power. Theoretical power levels are marked by the dashed line (c) Measurement setup where the harmonic generator is powered by a frequency generator and the output is monitored by an oscilloscope.

First, for the fundamental output frequency, it was observed that this mode is thermally stable, as seen by the output power of the fundamental frequency showing less than 1 dB of change throughout the whole temperature range. Then, the output power of the second harmonic (2 GHz) decreased somewhat at higher temperatures, indicating a small sensitivity to temperature. With a projected increase in power at higher temperatures (60°C to 80°C), the third harmonic (3 GHz) showed more noticeable oscillations. Interestingly, variations were noted in the third harmonic at severe temperatures, even though the measured values for the fundamental and first harmonic frequencies nearly matched the theoretical expectations. In the region of 0°C to 60°C, however, the theoretical model continues to be accurate.

There are two primary causes for the observed fluctuation in the third harmonic at very high temperatures. First, because higher-order harmonics are more susceptible to nonlinearities and parasitic effects, the analytical model employed for harmonic estimation is designed for approximation analysis and tends to lose precision with higher-order harmonics. In the input and output matching networks, temperature variations can cause impedance mismatches that disproportionately impact higher-frequency components, like the third harmonic. The disparities observed in the measured data under heat stress may be explained by these combined effects.

Since heat influences diminish the overall effectiveness of harmonic generation, a drop in the amplitude of the higher-order harmonics at high temperatures may be observed. On the other hand, the second and third harmonics typically have more power at lower temperatures as observed in Fig. 5.7b. Because less power is radiated towards the target at higher temperatures, the ranging measurement may suffer from a loss in harmonic amplitude, which lowers the SNR at the receiver. In the end, this may reduce the FFT resolution, which makes it more challenging to resolve precise target data.

Given the potential fluctuations of higher-order harmonics due to temperature variations or diode limitations, the fusion procedure is designed to be flexible, allowing the integration of only the reliably received sub-bands without compromising the overall reconstruction process. As a result, and depending on the application scenario, if only B_{fund} and B_{2nd} are effectively generated and transmitted, then the fused resolution would become $\delta_{r,fused} = c/2\,(B_{fund} + B_{2nd})$.

5.4.4 Radar Measurements Results

Experimental measurements were conducted in an anechoic chamber to verify the genuine resolution improvement of the proposed nonlinear sensing method. The block diagram and the actual connections of the measurement setup are presented in Fig. 5.8 and Fig. 5.9, respectively.

The M8196A AWG from Keysight is configured to output a FMCW signal from 0.95 to 1.05 GHz (100 MHz) within 1 us at a constant power level of 7 dBm, which drives the diode-based harmonic generator. Then, in the anechoic chamber, two targets are placed in front of the antenna, 1.9 m from the antennas to target 2, and 2.3 m from the antennas to target 1, resulting in 40 cm between the two targets. The two printed antennas are spaced 75 cm

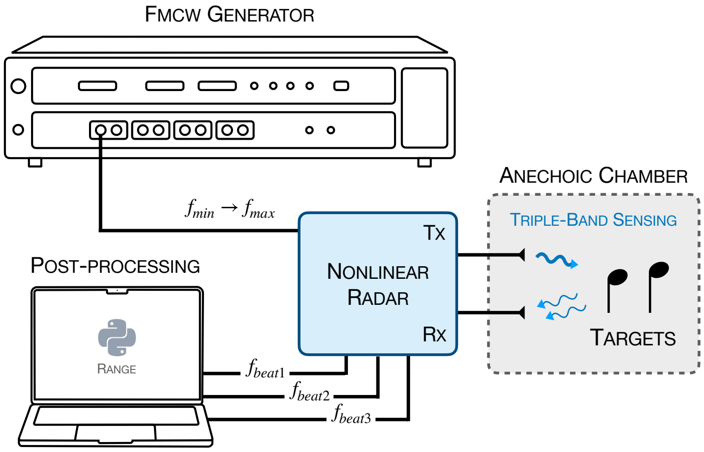

FIGURE 5.8 Block diagram of the experimental setup where an FMCW generator drives the nonlinear radar and where sensing measurement is performed in an anechoic chamber. Three bands B_{fund}, B_{2nd} and B_{3rd} are altered by the two targets and their original/reference signals are mixed with the altered ones for down-conversion before computation with the super fusion procedure in the computer.

apart horizontally (see Fig. 5.9). After being delayed proportionally to the target's distances, the return signal is received and down-converted in the reception chain.

Fig. 5.10 presents a comparison between actual beat signals retrieved after low-pass filtering driven by the proposed harmonic generator and those driven by the AWG.

The AWG is configured to output three simultaneous FMCW sweeps from 0.95 to 1.05 GHz (100 MHz), 1.9 GHz to 2.1 GHz (200 MHz) and 2.85 GHz to 3.15 GHz (300 MHz) and is connected instead of the harmonic generator, before the reference duplication sub-block (see Fig. 5.6). The same measuring conditions are observed to enable this comparison and the output power of each AWG's channel are set to correspond to the average output power of each harmonic sub-bands produced by the generator. It is seen from this comparison that the beat signals corresponding to the second and third harmonics are significantly more affected by the in-band power fluctuations of the generator, as seen in Fig. 5.7a. This results in less consistency throughout the chirps, thus affecting the SNR and the overall computed range resolution. Additionally, it is to be noted that the exploitable beat signals span 0.7 us for the second and third harmonic instead of 1 us, thus a diminution of 30 % of exploitable time duration. This can be explained by internal components of the architecture limiting the transmission at these frequencies.

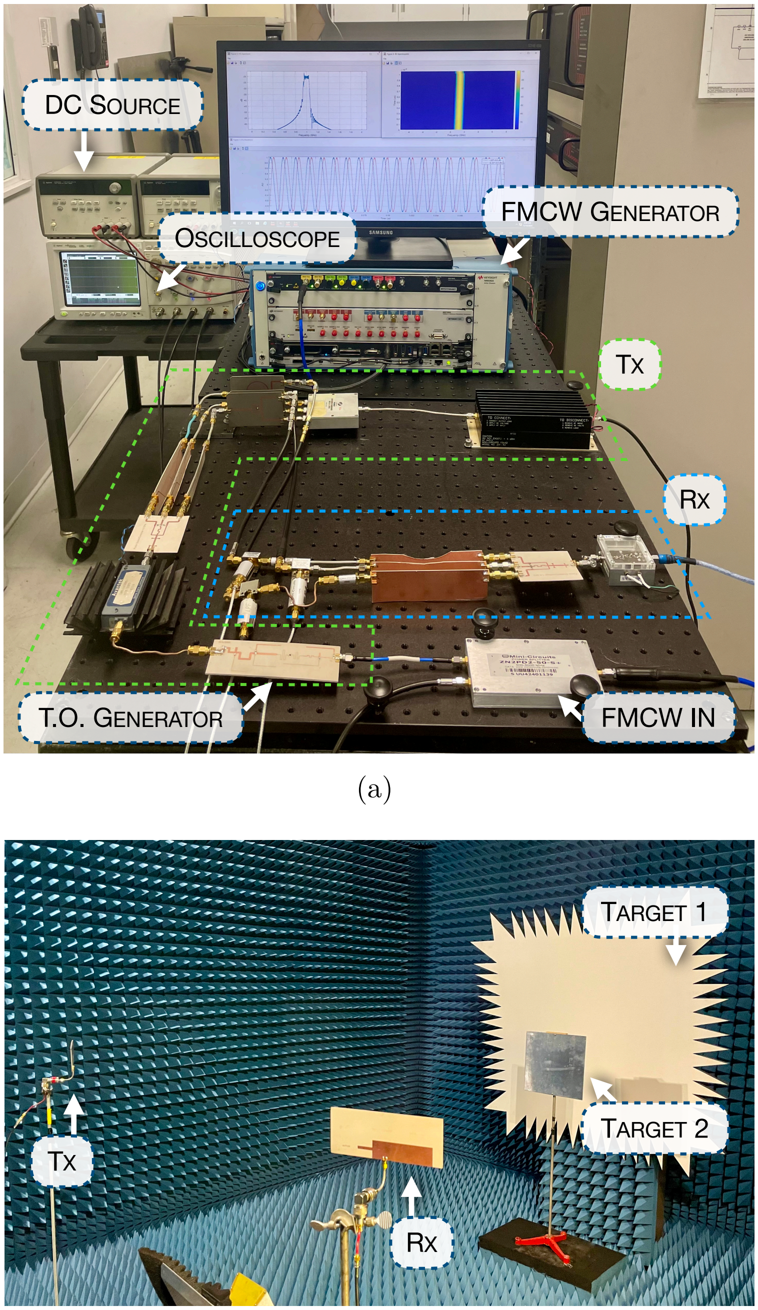

(a)

(b)

FIGURE 5.9 (a) Actual connections of the measurement setup featuring the nonlinear diode-based triple-band FMCW radar system with (b) the antennas and the targets in the anechoic chamber. TO : third-order.

Ultimately, the digital baseband fusion of the beat signals is achieved on the sampled beat signals, shown in Fig. 5.10, with a Python algorithm consisting of the following primary steps : (1) gathering beat signals from the fundamental and harmonic bands, (2) processing each

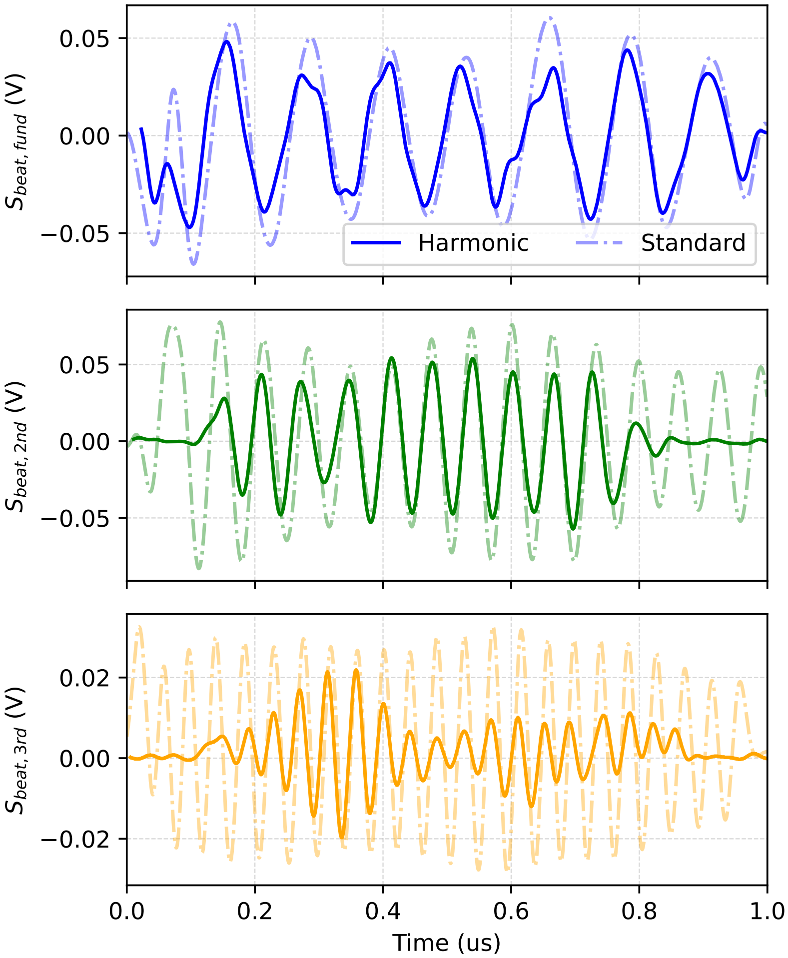

FIGURE 5.10 Measured beat signals $S_{beat,fund}$, $S_{beat,2nd}$ and $S_{beat,3rd}$ driven by the harmonic generator (plain line) and standard external generator (dashed line).

signal to align it with respect to time and frequency, and (3) combining the processed signals with the proper handling of phase to create a single high-resolution output. This method makes it possible to improve radar range resolution by utilizing spectral content from several harmonics.

The results of the measurements of the triple-band nonlinear sensing, aiming to compare the theoretical and measured results of both the fundamental band and the fused band, are presented in Fig. 5.11.

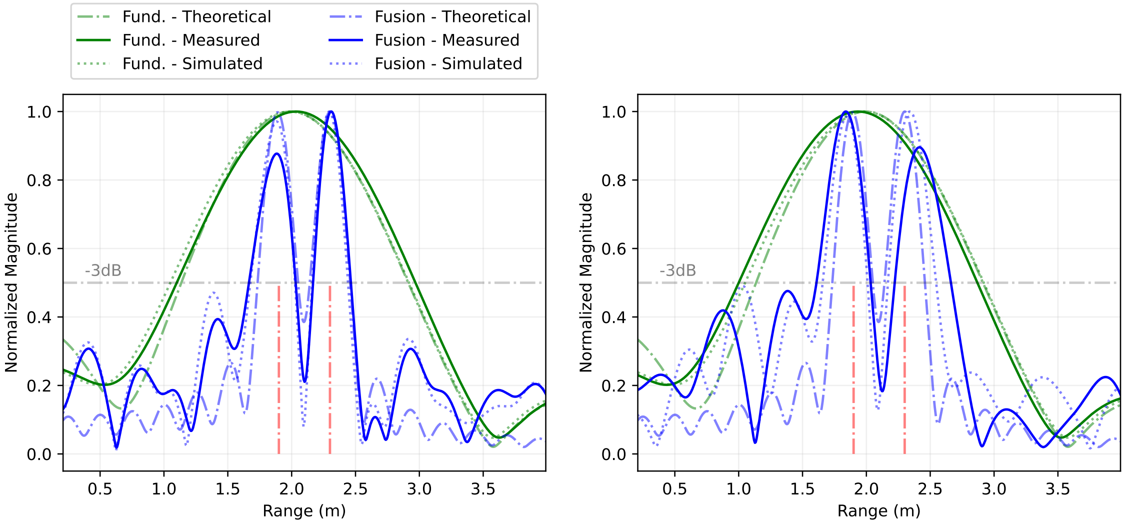

(a) (b)

Figure 5.11 Comparison of actual range profiles (FFT with Hamming window) between the input fundamental band of 100 MHz (if used alone) and the proposed fusion with sensing driven by (a) triple-band AWG and (b) harmonic generator. Target's locations are marked by the red dashed lines.

As a comparative reference, Fig. 5.11a presents the range profile measured with the AWG as the input and Fig. 5.11b with the harmonic generator.

The range resolution of the fundamental band is measured at 1.85 m, which represents a 5 % difference compared to the theoretical range resolution. With the effective transmission of the three harmonic bands (6×100 MHz), the measured resolution becomes 42 cm, hence yielding a resolution improvement factor compared to the fundamental theoretical band measured resolution of 4.40. The measured range resolution of the harmonic-based sensing (42 cm) represents a decrease of 20 % compared to the AWG-based sensing (35 cm). Such a decrease is understandable with respect to the reduction of usable periods in Fig. 5.10. Due to imperfections in the digital fusion procedure, mainly resulting from incoherent phase links in-between the stitched sub-bands, the FFT peaks may be shifted even thought the half-power beam still contains the actual target's location.

The main results of the experiment are summarized in TABLE **??** where measurement column (a) refers to the results of Fig. 5.11a and (b) refers to Fig. 5.11b. The theory and measured column results refer to the dashed and plain lines of Fig. 5.11, respectively.

TABLE 5.3 presents a comparison between state-of-the-art multiband radars and the proposed system regarding range resolution δ_r (m) with respect to the total input bandwidth BW_{input} (MHz) and applied procedure.

Tableau 5.3 Comparison with State-of-the-Art Multiband Radars

Reference	**Configuration**	**Frequency Bands (GHz)**	BW_{input} **(MHz)**	**Fusion Procedure**	δ_r **(cm)**	**FoM**
[214]	4× FMCW	18-20, 20-22, 22-24, 24-26	8000	Concatenation (= sub-bands)	2	160
[161]	3× FMCW	2.4-2.5, 5-5.2, 6-6.3	600	Concatenation ($\neq$ sub-bands)	32	192
[224]	2× FMCW	19-22, 34-37	3000	None	5.7	171
[225]	2× FMCW	10-11, 12-13	2000	Extrapolation	8	160
[226]	2× FMCW	2.459-2.499, 9.875-9.915	80	Concatenation (= sub-bands)	400	320
[227]	1× FMCW	4.7-5.7, 9.4-11.4, 14.1-17.1, 18.8-22.8	1000	Extrapolation	0.85	8.5
[This work]	1× FMCW	0.95-1.05, 1.9-2.1, 2.85-3.15	100	Concatenation ($\neq$ sub-bands)	42	42

To provide a comparison, a Figure of Merit (FoM) is defined in this work, where the lower the better :

$$FoM = BW_{input} \times \delta_r \tag{5.1}$$

The extrapolation-based fusion method enhances overall performance in [227] ; nonetheless, it incurs much greater computational complexity compared to the utilized concatenation strategy, which is lightweight and efficient. Additionally, other works rely on multiple input FMCW chirps, which disqualify them as spectrum-conscious approaches.

5.5 Conclusion

Focusing on drastically enhancing radar range resolution, this work has presented a detailed nonlinear modeling and experimental characterization of an SMS7630-based harmonic generator, demonstrating its ability to efficiently duplicate FMCW chirps across the fundamental, first, and second harmonic bands of a single input sweep. The study validates that such diode-based structures may support multiband radar signal generation and resolution enhancement, leveraging a previously published fusion procedure.

Built upon theoretical analysis, the proof-of-concept has shown that a fundamental 100-MHz input bandwidth, achieving a measured resolution of 1.87 m, can effectively drive the proposed nonlinear diode-based sensing method. This results in a substantial improvement over the state-of-the-art fundamental radar range resolution, achieving a factor of 4.40 enhancement with a measured resolution of 0.42 m. Furthermore, the output spectrum of the SMS7630-based harmonic generator exhibits remarkable stability across multiple harmonics and over a wide temperature range of 120°C. These findings provide critical insights for applications requiring consistent harmonic performance and minimal spectral drift. Additionally, the diode's reliable behavior under thermal variations further validates its suitability for RF applications in wireless sensing and radar systems operating in fluctuating environmental conditions.

Future research may include enhancing in-band output power stability to reduce any undesired influence on detection sensitivity and SNR. Furthermore, the harmonic bands create exciting opportunities to leverage spectral diversity to extract richer information from targets, which could lead to improved material characterization and classification capabilities.

CHAPITRE 6 ARTICLE 5 : MULTI-MODE MULTI-BAND ISAC TECHNIQUE FOR REAL-TIME HEALTHCARE MONITORING

Thomas Micallef, Xiaoqiang Gu et Ke Wu

Soumis à : *IEEE Microwave and Wireless Technology Letters*
Date de soumission : 19 Mai 2025

6.1 Abstract

A unique multi-mode, multi-band radar and communication system intended for real-time healthcare monitoring is presented in this paper. To enable high-accuracy position tracking and vital sign detection, especially for applications like indoor elderly surveillance. The proposed multi-band fusion technique enables both bidirectional data transmission and local processing for improved decision-making by seamlessly integrating wireless communication and dual mode radar sensing inside a single transceiver. Based on a preliminary theoretical analysis, our measurements demonstrated a phase-radar-based respiration rate fused resolution of ± 15.50 mHz and a fused position accuracy of 68.7 cm leveraging two bands ($B_1 =$ 100 MHz and $B_2 =$ 200 MHz) while allowing data communication during radar cycles. This multi-mode multi-band radar technique is believed to have great potential in establishing the next generation of wireless healthcare systems within radar networks.

6.2 Introduction

The rising demand for sophisticated healthcare monitoring solutions has propelled the advancement of contemporary radar-based sensing technologies for domestic surveillance [228]. Specifically, for older people living alone, non-intrusive radar devices present a viable substitute for conventional wearable sensors in terms of tracking mobility and monitoring vital signs [229, 230]. In this regard, we propose an innovative multi-mode, multi-band radar technique, settled on a hybrid multiplexing scheme, intended for healthcare monitoring and real-time surveillance. The ability of the suggested multifunctional radar system to seamlessly combine distinct radar operation modes into a single transceiver is one of its main advantages, which makes it adequately tailored for next-generation intelligent wireless systems [54]. This integration is essential for continuous monitoring of relevant metrics such as respiratory rate as well as for high-accuracy location tracking. Furthermore, the system's communication mode enables the measured data to be sent to a master node inside an in-home radar network [231]. Bidirectional data transmission is made possible by this dual capability, which also makes cloud storage and AI-driven analytics easier for better decision-making and anomaly detection in medical applications [232], as illustrated in Fig. 6.1.

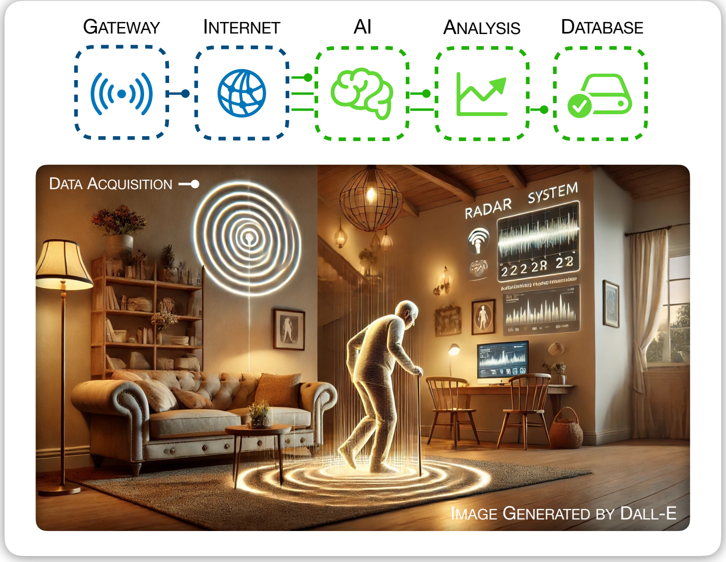

FIGURE 6.1 Application scenario of elderly surveillance from radar sensing to extensive AI-based medical analysis.

There are two main benefits to the proposed radar technique. First, by concatenating the received signals in the digital domain, the multi-carrier phase radar approach efficiently expands the observation duration. This improves the accuracy of monitoring by providing more real-time information on breathing cycles and patterns in a reduced time frame. Second, the proposed system enables flexible FMCW resolution by utilizing either one of the frequency bands independently—providing several distinct resolution levels—or all bands simultaneously, achieving a linear summation of the resolutions. Coarser range resolutions (≈150 cm) can suffice for coarse occupant detection in large rooms, whereas finer resolutions (≈50 cm) are advantageous for precise indoor tracking or fall detection scenarios. Because of its flexibility, the system may dynamically modify its resolution according to the needs of the application, guaranteeing peak performance in a variety of monitoring situations. This fusion procedure was previously demonstrated in [161].

Compared with our prior work, which focused exclusively on multi-band FMCW fusion for range resolution enhancement, the present work integrates both a phase-based multi-carrier

Doppler sensing mode (Mode 1) and an FMCW multi-band fusion mode (Mode 2) within the same reconfigurable RF front-end, alongside a dedicated communication mode (Mode 3). Although detailed communication performance measurements are beyond the present scope, the design allows time-shared ISAC operation between sensing and communication. This combination enables the same hardware to perform sequential sensing and communication functions, aligning with ISAC principles. The present prototype applies this architecture to respiration monitoring and position estimation using a human subject, demonstrating its applicability for healthcare scenarios.

A flexible hybrid multiplexing approach is also employed, allowing radar and communication functions to dynamically allocate time resources according to system requirements around 5 and 8 GHz. Fig. 6.2 depicts a typical multiplexing scheme intended for that usage.

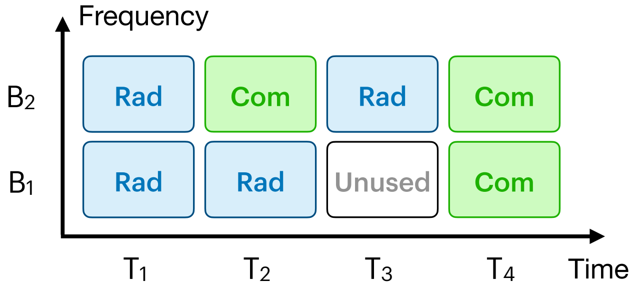

FIGURE 6.2 Flexible hybrid multiplexing scheme integrating radar and communication functions.

The design, deployment, and experimental verification of the suggested multi-mode, multi-band radar technique are presented in this study. In Section II, the multi-mode radar fusion approach is described in depth, along with the variable FMCW resolution and the multi-carrier phase radar's underlying concepts. The experimental setup employed for validation, the radar architecture and measurement data are described in Section III, demonstrating the effectiveness of the suggested strategy. A summary of the paper's main conclusions is provided in Section IV.

6.3 Multi-Mode Multi-Band Radar Fusion

6.3.1 Mode 1 : Multi-Carrier Doppler Radar

The proposed first radar mode is a multi-carrier phase radar technique consisting in the transmission of two Continuous Wave (CW) signals, $S_{TX,1}$ and $S_{TX,2}$, at two scattered center frequencies as depicted in Fig. 6.3.

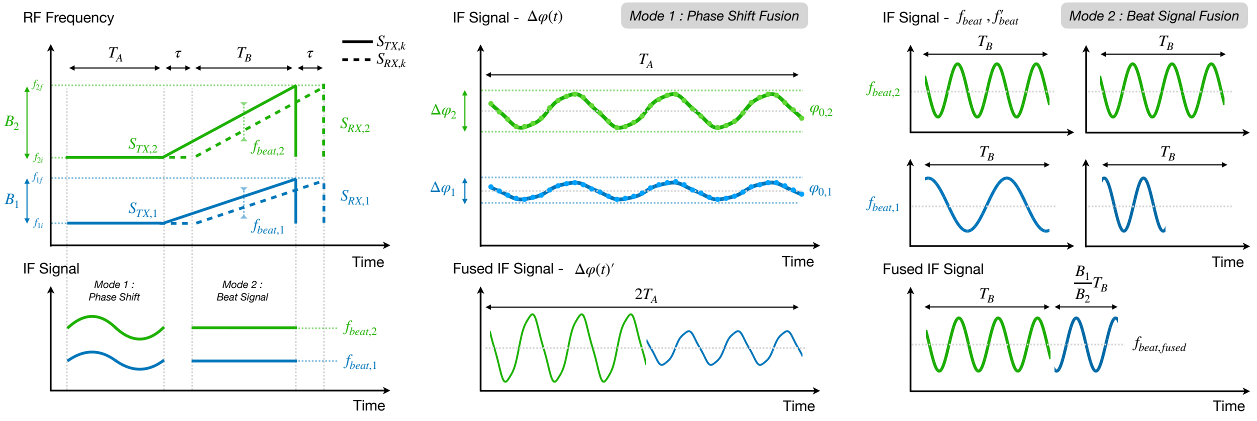

FIGURE 6.3 (Left) Tx and Rx signals of the phase radar and FMCW chirps over B1 and B2 and corresponding intermediate frequency (IF) signals, (Middle) fusion procedure of dual-carrier mono-frequency phase radar in mode 1 and (Right) multi-band fusion procedure of the beat signals of the FMCW chirps in mode 2.

The received signals are then processed to retrieve the chest wall displacement of the human body. Each transmitted signal $S_{TX,i}$ can be expressed as :

$$S_{TX,i} = A_{T,i}\cos\left(2\pi f_{c,i}t\right) \tag{6.1}$$

where $A_{T,i}$ is the amplitude of the transmitted wave and $f_{c,i}$ is the carrier frequency. After propagation and contact with the chest wall, the received signal $S_{RX,i}$ becomes :

$$S_{RX,i} = A_{R,i}\cos\left(2\pi f_{c,i}t + \Delta\varphi_i + \varphi_{0,i}\right) \tag{6.2}$$

where $\Delta\varphi_i = 4\pi/c \times f_{c,i}x(t)$ is the returned phase shift induced by the small displacement of the chest wall $x(t)$ and $\varphi_{0,i}$ is a constant phase due to the physical parameters of the measurements. The respiration movements are responsible, on average, for a chest wall displacement of 4 to 12 mm [230]. This corresponds to a phase variation of 0.8 to 2.5°, at a carrier frequency of 5 GHz. To counterbalance the null problem that may be occurring in the phase shift radar measurements when only one demodulation channel is used, previous works employed In-phase (I) and Quadrature (Q) demodulators [233]. Hence, the I/Q baseband signals after demodulation can be written as :

$$B_{I,i} = \sin\left(\Delta\varphi_i + \varphi_{0,i}\right) \tag{6.3}$$

$$B_{I,i} = \cos\left(\Delta\varphi_i + \varphi_{0,i}\right) \tag{6.4}$$

One can then retrieve the phase variation proportional to the chest wall displacement by applying the arctangent function :

$$\Delta\varphi_i = \arctan\left(\frac{B_{I,i}}{B_{Q,i}}\right) - \varphi_{0,i} \tag{6.5}$$

Finally, the respiration rate and heartbeat are identified through a FFT of $\Delta\varphi_i$. The frequency resolution of the FFT, which ultimately drives the ability to distinguish close frequencies in the spectrum, is inversely proportional to the number of observable periods during the observation time, N_{P,T_A}, of each $\Delta\varphi_i$ waveforms such as :

$$\delta f_{FFT} = \frac{1}{N_{P,T_A}} \tag{6.6}$$

The proposed technique aims to double the number of periods by concatenating the dual phase shift signals in the numerical domain, after sampling, as illustrated in Fig. 6.3. Hence, the total observable periods for the FFT will be :

$$N_{P,T_A,fusion} = 2N_{P,T_A} \tag{6.7}$$

This results in a doubled frequency resolution.

6.3.2 Mode 2 : Flexible FMCW Resolution

To effectively increase the resolution in the second part of the radar waveform, corresponding to the FMCW part, i.e. the second mode, [161] previously demonstrated that each bandwidth, B_1 and B_2 (Fig. 6.3) can be linearly summed through a super fusion procedure, resulting in an equivalent stitched bandwidth :

$$B_{eq} = B_1 + B_2 \tag{6.8}$$

Leveraging the hybrid multiplexing scheme of Fig. 6.2, it is possible to obtain variable range resolutions depending on which bandwidth is employed during each time slot. This technique allows for a usage of either B_1 or B_2 individually (case T_2 or T_3) or B_1 and B_2 jointly (case T_1). Hence, the adaptive fused resolution δ_{r,B_1}, δ_{r,B_2} and $\delta_{r,fused}$ can be expressed as :

$$\delta_{r,B_1} = \frac{c}{2B_1} \tag{6.9}$$

$$\delta_{r,B_2} = \frac{c}{2B_2} \tag{6.10}$$

$$\delta_{r,fused} = \frac{c}{2(B_1 + B_2)} \tag{6.11}$$

where c is the speed of light. The achievable FMCW equivalent bandwidths are $B_1 = 100$ MHz, $B_2 = 200$ MHz, and $B_1 + B_2 = 300$ MHz, corresponding to theoretical range resolutions of 150 cm, 75 cm, and 50 cm, respectively. In this work, the CW phase radar mode is employed for respiration monitoring, as its unmodulated carrier avoids range migration effects present in FMCW signals and thus maintains higher sensitivity to the small displacements associated with vital signs.

6.4 Experimental Verification

6.4.1 Radar Architecture

To verify the multi-mode radar techniques, a dual-band reconfigurable RF radar front-end architecture, depicted in Fig. 6.4, is proposed for demonstrative purposes and may differ from the final implemented architecture.

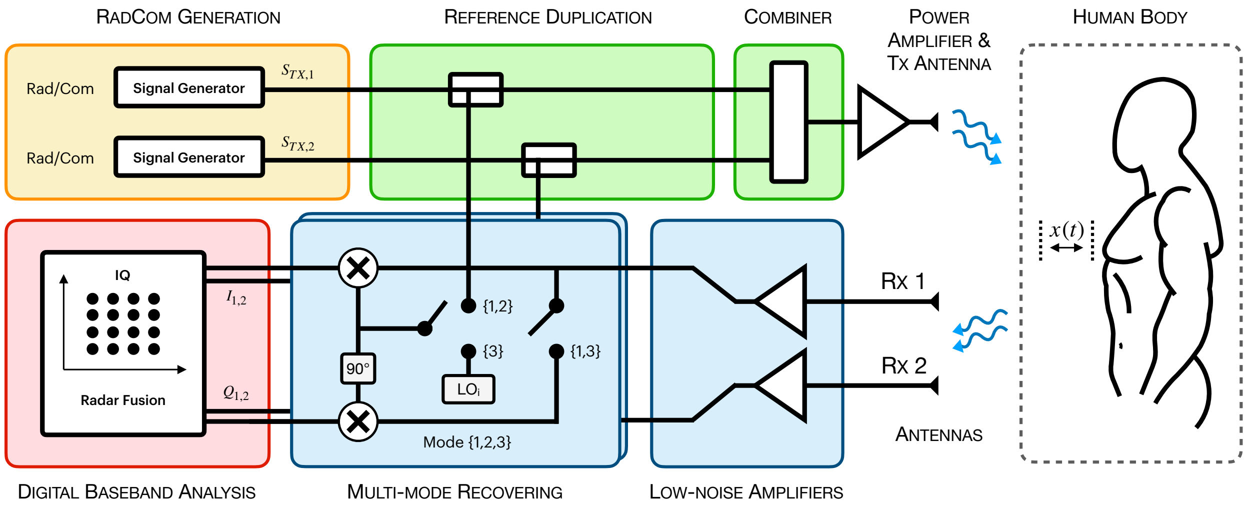

FIGURE 6.4 Block diagram of the multi-mode multi-band radar system from the RadCom signal generation to the digital baseband analysis with the human body.

First, two AWGs are employed to generate $S_{TX,1}$ and $S_{TX,2}$. These signals can either be radar waveforms (mode 1 and 2) or QAM signals (mode 3). A coupler is then used to keep a reference signal for the receiver, and the two main signals are combined and directed to the wideband PA and finally to the wideband horn antenna. In the experiments, $T_A = 20$ s and $T_B = 1$ ms.

After propagation, the received signals $S_{RX,1}$ and $S_{RX,2}$ are captured by two frequency-selective horn antennas. Then, these signals are demodulated in the multi-mode recovering block before digital analysis and multi-mode fusion techniques. The multi-mode recovering block consists of two selectors, two mixers and a 90° phase shifter. The LOs references are provided by the AWGs. The positions of the selectors depend on the selected mode. In mode 1 (phase radar), the RF incoming signal is mixed with its corresponding in-phase and quadrature references. In mode 2 (FMCW radar), the beat signal is straightforwardly retrieved by mixing the RF incoming signal with its time-varying in-phase chirp. In mode 3 (QAM communication), the RF QAM incoming signal is downconverted by the two mixers, powered by the LO. The AWGs drive this LO signal.

6.4.2 Measurements Results

Experimental measurements were conducted in our Poly-Grames labs to verify the operational viability of the proposed multi-mode multi-band radar technique. For that purpose, two high-frequency generators producing $S_{TX,1}$ and $S_{TX,2}$ are emitting the signals toward the human body, located 2 m in front of the antennas during the measurements, and the downconverted signals I_1/Q_1 and I_2/Q_2 are captured by the oscilloscope that samples the signals and transmits them to the Python program on the computer, as depicted in Fig. 6.5.

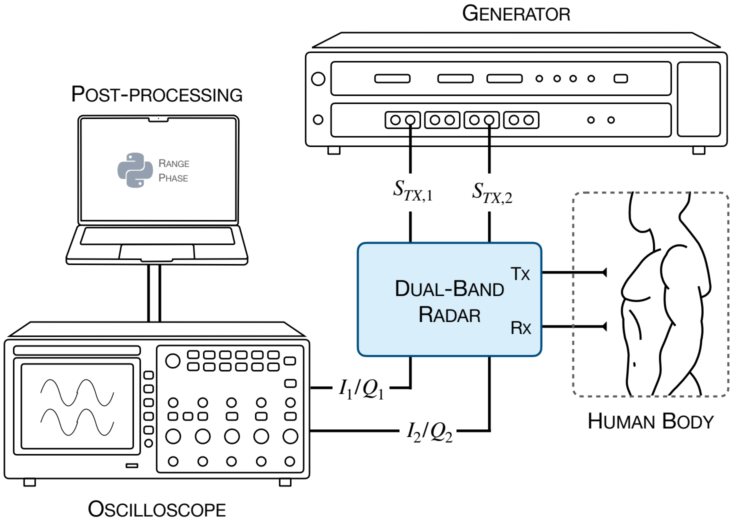

(a)

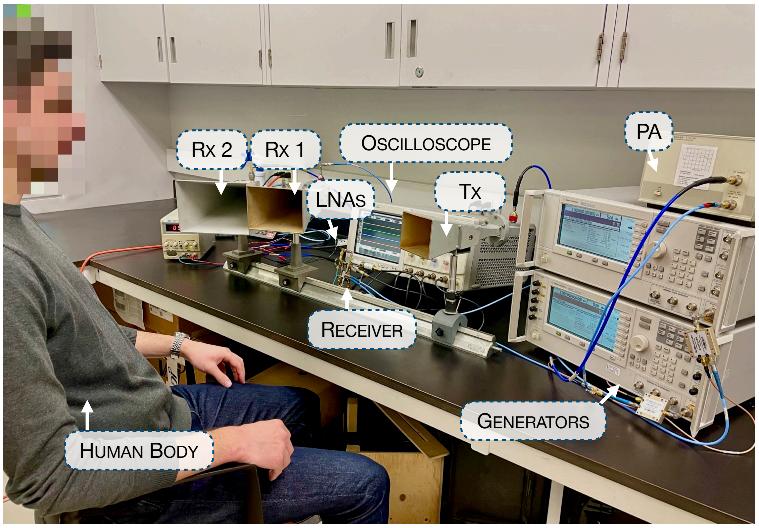

(b)

FIGURE 6.5 (a) Block diagram of the experimental setup and (b) corresponding real connections of the measurement setup. Dual-mode measurement is sequentially performed to retrieve the monitored human's position and respiration rate.

Fig. 6.6 plots the received phase shifted signals in mode 1 with carrier signals centered at f_{1i} $= 5$ GHz and $f_{2i} = 8$ GHz.

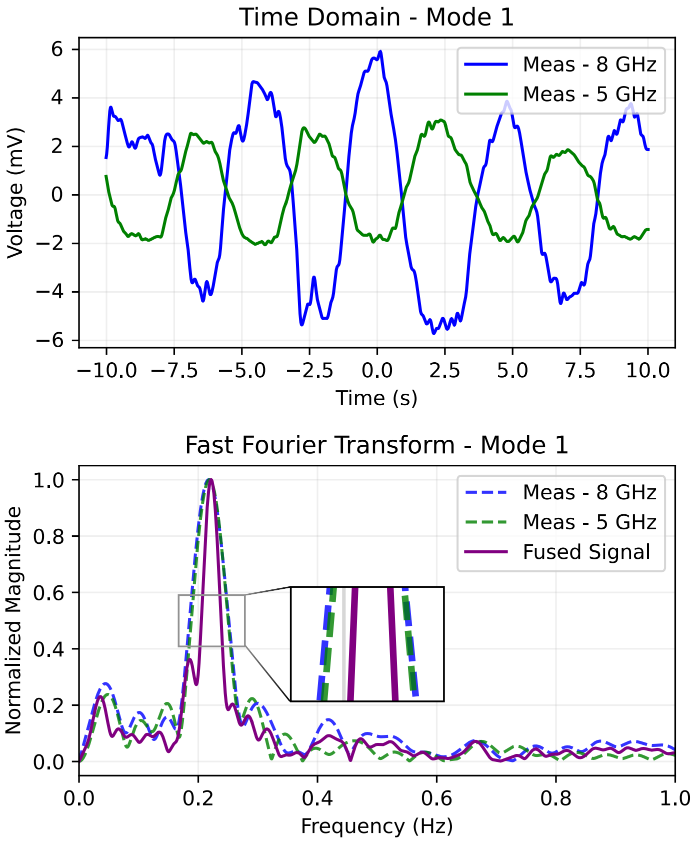

Figure 6.6 Time domain and FFT measurement results of the fusion of dual-carrier phase radar for respiration rate in mode 1.

The plotted signals are low pass filtered digitally and the mean DC value is removed. The time domain signal clearly depicts the respiration profile of the human target. Additional higher-frequency components likely stem from phase noise or minor subject movements. It is observed from the FFT (Hanning window) that the two individual signals are retrieving the main respiration frequency with similar accuracies (± 31.05 mHz @ 5 GHz and ± 32.80 mHz @ 8 GHz). The 8 GHz signal, exhibiting greater sensitivity than the 5 GHz signal, identifies smaller displacements ; yet, it is inadequate for detecting cardiac motion. Further iterations of this concept may introduce higher carrier frequencies to enable proper hearbeat detection. The fused signal, on the other hand, yields a frequency resolution of ± 15.50 mHz, twice as accurate as the resolution of the individual bands. Therefore, this validates the doubling effect of the observation time, resulting from the concatenation of the received signals.

Fig. 6.7 shows the results of the fusion procedure results in mode 2 with B_1, B_2 and $B_1 + B_2$.

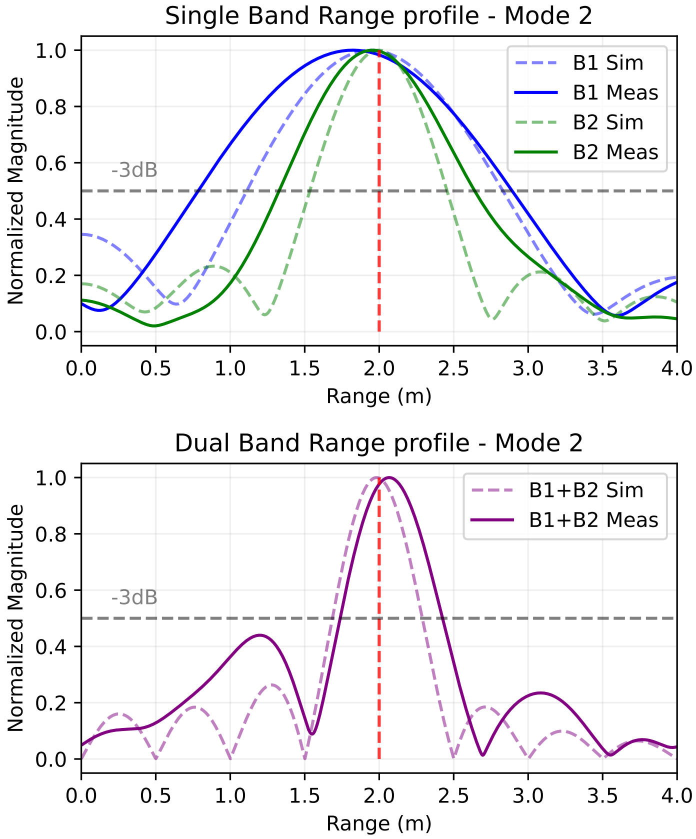

FIGURE 6.7 Comparison between simulated and measured range profiles with B_1 and B_2, individually, and the fusion of $B_1 + B_2$ in mode 2.

In this observation, the human target position is correctly retrieved with measured resolutions of δ_{r,B_1}= 211 cm, δ_{r,B_2}= 131 cm and $\delta_{r,B_{eq}}$= 68.7 cm. The measured range resolution was set to the -3dB width of the corresponding FFT's lobe.

Table 6.1 summarizes representative state-of-the-art healthcare radars and highlights that, to the best of our knowledge, this work is the only one combining multi-band radar fusion with ISAC capability.

Tableau 6.1 Comparison with State-of-the-Art Healthcare Radars

Ref	**Type and Band**	**ISAC**	**Note**
[229]	CW Doppler, 5.8 GHz	No	Compact quadrature radar sensor for cardiopulmonary monitoring
[230]	CW Doppler, 24 GHz	No	High-frequency six-port design with excellent sensitivity
[234]	FMCW, 134 GHz	No	Phased-array THz sensor
[161]	FMCW Fusion, 1, 2 and 3 GHz	No	Original multiband fusion procedure
[This work]	Multi-mode CW + FMCW, 5 & 8 GHz	Yes	Dual-mode fusion in both Doppler and range, unified RF chain with dedicated communication mode

6.5 Conclusion

Aiming to drastically expand the multifunction abilities of next-generation wireless systems, this work has presented and experimentally verified an innovative multi-mode multi-band radar technique featuring a phase radar multi-carrier fusion procedure for vital sign monitoring and a FMCW fusion procedure for enhancing the resolution with non-contiguous and scattered frequency bands in an adaptable and flexible hybrid multiplexing scheme. The proposed multifunction radar architecture enables bidirectional data communication with dedicated in-house radar networks. The measurements yield a respiration rate precision of ± 15.50 mHz and a relative position accuracy of 68.7 cm.

CHAPITRE 7 ARTICLE 6 : HARMONIC INTERFEROMETRIC RECEIVER FOR MULTIFUNCTION WIRELESS SYSTEMS

Thomas Micallef, Xiaoqiang Gu, Pascal Burasa et Ke Wu

Soumis à : *IEEE Transactions on Microwave Theory and Techniques*
Date de soumission : 10 Juillet 2025

7.1 Abstract

In next-generation wireless systems, harmonic diversity—across both sensing and communication functionalities—promises to redefine the design paradigm of RF receivers. This work proposes a four-port quad-band harmonic-responsive linear interferometric receiver capable of simultaneously performing multiband ISAC. The architecture leverages a hybrid multiplexing scheme up to the seventh odd harmonic of the design frequency to perform concurrent RF functionalities. Based upon a comprehensive theoretical framework, a proof-of-concept receiver is designed and fabricated to validate the architecture. Successful demodulation of up-to 128-QAM signals alongside multiband FMCW chirps, with desired performances at 2.75, 8.25, 13.75 and 19.25 GHz, demonstrate the feasibility and effectiveness of the approach. To the best of the author's knowledge, this is the very first up-to-the-seventh-harmonic multiband interferometric receiver that supports distinct RF functions simultaneously using a single, reusable circuit. Such harmonic expansion of the effective bandwidth of linear interferometric receivers is believed to have great potential in establishing of next-generation harmonically diverse wireless systems.

7.2 Introduction

Modern wireless systems increasingly demand multifunctional receivers that can support key RF functions, namely radar sensing, data communication, and WPT, within a unified platform [235, 236]. Indeed, ISAC techniques are poised to be combined with SWIPT concepts to meet the needs of 6G and above. For example, UWB systems have demonstrated simultaneous communication and radar operation over a shared aperture [237], while multiport front-ends can deliver dedicated power transfer alongside data reception. Interferometric multiport architectures have emerged as a promising approach for such tasks : they inherently offer wideband/multiband operation, low-power signal combining, reduced complexity and planar topologies, which are attractive for next-generation systems [54, 65, 66, 238–241].

Existing receiver solutions based on truly broadband front ends face fundamental challenges when supporting multifunction operations. Covering a very large bandwidth in one front end tends to increase design complexity, deteriorate the Noise Figure (NF) and reduce linearity, requiring high Analog-to-Digital Converter (ADC) sampling rates, sophisticated channelization, and increased power consumption [242, 243]. In the future, systems will often occupy several non-contiguous spectrum bands, e.g. carrier-aggregation in communications [244, 245] or multiband radars for enhanced resolution performances [161, 214, 246], rather than one continuous band. A conventional wideband receiver chain would have to process the entire frequency span, exacerbating interferer susceptibility and dynamic range requirements. These issues motivate receiver architectures that can selectively target multiple disjoint channels without incurring the penalties of a truly continuous multi-octave RF front-end.

An innovative approach is to leverage harmonic diversity and interferometric techniques to reuse hardware overheads across bands. Prior work has shown that harmonic components—usually considered unwanted—can be leveraged for spectrum-efficient operations [247], and enhancement of communication performances [248]. Previously published work [161] has demonstrated that sophisticated signal processing techniques can significantly increase range resolution in radar systems by leveraging the multiple IFs originating from multiband chirps. Additionally, it was previously shown that unwanted harmonics and DC resulting from the power detection can be filtered out and recycled for power harvesting to support SWIPT in interferometric receivers [26]. In this context, harmonic-responsive architectures offer a compelling method for enabling non-contiguous multiband reception using a unified analog front end without duplicating the RF chain. Appropriate candidates for such harmonic-responsive structures are six-, five- and four-port interferometric receivers, where their main difference is the number of outputs and baseband processing [249]. Four-port topologies are among the most straightforward types and they provide excellent performances in diverse applications [250, 251]. While widely used, six-port receivers require four ADCs, limiting their suitability for ultra-low-power applications. In contrast, four-port topologies need only two ADCs, effectively halving power consumption.

In pursuit of this goal, a quad-band, low-power, four-port linear harmonic interferometric receiver based on quarter-wavelength networks is proposed. The proposed receiver architecture operates simultaneously around odd harmonics of f_0, up to the seventh order, at 2.75, 8.25, 13.75 and 19.25 GHz. Based upon preliminary theoretical analysis, a proof-of-concept architecture employing quarter-wave Wilkinson Power Dividers (WPDs) to combine the received RF and reference harmonic signals in a passive manner is prototyped and tested under several operating conditions and modulation orders. This harmonic interferometric receiver can thus down-convert four non-contiguous harmonic channels concurrently in hardware without added complexity or power consumption. In addition, a hybrid harmonic multiplexing scheme is employed to interplay radar sensing and data communication functionalities over time and frequency. Furthermore, a flexible baseband recovery procedure to seamlessly integrate radar and communication functions is presented. On the other hand, in communication mode, the IFs are managed independently, guaranteeing the integrity of every data stream that is captured.

The presented work begins with an overview of the proposed hybrid multiplexing scheme alongside the radar and communication equations and the multifunction baseband recovery methodology in Section II. This leads to a theoretical analysis of the overall four-port receiver, up to the seventh harmonic in Section III. Section IV details the system-level implementation and presents the fabricated prototype. Following this, the experimental verification is conducted in Section V to assess and compare the performances of the proposed receiver. The conclusions are drawn in Section VI.

7.3 Multifunction Through Time And Harmonic Frequency Multiplexing

7.3.1 Hybrid Harmonic Multiplexing

Along with the CDM, other conventional multiplexing methods that usually lack the flexibility required to dynamically adapt to shifting operating requirements are FDM and TDM [252]. This work proposes a hybrid harmonic multiplexing scheme that allows for a dynamic assignment of radar and communication functions across multiple harmonic frequency bands and time slots to get around this limitation. At the same time, power transfer may be implemented by harvesting out-of-band signals and produced harmonics and DC in the demodulation process [106]. The proposed multifunction-ready hybrid scheme is depicted in Fig. 7.1.

Such a scheme allows full flexibility between radar and communication mode, integrating the concepts of FDM and TDM within the same structure while leveraging harmonic capacities.

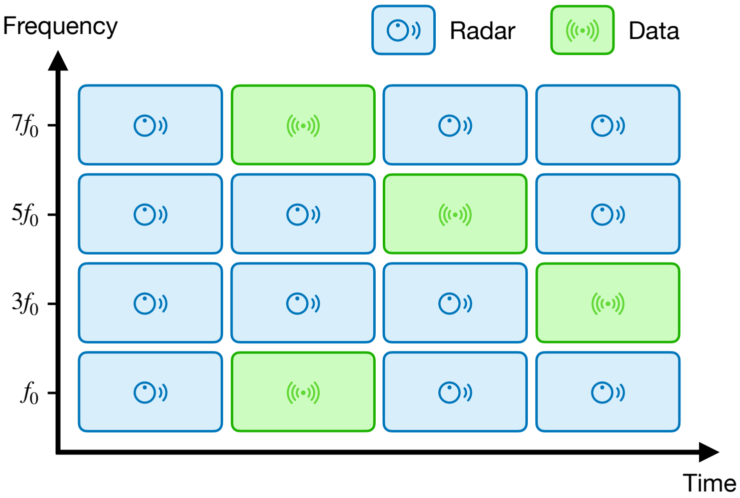

FIGURE 7.1 Hybrid harmonic multiplexing scheme for multiband radar sensing and data communication.

Therefore, scattered radar chirps can operate simultaneously during a predefined time slot while data flow is being captured.

7.3.2 Theoretical Analysis of Four-Port Receiver

The ideal behavior of the four-port correlator consists of the linear additive mixing of LO and RF signals with either no phase shift or quarter-phase shift for either in-phase or quadrature I/Q ports, respectively. Such a four-port correlator is illustrated in Fig.7.2.

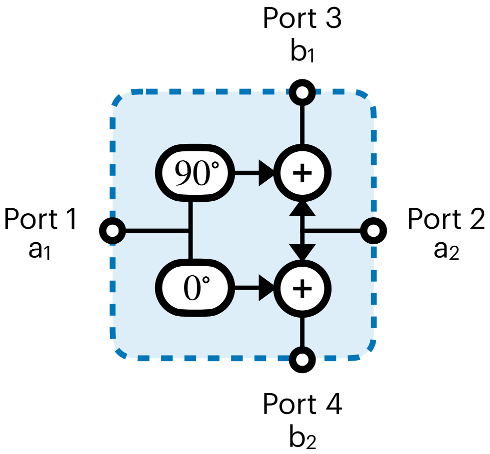

FIGURE 7.2 Simplified four-port receiver block diagram.

The scattering matrix $[S]$ for an ideal quadrature four-port network, as shown in Fig. 7.2, can be written as :

$$[S] = \frac{1}{\sqrt{2}} \begin{bmatrix} 0 & 0 & j & 1 \\ 0 & 0 & 1 & 1 \\ 0 & 0 & 0 & 0 \\ 0 & 0 & 0 & 0 \end{bmatrix} \tag{7.1}$$

In FMCW mode, the inputs $a_1(t)$ and $a_2(t)$ can be described as follows :

$$\begin{aligned} a_1(t) &= A_1 e^{j2\pi f_1 t} \\ a_2(t) &= A_2 e^{j2\pi f_2 t} \end{aligned} \tag{7.2}$$

where A_1, A_2, f_1 and f_2 are the amplitudes and frequencies of the signals, respectively. Following this, the outputs $b_1(t)$ and $b_2(t)$ can be expressed as :

$$b_1(t) = S_{31}a_1 + S_{32}a_2 = \frac{1}{\sqrt{2}} \left(jA_1 e^{j2\pi f_1 t} + A_2 e^{j2\pi f_2 t} \right) \tag{7.3}$$

$$b_2(t) = S_{41}a_1 + S_{42}a_2 = \frac{1}{\sqrt{2}} \left(A_1 e^{j2\pi f_1 t} + A_2 e^{j2\pi f_2 t} \right) \tag{7.4}$$

In multi-port networks, power detectors are usually employed at the outputs to retrieve the average power of $b_1(t)$ and $b_2(t)$. After power detection and low-pass filtering, useful components are contained in $V_1(t)$ and $V_2(t)$ at ports 3 and 4, respectively, such as :

$$V_i(t) = \beta b_i b_i^* \tag{7.5}$$

where β is the voltage sensitivity of the power detectors and b_i^* is the complex conjugates of b_i. After some treatments,

$$V_1(t) = \beta \left(\frac{A_1^2}{2} + \frac{A_2^2}{2} - A_1 A_2 \sin(2\pi(f_1 - f_2)) \right) \tag{7.6}$$

$$V_2(t) = \beta \left(\frac{A_1^2}{2} + \frac{A_2^2}{2} + A_1 A_2 \sin(2\pi(f_1 - f_2)) \right) \tag{7.7}$$

Note that in the assumption of a lossless network, the total output power is equal to the total input power, such as :

$$|b_1|^2 + |b_2|^2 = A_1^2 + A_2^2 \tag{7.8}$$

Consequently, $V_1(t)$ and $V_2(t)$ oscillate around their respective mean value with opposite phases due to the 90° phase shift inside the network. For the FMCW mode, the retrieved beat signal corresponds to the term $\sin(2\pi(f_1 - f_2))$, where the frequency is proportional to the target's range.

In the I/Q communication mode, the inputs can be replaced by [253] :

$$a_1(t) = A_1 e^{j2\pi f_1 t} \tag{7.9}$$

$$a_2(t) = A_2 m(t) e^{j2\pi f_1 t} \tag{7.10}$$

where $m(t) = I(t) + jQ(t)$ is the I/Q transmit bit. After some treatments, $V_1(t)$ and $V_2(t)$ become :

$$V_1(t) = \frac{\beta}{2} \left(A_1^2 + A_2^2 (I(t)^2 + Q(t)^2) + 2A_1 A_2 I(t) \right) \tag{7.11}$$

$$V_2(t) = \frac{\beta}{2} \left(A_1^2 + A_2^2 (I(t)^2 + Q(t)^2) + 2A_1 A_2 Q(t) \right) \tag{7.12}$$

Furthermore, (7.11) and (7.12) can be written as :

$$\frac{2V_1}{\beta A_2^2} = Q(t)^2 + \left(I(t) + \frac{A_1}{A_2} \right)^2 \tag{7.13}$$

$$\frac{2V_2}{\beta A_2^2} = I(t)^2 + \left(Q(t) + \frac{A_1}{A_2} \right)^2 \tag{7.14}$$

In the assumption that $\sqrt{I(t)^2 + Q(t)^2} \leq 1$ and $A_1 < A_2$, I and Q can be calculated by [249] :

$$I = \frac{1}{2A_1A_2}\left(\alpha + \sqrt{-\alpha^2 + 16V_2A_1}\right) \tag{7.15}$$

$$Q = \frac{1}{2A_1A_2}\left(-\alpha - 2A_1^2 + \sqrt{-\alpha^2 + 16V_2A_1}\right) \tag{7.16}$$

where $\alpha = 4V_1 - 4V_2 - A_1^2$. In practice, to correctly retrieve the QAM signals, the LO frequency in (7.9) may be shifted to f_1' leading to a communication baseband signal around $f_1 - f_1'$.

7.3.3 Baseband Recovery

The output ports b_1 and b_2 in the above-described four-port network are used as the baseband outputs for both FMCW radar and communication modes. These ports supply the I/Q components in communication mode, allowing for baseband signal recovery. In FMCW mode, the receive chirp with delay—which is reflected from a target—is captured at port 2 as a_2, and the reference chirp is injected at port 1 as a_1. The IF beat signal, which contains target range and velocity information, is represented by the resulting beat signals as $V_1(t)$ and $V_2(t)$. Leveraging the hybrid multiplexing scheme, both radar and communication functions share these baseband outputs simultaneously in Frequency Domain Diplexing (FDD), necessitating exact IF signal separation to guarantee independent processing of each functionality. Fig. 7.3 shows the frequency spectrum of $a_{1,2}$ and $V_{1,2}$ in the hypothetical case of three distinct FMCW operations around f_1, f_2 and f_3 and a communication signal around f_4.

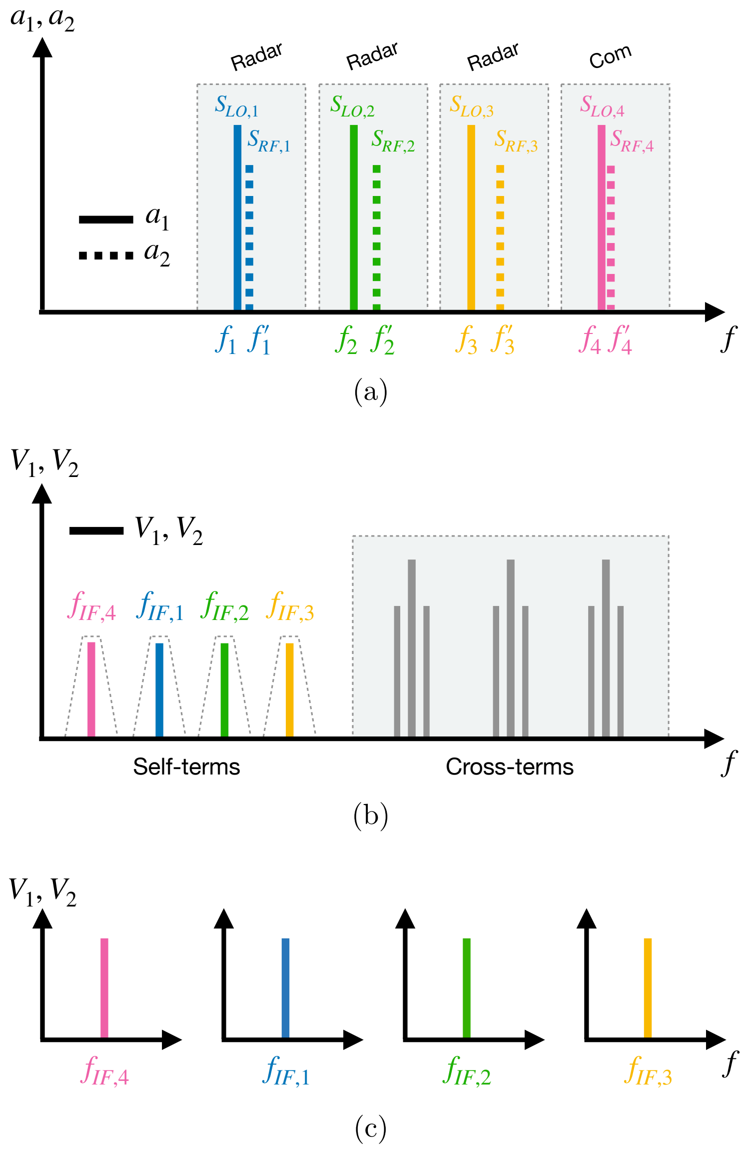

FIGURE 7.3 (a) RF input signals a_1 and a_2, and (b) output signals V_1 and V_2 in the frequency domain. (c) Retrieved IFs can be separated successfully. in the numerical domain, after numerical filtering. Only low-frequency components are kept for baseband processing, while high-frequency and DC components are rejected.

In such cases, $S_{LO,1,2,3}(t)$ and $S_{RF,1,2,3}(t)$ are the transmitted and received FMCW signals, respectively, of the three chirps and $S_{LO,4}(t)$ and $S_{RF,4}(t)$ are the local oscillator and captured external communication signal, respectively. At the receiver, the resulting signal S writes :

$$S(t) = \sum_{m=1}^{4} S_{L0,m}(t) + \sum_{m=1}^{4} S_{RF,m}(t) \tag{7.17}$$

where $S_{LO,m}(t) = \cos(2\pi f_m t)$ and $S_{RF,m}(t) = \cos(2\pi f'_m t)$. Unitary amplitudes are assumed for clarity. The power detector considered in this work is based on a zero-bias Schottky diode, and its current (I) – voltage (V) characteristics may be expressed by [185] :

$$I = I_S \left(e^{\frac{V_{\text{on}}}{nV_t}} - 1 \right) \tag{7.18}$$

where I_S is the saturation current, V_{on} is the voltage applied across the diode, n is the ideality factor and V_t is the thermal voltage. In the approximation of a small input signal power, (7.18) can be approximated by :

$$I \approx I_S \sum_{k=1}^{\infty} \left(\frac{V_{\text{on}}^k}{k!(nV_t)^k} \right) \tag{7.19}$$

By replacing V_{on} by the sum signal S, the first terms of (7.19) are :

$$\begin{aligned} I(t) \approx \frac{I_s}{nV_t} & \left(\sum_{m=1}^{4} S_{L0,m}(t) + \sum_{m=1}^{4} S_{RF,m}(t) \right) + \\ & \frac{I_s}{2(nV_t)^2} \left(\sum_{m=1}^{4} S_{L0,m}(t) + \sum_{m=1}^{4} S_{RF,m}(t) \right)^2 + \\ & \qquad \frac{I_s}{6(nV_t)^3} \left(\sum_{m=1}^{4} S_{L0,m}(t) + \sum_{m=1}^{4} S_{RF,m}(t) \right)^3 + \dots \end{aligned} \tag{7.20}$$

The first order term with factor I_S/nV_t contains the frequencies f_m and f'_m. Then, the second order term with factor $I_S/2(nV_t)^2$ contains the DC and the second harmonic frequencies $2f_m$ and $2f'_m$. It also contains the difference frequencies $f_m - f'_n$ and the sum frequencies $f_m + f'_n$ with factor 1/2. Finally, the third order with factor $I_S/6(nV_t)^6$ contains the third harmonics $3f_m$ and $3f'_m$ and intermodulation products such as $2f_m - f'_n$, $2f'_n - f_m$, etc. Higher orders are considered negligible in this work.

After low-pass filtering, the normalized wanted baseband signal can be written as $S_{bb}(t)$:

$$S_{bb}(t) \approx \frac{I_s}{4(nV_t)^2} \sum_{m=1}^{4} \cos(2\pi(f_m - f'_m)t) \tag{7.21}$$

Note that this technique, by nature, does not allow the usage of equal or close bandwidths for the FMCW chirps. Indeed, identical bandwidths would result in the same beat signal frequency, therefore not allowing any further baseband separation. Additionally, if the bandwidths are too close, resulting in close beat signal frequencies, the baseband filtering would be highly challenging. As a design criterion, the bandwidths should remain distinct enough. Regarding the communication mode, its IF frequency bandwidth is related to the symbol rate and modulation type. In the usage of such multi-port architecture for baseband recovery, all the IF signals of interest should be distinguishable in the output frequency spectrum.

7.3.4 Numerical Filtering

A key element of this baseband procedure is the ability to distinguish IF signals in the output spectrum. Indeed, the IF filtering should be adaptive to accommodate changing chirps' bandwidths or communication modulations in terms of bandwidths or center IF frequency. Two types of filtering may be employed in this scenario, namely, reconfigurable analog filters [254] or numerical filters [255]. For analog filters, the main drawbacks are their physical implementation, which can be of considerable size and be challenging. The proposed baseband recovery procedure leverages numerical filters to separate the different IF signals, as illustrated in Fig. 7.3. While numerous numerical filters are available for baseband procedures within libraries from Python, such an implementation offers several advantages, such as reconfigurability and the ability to process complex modulations and fusion techniques. TABLE 7.1 summarizes the main numerical filters that qualify for the proposed baseband procedure regarding roll-off speed, passband/stopband ripples and linear phase shift.

Tableau 7.1 Main Numerical Band-Pass Filters

Filter	**Roll-off Speed**	**Passband Ripple**	**Stopband Ripple**	**Linear Phase**	**Use Cases**
Butterworth	Medium	No	No	No	General use
Chebyshev I	Fast	Yes	No	No	Sharper filtering
Chebyshev II	Fast	No	Yes	No	Clean passband
Elliptic	Fastest	Yes	Yes	No	Tight bandwidth
Bessel	Slow	No	No	Yes	Waveform integrity

Although a relatively fast roll-off speed may be necessary if the bandgap between consecutive IFs is highly narrow, for the intended use scenarios, the most relevant characteristics are the linear phase and passband ripples. Fig. 7.4 presents a comparison between the frequency responses of the main 5^{th}-order numerical bandpass filters. The bandpass is set to $f_0 \pm 10\%$.

For the Chebyshev I and Elliptic ones, a maximum passband ripple of 0.5 dB is selected.

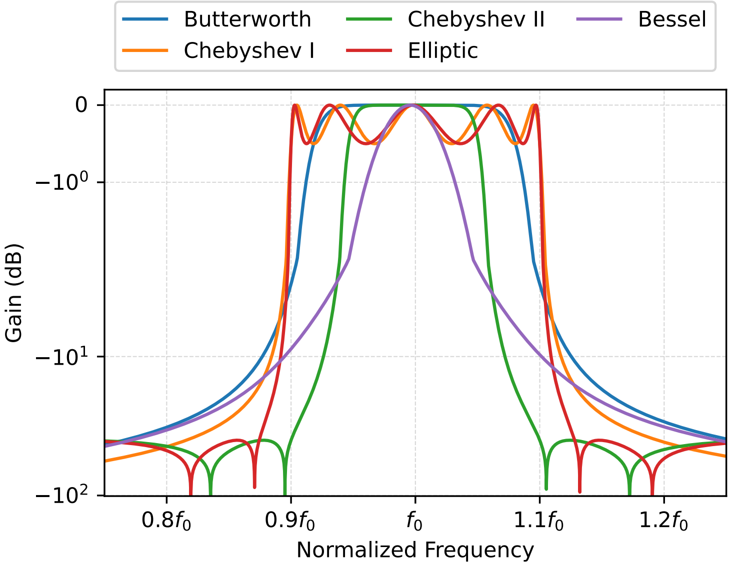

FIGURE 7.4 Frequency responses of the main 5^{th}-order numerical bandpass filters.

Passband ripples present inherent drawbacks for FMCW beat signal recovery, as they may introduce additional modulation-like components in the retrieved time-domain waveform, potentially leading to oscillations that may falsely suggest the presence of multiple closely spaced targets. Due to such limitations, a numerical Bessel bandpass filter is selected in this work to ensure waveform integrity.

7.4 Harmonic Multi-Port Architecture

7.4.1 Harmonic Power Divider

To enable multiband harmonic behavior of the four-port receiver, this work leverages the physical characteristics of a traditional Wilkinson power divider. Indeed, such a divider employs quarter-wavelength arms of the fundamental frequency and an isolation resistor to divide the input power of port 1 to ports 2 and 3, as illustrated in Fig. 7.5a. As a result, every odd harmonic of the fundamental frequency is theoretically susceptible to being employed within the same structure.

A harmonically extended odd-even mode analysis can be conducted to verify the harmonic behavior of the divider, taking advantage of the intrinsic symmetry of the divider, as depicted in Figs. 7.5b and 7.5c. Throughout the analysis, $Z_{50} = 50\Omega$, $Z_1 = \sqrt{2}Z_{50}$ and $R = 100\ \Omega$.

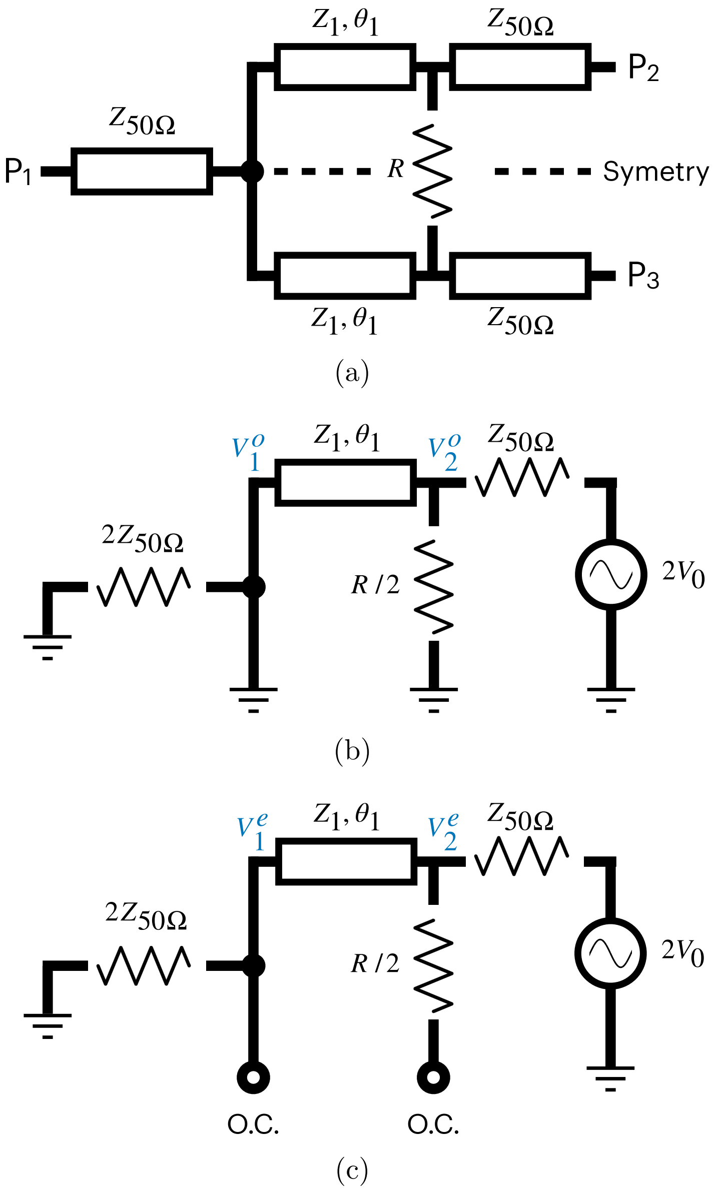

FIGURE 7.5 (a) Topology of the Wilkinson power divider ; (b) Odd- and (c) even-mode equivalent circuits.

Even Mode

Along the microstrip arms, with $x = 0$ at port 1, the voltage can be expressed as :

$$V(x) = V^+ \left(e^{-j\beta x} + \Gamma e^{j\beta x}\right) \tag{7.22}$$

where V^+ is a constant voltage and Γ is the reflection coefficient :

$$\Gamma = \frac{2Z_{50} - Z_1}{2Z_{50} + Z_1} = \frac{2 - \sqrt{2}}{2 + \sqrt{2}} \tag{7.23}$$

At the fundamental frequency, the lengths of the arms are $\lambda/4$, thus $V_2^e\Big|_{f_0}$ writes :

$$V_2^e\Big|_{f_0} = V\left(-\frac{\lambda}{4}\right) = jV^+[1 - \Gamma] = V_0 \tag{7.24}$$

Similarly, $V_1^e\Big|_{f_0}$ can be expressed as :

$$V_1^e\Big|_{f_0} = V(0) = V^+[1 + \Gamma] = jV_0\frac{\Gamma + 1}{\Gamma - 1} \tag{7.25}$$

Combining (7.24) and (7.25) gives :

$$V_1^e\Big|_{f_0} = -j\sqrt{2}V_0 \tag{7.26}$$

For the third harmonic, the lengths of the arms are $3\lambda/4$, thus $V_2^e\Big|_{3f_0}$ becomes :

$$V_2^e\Big|_{3f_0} = V\left(-\frac{3\lambda}{4}\right) = -jV^+[1 - \Gamma] = V_0 \tag{7.27}$$

Similar to (7.25), $V_1^e\Big|_{3f_0}$ writes :

$$V_1^e\Big|_{3f_0} = -jV_0\frac{\Gamma + 1}{\Gamma - 1} \tag{7.28}$$

(7.28) can be rewritten as :

$$V_1^e\Big|_{3f_0} = j\sqrt{2}V_0 \tag{7.29}$$

The fifth and seventh harmonics appear in a cycle where the fifth harmonic has the same behavior as the first harmonic, and the seventh harmonic has the same behavior as the third harmonic. This can be summarized as follows :

$$V_2^e\Big|_{5f_0} = V_2^e\Big|_{f_0} \tag{7.30}$$

$$V_1^e\Big|_{5f_0} = V_1^e\Big|_{f_0} \tag{7.31}$$

$$V_2^e\Big|_{7f_0} = V_2^e\Big|_{3f_0} \tag{7.32}$$

$$V_1^e\Big|_{7f_0} = V_1^e\Big|_{3f_0} \tag{7.33}$$

Odd Mode

The voltages V_2^o and V_1^o can be straightforwardly deduced from Fig. 7.5b :

$$V_2^o\Big|_{f_0,3f_0,5f_0,7f_0} = V_0 \tag{7.34}$$

$$V_1^o\Big|_{f_0,3f_0,5f_0,7f_0} = 0 \tag{7.35}$$

Based upon previous calculations, the transmission coefficient from port 1 to port 2 (or port 3), across odd harmonics (n=1,3,5,7) can be computed via :

$$S_{21}|_{nf_0} = \frac{V_1^e|_{nf_0} + V_1^o|_{nf_0}}{V_2^e|_{nf_0} + V_2^o|_{nf_0}} \tag{7.36}$$

Hence,

$$S_{21}\Big|_{f_0,5f_0} = -\frac{j}{\sqrt{2}} \tag{7.37}$$

$$S_{21}\Big|_{3f_0,7f_0} = \frac{j}{\sqrt{2}} \tag{7.38}$$

Additionally, the input impedance Z_{IN}^e (port 1) and output impedance Z_{OUT}^e, across all odd harmonics, are expressed as :

$$Z^e_{\mathrm{IN}} = Z^e_{\mathrm{OUT}} = \sqrt{\frac{1}{2}Z_1^2} = \frac{Z_1}{\sqrt{2}} = Z_{50} \tag{7.39}$$

In contrast, Z^o_{IN} and Z^o_{OUT} differ from Z_{50}, hence the ports are not matched. The above results can finally be summarized in the following scattering matrixes :

$$[S]_{f_0,5f_0} = -\frac{1}{\sqrt{2}}\begin{bmatrix} 0 & j & j \\ j & 0 & 0 \\ j & 0 & 0 \end{bmatrix} \tag{7.40}$$

$$[S]_{f_0,5f_0} = \frac{1}{\sqrt{2}}\begin{bmatrix} 0 & j & j \\ j & 0 & 0 \\ j & 0 & 0 \end{bmatrix} \tag{7.41}$$

From (7.40) and (7.41), theoretically, every odd harmonic of the fundamental frequency may employ the same dividing structure. As a result, at f_0, $3f_0$, $5f_0$ and $7f_0$, the power dividing ratio remains constant at -3 dB between ports 2 and 3. However, the phase conditions are different :

$$\varphi_{S_{21}}\Big|_{f_0,5f_0} - \varphi_{S_{21}}\Big|_{3f_0,7f_0} = \pi \tag{7.42}$$

Note that the previous demonstration can be extended further than the seventh harmonic. In practice, due to insertion losses, dispersion and nonlinear substrate effects, the behavior is expected to be degraded at high-order harmonics.

7.4.2 Overall Architecture

Fig. 7.6 shows the overall four-port harmonic architecture, including four harmonic Wilkinson power dividers, a 90° phase shifter and a pair of diode-based power detectors.

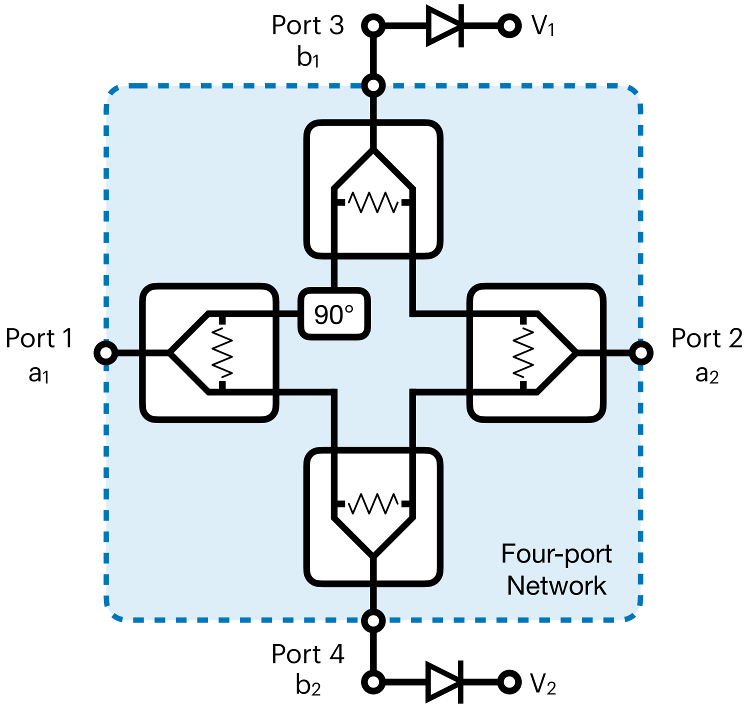

FIGURE 7.6 Overall four-port harmonic receiver block diagram.

As demonstrated in the previous section, Wilkinson power dividers are inherently harmonic-responsive as they are based on quarter-wavelength physical dimensions. Hence, the overall four-port receiver will provide favorable results at its fundamental frequency f_0, but also around its odd harmonics $3f_0$, $5f_0$, $7f_0$, etc.

To provide accurate measurements in I/Q demodulation, the 90° phase shifter is designed to be an additional transmission line of length $\lambda_0/4$. By nature, compared to a fixed transmission line of length L, an extended line of length $L + \lambda_0/4$ will provide a 90° phase shift due to $\Delta L = L+\lambda_0/4-L = \lambda_0/4$, modulo π, at every odd harmonic of f_0. Indeed, assuming constant phase velocity, the phase shift φ induced by a lengthy transmission line can be expressed as :

$$\varphi = \frac{2\pi}{\lambda}\Delta L \tag{7.43}$$

The general rule for odd harmonics $f = (2n + 1) \times f_0$ becomes :

$$\varphi = \frac{2\pi}{\frac{\lambda_0}{2n+1}}\frac{\lambda_0}{4} = (2n+1)\frac{\pi}{2} \equiv \frac{\pi}{2}[\pi] \tag{7.44}$$

Thus, the phase shifts at f_0, $3f_0$, $5f_0$, $7f_0$ are $\pi/2$, $3\pi/2$, $5\pi/2$ and $7\pi/2$, respectively. In the assumption that all ports are fully matched and ignoring losses, one can give the transmission coefficients of the four-port receiver with respect to the unique phase shifts of odd harmonics. Regarding S_{31} and S_{32} :

$$S_{31}\Big|_{f_0,5f_0} = j\left(-\frac{j}{\sqrt{2}}\right)^2 = -\frac{j}{2} \tag{7.45}$$

$$S_{32}\Big|_{f_0,5f_0} = \left(-\frac{j}{\sqrt{2}}\right)^2 = -\frac{1}{2} \tag{7.46}$$

$$S_{31}\Big|_{3f_0,7f_0} = -j\left(\frac{j}{\sqrt{2}}\right)^2 = \frac{j}{2} \tag{7.47}$$

$$S_{32}\Big|_{3f_0,7f_0} = \left(\frac{j}{\sqrt{2}}\right)^2 = -\frac{1}{2} \tag{7.48}$$

Regarding S_{41} and S_{42} :

$$S_{41}\Big|_{f_0,5f_0} = \left(-\frac{j}{\sqrt{2}}\right)^2 = -\frac{1}{2} \tag{7.49}$$

$$S_{42}\Big|_{f_0,5f_0} = \left(-\frac{j}{\sqrt{2}}\right)^2 = -\frac{1}{2} \tag{7.50}$$

$$S_{41}\Big|_{3f_0,7f_0} = \left(\frac{j}{\sqrt{2}}\right)^2 = -\frac{1}{2} \tag{7.51}$$

$$S_{42}\Big|_{3f_0,7f_0} = \left(\frac{j}{\sqrt{2}}\right)^2 = -\frac{1}{2} \tag{7.52}$$

In an interferometric receiver, the relative phase shift between ports 3 and 4 is more critical than their individual absolute phase values. Indeed, across all odd harmonics, $\varphi_{S_{31}} - \varphi_{S_{41}}$ should remain at $\pi/2$ modulo π. In the proposed scenario :

$$\varphi_{S_{31}} - \varphi_{S_{41}}\Big|_{f_0,5f_0} = -\frac{\pi}{2} + \pi = \frac{\pi}{2} \tag{7.53}$$

$$\varphi_{S_{31}} - \varphi_{S_{41}}\Big|_{3f_0,7f_0} = \frac{\pi}{2} + \pi = -\frac{\pi}{2} \tag{7.54}$$

Finally, it is shown that, across all odd harmonics of f_0, the harmonic four-port receiver maintains consistent phase shift conditions that enable proper linear mixing of the signals. Note that, assuming ideal isolation, for all odd harmonics, $S_{21} = S_{12} = 0$ and $S_{11} = S_{22} = S_{33} = S_{44} = 0$. Also, by symmetry, $S_{31} = S_{13}$, $S_{41} = S_{14}$, $S_{32} = S_{23}$ and $S_{42} = S_{24}$. The overall lossless scattering matrices of the four-port receiver may then be written as :

$$[S]_{f_0.5f_0} = -\frac{1}{2}\begin{bmatrix} 0 & 0 & j & 1 \\ 0 & 0 & 1 & 1 \\ j & 1 & 0 & 0 \\ 1 & 1 & 0 & 0 \end{bmatrix} \tag{7.55}$$

$$[S]_{3f_0,7f_0} = -\frac{1}{2}\begin{bmatrix} 0 & 0 & -j & 1 \\ 0 & 0 & 1 & 1 \\ -j & 1 & 0 & 0 \\ 1 & 1 & 0 & 0 \end{bmatrix} \tag{7.56}$$

7.4.3 Losses

For microstrip lines, the dielectric losses α_d are the most predominant losses and are linearly dependent on the frequency f_0, and can be expressed as [256] :

$$\alpha_d = \frac{\pi f_0 \sqrt{\varepsilon_r}}{c} \tan\delta \tag{7.57}$$

where ϵ_r is the relative permittivity of the substrate, c is the speed of light and $\tan\delta$ is the loss tangent of the substrate. For each harmonic, the dielectric losses increase with the harmonic index, such as :

$$\alpha_d\Big|_{7f_0} = \frac{7}{5}\alpha_d\Big|_{5f_0} = \frac{7}{3}\alpha_d\Big|_{3f_0} = 7\alpha_d\Big|_{f_0} \tag{7.58}$$

Hence, to minimize the dielectric losses in the circuit, a substrate with a low relative permittivity and a low loss tangent must be selected.

7.5 System Level Implementation

7.5.1 Design and Analysis of Individual Circuits

To fulfil the requirements of the compact harmonic power division, a mono-section quarter-wavelength Wilkinson power divider is considered in this work, as illustrated in Fig. 7.5a. The electrical length θ_1 is fixed at 90° for the center frequency of 2.75 GHz, $Z_1 = \sqrt{2}Z_{50} = 70.7$ Ω and $R_1 = 100$ Ω.

The fabricated circuit is settled on ROGERS RT/Duroid 6002 with 20-mil thickness and a relative permittivity ϵ_r of 2.94. Hence, the optimized physical parameters, in mm, are $w_{50\,\Omega}$ $= 1.287$, $w_1 = 0.71$ and $l_1 = 16.17$. The resistors are in a 0402 package.

The S-parameter results comparison between simulation and actual measurements is shown in Fig. 7.7.

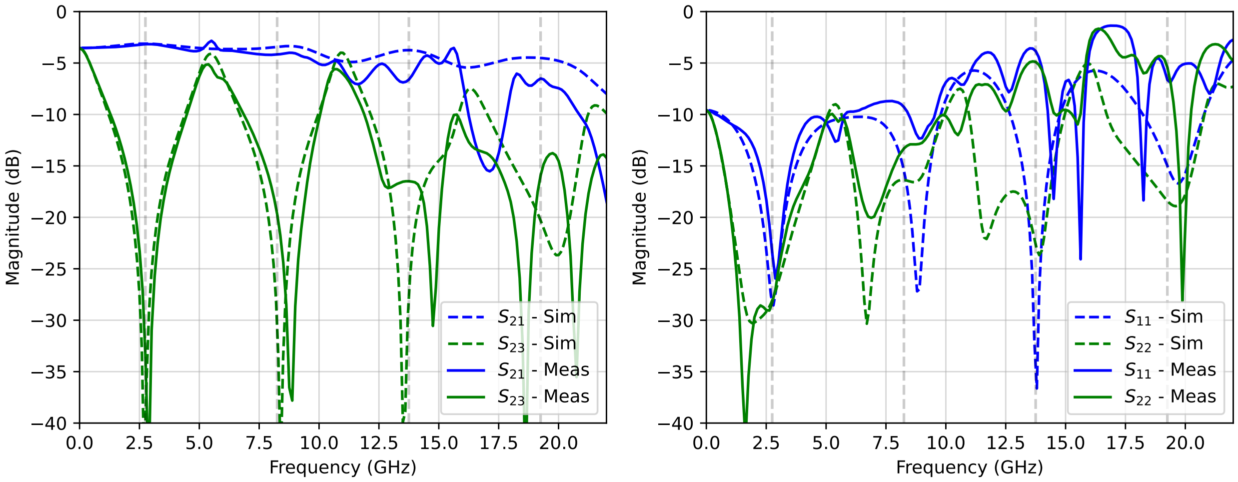

(a) (b)

FIGURE 7.7 Simulated and measured S-parameters (a) S_{21} and S_{23} (b) S_{11} and S_{22}. The dashed lines mark the harmonics.

Regarding transmission coefficients, the power divider exhibits acceptable performances, with measured insertion losses of -3.3 dB at f_0, -4.3 dB at $3f_0$, and -6.7 dB at $5f_0$ and $7f_0$. The output port isolation is below -15 dB, which is satisfactory. The poorer insertion losses at $5f_0$ and $7f_0$ may be explained by the parasitics of the 0402 SMD resistor–not negligible at high frequency–and the degradation of reflection losses at the input port around fifth and seventh harmonics. Overall, such a Wilkinson power divider can be employed up to its seventh harmonic.

Then, at ports 3 and 4 of Fig. 7.6, the power detectors are used to realize a nonlinear mixing of the input signals. The topology of the proposed harmonic power detector is depicted in Fig. 7.8, which consists of tapered lines to match the input and output impedance of the diode to the 50 Ω lines and a zero-bias Schottky diode.

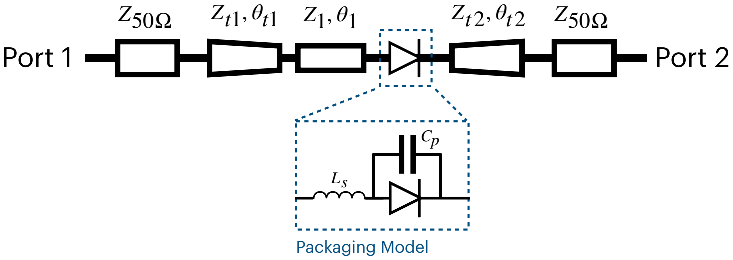

FIGURE 7.8 Topology of the diode based harmonic power detector.

Those matching networks are essential to allow more RF power to be converted and thus enhance the performance of the receiver. In the system-level implementation, a low-pass filter is used to retain the low-frequency components.

The diode employed is the SMS7630-079LF from Skyworks, and to accurately predict the behavior of the power detector, the parasitic components of the diode's packaging are simulated with the values provided in the datasheet : $L_s = 0.7$ nH and $C_p = 0.16$ pF. The key SPICE parameters of the diode are $C_{j0} = 0.14$ pF, $I_S = 5$ uA, $R_S = 20$ Ω, $n = 1.05$, $M = 0.4$ and $V_j = 0.34$ V. After optimization, the line impedances are Z_{t1} from $Z_{50\,\Omega}$ to Z_1, $Z_1 = 128.5$ Ω, Z_{t2} from 84.6 Ω to $Z_{50\,\Omega}$. With the RT/Duroid 6002, the optimized physical parameters, in mm, are w_{t1} from $w_{50\,\Omega}(1.287)$ to w_1, $w_1 = 0.17$, w_{t2} from 0.5 to $w_{50\,\Omega}$, $l_{t1} = 4.18$, $l_1 = 12.7$ and $l_{t2} = 22.2$.

Fig. 7.9 presents a comparison between simulated and measured input reflection coefficients S_{11}.

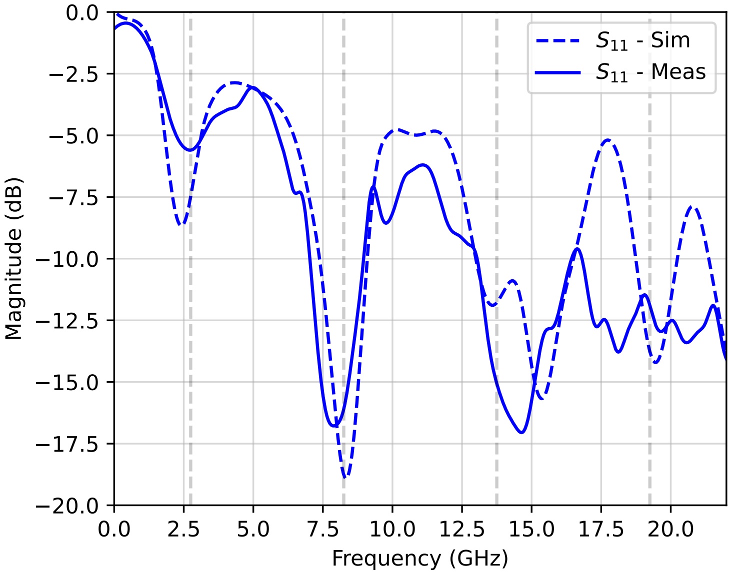

FIGURE 7.9 Simulated and measured S-parameter S_{11}. The dashed lines mark the harmonics.

While minor discrepancies are observed—most notably a 2 dB drop near 2.75 GHz—the overall agreement is satisfactory up to the seventh harmonic, with values of −5.6 dB, −16.1 dB, −15.1 dB, and −12 dB at f_0, $3f_0$, $5f_0$ and $7f_0$, respectively.

Fig. 7.10a also shows the measured output DC voltage at port 2 of the power detector as a function of input power ranging from −50 to 20 dBm.

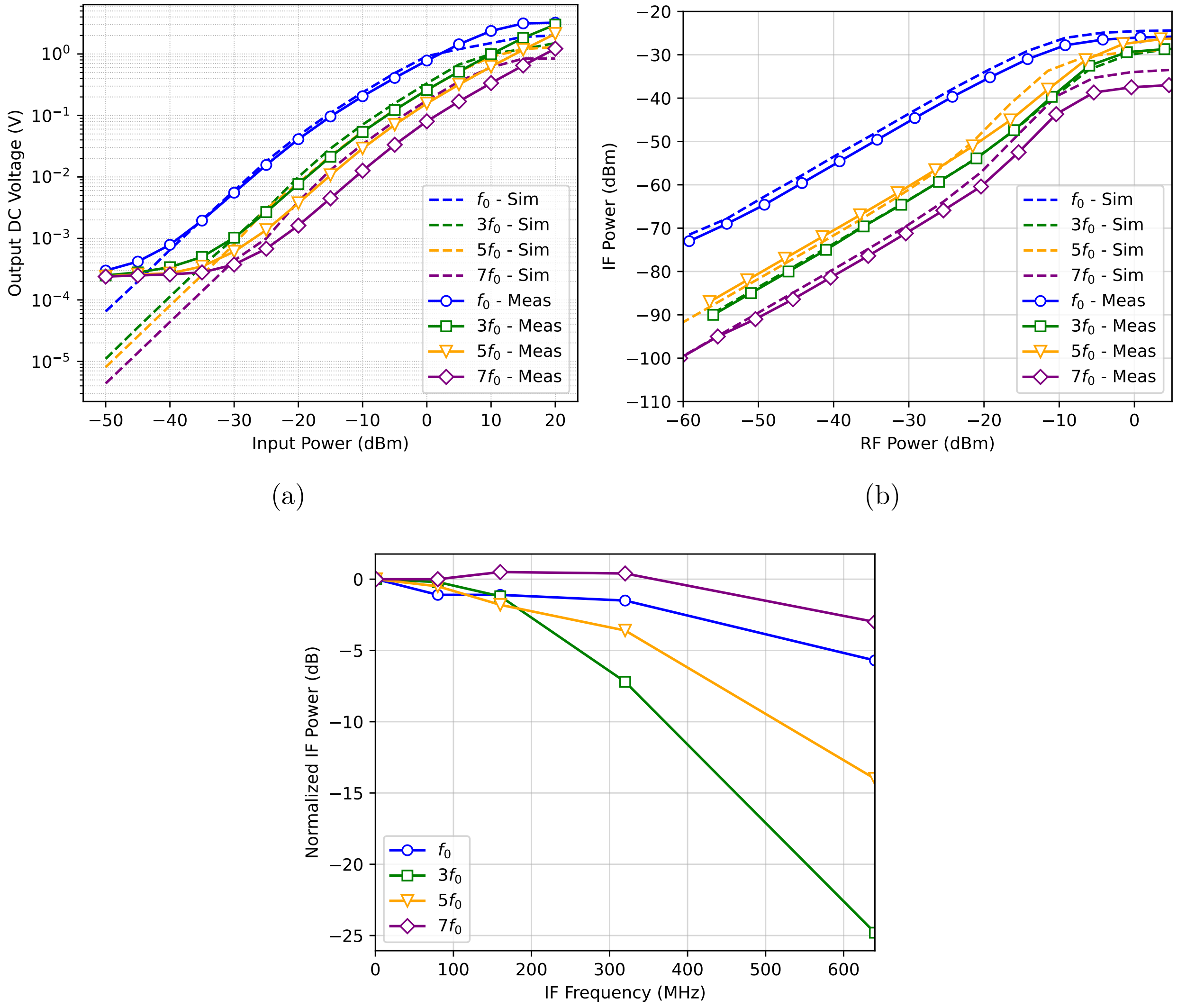

(a)

(b)

(c)

FIGURE 7.10 (a) Simulated and measured output DC voltage versus input power. (b) Simulated and measured IF power versus input RF power with constant LO power of −15dBm. (c) Measured normalized IF power versus IF frequency with constant RF and LO power of −15 dBm.

The square-law operating regions are identified as −35 to 5 dBm for f_0, −30 to 0 dBm for both $3f_0$ and $5f_0$, and −25 to 5 dBm for $7f_0$. The good agreement between simulation and measurement results confirms the validity of the employed diode model. In addition, Fig. 7.10b illustrates the evolution of IF power versus input RF power, spanning from −60 to 5 dBm with a fixed LO power of −15 dBm. The minimal discrepancy between simulated and measured results ensures accurate prediction of power levels. As expected, higher input frequencies result in reduced IF output power, which in turn lowers the SNR due to an increase in CLs. Also, it is seen that, across harmonics, the sensitivity remains relatively constant with slopes of 0.950, 1.021, 1.024 and 1.018 dBm/dBm at f_0, $3f_0$, $5f_0$ and $7f_0$, respectively, in their respective square-law region.

To further evaluate the power detector's performance, Fig. 7.10c investigates its IF bandwidth by symmetrically varying the frequency difference between RF and LO signals around each harmonic of f_0. For consistency, the IF bandwidth is defined here as the 3-dB drop in normalized IF power, although broader bandwidths are feasible at the expense of lower IF power. The measured IF bandwidths are 430 MHz, 206 MHz, 263 MHz, and 634 MHz for f_0, $3f_0$, $5f_0$ and $7f_0$, respectively. Notably, the widest bandwidth is achieved at the highest harmonic. Such IF bandwidths are primarily explained by the variation of the power detector's S_{11} around each harmonic.

7.5.2 Overall System Characterization

The four-port architecture of Fig. 7.6, including four Wilkinson power dividers and the power detectors, is fabricated on ROGERS RT/Duroid 6002 with 20-mil thickness and is presented in Fig. 7.11. Aluminium backplates for all circuits are fabricated to ensure physical rigidity.

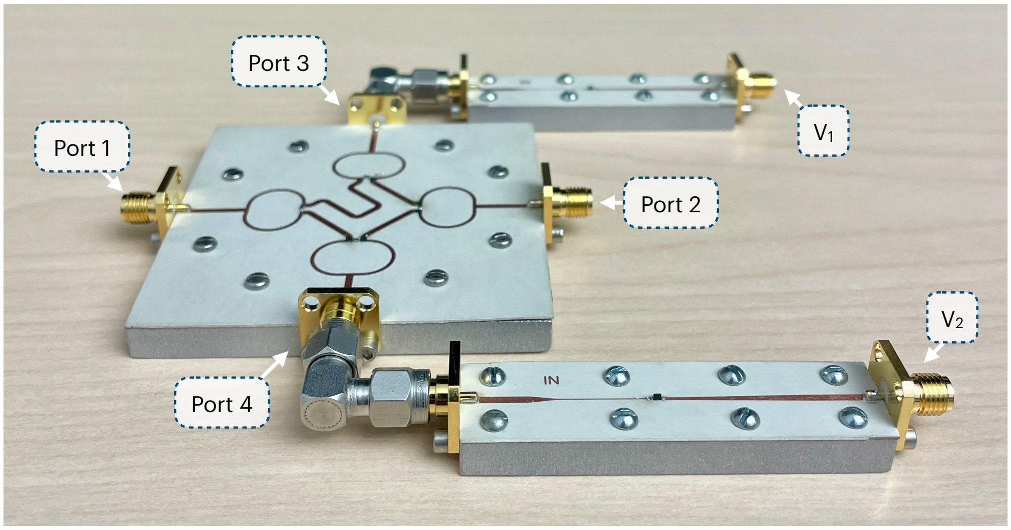

FIGURE 7.11 Manufactured four-port harmonic receiver with power detectors.

Fig. 7.12a compares the simulated and measured input reflection coefficients at all the four ports (without power detectors).

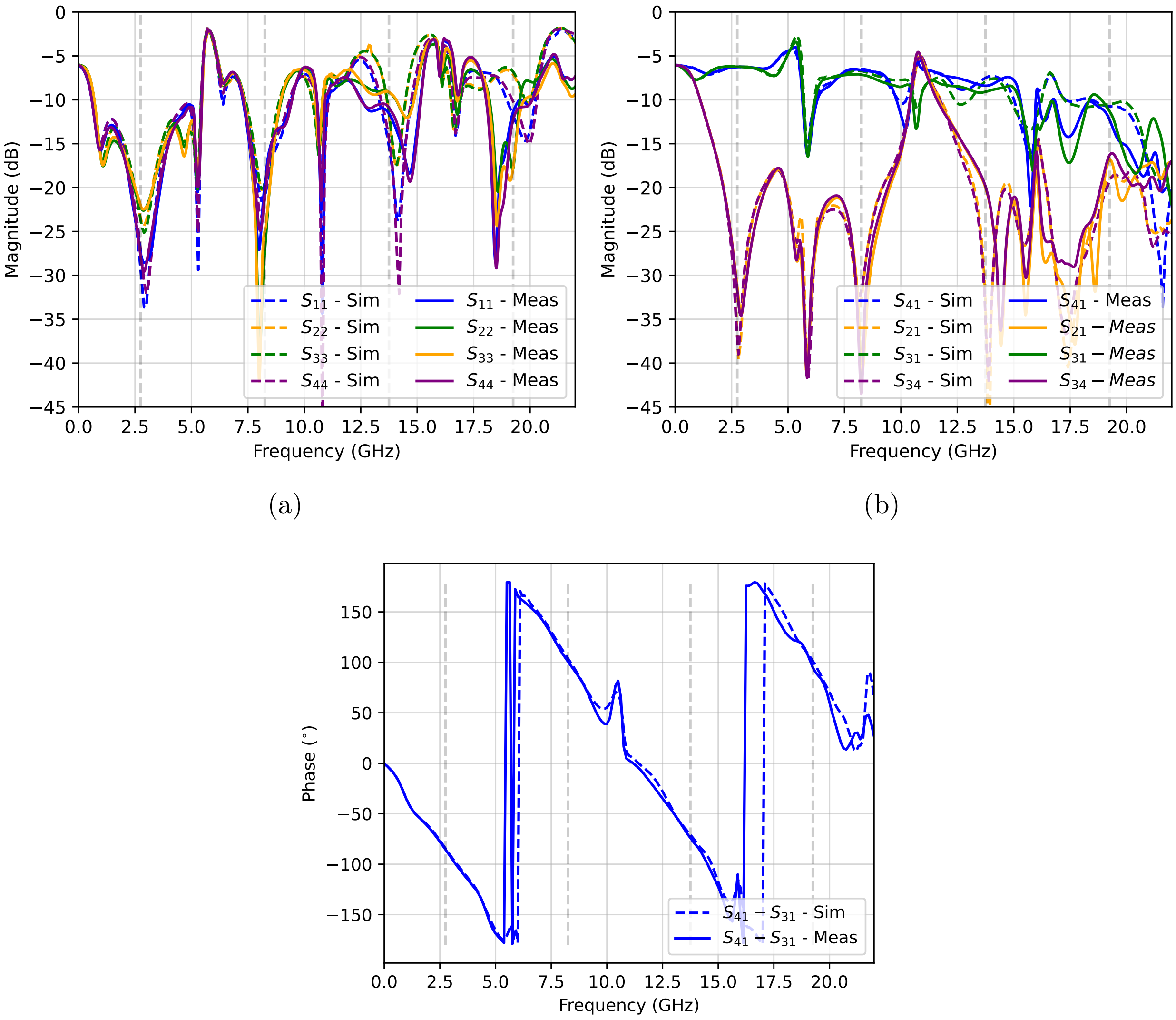

(a)

(b)

(c)

FIGURE 7.12 Simulated and measured S-parameters (a) S_{11}, S_{22}, S_{33} and S_{44} (b) S_{41}, S_{21}, S_{31} and $S_{3}4$. (c) Simulated and measured phase shifts between port 3 and port 4. The dashed lines mark the harmonics.

Across the harmonic frequencies, the S_{11} values remain below -10 dB, with consistent performance observed across all the ports. Fig. 7.12b presents the simulated and measured transmission coefficients. For S_{41} and S_{31}, the measured insertion losses are -6.4 dB at f_0, -6.7 at $3f_0$, -8.6 dB at $5f_0$ and -11.5 dB at $7f_0$, which align well with the losses expected from the standalone Wilkinson power divider. The port-to-port isolation coefficients S_{21} and S_{34} are below -15 dB, ensuring effective isolation and the absence of crosstalk between input and output ports. Fig. 7.12c further examines the phase differences between the output ports across the harmonics. The measured phase shifts between ports 4 and 3 are $-87°$, $99°$, $-75°$, and $93°$ at f_0, $3f_0$, $5f_0$ and $7f_0$, respectively, supporting accurate I/Q signal recovery. Notably, these measured phase differences alternate between approximately $-\pi/2$ and $\pi/2$, consistent with the preliminary expectations derived from (7.53) and (7.54).

7.6 System-Level Experimental Verification

7.6.1 Communication Mode

To verify the communication performance of the proposed receiver, a system-level experimental verification is conducted in our Poly-Grames Research Center, and the experimental setup is depicted in Figs. 7.13a and 7.13b.

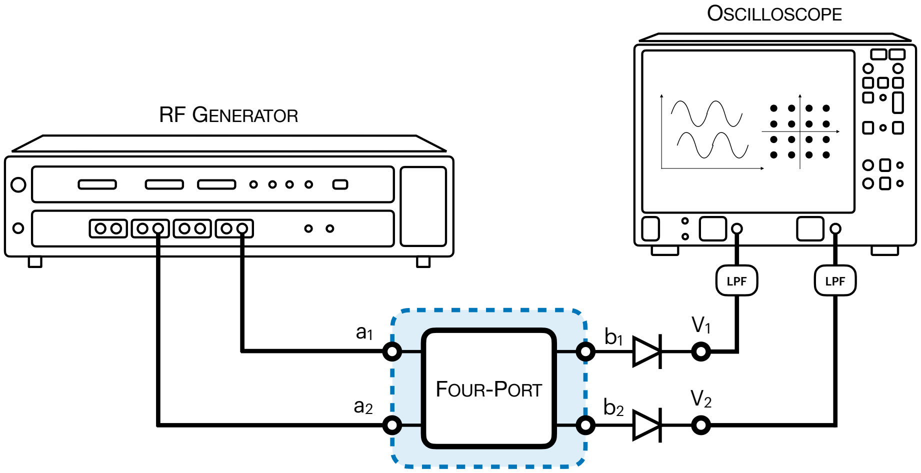

(a)

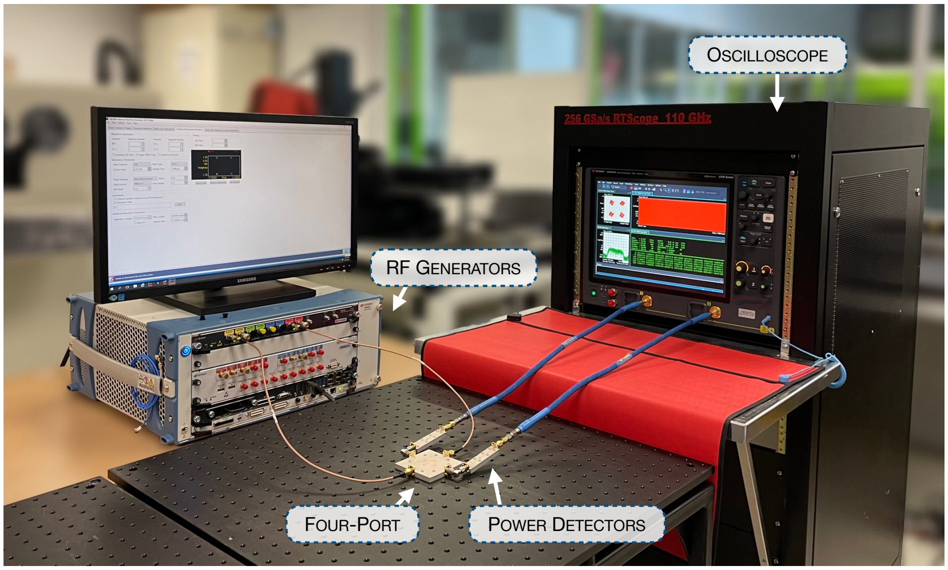

(b)

FIGURE 7.13 (a) Block diagram and (b) real connections of the experimental setup. The RF signal is connected as a_1 and the LO signal is connected as a_2. The power detectors, followed by low-pass filters ($f_c = 1$ GHz) are attached to the four-port as b_1 and b_2, and the outputs are monitored by an oscilloscope

The RF and LO signals are driven by the Keysight M8196A AWG are connected to the four-port as a_1 and a_2, respectively. The RF signals incorporate QAM. The output signals are retrieved with the Keysight UXR0702AP oscilloscope.

TABLE 7.2 summarizes the retrieved constellation diagrams for several QAM modulation orders (4, 32, 64 and 128) around f_0, $3f_0$, $5f_0$ and $7f_0$ using the proposed harmonic four-port receiver in Fig. 7.11. The Error Vector Magnitude (EVM) metric is used to compare the performance across harmonics and modulation orders.

Note that the LO and RF signal power levels are fixed across all measurements. For this experiment, a root-raised cosine pulse filter ($\alpha = 0.35$) is selected.

TABLEAU 7.2 Summary of retrieved constellation diagrams and SNR metric with different modulation orders (M-QAM) and center frequencies.

Frequency	f_0	$3f_0$	$5f_0$	$7f_0$

Modulation : 4-QAM				
Symbol Rate	50 Mbps	50 Mbps	50 Mbps	10 Mbps
EVM (dB)	-18.3	-15.5	-11.7	-11.0
Constellation	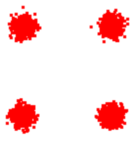	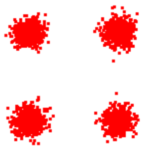	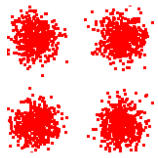	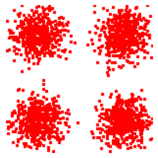

Modulation : 32-QAM				
Symbol Rate	50 Mbps	30 Mbps	10 Mbps	1 Mbps
EVM (dB)	-22.5	-21.7	-22.8	-24.7
Constellation	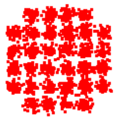	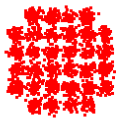	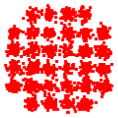	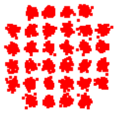

Modulation : 64-QAM				
Symbol Rate	30 Mbps	10 Mbps	5 Mbps	500 kbps
EVM (dB)	-26.2	-30.4	-25.5	-26.7
Constellation	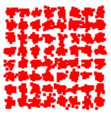	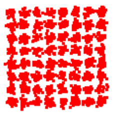	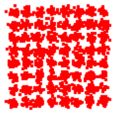	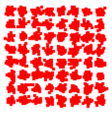

Modulation : 128-QAM				
Symbol Rate	10 Mbps	5 Mbps	1 Mbps	100 kbps
EVM (dB)	-30.7	-30.4	-33.1	-30.7
Constellation				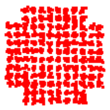

It is observed that for a given modulation order, performance generally worsens as the harmonic index increases, while being overall satisfactory. This is expected given the lower SNR and larger CLs (see Fig. 7.10b). For example, the 4-QAM modulation exhibits EVM degradation from 12.1% to 28% despite a decrease in symbol rate at the seventh harmonic.

Then, for a given frequency, EVM is affected positively with a higher modulation order due to smaller constellation spacing. Even at higher orders, such as 128-QAM, adequate demodulation is obtained across all harmonic bands, with EVM values less than 5% at low symbol rates. It is worth mentioning that the proposed system successfully demodulates 128-QAM at $7f_0$ with an EVM of 2.9%, exhibiting the harmonic receiver's ability to sustain linearity and coherent detection up to the seventh harmonic.

Finally, it is to be noted that the symbol rate must be lowered as the frequency and modulation order rise. This trade-off reflects bandwidth constraints and increasing Intersymbol Interference (ISI) at higher harmonics. Indeed, at $7f_0$, reliable 64-QAM and 128-QAM are possible at 500 kbps and 100 kbps, respectively.

Overall, the data show that the proposed harmonic receiver largely supports multiband operation with reasonable performance as harmonic order and modulation complexity grow.

7.6.2 Radar Mode

For the radar mode, the proof-of-concept experimental setup, illustrated in Fig. 7.13b, is conserved to evaluate the performance of the proposed harmonic four-port receiver, specifically with respect to its multiband capabilities. To emulate the transmitted and received FMCW chirps, the AWG is utilized to produce the following frequencies : f_{1a}, f_{1b}, f_{2a}, f_{2b}, f_{3a}, f_{3b}, f_{4a}, f_{4b}. The signals at f_{1a}, f_{2a}, f_{3a}, f_{4a} are fed into a_1, while those at f_{1b}, f_{2b}, f_{3b}, f_{4b} are applied to a_2. Consequently, the resulting beat frequencies are $f_{beat,1} = f_{1b} - f_{1a}$, $f_{beat,2} = f_{2b} - f_{2a}$, $f_{beat,3} = f_{3b} - f_{3a}$ and $f_{beat,4} = f_{4b} - f_{4a}$. The parameters of this experimental verification are detailed in TABLE 7.3.

TABLEAU 7.3 Experimental Parameters

Center Frequency (GHz)	**Stop Frequency (GHz)**	**Power (dBm)**	**Beat Frequency (MHz)**
$f_0 = 2.75$	$f_{1a} = 2.71$ $f_{1b} = 2.79$	-15	$f_{beat,1} = 80$
$3f_0 = 8.25$	$f_{2a} = 8.22$ $f_{2b} = 8.28$	-15	$f_{beat,2} = 60$
$5f_0 = 13.75$	$f_{3a} = 13.73$ $f_{3b} = 13.77$	-15	$f_{beat,3} = 40$
$7f_0 = 19.25$	$f_{4a} = 19.24$ $f_{4b} = 19.26$	-15	$f_{beat,4} = 20$

It is important to note that this scenario corresponds to a single fixed target. Fig. 7.14 depicts the time-domain signal captured at b_1 and the associated measured frequency spectrum.

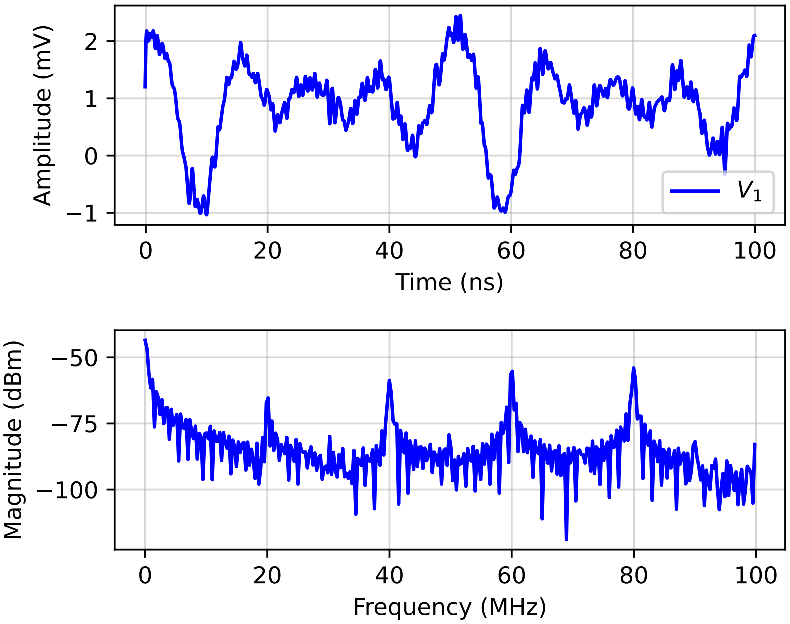

FIGURE 7.14 Measured (top) low-pass filtered time-domain signal and (bottom) frequency spectrum with four simultaneous FMCW chirps.

The four beat frequencies, which result from the emulation of four distinct FMCW chirps, are clearly visible in the spectrum domain. Due to the variation in RF-to-IF CL across the harmonic bands, the spectral peaks have different amplitudes, with the fundamental band having the highest power. Note that the DC power is predominant in the output signal. From the recorded time-domain signal, numerical band-pass filtering can be used to separate each beat frequency, allowing for further baseband signal processing procedures.

7.6.3 Dual-Mode Operation

An experimental validation was performed to demonstrate the harmonic receiver's capability to support dual-mode operation. In addition to the RF and LO signals shown in Fig. 7.14, an FMCW chirp was emulated by injecting a signal at $f_{2a} = 8.2$ GHz into port a_1, while injecting a signal at $f_{2b} = 8.3$ GHz to port a_1 with the AWG, producing a beat frequency of 100 MHz. It is important to note that the IF of the QAM modulation was centered at 50 MHz with a symbol rate of 50 Mbps.

Fig. 7.15 shows the comparison of measurements between the constellations and spectra with the communication signal alone and together with the emulated FMCW signal.

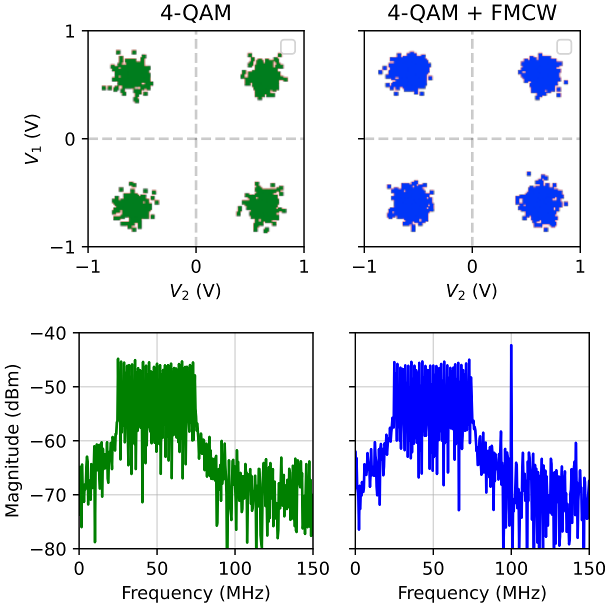

Figure 7.15 Measurement comparison between (left) 4-QAM signal alone and (right) 4-QAM alongside emulated FMCW signal. Top figures are constellations and bottom ones are corresponding spectra.

In the first case (4-QAM), the measured EVM is 12.1%, and in the second case (4-QAM + FMCW), the measured EVM is 12.2%. Hence, when the FMCW beat signal is outside of the communication band, there is no influence on the QAM demodulation performances nor on the beat signal itself. This demonstrates that multiple functions can be operated simultaneously with the proposed harmonic receiver.

7.6.4 Comparison

TABLE 7.4 compares the performance of the proposed four-port linear harmonic interferometric receiver with respect to current multiband interferometric systems.

Tableau 7.4 Performance summary and comparison of state-of-the-art multiband interferometric receivers

Reference	**Topology**	**Modulation**	**Frequency (GHz)**	**Symbol Rate**	**EVM (dB)**	**Harmonic-Responsive**
[240]	Dual-Band Six-port	4/16/32/64-QAM	5.8	60/120/150/180 Mbps	–30.81/–33.59/–35.08/–34.15	No
		4/16/32/64-QAM	150	1/2/2.5/3 Gbps	–24.58/–26.51/–27.63/–27.72	
[257]	Dual-Band Six-port	64-QAM	2.3	2 Mbps	–34.89	No
		16-QAM	2.6	2 Mbps	–37.72	
[258]	Dual-Band Four-port	16-QAM	2.3	2 Mbps	–34.89	No
		64-QAM	2.6	2 Mbps	–37.72	
[This work]	Quad-Band Harmonic Four-port	4-/32-/64-/128-QAM	2.75	50/50/30/10 Mbps	–18.3/–22.4/–26.2/–30.7	Yes
		4-/32-/64-/128-QAM	8.25	50/30/10/5 Mbps	–15.5/–21.7/–30.4/–30.4	
		4-/32-/64-/128-QAM	13.75	50/10/5/1 Mbps	–11.7/–22.8/–25.5/–33.1	
		4-/32-/64-/128-QAM	19.25	10/1/0.5/0.1 Mbps	–11/–24.7/–26.7/–30.7	

This is the first quad-band harmonic-responsive receiver that can operate over multiple distinct frequency bands while utilizing a single, reusable architecture. The suggested receiver performs well from 2.75 GHz to 19.25 GHz, with low EVM values and support for high-order QAM modulation.

7.7 Conclusion

In this work, a quad-band, low-power, four-port linear harmonic interferometric receiver has been proposed, studied and experimentally assessed. The proposed system can perform simultaneous multiband ISAC operations by taking advantage of the harmonic diversity allowed by the hybrid harmonic multiplexing scheme and a fully passive structure based on quarter-wavelength networks, which allows for operation at the fundamental and up to the seventh harmonic of the design frequency. A preliminary thorough theoretical analysis was conducted, followed by the development and assessment of a proof-of-concept prototype.

The harmonic receiver successfully demodulated high-order QAM signals (up to 128-QAM) and extracted beat signals from FMCW chirps at 2.75, 8.25, 13.75, and 19.25 GHz. These results demonstrate the feasibility and robustness of the harmonic interferometric approach over a wide spectral range with low complexity and high reusability, which provides a genuinely compact topology for multifunction RF front ends. The concept of harmonic expansion in linear interferometric receivers offers a promising solution to efficient spectrum reuse and scalable integration in next-generation wireless platforms.

Looking ahead, extensions of this work may include an even further expansion of the operational bandwidth around even and odd harmonics, and an implementation for mmWave and sub-THz systems.

CHAPITRE 8 CONCLUSION

8.1 Conclusion générale

Cette thèse s'est attachée à explorer de nouvelles pistes architecturales et fonctionnelles pour les systèmes sans fil de prochaine génération, dans un contexte marqué par l'exigence croissante d'intégration multifonctionnelle, de gestion intelligente du spectre, et de sobriété énergétique. En mobilisant à la fois des approches théoriques, expérimentales et conceptuelles, cette thèse a permis de poser les bases de nouveaux paradigmes en matière de transcepteurs radiofréquence, en particulier autour de l'utilisation innovante des harmoniques, de la fusion multi-bande, et de la détection non-linéaire.

Le premier article a permis d'ancrer les travaux dans une vision d'ensemble du domaine, en identifiant les principales synergies et verrous technologiques liés à l'intégration conjointe de la communication, de la détection radar et du transfert de puissance. Cette analyse a établi une feuille de route vers les systèmes véritablement multifonctionnels et adaptatifs de demain.

Le deuxième article a introduit une modélisation rigoureuse de la génération harmonique large bande par des diodes non-linéaires, validée par des prototypes expérimentaux. Ces travaux ont démontré la possibilité d'un contrôle précis des harmoniques dans des régimes à faible puissance, ouvrant la voie à des capteurs sans batterie, compacts et économes en énergie.

Dans le troisième article, une approche originale de fusion de sous-bandes non-contiguës a été proposée afin d'améliorer les performances radar tout en tenant compte de la congestion spectrale. La capacité à distinguer des cibles très rapprochées avec des ressources dispersées dans le spectre démontre la pertinence de cette approche dans des environnements radiofréquences de plus en plus fragmentés.

Le quatrième article a renforcé cette dynamique en démontrant que la fusion de bandes harmoniques pouvait, à partir d'une seule excitation fondamentale, aboutir à une résolution radar équivalente à celle obtenue avec une bande passante six fois plus large. Cette méthode, à la fois performante et stable thermiquement, démontre l'intérêt des techniques de détection non-linéaires dans les architectures modernes et les applications spatiales.

Le cinquième article a concrétisé les travaux précédents dans une application de surveillance médicale, illustrant comment un système intégré de communication et de détection multibande peut simultanément assurer la transmission de données et la détection de signes vitaux avec une grande précision, dans un contexte intra domum. Ce cas d'usage illustre la polyvalence et la pertinence sociétale des architectures multifonctions.

Enfin, le sixième article a présenté une architecture pionnière de récepteur interférométrique multifonction exploitant jusqu'à la septième bande harmonique. Ce prototype a permis de valider la faisabilité d'un fonctionnement parallèle entre communication (jusqu'au 128-QAM) et détection radar sur quatre bandes de fréquence. Il s'agit là d'une avancée notable vers la convergence réelle des fonctions radiofréquence.

8.2 Perspectives et extensions

Les travaux présentés dans cette thèse ouvrent différentes perspectives de recherche prometteuses, tant sur le plan théorique que technologique. Des exemples d'extensions sont détaillés ci-après.

— Une première direction naturelle consisterait à étendre la bande de fréquence exploitable par les générateurs harmoniques à base de diodes. Cela nécessiterait l'optimisation des structures physiques, notamment via des topologies adaptatives d'impédance ou l'utilisation de nouveaux matériaux dont la non-linéarité pourrait être contrôlée. L'objectif serait de couvrir des plages fréquentielles encore plus larges pour répondre aux demandes des applications avec les ondes millimétriques, tout en maintenant la stabilité thermique et la compacité des dispositifs.

— L'approche de fusion multi-bande pourrait être améliorée par des traitements du signal plus sophistiqués intégrant la diversité fréquentielle comme levier d'analyse. En exploitant les riches signatures spectrales provenant des différentes sous-bandes, il serait envisageable de caractériser non seulement la distance ou la vitesse d'une cible, mais aussi sa forme, sa matière ou sa texture, ouvrant ainsi la voie à des fonctions avancées de reconnaissance ou d'imagerie radar à large bande synthétique.

— Les idées développées autour de la récupération d'énergie peuvent être appliquées directement au sein du récepteur harmonique multifonction. Il serait notamment pertinent d'explorer des configurations où le courant continu et les harmoniques inutilisés à la suite des détecteurs de puissance pourraient être recycler, tout en maintenant les performances actuelles. Cette cointégration d'un module d'alimentation radiofréquence permettrait de concevoir des récepteurs partiellement autoalimentés, jusqu'à la 7e harmonique, optimisant l'autonomie énergétique des systèmes embarqués.

- La mise en œuvre des solutions proposées dans des technologies intégrées comme CMOS ou RFIC représente une étape essentielle pour leur industrialisation. Une miniaturisation complète des fonctions de génération harmonique, de multiplexage, de réception harmonique et de traitement permettrait d'aboutir à des circuits intégrés multifonctionnels, à faible coût, prêts à être industrialisés pour l'internet des objets, les capteurs intégrés, etc.
- Enfin, les concepts développés dans cette thèse peuvent être étendus à des configurations MIMO ou à des réseaux distribués de capteurs intelligents. Cela permettrait d'exploiter simultanément la diversité spatiale et fréquentielle, pour améliorer la robustesse des liaisons, la résolution radar 4D, et la capacité de couverture dans des environnements complexes. La synchronisation harmonique entre antennes pourrait également être étudiée comme alternative aux méthodes classiques de calibration.

RÉFÉRENCES

[1] I. F. Akyildiz, A. Kak et S. Nie, “6g and beyond : The future of wireless communications systems,” *IEEE access*, vol. 8, p. 133 995–134 030, 2020.

[2] K. Sujatha, G. Karthiga, N. Bhavani, A. Kalaivani et N. Janaki, *Real-Time Brain Mapping Using Wireless Technology for the Future.* IGI Global, 2023, p. 48–62.

[3] K. Wu, “Mhz-through-thz (mtt) challenges and opportunities [president’s column],” *IEEE Microwave Magazine*, vol. 17, n°. 2, p. 8–10, 2016.

[4] L. Deng, Y. Rui, P. Cheng, J. Zhang, Q. T. Zhang et M. Li, “A unified energy efficiency and spectral efficiency tradeoff metric in wireless networks,” *IEEE Communications Letters*, vol. 17, n°. 1, p. 55–58, 2013.

[5] L. Han et K. Wu, “Multifunctional transceiver for future intelligent transportation systems,” *IEEE Transactions on Microwave Theory and Techniques*, vol. 59, n°. 7, p. 1879–1892, 2011.

[6] ——, “24-ghz integrated radio and radar system capable of time-agile wireless communication and sensing,” *IEEE Transactions on Microwave Theory and Techniques*, vol. 60, n°. 3, p. 619–631, 2012.

[7] P. W. Moo et D. J. DiFilippo, “Multifunction rf systems for naval platforms,” *Sensors*, vol. 18, n°. 7, p. 2076, 2018.

[8] G. Tavik, C. Hilterbrick, J. Evins, J. Alter, J. Crnkovich, J. de Graaf, W. Habicht, G. Hrin, S. Lessin, D. Wu et S. Hagewood, “The advanced multifunction rf concept,” *IEEE Transactions on Microwave Theory and Techniques*, vol. 53, n°. 3, p. 1009–1020, 2005.

[9] B. Clerckx, R. Zhang, R. Schober, D. W. K. Ng, D. I. Kim et H. V. Poor, “Fundamentals of wireless information and power transfer : From rf energy harvester models to signal and system designs,” *Ieee Journal on Selected Areas in Communications*, vol. 37, n°. 1, p. 4–33, 2019.

[10] Y. Guo, C. Skouroumounis et I. Krikidis, “A linear mmse receiver for multi-antenna swipt-enabled wireless networks,” dans *ICC 2022 - IEEE International Conference on Communications*, 2022, Conference Proceedings, p. 3166–3171.

[11] F. Jameel, Faisal, M. A. A. Haider et A. A. Butt, “A technical review of simultaneous wireless information and power transfer (swipt),” dans *2017 International Symposium*

on Recent Advances in Electrical Engineering (RAEE), 2017, Conference Proceedings, p. 1–6.

[12] M. R. A. Khandaker, K. K. Wong, Y. Zhang et Z. Zheng, “Probabilistically robust swipt for secrecy misome systems,” *IEEE Transactions on Information Forensics and Security*, vol. 12, n°. 1, p. 211–226, 2017.

[13] V. Khodamoradi, A. Sali, O. Messadi, A. Khalili et B. B. M. Ali, “Energy-efficient massive mimo swipt-enabled systems,” *IEEE Transactions on Vehicular Technology*, vol. 71, n°. 5, p. 5111–5127, 2022.

[14] G. Paolini, A. Quddious, D. Chatzichristodoulou, D. Masotti, S. Nikolaou et A. Costanzo, “An energy-autonomous swipt rfid tag for communication in the 2.4 ghz ism band,” dans *2022 3rd URSI Atlantic and Asia Pacific Radio Science Meeting (AT-AP-RASC)*, 2022, Conference Proceedings, p. 1–4.

[15] T. D. P. Perera, D. N. K. Jayakody, S. K. Sharma, S. Chatzinotas et J. Li, “Simultaneous wireless information and power transfer (swipt) : Recent advances and future challenges,” *Ieee Communications Surveys and Tutorials*, vol. 20, n°. 1, p. 264–302, 2018.

[16] A. Quddious, M. A. B. Abbasi, M. H. Tariq, M. A. Antoniades, P. Vryonides et S. Nikolaou, “On the use of tunable power splitter for simultaneous wireless information and power transfer receivers,” *International Journal of Antennas and Propagation*, vol. 2018, p. 6183412, 2018.

[17] N. Van Huynh, D. T. Hoang, X. Lu, D. Niyato, P. Wang et D. I. Kim, “Ambient backscatter communications : A contemporary survey,” *IEEE Communications Surveys Tutorials*, vol. 20, n°. 4, p. 2889–2922, 2018.

[18] X. Gu, P. Burasa, S. Hemour et K. Wu, “Recycling ambient rf energy : Far-field wireless power transfer and harmonic backscattering,” *IEEE Microwave Magazine*, vol. 22, n°. 9, p. 60–78, 2021.

[19] X. Gu, K. Wu et S. Hemour, “Remote temperature sensing based on battery-free harmonic backscattering,” dans *2020 IEEE International Symposium on Antennas and Propagation and North American Radio Science Meeting*, 2020, Conference Proceedings, p. 1429–1430.

[20] J. Zhang, S. D. Joseph, Y. Huang et J. Zhou, “Compact single-port harmonic transponder for backscattering communications and energy harvesting applications,” *IEEE Transactions on Microwave Theory and Techniques*, p. 1–8, 2023.

[21] J. A. Zhang, Y. J. Guo et K. Wu, *Signal Processing Fundamentals for JCAS.* IEEE, 2023, p. 31–58.

[22] M. Bekar, C. J. Baker, E. G. Hoare et M. Gashinova, "Joint mimo radar and communication system using a psk-lfm waveform with tdm and cdm approaches," *IEEE Sensors Journal*, vol. 21, n°. 5, p. 6115–6124, 2021.

[23] T. Jeong, J. Kim et S. Lee, "Signal modulation and demodulation for sharing detection results between vehicles in fdm mimo radar system," *IEEE Sensors Letters*, vol. 7, n°. 10, p. 1–4, 2023.

[24] W. Scheiblhofer, R. Feger, A. Haderer, S. Scheiblhofer et A. Stelzer, "In-chirp fsk communication between cooperative 77-ghz radar stations integrating variable power distribution between ranging and communication system," *International Journal of Microwave and Wireless Technologies*, vol. 8, n°. 4-5, p. 825–832, 2016.

[25] O. L. A. López, H. Alves, R. D. Souza, S. Montejo-Sánchez, E. M. G. Fernández et M. Latva-Aho, "Massive wireless energy transfer : Enabling sustainable iot toward 6g era," *IEEE Internet of Things Journal*, vol. 8, n°. 11, p. 8816–8835, 2021.

[26] I. Hussain et K. Wu, "Power-recycling microwave mixer with wide linear instantaneous bandwidth," *IEEE Microwave and Wireless Components Letters*, vol. 30, n°. 4, p. 425–428, 2020.

[27] O. Elsayed, M. Abouzied, V. Vaidya, K. Ravichandran et E. Sánchez-Sinencio, "An ultralow-power rf wireless receiver with rf blocker energy recycling for iot applications," *IEEE Transactions on Microwave Theory and Techniques*, vol. 66, n°. 11, p. 4927–4942, 2018.

[28] V. Palazzi, R. Correia, X. Gu, S. Hemour, K. Wu, A. Costanzo, D. Masotti, E. Fazzini, A. Georgiadis, H. Kazemi, R. Pereira, N. Shinohara, D. Schreurs, J. C. Chiao, A. Takacs, D. Dragomirescu et N. B. Carvalho, "Radiative wireless power transfer : Where we are and where we want to go," *IEEE Microwave Magazine*, vol. 24, n°. 2, p. 57–79, 2023.

[29] X. Gu, S. Hemour et K. Wu, "Enabling far-field ambient energy harvesting through multi-physical sources," dans *2018 Asia-Pacific Microwave Conference (APMC)*, 2018, Conference Proceedings, p. 204–206.

[30] ——, "Far-field wireless power harvesting : Nonlinear modeling, rectenna design, and emerging applications," *Proceedings of the IEEE*, vol. 110, n°. 1, p. 56–73, 2022.

[31] X. Lu, P. Wang, D. Niyato, D. I. Kim et Z. Han, “Wireless networks with rf energy harvesting : A contemporary survey,” *IEEE Communications Surveys Tutorials*, vol. 17, n°. 2, p. 757–789, 2015.

[32] T. Sanislav, G. D. Mois, S. Zeadally et S. C. Folea, “Energy harvesting techniques for internet of things (iot),” *IEEE Access*, vol. 9, p. 39 530–39 549, 2021.

[33] Z. Feng, Z. Fang, Z. Wei, X. Chen, Z. Quan et D. Ji, “Joint radar and communication : A survey,” *China Communications*, vol. 17, n°. 1, p. 1–27, 2020.

[34] R. S. Thomä, T. Dallmann, S. Jovanoska, P. Knott et A. Schmeink, “Joint communication and radar sensing : An overview,” *2021 15th European Conference on Antennas and Propagation (EuCAP)*, p. 1–5, 2021.

[35] S. H. Dokhanchi, B. S. Mysore, K. V. Mishra et B. Ottersten, “A mmwave automotive joint radar-communications system,” *IEEE Transactions on Aerospace and Electronic Systems*, vol. 55, n°. 3, p. 1241–1260, 2019.

[36] W. Zhai, X. Wang, X. Cao, M. S. Greco et F. Gini, “Reinforcement learning based dual-functional massive mimo systems for multi-target detection and communications,” *IEEE Transactions on Signal Processing*, vol. 71, p. 741–755, 2023.

[37] L. Zheng, M. Lops, Y. C. Eldar et X. Wang, “Radar and communication coexistence : An overview : A review of recent methods,” *IEEE Signal Processing Magazine*, vol. 36, n°. 5, p. 85–99, 2019.

[38] A. R. Chiriyath, B. Paul et D. W. Bliss, “Radar-communications convergence : Coexistence, cooperation, and co-design,” *IEEE Transactions on Cognitive Communications and Networking*, vol. 3, n°. 1, p. 1–12, 2017.

[39] F. Liu, C. Masouros, A. P. Petropulu, H. Griffiths et L. Hanzo, “Joint radar and communication design : Applications, state-of-the-art, and the road ahead,” *IEEE Transactions on Communications*, vol. 68, n°. 6, p. 3834–3862, 2020.

[40] N. C. Luong, X. Lu, D. T. Hoang, D. Niyato et D. I. Kim, “Radio resource management in joint radar and communication : A comprehensive survey,” *IEEE Communications Surveys Tutorials*, vol. 23, n°. 2, p. 780–814, 2021.

[41] D. Ma, N. Shlezinger, T. Huang, Y. Liu et Y. C. Eldar, “Joint radar-communication strategies for autonomous vehicles : Combining two key automotive technologies,” *IEEE Signal Processing Magazine*, vol. 37, n°. 4, p. 85–97, 2020.

[42] D. Cong, S. Guo, S. Dang et H. Zhang, “Vehicular behavior-aware beamforming design for integrated sensing and communication systems,” *IEEE Transactions on Intelligent Transportation Systems*, p. 1–13, 2023.

[43] K. Zhao, M. Zhu, B. Xiao, X. Yang, C. Gong et J. Wu, “Joint rfid and uwb technologies in intelligent warehousing management system,” *IEEE Internet of Things Journal*, vol. 7, n^{o}. 12, p. 11 640–11 655, 2020.

[44] T. Wild, V. Braun et H. Viswanathan, “Joint design of communication and sensing for beyond 5g and 6g systems,” *IEEE Access*, vol. 9, p. 30 845–30 857, 2021.

[45] A. Hassanien, M. G. Amin, E. Aboutanios et B. Himed, “Dual-function radar communication systems : A solution to the spectrum congestion problem,” *IEEE Signal Processing Magazine*, vol. 36, n^{o}. 5, p. 115–126, 2019.

[46] H. T. Hayvaci et B. Tavli, “Spectrum sharing in radar and wireless communication systems : A review,” dans *2014 International Conference on Electromagnetics in Advanced Applications (ICEAA)*, 2014, Conference Proceedings, p. 810–813.

[47] J. Moghaddasi et K. Wu, “Multifunctional transceiver for future radar sensing and radio communicating data-fusion platform,” *IEEE Access*, vol. 4, p. 818–838, 2016.

[48] Y. Li, L. Zheng, M. Lops et X. Wang, “Interference removal for radar/communication co-existence : The random scattering case,” *IEEE Transactions on Wireless Communications*, vol. 18, n^{o}. 10, p. 4831–4845, 2019.

[49] Y. Zheng, W. Zhang et H. Wan, “Ofdm radar communication systems based on index modulation,” dans *2023 International Conference on Microwave and Millimeter Wave Technology (ICMMT)*, 2023, p. 1–3.

[50] H. Du, J. Kang, D. Niyato, J. Zhang et D. I. Kim, “Reconfigurable intelligent surface-aided joint radar and covert communications : Fundamentals, optimization, and challenges,” *IEEE Vehicular Technology Magazine*, vol. 17, n^{o}. 3, p. 54–64, 2022.

[51] L. G. De Oliveira, B. Nuss, M. B. Alabd, Y. Li, L. Yu et T. Zwick, “Mimo-ocdm-based joint radar sensing and communication,” dans *2021 15th European Conference on Antennas and Propagation (EuCAP)*. IEEE, 2021, Conference Proceedings, p. 1–5.

[52] W. Bai, X. Zou, P. Li, J. Ye, Y. Yang, L. Yan, W. Pan et L. Yan, “Photonic millimeter-wave joint radar communication system using spectrum-spreading phase-coding,” *IEEE Transactions on Microwave Theory and Techniques*, vol. 70, n^{o}. 3, p. 1552–1561, 2022.

[53] Y. Liu, T. Huang, F. Liu, D. Ma, W. Huangfu et Y. C. Eldar, “Next-generation multiple access for integrated sensing and communications,” *Proceedings of the IEEE*, 2024.

[54] J. Moghaddasi et K. Wu, “Multifunction, multiband, and multimode wireless receivers : A path toward the future,” *IEEE Microwave Magazine*, vol. 21, n°. 12, p. 104–125, 2020.

[55] J. Li, R. Bosisio et K. Wu, “A six-port direct digital millimeter wave receiver,” dans *Proceedings of IEEE National Telesystems Conference - NTC ’94*, 1994, p. 79–82.

[56] A. Hasan et M. Helaoui, “Performance driven six-port receiver and its advantages over low-if receiver architecture,” *JECE*, vol. 2014, p. Article 1, 2014.

[57] K. Wu, “Multiport interferometer techniques for innovative transceiver applications,” dans *2010 IEEE Radio and Wireless Symposium (RWS)*, 2010, Conference Proceedings, p. 531–534.

[58] D. Onori, F. Scotti, M. Scaffardi, A. Bogoni et F. Laghezza, “Coherent interferometric dual-frequency laser radar for precise range/doppler measurement,” *Journal of Lightwave Technology*, vol. 34, n°. 20, p. 4828–4834, 2016.

[59] J. Lu, Z. Shao, C. Li, C. Gu et J. Mao, “A portable 5.8 ghz dual circularly polarized interferometric radar sensor for short-range motion sensing,” *IEEE Transactions on Antennas and Propagation*, vol. 70, n°. 7, p. 5849–5859, 2022.

[60] X. Xinyu, R. G. Bosisio et K. Wu, “Analysis and implementation of six-port software-defined radio receiver platform,” *IEEE Transactions on Microwave Theory and Techniques*, vol. 54, n°. 7, p. 2937–2943, 2006.

[61] E. E. Djoumessi, S. O. Tatu et K. Wu, “Frequency-agile dual-band direct conversion receiver for cognitive radio systems,” *IEEE Transactions on Microwave Theory and Techniques*, vol. 58, n°. 1, p. 87–94, 2010.

[62] C. H. Wang, H. Y. Chang, P. S. Wu, K. Y. Lin, T. W. Huang, H. Wang et C. H. Chen, “A 60ghz low-power six-port transceiver for gigabit software-defined transceiver applications,” dans *2007 IEEE International Solid-State Circuits Conference. Digest of Technical Papers*, 2007, Conference Proceedings, p. 192–596.

[63] P. Burasa, J. Deng et K. Wu, “A 300-ghz dual-polarized cmos waveguide receiver for high-density terahertz integrated multichannel wireless systems-on-chip,” *IEEE Transactions on Microwave Theory and Techniques*, 2024.

[64] G. N. Saddik, R. S. Singh et E. R. Brown, “Ultra-wideband multifunctional communications/radar system,” *IEEE Transactions on Microwave Theory and Techniques*, vol. 55, n°. 7, p. 1431–1437, 2007.

[65] S. A. Keivaan, P. Burasa et K. Wu, “Interferometric receiver architecture for multi-function wireless systems,” dans *2022 52nd European Microwave Conference (EuMC)*, 2022, Conference Proceedings, p. 16–19.

[66] J. Moghaddasi et K. Wu, “Millimeter-wave multifunction multiport interferometric receiver for future wireless systems,” *IEEE Transactions on Microwave Theory and Techniques*, vol. 66, n°. 3, p. 1452–1466, 2018.

[67] ——, “Unified radar-communication (radcom) multi-port interferometer transceiver,” dans *2013 European Microwave Conference*, 2013, Conference Proceedings, p. 1791–1794.

[68] D. Shmakov, R. Ebelt et M. Vossiek, “Wireless sensor network with 24 ghz local positioning transceiver,” dans *2012 IEEE/MTT-S International Microwave Symposium Digest*, 2012, Conference Proceedings, p. 1–3.

[69] S. Roehr, P. Gulden et M. Vossiek, “Precise distance and velocity measurement for real time locating in multipath environments using a frequency-modulated continuous-wave secondary radar approach,” *IEEE Transactions on Microwave Theory and Techniques*, vol. 56, n°. 10, p. 2329–2339, 2008.

[70] A. Stelzer, M. Jahn et S. Scheiblhofer, “Precise distance measurement with cooperative fmcw radar units,” dans *2008 IEEE Radio and Wireless Symposium*, 2008, Conference Proceedings, p. 771–774.

[71] W. Scheiblhofer, R. Feger, A. Haderer et A. Stelzer, “Method to embed a data-link on fmcw chirps for communication between cooperative 77-ghz radar stations,” dans *2015 European Radar Conference (EuRAD)*, 2015, Conference Proceedings, p. 181–184.

[72] I. Hussain et K. Wu, “Cooperative interferometric receiver with time-agile radar sensing and radio communication capability,” *IEEE Sensors Journal*, vol. 22, n°. 24, p. 23 896–23 905, 2022.

[73] F. Sangare, D. H. N. Nguyen et Z. Han, “Learning frameworks for dynamic joint rf energy harvesting and channel access,” *IEEE Access*, vol. 7, p. 84 524–84 535, 2019.

[74] A. Tribak, *Compact Ultra-Wideband Printed Monopole Antenna with Inverted L-Shaped Slots for Data Communication and RF Energy Harvesting.* World Academy of Science, Engineering and Technology, 2015.

[75] D. D. Donno, L. Catarinucci et L. Tarricone, “Ramses : Rfid augmented module for smart environmental sensing,” *IEEE Transactions on Instrumentation and Measurement*, vol. 63, n°. 7, p. 1701–1708, 2014.

[76] K. B. Huang et E. Larsson, “Simultaneous information and power transfer for broadband wireless systems,” *Ieee Transactions on Signal Processing*, vol. 61, n°. 23, p. 5972–5986, 2013.

[77] I. Krikidis, S. Timotheou, S. Nikolaou, G. Zheng, D. W. K. Ng et R. Schober, “Simultaneous wireless information and power transfer in modern communication systems,” *Ieee Communications Magazine*, vol. 52, n°. 11, p. 104–110, 2014.

[78] Y. W. Liu, Z. G. Ding, M. Elkashlan et H. V. Poor, “Cooperative non-orthogonal multiple access with simultaneous wireless information and power transfer,” *Ieee Journal on Selected Areas in Communications*, vol. 34, n°. 4, p. 938–953, 2016.

[79] R. Zhang et C. K. Ho, “Mimo broadcasting for simultaneous wireless information and power transfer,” *Ieee Transactions on Wireless Communications*, vol. 12, n°. 5, p. 1989–2001, 2013.

[80] X. Zhou, R. Zhang et C. K. Ho, “Wireless information and power transfer : Architecture design and rate-energy tradeoff,” *IEEE Transactions on Communications*, vol. 61, n°. 11, p. 4754–4767, 2013.

[81] V. C. Gungor, B. Lu et G. P. Hancke, “Opportunities and challenges of wireless sensor networks in smart grid,” *Ieee Transactions on Industrial Electronics*, vol. 57, n°. 10, p. 3557–3564, 2010.

[82] F. K. Shaikh et S. Zeadally, “Energy harvesting in wireless sensor networks : A comprehensive review,” *Renewable Sustainable Energy Reviews*, vol. 55, p. 1041–1054, 2016.

[83] J. Yick, B. Mukherjee et D. Ghosal, “Wireless sensor network survey,” *Computer Networks*, vol. 52, n°. 12, p. 2292–2330, 2008.

[84] L. Guo, X. Gu, P. Chu, S. Hemour et K. Wu, “Collaboratively harvesting ambient radiofrequency and thermal energy,” *IEEE Transactions on Industrial Electronics*, vol. 67, n°. 5, p. 3736–3746, 2020.

[85] X. Gu, S. Hemour et K. Wu, “Integrated cooperative radiofrequency (rf) and kinetic energy harvester,” dans *2017 IEEE Wireless Power Transfer Conference (WPTC)*, 2017, Conference Proceedings, p. 1–3.

[86] Z. Ding, C. Zhong, D. Wing Kwan Ng, M. Peng, H. A. Suraweera, R. Schober et H. V. Poor, “Application of smart antenna technologies in simultaneous wireless information and power transfer,” *IEEE Communications Magazine*, vol. 53, n°. 4, p. 86–93, 2015.

[87] V. S. Silva, H. P. Paz, E. V. Cambero, E. T. Pereira, I. R. Casella et C. E. Capovilla, “Double patch antenna array for communication and out-of-band rf energy harvesting,”

Journal of Microwaves, Optoelectronics and Electromagnetic Applications, vol. 19, p. 356–365, 2020.

[88] T. M. Hoang, L. T. T. Huyen, X. N. Tran et P. T. Hiep, "Outage probability of aerial base station noma mimo wireless communication with rf energy harvesting," *IEEE Internet of Things Journal*, vol. 9, n°. 22, p. 22 874–22 886, 2022.

[89] J. J. Park, J. H. Moon et D. I. Kim, "Time-switching based in-band full duplex wireless powered two-way relay," dans *2016 URSI Asia-Pacific Radio Science Conference (URSI AP-RASC)*, 2016, Conference Proceedings, p. 438–441.

[90] S. K. Zaidi, S. F. Hasan et X. Gui, "Time switching based relaying for coordinated transmission using noma," dans *2018 Eleventh International Conference on Mobile Computing and Ubiquitous Network (ICMU)*, 2018, Conference Proceedings, p. 1–5.

[91] M. Bohra, D. Saith et S. Bitragunta, "Spectral efficiency optimization and analysis of time switching-based, energy harvesting spectrum sharing cooperative wireless system," dans *2021 IEEE International Conference on Electronics, Computing and Communication Technologies (CONECCT)*, 2021, Conference Proceedings, p. 1–5.

[92] A. A. Nasir, X. Zhou, S. Durrani et R. A. Kennedy, "Wireless-powered relays in cooperative communications : Time-switching relaying protocols and throughput analysis," *IEEE Transactions on Communications*, vol. 63, n°. 5, p. 1607–1622, 2015.

[93] K. Calautit, D. S. N. M. Nasir et B. R. Hughes, "Low power energy harvesting systems : State of the art and future challenges," *Renewable and Sustainable Energy Reviews*, vol. 147, p. 111230, 2021.

[94] B. Chowkwale, D. Yadav et R. Abhyankar, "Energy harvesting techniques for low power rf sensors," dans *2015 17th International Conference on Advanced Communication Technology (ICACT)*, 2015, p. 49–53.

[95] D. T. Vo, T. Van Chien, T. N. Nguyen, D.-H. Tran, M. Voznak, B. S. Kim et L. T. Tu, "Swipt-enabled cooperative wireless iot networks with friendly jammer and eavesdropper : Outage and intercept probability analysis," *IEEE Access*, vol. 11, p. 86 165–86 177, 2023.

[96] A. Salhieh, J. Weinmann, M. Kochhal et L. Schwiebert, "Power efficient topologies for wireless sensor networks," dans *International Conference on Parallel Processing, 2001.* IEEE, 2001, Conference Proceedings, p. 156–163.

[97] A. Esse, K. Abdullah, M. H. Habaebi et H. A. M. Ramli, "Dynamic power splitting simultaneous wireless information and power transfer split receiver for wireless sensor

networks," *IEEE Access*, vol. 9, p. 129 407–129 416, 2021.

[98] M. B. Ghorbel, M. Guizani, B. Khalfi et B. Hamdaoui, "Cooperative joint power splitting and allocation approach for simultaneous energy delivery and data transfer," dans *2015 International Wireless Communications and Mobile Computing Conference (IWCMC)*, 2015, Conference Proceedings, p. 184–187.

[99] B. Li, M. Zhang, H. Cao, Y. Rong et Z. Han, "Transceiver design for af mimo relay systems with a power splitting based energy harvesting relay node," *IEEE Transactions on Vehicular Technology*, vol. 69, n°. 3, p. 2376–2388, 2020.

[100] C. Hu et Y. Dong, "Age of information of two-way data exchanging systems with power-splitting," *Journal of Communications and Networks*, vol. 21, n°. 3, p. 295–306, 2019.

[101] D. Wang, R. Zhang, X. Cheng et L. Yang, "Capacity-enhancing full-duplex relay networks based on power-splitting (ps-)swipt," *IEEE Transactions on Vehicular Technology*, vol. 66, n°. 6, p. 5445–5450, 2017.

[102] Y. Zhao, Y. Wu, J. Hu et K. Yang, "Time-index modulation for integrated data and energy transfer : A remedy for time switching," *IEEE Wireless Communications Letters*, vol. 11, n°. 9, p. 1815–1819, 2022.

[103] B. Yi, M. Xiang, W. Yao, K. Qiu, T. Huang et Q. Xie, "Simultaneous wireless information and power transfer in wireless sensor networks with fountain codes," dans *2017 IEEE International Conference on Internet of Things (iThings) and IEEE Green Computing and Communications (GreenCom) and IEEE Cyber, Physical and Social Computing (CPSCom) and IEEE Smart Data (SmartData)*, 2017, Conference Proceedings, p. 516–521.

[104] X. Zhou, R. Zhang et C. K. Ho, "Wireless information and power transfer in multiuser ofdm systems," *IEEE Transactions on Wireless Communications*, vol. 13, n°. 4, p. 2282–2294, 2014.

[105] M. Rajabi, N. Pan, S. Claessens, S. Pollin et D. Schreurs, "Modulation techniques for simultaneous wireless information and power transfer with an integrated rectifier–receiver," *IEEE Transactions on Microwave Theory and Techniques*, vol. 66, n°. 5, p. 2373–2385, 2018.

[106] I. Hussain et K. Wu, "Low-power receiver architecture for 5g and iot-oriented wireless information and power transfer applications," dans *2019 IEEE MTT-S International Microwave Symposium (IMS)*, 2019, Conference Proceedings, p. 1148–1151.

[107] D. Rodriguez, A. Flores et C. Li, “Self-powered 24-ghz doppler radar for building entrance monitoring using cross correlation and envelope detection,” dans *2019 IEEE Topical Conference on Wireless Sensors and Sensor Networks (WiSNet)*, 2019, Conference Proceedings, p. 1–4.

[108] A. Traille, A. Coustou, H. Aubert, S. Kim, J. Kimionis, M. M. Tentzeris, A. Georgiadis et A. Collado, “Novel inkjet printed modules for sensing, radar and energy harvesting applications,” dans *2014 44th European Microwave Conference*, 2014, Conference Proceedings, p. 1–4.

[109] Z. M. Jiang, P. C. Zhang, L. Huang, J. H. Zhang, X. He et M. Rihan, “Lens antenna arrays aided co-existing radar and communication systems with energy harvesting,” *Ieee Access*, vol. 8, p. 56 160–56 169, 2020.

[110] A. Jay, “Number of internet of things (iot) connected devices worldwide 2024 : Breakdowns, growth predictions,” Nov 2024.

[111] K. Rasilainen, J. Ilvonen, A. Lehtovuori, J. M. Hannula et V. Viikari, “On design and evaluation of harmonic transponders,” *Ieee Transactions on Antennas and Propagation*, vol. 63, n°. 1, p. 15–23, 2015.

[112] H. Y. Hsu, B. M. Chen, Y. H. Lin, Z. M. Tsai, Y. Y. Chiang, M. C. Chiu, C. F. Kao, S. C. Lin et Ieee, “Harmonic radar using multiple receivers and angle of arrival positioning technique for environment with obstacles,” dans *45th European Microwave Conference (EuMC)*, ser. European Microwave Conference, 2015, Conference Proceedings, p. 975–978.

[113] G. Andíia Vera, Y. Duroc et S. Tedjini, “Third harmonic exploitation in passive uhf rfid,” *IEEE Transactions on Microwave Theory and Techniques*, vol. 63, n°. 9, p. 2991–3004, 2015.

[114] J. L. Osborne, S. J. Clark, R. J. Morris, I. H. Williams, J. R. Riley, A. D. Smith, D. R. Reynolds et A. S. Edwards, “A landscape-scale study of bumble bee foraging range and constancy, using harmonic radar,” *Journal of Applied Ecology*, vol. 36, n°. 4, p. 519–533, 1999.

[115] E. T. Cant, A. D. Smith, D. R. Reynolds et J. L. Osborne, “Tracking butterfly flight paths across the landscape with harmonic radar,” *Proceedings of the Royal Society B-Biological Sciences*, vol. 272, n°. 1565, p. 785–790, 2005.

[116] Z. M. Tsai, P. H. Jau, N. C. Kuo, J. C. Kao, K. Y. Lin, F. R. Chang, E. C. Yang et H. Wang, “A high-range-accuracy and high-sensitivity harmonic radar using pulse

pseudorandom code for bee searching," *Ieee Transactions on Microwave Theory and Techniques*, vol. 61, n°. 1, p. 666–675, 2013.

[117] F. Kocer et M. P. Flynn, "A new transponder architecture with on-chip adc for long-range telemetry applications," *IEEE Journal of Solid-State Circuits*, vol. 41, n°. 5, p. 1142–1148, 2006.

[118] M. Khaliel, A. Batra, A. Fawky et T. Kaiser, "Low-profile harmonic transponder for iot applications," *Electronics*, vol. 10, n°. 17, p. 2053, 2021.

[119] P. Kamalvand, G. Kumar Pandey, M. Kumar Meshram et A. Mallahzadeh, "A single sided dual-antenna structure for uhf rfid tag applications," *International Journal of RF and Microwave Computer-Aided Engineering*, vol. 25, n°. 7, p. 619–628, 2015.

[120] S. Bhaskar et A. K. Singh, "A dual band dual antenna with read range enhancement for uhf rfid tags," *International Journal of RF and Microwave Computer-Aided Engineering*, vol. 29, n°. 7, p. e21717, 2019.

[121] A. Lavrenko, B. Litchfield, G. Woodward et S. Pawson, "Design and evaluation of a compact harmonic transponder for insect tracking," *IEEE Microwave and Wireless Components Letters*, vol. 30, n°. 4, p. 445–448, 2020.

[122] A. Agarwal, M. Machnoor, R. Kumar, J. G. S. et V. G. A., "Coupled rf signal cancellation based transceiver arrangement for backscatter communication," dans *2016 IEEE MTT-S International Microwave and RF Conference (IMaRC)*, 2016, p. 1–4.

[123] M. Wagih, Y. Wei, A. Komolafe, R. Torah et S. Beeby, "Reliable uhf long-range textile-integrated rfid tag based on a compact flexible antenna filament," *Sensors*, vol. 20, n°. 12, p. 3435, 2020.

[124] X. Gu, N. N. Srinaga, L. Guo, S. Hemour et K. Wu, "Diplexer-based fully passive harmonic transponder for sub-6-ghz 5g-compatible iot applications," *IEEE Transactions on Microwave Theory and Techniques*, vol. 67, n°. 5, p. 1675–1687, 2019.

[125] R. K. Singh, A. Michel, P. Nepa et A. Salvatore, "Wearable dual-band quasi-yagi antenna for uhf-rfid and 2.4 ghz applications," *Ieee Journal of Radio Frequency Identification*, vol. 4, n°. 4, p. 420–427, 2020.

[126] P. Hirsch, A. R. Weily, P. de Souza et Ieee, "Compact dual-band parasitic dipole antenna for harmonic transponders," dans *International Symposium on Antennas and Propagation (ISAP)*, 2015, Conference Proceedings.

[127] C. Bajaj, D. K. Upadhyay, S. Kumar et B. K. Kanaujia, “A dual-band circularly polarized hexagonal ring antenna for handheld rfid readers,” *Wireless Personal Communications*, vol. 125, n°. 4, p. 3101–3115, 2022.

[128] M. Polivka, V. Hubata-Vacek et M. Svanda, “Wearable harmonic transponder for iot applications,” dans *2022 16th European Conference on Antennas and Propagation (EuCAP)*, 2022, Conference Proceedings, p. 1–5.

[129] X. Gu, W. Lin, S. Hemour et K. Wu, “Readout distance enhancement of battery-free harmonic transponder,” *IEEE Transactions on Microwave Theory and Techniques*, vol. 69, n°. 7, p. 3413–3424, 2021.

[130] J. Gao, R. Wu, J. Hao, C. Xu et H. Guo, “Swipt-based energy scheduling for solar-powered wsn in full-duplex mode,” *IEEE Sensors Journal*, vol. 22, n°. 13, p. 13 668–13 681, 2022.

[131] Y. Chen, H. Hua, J. Xu et D. W. K. Ng, “Isac meets swipt : Multi-functional wireless systems integrating sensing, communication, and powering,” *IEEE Transactions on Wireless Communications*, vol. 23, n°. 8, p. 8264–8280, 2024.

[132] Z. M. Jiang, P. Zhang, L. Huang, M. Rihan et J. Zhang, “A novel energy harvesting-enabled design for radar and communication coexistence,” dans *2019 6th Asia-Pacific Conference on Synthetic Aperture Radar (APSAR)*, 2019, Conference Proceedings, p. 1–5.

[133] J. Kellett, W. Dawber, W. Wallace et J. Branson, “Multifunction maritime radar and rf systems—technology challenges and areas of development,” *IEEE Aerospace and Electronic Systems Magazine*, vol. 37, n°. 4, p. 6–20, 2022.

[134] P. W. Moo et D. J. DiFilippo, “Overview of naval multifunction rf systems,” dans *2018 15th European Radar Conference (EuRAD)*, 2018, p. 178–181.

[135] A. Venkataramani, A. R. Chiriyath, A. Dutta, A. Herschfelt et D. W. Bliss, “The dash soc : Enabling the next generation of multi-function rf systems,” dans *2022 56th Asilomar Conference on Signals, Systems, and Computers*, 2022, p. 905–912.

[136] Y. Zhou, H. Zhou, F. Zhou, Y. Wu et V. C. Leung, “Resource allocation for a wireless powered integrated radar and communication system,” *IEEE Wireless Communications Letters*, vol. 8, n°. 1, p. 253–256, 2018.

[137] P. K. Dutta, A. K. Arora et S. B. Bibyk, “Towards radar-enabled sensor networks,” dans *Proceedings of the 5th international conference on Information processing in sensor networks*, 2006, Conference Proceedings, p. 467–474.

[138] S. Guan, J. A. Bridge, C. Li et N. J. DeMello, “Smart radar sensor network for bridge displacement monitoring,” *Journal of Bridge Engineering*, vol. 23, n°. 12, p. 04018102, 2018.

[139] M. Li, T. Yan, D. Ganesan, E. Lyons, P. Shenoy, A. Venkataramani et M. Zink, “Multi-user data sharing in radar sensor networks,” dans *Proceedings of the 5th international conference on Embedded networked sensor systems*, 2007, Conference Proceedings, p. 247–260.

[140] L. Bai, J. Liu, R. Han et W. Zhang, “Wireless radar sensor networks : Epidemiological modeling and optimization,” *IEEE Journal on Selected Areas in Communications*, vol. 40, n°. 6, p. 1993–2005, 2022.

[141] K. J. Flattery, B. Henry, M. Muadi, K. Walters, A. Eroglu et J. Rickman, “Crane position detection with sensor network using energy harvesting,” dans *2016 IEEE/ACES International Conference on Wireless Information Technology and Systems (ICWITS) and Applied Computational Electromagnetics (ACES)*, 2016, Conference Proceedings, p. 1–2.

[142] H. Griffiths, S. Blunt, L. Cohen et L. Savy, “Challenge problems in spectrum engineering and waveform diversity,” dans *2013 IEEE Radar Conference (RadarCon13)*. IEEE, 2013, Conference Proceedings, p. 1–5.

[143] L. Han et K. Wu, “Joint wireless communication and radar sensing systems–state of the art and future prospects,” *IET Microwaves, Antennas Propagation*, vol. 7, n°. 11, p. 876–885, 2013.

[144] S. A. Keivaan, P. Burasa et K. Wu, “Virtual receiver matrix and combinatory analog operations for future multifunction reconfigurable sensing and communication wireless systems,” *IEEE Transactions on Microwave Theory and Techniques*, vol. 71, n°. 1, p. 424–433, 2023.

[145] A. Sabharwal, P. Schniter, D. Guo, D. W. Bliss, S. Rangarajan et R. Wichman, “In-band full-duplex wireless : Challenges and opportunities,” *IEEE Journal on Selected Areas in Communications*, vol. 32, n°. 9, p. 1637–1652, 2014.

[146] A. Afshani et K. Wu, “Combining polarization-division multiplexing and ferromagnetic nonreciprocity to achieve in-band ultra-high isolation for full-duplex wireless systems,” *Engineering*, 2024.

[147] N. I. Bhopale et S. N. Pawar, “Challenges for designing a multiband ultra-wide band (uwb) antenna with its solutions,” dans *2022 International Conference on Disruptive*

Technologies for Multi-Disciplinary Research and Applications (CENTCON), vol. 2, 2022, p. 87–91.

[148] R. Langwieser et G. Lasser, “Measurement and simulation of crosstalk and crosstalk compensation in uhf rfid,” dans *2012 Fourth International EURASIP Workshop on RFID Technology*, 2012, p. 22–26.

[149] X. Zeng, L. Xing, Y. Wu et Y. Shi, “Beamforming design for integrated sensing and swipt system,” dans *2022 IEEE 33rd Annual International Symposium on Personal, Indoor and Mobile Radio Communications (PIMRC)*, 2022, Conference Proceedings, p. 403–408.

[150] X. Li, X. Yi, Z. Zhou, K. Han, Z. Han et Y. Gong, “Multi-user beamforming design for integrating sensing, communications, and power transfer,” dans *2023 IEEE Wireless Communications and Networking Conference (WCNC)*. IEEE, 2023, Conference Proceedings, p. 1–6.

[151] K. Saarinen, L. Frisk et L. Ukkonen, “Effects of cycling humidity on the performance of rfid tags with aca joints,” *IEEE Transactions on Reliability*, vol. 61, n°. 1, p. 23–31, 2012.

[152] H.-H. Yang, H. Zareie et G. M. Rebeiz, “A high power stress-gradient resilient rf mems capacitive switch,” *Journal of Microelectromechanical Systems*, vol. 24, n°. 3, p. 599–607, 2015.

[153] A.-D. Riadh, “Dubai, the sustainable, smart city,” *Renewable Energy and Environmental Sustainability*, vol. 7, p. 3, 2022.

[154] F. Mohammed, A. Idries, N. Mohamed, J. Al-Jaroodi et I. Jawhar, “Opportunities and challenges of using uavs for dubai smart city,” dans *2014 6th international conference on new technologies, mobility and security (NTMS)*. IEEE, 2014, Conference Proceedings, p. 1–4.

[155] E. S. Lu, V. S. Reppucci, S. S. Houston III, A. L. Kras et J. B. Miller, “Three-dimensional telesurgery and remote proctoring over a 5g network,” *Digital Journal of Ophthalmology : DJO*, vol. 27, n°. 3, p. 38, 2021.

[156] W. Brown, M. King et Y. M. Goh, “Uk smart cities present and future : An analysis of british smart cities through current and emerging technologies and practices,” *Emerald Open Research*, vol. 1, n°. 5, 2023.

[157] A. Alabsi, A. Hawbani, X. Wang, A. Al-Dubai, J. Hu, S. A. Aziz, S. Kumar, L. Zhao, A. V. Shvetsov et S. H. Alsamhi, “Wireless power transfer technologies, applications,

and future trends : a review," *IEEE Transactions on Sustainable Computing*, 2024.

[158] G. K. Ijemaru, K. L.-M. Ang et J. K. Seng, "Wireless power transfer and energy harvesting in distributed sensor networks : Survey, opportunities, and challenges," *International journal of distributed sensor networks*, vol. 18, n°. 3, p. 15501477211067740, 2022.

[159] M. E. Hines, "The virtues of nonlinearity - detection, frequency conversion, parametric amplification and harmonic generation," *IEEE Transactions on Microwave Theory and Techniques*, vol. 32, n°. 9, p. 1097–1104, 1984.

[160] R. Feger et A. Stelzer, "Modulated mm-wave radar signal generation using frequency multipliers," dans *2015 IEEE MTT-S International Conference on Microwaves for Intelligent Mobility (ICMIM)*, 2015, Conference Proceedings, p. 1–4.

[161] T. Micallef, X. Gu et K. Wu, "Resolution enhancement of radar systems through super fusion of non-contiguous frequency bands," dans *2024 21st European Radar Conference (EuRAD)*, 2024, Conference Proceedings, p. 356–359.

[162] K. Neumann, L. Kühnel, F. Langer, A. Rennings, N. Benson, R. Schmechel et D. Erni, "A stochastic large-signal model for printed high-frequency rectifiers used for efficient generation of higher harmonics," *IEEE Transactions on Microwave Theory and Techniques*, vol. 68, n°. 6, p. 2151–2160, 2020.

[163] D. D. Prajapati et U. Neelkanthan, "Review paper on frequency multiplier at terahertz range," *International Journal on Recent and Innovation Trends in Computing and Communication*, vol. 5, n°. 2, p. 228–232, 2017.

[164] R. V, M. S et S. Hari, "Design of active frequency multiplier for x-band radar application," dans *2022 6th International Conference on Computation System and Information Technology for Sustainable Solutions (CSITSS)*, 2022, Conference Proceedings, p. 1–6.

[165] A. Aghighi, M. Essawy et A. S. Natarajan, "A frequency doubler with second harmonic feedback for wideband, efficient frequency multiplication at millimeter-wave," *IEEE Transactions on Microwave Theory and Techniques*, vol. 72, n°. 5, p. 2704–2715, 2024.

[166] X. Gu, P. Burasa, S. Hemour et K. Wu, "Recycling ambient rf energy : Far-field wireless power transfer and harmonic backscattering," *IEEE Microwave Magazine*, vol. 22, n°. 9, p. 60–78, 2021.

[167] J. Guo, J. Xu et C. Qian, "Design of dual-mode frequency multiplier with schottky diodes," *IEEE Microwave and Wireless Components Letters*, vol. 24, n°. 8, p. 554–556, 2014.

[168] K. Neumann, L. Kuehnel, F. Langer, A. Rennings, N. Benson, R. Schmechel et D. Erni, “Analysis of stochastic schottky barrier variations within printed high frequency rectifiers for harmonics generation,” dans *2019 IEEE MTT-S International Microwave Workshop Series on Advanced Materials and Processes for RF and THz Applications (IMWS-AMP)*, 2019, Conference Proceedings, p. 169–171.

[169] T. Li et Z. Luo, “A metasurface unit cell for harmonic generation and backscattering,” dans *2024 IEEE International Conference on Computational Electromagnetics (ICCEM)*, 2024, Conference Proceedings, p. 1–3.

[170] L. Xiang, Y. Zhu, Q. Ding, Y. Luo, J. Sun, Z. Zeng, J. Zhang, X. Li, L. Jin, Y. Shangguan *et al.*, “A microwave comb generator based on algan/gan heterostructure schottky diodes nonlinear transmission line,” *Applied Physics Express*, vol. 16, n°. 7, p. 074001, 2023.

[171] M. Saeed, A. Hamed, P. Palacios, B. Uzlu, Z. Wang, E. Baskent et R. Negra, “Voltage-tunable thin film graphene-diode-based microwave harmonic generator,” *IEEE Microwave and Wireless Components Letters*, vol. 31, n°. 6, p. 733–736, 2021.

[172] S. Mondal et P. Chahal, “A passive harmonic rfid tag and interrogator development,” *IEEE Journal of Radio Frequency Identification*, vol. 3, n°. 2, p. 98–107, 2019.

[173] H. Dossal, R. Bradley et R. Mattauch, “A planar varactor diode for harmonic generation at gigahertz frequencies,” dans *IEEE Proceedings of the SOUTHEASTCON’91*. IEEE, 1991, Conference Proceedings, p. 968–972.

[174] M. Abuelma’atti, “Harmonic generation by nondegenerate pn junction varactor diodes,” *Active and Passive Electronic Components*, vol. 19, p. 205–215, 1997.

[175] A. Younis, M. Shaltout, M. Hanafy et M. Abdalsamie, “Varactor diode : A comprehensive overview on all aspects,” 2024.

[176] A. Suarez et R. Melville, “Simulation-assisted design and analysis of varactor-based frequency multipliers and dividers,” *IEEE Transactions on Microwave Theory and Techniques*, vol. 54, n°. 3, p. 1166–1179, 2006.

[177] R. Rai et N. Lohchaab, “Higher order harmonic generation using capacitive nonlinearity of the step recovery diode,” dans *2023 IEEE Microwaves, Antennas, and Propagation Conference (MAPCON)*, 2023, Conference Proceedings, p. 1–4.

[178] Y. Ahajjam, O. Aghzout, J. M. Catala-Civera, F. Peñaranda-Foix et A. Driouach, “An accurate and compact high power monocycle pulse transmitter for microwave ultra-wideband radar sensors with an enhanced srd model : Applications for distance

measurement for lossy materials," *Advanced Electromagnetics*, vol. 8, nº. 3, p. 76–82, Sep. 2019.

[179] S. M. Krakauer, "Harmonic generation, rectification, and lifetime evaluation with the step recovery diode," *Proceedings of the IRE*, vol. 50, nº. 7, p. 1665–1676, 1962.

[180] N. R. Trivedi et V. Kodali, "Design and study of a broadband step-recovery diode harmonic generator," *IETE Journal of Research*, vol. 17, nº. 12, p. 464–469, 1971.

[181] J. L. Moll et S. A. Hamilton, "Physical modeling of the step recovery diode for pulse and harmonic generation circuits," *Proceedings of the IEEE*, vol. 57, nº. 7, p. 1250–1259, 1969.

[182] K. E. Kolodziej, "Comb generator design for swap-constrained applications," dans *2016 IEEE Radio and Wireless Symposium (RWS)*, 2016, Conference Proceedings, p. 200–203.

[183] Q. Li, W. Jiang, Y. Xu et F. Nian, "Analysis and design of wide-band comb generator based on srd," dans *2012 International Conference on Microwave and Millimeter Wave Technology (ICMMT)*, vol. 1, 2012, Conference Proceedings, p. 1–3.

[184] R. Du, L. Guo, Y. Zhao et K. Wu, "A repeater enabling small signal backscattering amplification and forward harmonic generation," dans *2023 IEEE MTT-S International Microwave Workshop Series on Advanced Materials and Processes for RF and THz Applications (IMWS-AMP)*, 2023, Conference Proceedings, p. 1–3.

[185] W. Shockley, "The theory of p-n junctions in semiconductors and p-n junction transistors," *The Bell System Technical Journal*, vol. 28, nº. 3, p. 435–489, 1949.

[186] C. Stefanucci, P. Buccella, M. Kayal et J. M. Sallese, "Modeling avalanche breakdown for esd diodes in integrated circuits," dans *2015 10th International Conference on Design Technology of Integrated Systems in Nanoscale Era (DTIS)*, 2015, Conference Proceedings, p. 1–3.

[187] A. Jain et A. Kapoor, "Exact analytical solutions of the parameters of real solar cells using lambert w-function," *Solar Energy Materials and Solar Cells*, vol. 81, nº. 2, p. 269–277, 2004.

[188] W. Lai, "Fourier analysis of complex impedance (amplitude and phase) in nonlinear systems : A case study of diodes," *Electrochimica Acta*, vol. 55, nº. 19, p. 5511–5518, 2010.

[189] F. Storke, “High-order harmonic generation wih varactor diodes,” dans *1962 IEEE International Solid-State Circuits Conference. Digest of Technical Papers*, vol. V, 1962, Conference Proceedings, p. 16–17.

[190] R. Lindner, “Semiconductor surface varactor,” *The Bell System Technical Journal*, vol. 41, n°. 3, p. 803–831, 1962.

[191] J. L. Moll, S. Krakauer et R. Shen, “P-n junction charge-storage diodes,” *Proceedings of the IRE*, vol. 50, n°. 1, p. 43–53, 1962.

[192] Z. Jian et A. V. Raisanen, “Computer-aided design of step recovery diode frequency multipliers,” *IEEE Transactions on Microwave Theory and Techniques*, vol. 44, n°. 12, p. 2612–2616, 1996.

[193] A. Kamal, “Low-cost and low-ringing microstrip based ultra-wideband pulse generators using step-recovery diode for ground penetrating radar applications,” Thesis, Indian Institute of Technology Kharagpur, 2015.

[194] J. Zhang et A. Raisanen, “A new model of step recovery diode for cad,” dans *Proceedings of 1995 IEEE MTT-S International Microwave Symposium*, 1995, Conference Proceedings, p. 1459–1462 vol.3.

[195] T. Harzheim, H. Heuermann et M. Marso, “An adaptive biasing method for srd comb generators,” dans *2016 German Microwave Conference (GeMiC)*, 2016, Conference Proceedings, p. 289–292.

[196] R. Raju et G. E. Bridges, “A compact wireless passive harmonic sensor for packaged food quality monitoring,” *IEEE Transactions on Microwave Theory and Techniques*, vol. 70, n°. 4, p. 2389–2397, 2022.

[197] K. Pushpa et P. Mondal, “A frequency tripler with suppressed harmonics for millimeter-wave applications,” dans *2018 3rd International Conference on Microwave and Photonics (ICMAP)*, 2018, Conference Proceedings, p. 1–2.

[198] I. S. Vasiljević, M. M. Krstić, J. V. Crnjanski, M. Banović et D. M. Gvozdić, “Generation of dual optical frequency combs by pulse modulation of a single semiconductor laser using a step recovery diode,” dans *2021 29th Telecommunications Forum (TELFOR)*, 2021, Conference Proceedings, p. 1–4.

[199] Z. Hameed et K. Moez, “Design of impedance matching circuits for rf energy harvesting systems,” *Microelectronics Journal*, vol. 62, p. 49–56, 2017.

[200] H. Griffiths, L. Cohen, S. Watts, E. Mokole, C. Baker, M. Wicks et S. Blunt, “Radar spectrum engineering and management : Technical and regulatory issues,” *Proceedings of the IEEE*, vol. 103, n°. 1, p. 85–102, 2015.

[201] H. Arisesa, A. N. Rahman, P. Putranto, W. Desvasari, D. P. K, P. Daud et S. Hardiati, “The effect of external interference on the performance of navigation radar,” dans *2016 International Conference on Radar, Antenna, Microwave, Electronics, and Telecommunications (ICRAMET)*, 2016, Conference Proceedings, p. 59–62.

[202] G. M. Brooker, “Mutual interference of millimeter-wave radar systems,” *IEEE Transactions on Electromagnetic Compatibility*, vol. 49, n°. 1, p. 170–181, 2007.

[203] M. Goppelt, H. L. Blöcher et W. Menzel, “Automotive radar – investigation of mutual interference mechanisms,” *Adv. Radio Sci.*, vol. 8, p. 55–60, 2010.

[204] U. Kumbul, Y. Chen, N. Petrov, C. S. Vaucher et A. Yarovoy, “Impacts of mutual interference analysis in fmcw automotive radar,” dans *2023 17th European Conference on Antennas and Propagation (EuCAP)*, 2023, Conference Proceedings, p. 1–5.

[205] M. I. Ahbar, W. Tahir et N. S. Osman, “Performance comparison between s-band and c-band radar in quantitative precipitation estimation,” dans *2023 IEEE Symposium on Computers Informatics (ISCI)*, 2023, Conference Proceedings, p. 70–75.

[206] M. Frech, C. Hald, M. Schaper, B. Lange et B. Rohrdantz, “Assessing and mitigating the radar–radar interference in the german c-band weather radar network,” *Atmos. Meas. Tech.*, vol. 16, n°. 2, p. 295–309, 2023.

[207] E. Saltikoff, J. Y. N. Cho, P. Tristant, A. Huuskonen, L. Allmon, R. Cook, E. Becker et P. Joe, “The threat to weather radars by wireless technology,” *Bulletin of the American Meteorological Society*, vol. 97, n°. 7, p. 1159–1167, 2016.

[208] S. Alland, W. Stark, M. Ali et M. Hegde, “Interference in automotive radar systems : Characteristics, mitigation techniques, and current and future research,” *IEEE Signal Processing Magazine*, vol. 36, n°. 5, p. 45–59, 2019.

[209] L. Piotrowsky, S. Kueppers, T. Jaeschke et N. Pohl, “Distance measurement using mmwave radar : Micron accuracy at medium range,” *IEEE Transactions on Microwave Theory and Techniques*, vol. 70, n°. 11, p. 5259–5270, 2022.

[210] D. Zhu, W. Chen, J. Ding, C. Ma, Y. Yang, X. Hu et S. Pan, “Microwave photonic cognitive radar with a subcentimeter resolution,” *IEEE Transactions on Microwave Theory and Techniques*, vol. 72, n°. 9, p. 5519–5529, 2024.

[211] A. Sharma, S. Chaudhary, J. Malhotra, A. Parnianifard, S. Kumar et L. Wuttisittikulkij, “Impact of bandwidth on range resolution of multiple targets using photonic radar,” *IEEE Access*, vol. 10, p. 47 618–47 627, 2022.

[212] K. M. Cuomo, J. E. Pion et J. T. Mayhan, “Ultrawide-band coherent processing,” *IEEE Transactions on Antennas and Propagation*, vol. 47, n°. 6, p. 1094–1107, 1999.

[213] D. Huang, Y. Zhang, H. Zhao, M. He, Y. Wang et X. Qin, “Research progress on sub-band fusion technology for ultra-wideband radar signals,” dans *2024 Photonics Electromagnetics Research Symposium (PIERS)*. IEEE, 2024, Conference Proceedings, p. 1–11.

[214] X. Zhu, F. Zhang, B. Gao, S. Pan, Y. Zhou et G. Sun, “High-resolution detection by multiband fusion of photonics-based radars,” dans *2021 Photonics Electromagnetics Research Symposium (PIERS)*, 2021, Conference Proceedings, p. 794–800.

[215] B.-S. Kim, Y. Jin, J. Lee et S. Kim, “Fmcw radar estimation algorithm with high resolution and low complexity based on reduced search area,” *Sensors*, vol. 22, n°. 3, p. 1202, 2022.

[216] V. Gracheva et J. Ender, “Multichannel analysis and suppression of sea clutter for airborne microwave radar systems,” *IEEE Transactions on Geoscience and remote Sensing*, vol. 54, n°. 4, p. 2385–2399, 2016.

[217] Kasar, “A low profile compact three-way wilkinson power divider with size reduction,” *Journal of Electrical Engineering*, vol. 71, n°. 6, p. 419–422, 2020.

[218] K. G. Thomas et G. Praveen, “A novel wideband circularly polarized printed antenna,” *IEEE transactions on antennas and propagation*, vol. 60, n°. 12, p. 5564–5570, 2012.

[219] Z. Xu et M. Yuan, “An interference mitigation technique for automotive millimeter wave radars in the tunable q-factor wavelet transform domain,” *IEEE Transactions on Microwave Theory and Techniques*, vol. 69, n°. 12, p. 5270–5283, 2021.

[220] J. Wang, M. Ding et A. Yarovoy, “Matrix-pencil approach-based interference mitigation for fmcw radar systems,” *IEEE Transactions on Microwave Theory and Techniques*, vol. 69, n°. 11, p. 5099–5115, 2021.

[221] J. Grajal, V. Krozer, E. González, F. Maldonado et J. Gismero, “Modeling and design aspects of millimeter-wave and submillimeter-wave schottky diode varactor frequency multipliers,” *IEEE Transactions on microwave theory and techniques*, vol. 48, n°. 4, p. 700–711, 2000.

[222] X. Gu, S. Hemour, R. Khazaka et K. Wu, "Improving temperature stability of dickson charge pump rectifiers for battery-free wireless sensing applications," dans *2023 IEEE/MTT-S International Microwave Symposium - IMS 2023*, 2023, Conference Proceedings, p. 1160–1163.

[223] X. Gu, S. Hemour et K. Wu, "Improving conversion loss performance of fully passive harmonic transponder at low temperature," dans *2019 IEEE Wireless Power Transfer Conference (WPTC)*, 2019, p. 395–398.

[224] B. Gao, F. Zhang, Y. Yao et S. Pan, "Photonics-based multiband radar applying an optical frequency sweeping comb and photonic dechirp receiving," dans *2018 Asia Communications and Photonics Conference (ACP)*, Conference Proceedings, p. 1–3.

[225] Y. Ning, F. Zhou, L. Liu et X. Bai, "Isar multi-band fusion based on attributed scattering center," dans *2018 International Conference on Radar (RADAR)*, Conference Proceedings, p. 1–5.

[226] P. Ghelfi, F. Laghezza, F. Scotti, D. Onori et A. Bogoni, "Photonics for radars operating on multiple coherent bands," *Journal of Lightwave Technology*, vol. 34, n°. 2, p. 500–507, 2016.

[227] P. Li, W. Bai, X. Zou, N. Zhong, W. Pan et L. Yan, "Millimeter-level resolution photonic multiband radar using a single mzm and sub-ghz-bandwidth electronics," dans *2023 Optical Fiber Communications Conference and Exhibition (OFC)*, Conference Proceedings, p. 1–3.

[228] J.-M. Muñoz-Ferreras, Z. Peng, R. Gómez-García et C. Li, "Review on advanced short-range multimode continuous-wave radar architectures for healthcare applications," *IEEE Journal of Electromagnetics, RF and Microwaves in Medicine and Biology*, vol. 1, n°. 1, p. 14–25, 2017.

[229] W. Hu, Z. Zhao, Y. Wang, H. Zhang et F. Lin, "Noncontact accurate measurement of cardiopulmonary activity using a compact quadrature doppler radar sensor," *IEEE Transactions on Biomedical Engineering*, vol. 61, n°. 3, p. 725–735, 2013.

[230] G. Vinci, S. Lindner, F. Barbon, S. Mann, M. Hofmann, A. Duda, R. Weigel et A. Koelpin, "Six-port radar sensor for remote respiration rate and heartbeat vital-sign monitoring," *IEEE Transactions on Microwave Theory and Techniques*, vol. 61, n°. 5, p. 2093–2100, 2013.

[231] S. A. Shah et F. Fioranelli, "Rf sensing technologies for assisted daily living in healthcare : A comprehensive review," *IEEE Aerospace and Electronic Systems Magazine*,

vol. 34, n°. 11, p. 26–44, 2019.

[232] D. Krauss, L. Engel, T. Ott, J. Bräunig, R. Richer, M. Gambietz, N. Albrecht, E. M. Hille, I. Ullmann et M. Braun, "A review and tutorial on machine learning-enabled radar-based biomedical monitoring," *IEEE Open Journal of Engineering in Medicine and Biology*, 2024.

[233] B.-K. Park, O. Boric-Lubecke et V. M. Lubecke, "Arctangent demodulation with dc offset compensation in quadrature doppler radar receiver systems," *IEEE transactions on Microwave theory and techniques*, vol. 55, n°. 5, p. 1073–1079, 2007.

[234] E. Antolinos et J. Grajal, "Improving vital signs monitoring in real-world environments with w-band phased-array radars," *IEEE Transactions on Microwave Theory and Techniques*, p. 1–12, 2025.

[235] T. Micallef, I. Hussain et K. Wu, "Multifunction transceiver for data communication, radar sensing and power transfer," *Electromagnetic Science*, 2025.

[236] X. Li, Z. Han, G. Zhu, Y. Shi, J. Xu, Y. Gong, Q. Zhang, K. Huang et K. B. Letaief, "Integrating sensing, communication, and power transfer : From theory to practice," *IEEE Communications Magazine*, vol. 62, n°. 9, p. 122–127, 2024.

[237] Z. Fang, W. Wang, J. Wang, B. Liu, K. Tang, L. Lou, C.-H. Heng, C. Wang et Y. Zheng, "Integrated wideband chip-scale rf transceivers for radar sensing and uwb communications : A survey," *IEEE Circuits and Systems Magazine*, vol. 22, n°. 1, p. 40–76, 2022.

[238] I. Hussain et K. Wu, "Concurrent dual-band heterodyne interferometric receiver for multistandard and multifunction wireless systems," *IEEE Transactions on Microwave Theory and Techniques*, vol. 69, n°. 11, p. 4995–5007, 2021.

[239] J. Deng, P. Burasa et K. Wu, "Multichannel and multifunction interferometric receiver architectures for multistandard millimeter-wave and terahertz applications," dans *2024 IEEE Wireless and Microwave Technology Conference (WAMICON)*. IEEE, Conference Proceedings, p. 1–4.

[240] ——, "Joint multiband linear interferometric receiver for integrated microwave and terahertz sensing and communication systems," *IEEE Transactions on Microwave Theory and Techniques*, vol. 72, n°. 9, p. 5550–5562, 2024.

[241] ——, "Self-contained dual-input interferometric receiver for paralleled-multichannel wireless systems," *IEEE Transactions on Circuits and Systems I : Regular Papers*, vol. 71, n°. 2, p. 934–947, 2023.

[242] S. Rapuano, “Analog-to-information converters : research trends and open problems,” dans *2016 26th International Conference Radioelektronika (RADIOELEKTRONIKA)*. IEEE, Conference Proceedings, p. 10–17.

[243] A. Mohammadian et C. Tellambura, “Rf impairments in wireless transceivers : Phase noise, cfo, and iq imbalance–a survey,” *IEEE access*, vol. 9, p. 111 718–111 791, 2021.

[244] Z. Wei, H. Liu, X. Yang, W. Jiang, H. Wu, X. Li et Z. Feng, “Carrier aggregation enabled integrated sensing and communication signal design and processing,” *IEEE Transactions on Vehicular Technology*, vol. 73, n^o. 3, p. 3580–3596, 2023.

[245] H. Liu, Z. Wei, J. Piao, H. Wu, X. Li et Z. Feng, “Carrier aggregation enabled mimo-ofdm integrated sensing and communication,” *IEEE Transactions on Wireless Communications*, 2025.

[246] N. Zhong, Y. Du, X. Zou, X. Deng, W. Bai, C. Yang, W. Pan et L. Yan, “Multiple-in-one photonic integrated transceiver for multi-chirp-rate multi-band isar system and coherent fusion processing,” *Journal of Lightwave Technology*, 2024.

[247] T. Micallef, X. Gu et K. Wu, “Diode-based wideband harmonic generation for future nonlinear sensing applications,” *IEEE Transactions on Microwave Theory and Techniques*, 2025.

[248] P. Cheong, K. Wu et K.-W. Tam, “Nonlinear communication system with harmonic diversity,” *IEEE Transactions on Microwave Theory and Techniques*, vol. 63, n^o. 12, p. 4130–4149, 2015.

[249] J. Östh, M. Karlsson, O. Owais, A. Serban et S. Gong, “Baseband complexity comparison of six-, five-, and four-port receivers,” *Microwave and Optical Technology Letters*, vol. 54, n^o. 6, p. 1502–1506, 2012.

[250] K. Haddadi, M. Wang, D. Glay et T. Lasri, “A new range finder based on a four-port junction,” *IEEE Sensors Journal*, vol. 9, n^o. 6, p. 697–698, 2009.

[251] I. Hussain et K. Wu, “Low-if interferometric receiver architecture for massive-iot wireless systems,” dans *2020 50th European Microwave Conference (EuMC)*. IEEE, Conference Proceedings, p. 694–697.

[252] B. Clerckx, Y. Mao, Z. Yang, M. Chen, A. Alkhateeb, L. Liu, M. Qiu, J. Yuan, V. W. S. Wong et J. Montojo, “Multiple access techniques for intelligent and multifunctional 6g : Tutorial, survey, and outlook,” *Proceedings of the IEEE*, vol. 112, n^o. 7, p. 832–879, 2024.

[253] K. Haddadi, H. El Aabbaoui, C. Loyez, D. Glay, N. Rolland et T. Lasri, “Wide-band 0.9 ghz to 4 ghz four-port receiver,” dans *2006 13th IEEE International Conference on Electronics, Circuits and Systems.* IEEE, Conference Proceedings, p. 1316–1319.

[254] D. Psychogiou, R. Gómez-García et D. Peroulis, “Recent advances in reconfigurable microwave filter design.” IEEE, Conference Proceedings, p. 1–6.

[255] K. Biswal, S. Swain, M. C. Tripathy et S. K. Kar, “Re-configurable band-stop and all-pass filter using fractional-order topology,” *International Journal of Advanced Technology and Engineering Exploration*, vol. 9, n°. 97, p. 1773, 2022.

[256] E. J. Denlinger, “Losses of microstrip lines,” *IEEE Transactions on Microwave Theory and Techniques*, vol. 28, n°. 6, p. 513–522, 2003.

[257] A. O. Olopade, A. Hasan et M. Helaoui, “Concurrent dual-band six-port receiver for multi-standard and software defined radio applications,” *IEEE Transactions on microwave theory and techniques*, vol. 61, n°. 12, p. 4252–4261, 2013.

[258] Y. Xu et R. G. Bosisio, “Four-port digital millimetric receiver (fp/dmr),” *Microwave and Optical Technology Letters*, vol. 22, n°. 5, p. 350–355, 1999.

ANNEXE A LISTE DES PUBLICATIONS ET PRIX

Articles de journaux évalués par les pairs

[J1] **T. Micallef**, X. Gu, P. Burasa and K. Wu, "Harmonic Interferometric Receiver for Multifunction Wireless Systems," in IEEE Transactions on Microwave Theory and Techniques (Under review).

[J2] **T. Micallef**, X. Gu and K. Wu, "Multi-Mode Multi-Band ISAC Technique for Real-Time Healthcare Monitoring," in IEEE Microwave and Wireless Technology Letters (Under review).

[J3] **T. Micallef**, X. Gu and K. Wu, "Resolution Enhancement of Radar Systems through Nonlinear Sensing," in IEEE Transactions on Microwave Theory and Techniques (Under review).

[J4] **T. Micallef**, A. Murcott, X. Gu and K. Wu, "Enhancing Radar System Performances via the Fusion of Scattered Non-Contiguous Frequency Sub-Bands," in IEEE Transactions on Microwave Theory and Techniques (Under review).

[J5] **T. Micallef**, X. Gu and K. Wu, "Diode-Based Wideband Harmonic Generation for Future Nonlinear Sensing Applications," in IEEE Transactions on Microwave Theory and Techniques, vol. 73, no. 9, pp. 6180-6191, Sept. 2025, doi : 10.1109/TMTT.2025.3557189.

[J6] **T. Micallef**, Intikhab Hussain, and Ke Wu, “Multifunction transceiver for data communication, radar sensing and power transfer,” Electromagnetic Science, vol. 3, no. 2, article no. 0100491, 2025. doi : 10.23919/emsci.0024.0049

[J7] **T. Micallef**, X. Gu and K. Wu, "Electric Field Energy Harvesting From High-Voltage Power Lines for Consumer Batteryless Wireless Sensor Networks," in IEEE Transactions on Consumer Electronics, vol. 71, no. 1, pp. 2322-2331, Feb. 2025, doi : 10.1109/TCE.2024.3503492.

Articles de magazines

[M1] **T. Micallef**, "Deep Integration of Wireless Multifunctionality : A Vision for Future-Ready Systems [Tom Brazil Award Essay Competition]," in IEEE Potentials (Under review)

[M2] **T. Micallef** and A. Ghadimi, "The IEEE Student Branch of Polytechnique Montreal in Action for Innovation, Collaboration, and Celebration [MTT-S Society News]," in IEEE Microwave Magazine, vol. 25, no. 12, pp. 140-141, Dec. 2024, doi :10.1109/ MMM.2024.3441516.

Articles de conférences à comité de lecture

[C1] X. Gu, **T. Micallef**, N. Barbot, K. Wu and S. Hemour, "Leveraging Nonlinearity for Joint RF Power Harvesting, Sensing and Communications," 2025 IEEE International Conference on RFID Technology and Applications (RFID-TA), Valence, France (Accepted for presentation).

[C2] **T. Micallef**, R. Marcelino, X. Gu and K. Wu, "Thermal Effect on Wideband Harmonic Generation for Future Wireless Sensing," 2025 IEEE International Symposium on Antennas & Propagation and North American Radio Science Meeting, Ottawa, Canada (To be published).

[C3] **T. Micallef**, X. Gu and K. Wu, "Multi-Band Wireless Sensing Fusion and Communication through Hybrid Multiplexing," 2025 IEEE International Symposium on Antennas & Propagation and North American Radio Science Meeting, Ottawa, Canada (To be published).

[C4] **T. Micallef**, X. Gu and K. Wu, "Resolution Enhancement of Radar Systems through Super Fusion of Non-Contiguous Frequency Bands," 2024 21st European Radar Conference (EuRAD), Paris, France, 2024, pp. 356-359, doi : 10.23919/EuRAD61604.2024 .10734957.

[C5] **T. Micallef**, X. Gu and K. Wu, "Electric Field Energy Harvesting from High-Voltage Power Lines for Batteryless LoRaWAN," 2024 IEEE Wireless Power Technology Conference and Expo (WPTCE), Kyoto, Japan, 2024, pp. 41-44, doi : 10.1109/WPTCE59894 .2024.10557305.

[C6] X. Gu, M. Gulshan, **T. Micallef**, R. Khazaka, and K. Wu, "Evaluation of Discrepancies in Theoretical and Experimental RF Energy Harvesting Efficiency From Measured Diode Parameters," 2024 IEEE MTT-S International Conference on Numerical Electromagnetic and Multiphysics Modeling and Optimization (NEMO'2024), Montreal, Canada, 2024, in proceedings.

Présentations par affiches

[P1] **T. Micallef**, X. Gu and K. Wu, "Electric Field Energy Harvesting from High-Voltage Power Lines for Batteryless LoRaWAN," 2024 IEEE Wireless Power Technology Conference and Expo (WPTCE), Kyoto, Japan, 2024.

Mémoire de maîtrise

[R1] **T. Micallef**, "Récupération de l'énergie des champs électromagnétiques à proximité des lignes à haute tension pour des réseaux de capteurs sans fils," End-of-studies Project Report, École Nationale Supérieure de Physique, Électronique, Matériaux (INP-Phelma), Grenoble, France, 2022.

Brevets

[B1] **T. Micallef** and K. Wu, "Systems and Methods for Enhancing Signal Resolution via Time-Domain Fusion of Beat Signals Obtained From a Plurality of Frequency Sub-Bands", 2025 (Submitted).

Prix

[P1] The Marconi Society - Paul Baran Young Scholar Award, Oct. 2025.

[P2] 1^{st} Prize - European Microwave Week Tom Brazil Fellowship Award - Essay Competition, Sept. 2025.

[P3] European Microwave Association Internship Award, 2025.

[P4] 1^{st} Prize - Student Innovation Competition - Communications for a Sustainable Space Ecosystem, Co-located with IEEE International Conference on Communications, Montréal, Canada, June 2025.

[P5] MTT-S T-Shirt Design Competition Award, May 2025.

[P6] Excellence Award - Best Oral Presentation - PolyCongRÉ, Montréal, Canada, March 2025.

[P7] Best Section Volunteer - IEEE Montréal Section, Montréal, Canada, Nov. 2024.

[P8] Travel Grant Award - European Microwave Week, Paris, France, Sept. 2024.

[P9] Travel Grant Award - Wireless Power Technology Conference and Expo, Kyoto, Japan, May 2024.

[P10] Best Student Paper Award - Wireless Power Technology Conference and Expo, Kyoto, Japan, May 2024.

[P11] 1^{st} Prize – Student Rectenna Design Competition - IEEE Montreal Section, Montréal, Canada, May 2024.

[P12] Best Section Volunteer - IEEE Montreal Section, Montréal, Canada, Nov. 2023.

[P13] Team Bronze Medal (Team Leader) – French Physicist's Tournament, Paris, France, Feb. 2020.

Distinctions

[D1] IEEE MTT-S Student Ambassador, 2025.

[D2] IEEE Day Ambassador, 2025.

[D3] IEEE Day Ambassador, 2024.

[D4] IEEE Day Ambassador, 2023.